UNIVERSITE MATIERE BRETAGNE MOLECULES LOIRE ET MATERIAUX

UNIVERSITÉ DE RENNES 1

Thèse de doctorat de

L'UNIVERSITÉ DE RENNES 1
Comue Université Bretagne Loire

Ecole Doctorale N° 596
Matière Molécules et Matériaux
Spécialité: Sciences des Matériaux

Par

Marcello MENEGHETTI

Microstructured optical fibers based on chalcogenide glasses for mid-IR supercontinuum generation

Thèse présentée et soutenue à Rennes le 20 Décembre 2019
Unité de recherche 6226 - Institut des Sciences Chimiques de Rennes
Thèse N°:

Composition du Jury:

Président:		
Rapporteurs:	Laurent BIGOT	Directeur de recherche CNRS, Université Lille 1
	Laeticia PETIT	Professeur, Tampere University of Technology
Examinateurs:	Jean-Luc ADAM	Directeur de recherche CNRS, Université de Rennes 1
	Maurizio FERRARI	Directeur de recherche CNR, IFN-CNR Trento
	Franck JOULAIN	Ingénieur R&D, Le Verre Fluoré
Directeur de thèse:	Johann TROLES	Professeur, Université de Rennes 1

Contents

List of Figures

List of Tables

Résumé de la thèse

Introduction

Cette thèse a été effectuée dans le cadre d'un projet ITN (Innovative training network) Marie Curie, dénommé SUPUVIR (SUPercontinuum broadband light sources covering UV to IR applications), financé par l'union européenne qui combine les efforts de 6 universités et 4 entreprises européennes. Ce projet finance alors 15 thèses différentes reparties entre les 10 partenaires. Les sujets de thèse proposées dans le projet abordent aussi bien la réalisation de fibres en verres de silice ou verres plus exotiques (verres d'oxydes de tellure, verres de fluorures et verres de chalcogénures), que la modélisation et la réalisation de supercontinuum de l'UV jusqu'au moyen infrarouge. Les travaux de la présente thèse s'inscrivent donc dans ce contexte avec un sujet focalisé sur le développement de verres et fibres en verres de chalcogénures pour la génération de supercontinuum dans le moyen infrarouge a été effectué. La génération de nouvelles sources dans le moyen infrarouge est un sujet en pleine effervescence. En effet, la réalisation de ces nouvelles sources ouvrirait des champs d'applications gigantesques dans le domaine de l'imagerie et la spectroscopie infrarouge (détection d'espèces chimiques dangereuses, diagnostiques médicaux, suivis de procédés industriels...). Plus précisément, l'objectif de ces travaux de thèse est de réaliser des fibres infrarouges de haute pureté (dans la gamme de longueurs d'onde de 2 à 12 μm) à base de verres de chalcogénures, avec un profil de dispersion chromatique taillé sur mesure, en combinant les sciences du verre et des techniques innovantes de mise en forme des fibres. La conception de la fibre devra présenter le meilleur compromis entre les paramètres non linéaires (principalement contrôlés par la taille du cœur et la composition du verre), la position de la longueur d'onde de dispersion nulle (en fonction de la longueur d'onde de pompage souhaitée ou choisie) et la largeur de la fenêtre de transmission. Les fibres fabriquées seront testées et utilisées pour la génération de supercontinuum en coopération avec différents membres et partenaires du projet SUPUVIR ou d'autres partenaires comme la société Le Verre Fluoré. Le travail présenté ici a été réalisé en étroite collaboration avec la société SelenOptics (partenaire associé du projet SUPUVIR) plus particulièrement pour la mise en forme et l'étirage des fibres microstructurées.
Les travaux de la thèse sont présentés en quatre grands chapitres. Le premier chapitre introduit le sujet et quelques notions théoriques et présente également un état de l'art sur la génération de supercontinuum dans le moyen infrarouge. Le deuxième chapitre présente la réalisation de verres de haute qualité optique, étape fondamentale à la réalisation de fibres optiques performantes. Les travaux de ce cette thèse se sont fortement focalisés sur la réalisation de fibres microstructurées en verres de chalcogénures véritable spécialité de l'Université de Rennes et de sa spin off la société SelenOptics. Le chapitre 3 décrit sur la réalisation de ces fibres microstructurées et leurs utilisations pour la génération supercontinuum. Enfin, le chapitre 4, présente la réalisation très originale et inédite d'une fibre en verres de chalcogénures à gradient d'indice.

Chapitre 1: Introduction et état de l'art

Ce premier chapitre est consacré à la description de quelques notions théoriques et notions de bases permettant de placer les travaux de thèse dans leur environnement. Les propriétés des verres de chalcogénures sont présentées et placées dans le contexte de leurs utilisations pour la génération de nouvelles sources dans le moyen infrarouge. En effet, dans ce contexte les verres de chalcogénures et plus particulièrement les verres à base de sélénium présentent deux avantages

majeurs. Ils sont transparents dans le moyen infrarouge jusqu' à 18-20 μm pour des verres massifs (épaisseur $<$ à 3 mm) et transparents jusqu'à 10-12 μm sur fibres (longueur $>$ 1 m). De plus, les verres de chalcogénures présentent des propriétés optiques non linéaires élevées, propices à l'obtention de forts effets non linéaires même avec de faibles intensités lumineuses. Sous forme de fibres optiques ces deux propriétés seront exploitées pour la génération de sources supercontinuum dans le moyen infrarouge. La génération de telles sources à large bande est obtenue par l'addition de multiples effets non linéaires (modulation de phase, mélange à quatre ondes, génération de solitons...) permettant à partir d'une forte impulsion laser de générer un large continuum de longueurs d'onde.
Le tableau A présente quelques supercontinua obtenus dans différentes fibres de verres.
Les supercontinua générés dans la silice, même fortement dopée en germanium ne peuvent pas atteindre des longueurs d'onde au-delà de 3 μm. Il est possible d'obtenir des supercontinua jusqu'à 5 μm avec des fibres en verres d'oxydes de tellure ou des fibres en verres de fluorures. Enfin des supercontinua au-delà de 13 μm ont été observés et mesurés dans des fibres en verres de chalcogénures.

Tableau A: *Exemples de supercontinua obtenus dans différentes fibres.*
(MOPA: Master Oscillator Power Amplifier; TDF: Thulium Doped Fiber; TDFL: Thulium Doped Fiber Laser; TDFA: Thulium Doped Fiber Amplifier; EDFA: Erbium Doped Fiber Amplifier; EYDFA: Erbium Ytterbium Doped Fiber Amplifier; OPG: Optical Parametric Generator; OPO: Optical Parametric Oscillator; OPA: Optical Parametric Amplifier; NDFG: Noncollinear Difference Frequency Generator; SPPG: Single-Pass Parametric Generation.)

Glass system	Type of fiber	Pumping	Output spectral range	Output power
$GeO_2 - SiO_2$	Graded index	MOPA	0.7 μm – 3.2 μm	1.44 W
$GeO_2 - SiO_2$	Step index	TDFL + TDFA	2 μm – 3 μm	30 W
ZBLAN	Step index	1550nm + TDF	1.75 μm – 4.75 μm	1.2 W
ZBLAN	Step index	1550nm + EDFA + EYDFA + TDFA	1.9 μm – 4.2 μm	15.2 W
Fluoroindate	Step index	OPG + EDFA	2.4 μm – 5.4 μm	10 mW
Fluoroindate	Step index	Tm-doped MOPA	0.8 μm – 4.7 μm	11.3 W
Tellurite	Step index	Post-amplified OPO	1.3 μm – 5.3 μm	150 mW
Chalcogenide	Step index	OPA + NDFG	1.4 μm – 13.3 μm	150 μW
Chalcogenide	Tapered PCF	SPPG	1 μm – 11.5 μm	35.4 mW
Chalcogenide	Step index	Cascaded	2 – 11 μm	417 mW

Chapitre 2 : Synthèse de verres de chalcogénures de haute pureté

Le chapitre 2 est consacré à la description de la synthèse et à l'étude de la synthèse de verres de chalcogénures de haute pureté. Ce travail est essentiel à l'obtention de fibres microstructurées performantes.

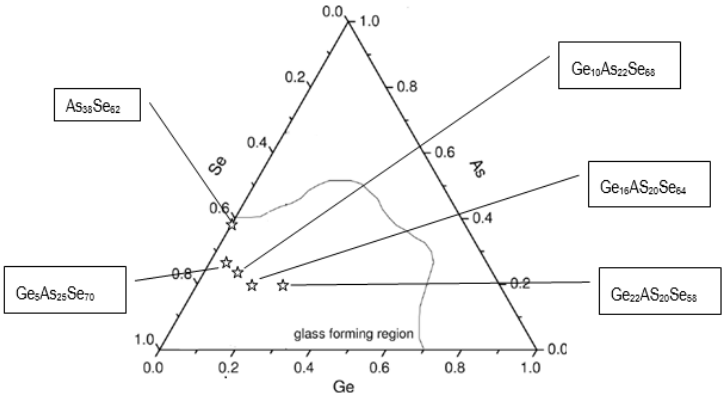

Figure A: *Système vitreux Ge-As-Se et compositions principalement étudiées pendant les travaux de thèse.*

Les compositions de verres étudiées dans ces travaux de thèse sont des compositions de verres de sélénures du système Ge-As-Se (figure A). Ce système ternaire vitreux offre de bons compromis entre les propriétés thermiques (propriétés viscoplastiques, stabilité face à la cristallisation), leur transmission dans le proche et moyen infrarouge et leurs propriétés optiques non linéaires et plus particulièrement leur indice de réfraction non linéaire entre 500 et 1000 fois supérieur à celui de la silice. Les compositions les plus étudiées au cours de ces travaux de thèse sont présentées dans le tableau B.

Tableau B: *Principales caractéristiques physiques des principaux verres étudiés.*

Composition	$As_{38}Se_{62}$	$Ge_5As_{25}Se_{70}$	$Ge_5As_{30}Se_{65}$	$Ge_{10}As_{22}Se_{68}$	$Ge_{16}As_{20}Se_{64}$	$Ge_{22}As_{20}Se_{58}$
Average coordination number	2.38	2.35	2.40	2.42	2.52	2.64
T_g(℃, ±2℃)	165	139	165	175	235	292
T($\eta = 10^5$ Pa · s) (℃, ±5℃)	258	-	269	291	357	-
Refractive index @1.55μm	2.808	-	2.704	2.618	2.579	2.542

Les verres de chalcogénures sont fabriqués par fusion sous vide dans un tube scellé de silice à des températures comprises entre 650 et 950℃ suivant les compositions. Malgré l'utilisation de produits de départ de haute pureté ($>$ 99.99%), si aucune purification n'est mise en œuvre de nombreuses bandes d'absorption liées à la présence d'impuretés sont observées sur les courbes d'atténuation des fibres (courbe noire, figure B). On notera par exemple la présence de liaisons O-H (à 2,92 μm), Se-H (à 4,57 et 4,12 μm) Ge-O (à 7,9 μm) et As-O (à 8,9 μm). La mise en place de procédés de purification et notamment de multiples distillations des verres avec l'utilisation de "getters" (piégeurs, attrapeurs en français), a permis notamment de piéger les oxygènes, les hydrogènes et les particules de carbone, et ainsi permis d'éliminer la plupart des bandes d'impuretés et d'obtenir un minimum d'atténuation inférieur à 0,1 dB/m à 5,5 μm. De telles pertes correspondent à l'état de l'art dans ce type de verres (courbe rouge, figure B). Au cours de ces travaux, l'utilisation du couple magnésium métallique et de $TeCl_4$ s'est révélée comme étant la meilleure combinaison de "getters". Ces travaux ont également montré, que leur quantité doit être adaptée à la qualité des produits de départs et que la quantité de chacun d'entre eux influe sur l'efficacité de l'autre.
Les verres fabriqués et optimisés ont ensuite été utilisés pour la réalisation de fibres microstructurées (chapitre 3) et de fibres à gradient d'indice (chapitre 4).

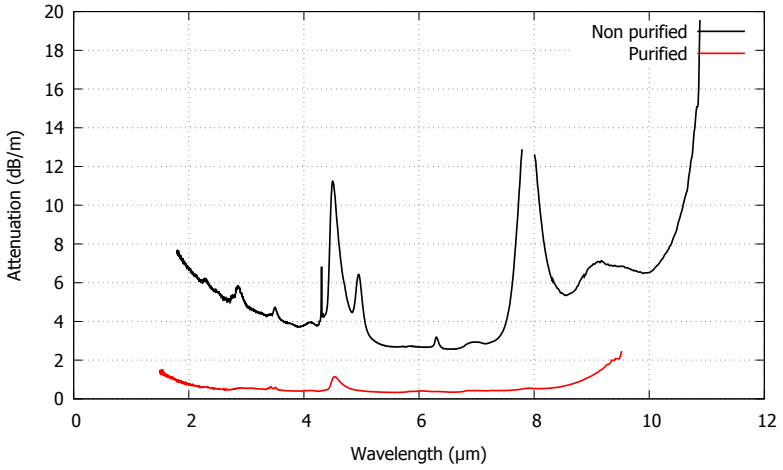

Figure B: *Comparaison de courbes d'atténuation de deux fibres issues d'un verre purifié et non purifié.*

Chapitre 3 : Fibres microstructurées en verres de chalcogénures

Ce chapitre représente le cœur de ces travaux de thèse. L'intérêt de cette étude est de combiner les propriétés des fibres en verres de chalcogénures (transmission dans le moyen infrarouge et propriétés optiques non linéaires) aux propriétés optiques de propagation des fibres microstructurées (propagation infiniment monomode, gestion de la dispersion, possibilité de réaliser des fibres à maintien de polarisation...).
La méthode de fabrication choisie pour la réalisation des fibres microstructurées est la méthode du moulage. Cette technique a été mise au point à Rennes avec la collaboration de la plateforme PERFOS et est à l'origine de la création de la société SelenOptics en 2015.

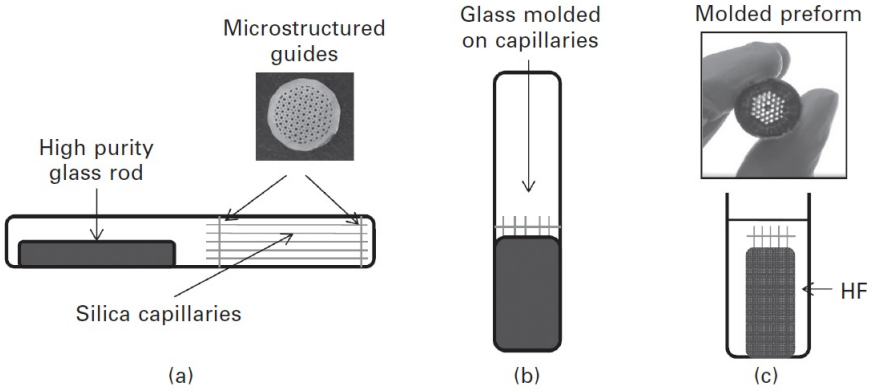

Figure C: *Fabrication d'une préforme microstructurées par la méthode de moulage.*

La méthode de moulage est illustrée par la figure C. Elle consiste à faire couler, sous l'action de la température, un verre de haute pureté sur un moule de silice. Puis l'ensemble, verre de chalcogénures-moule, est trempé afin de figer la préforme microstructurée. Après un recuit, proche de la température de transition vitreuse du verre, la préforme, dans laquelle restent emprisonnés les capillaires du moule de silice, est retirée de l'ampoule extérieure du moule et placée dans une solution d'acide fluorhydrique (HF). Ce traitement au HF permet de dissoudre entièrement les capillaires de silice et d'obtenir une préforme monolithique. Les fibres microstructurées sont ensuite obtenues par étirage de ces préformes avec l'ajout d'une pression dans les trous de la préforme microstructurée, si la géométrie recherchée le demande. La figure D présente un exemple de fibre microstructurée et de sa courbe d'atténuation.

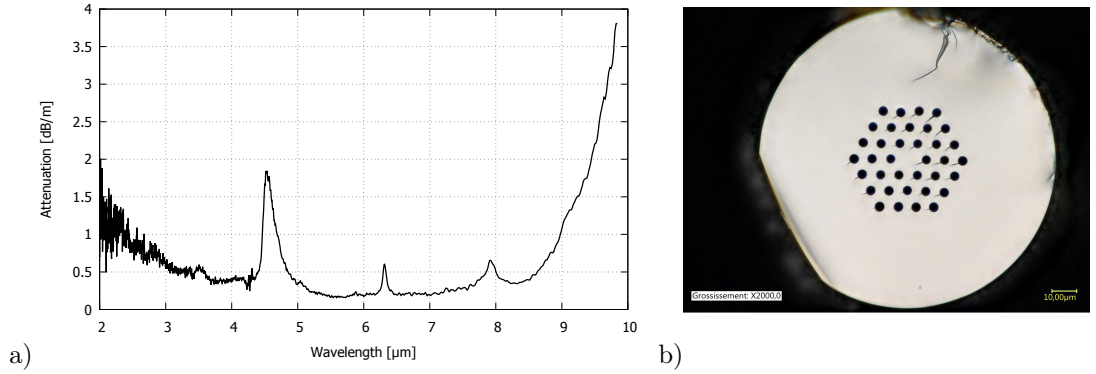

Figure D: *Exemple d'une fibre microstructurée en verre Ge-As-Se et sa courbe d'atténuation.*

Les fibres réalisées ont notamment permis de réaliser la première génération de supercontinuum dans une fibre de chalcogénures microstructurée à maintien de polarisation. Ces résultats ont

été obtenus en étroite collaboration avec deux partenaires du consortium du projet SUPUVIR (FEMTO-ST et DTU). Bien que les supercontinua ne s'étendent que de 3 à 6 μm, une forte dépendance des longueurs d'onde générées a été observée en fonction de l'angle de polarisation des impulsions incidentes et ce avec une périodicité de 90° (figure E). Les supercontinua ont été obtenus par pompage de la fibre chalcogénures par des impulsions d'environ 250 fs générées à 4,0 μm ou 4, 53 μm dans un assemblage périodique de MgO :LiNbO3 (Magnesium-doped Periodically Poled Lithium Niobate , MgO PPLN). La puissance moyenne en sortie de fibre de chalcogénures a été mesurée à 11 mW avec un spectre étendu de 3 à 6 μm.

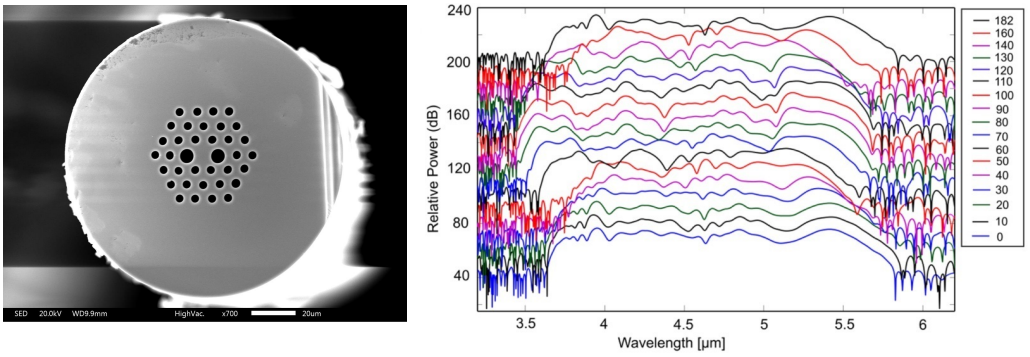

Figure E: *Dépendance de la génération supercontinuum en fonction de l'ongle de polarisation de l'impulsion incidente dans une fibre microstructurée en verre de chalcogénures à maintien de polarisation.*

La voie la plus prometteuse pour le développement de sources lasers à larges bandes dans le moyen infrarouge est probablement la génération de supercontinuum par concaténation de fibres et par la même occasion la concaténation de supercontinua.
Par exemple, les travaux menés au cours de cette thèse ont permis grâce à une "concaténation" de collaborations étroites avec les sociétés LEUKOS, le verre fluoré , Selenoptics et l'Université de Rennes 1, d'obtenir des supercontinua dans des fibres de composition $As_{38}Se_{62}$ d'environ 4 à 7 m de long.

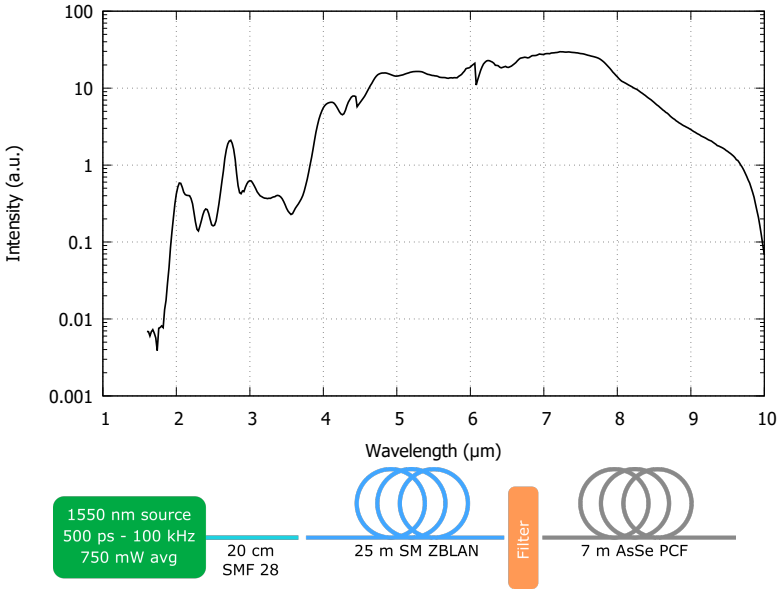

Figure F: *Spectre supercontinuum généré par concaténation dans une fibre microstructurée de composition* $As_{38}Se_{62}$.

Les spectres obtenus s'étendent de 2 à 10 μm avec une puissance moyenne entre 10 et 15 mW. On notera que pour des applications en spectroscopie et/ou biologie la puissance est largement suffisante. La figure F présente la concaténation de fibres et un exemple de supercontinuum obtenu en sortie de fibre de chalcogénures. On notera ici que le maximum de puissance de sortie est situé entre 4 et 9 μm, longueurs d'onde qui ne sont habituellement jamais disponibles sous forme de source fibrée. Ces résultats sont les prémices au développement de nouvelles sources qui seront bientôt disponibles à la vente par le consortium LEUKOS, Le Verre Fluoré et SelenOptics.
Enfin, un supercontinuum généré dans une fibre microstructurée en verres de chalcogénures a été utilisé comme source dans une expérience de spectroscopie dans le moyen infrarouge. Pour cela, un composé organique (quelques gouttes de méthyl salicylate placées entre deux lames de KBr transparentes dans le MIR) a été placé sur le trajet optique du supercontinuum obtenu par concaténation afin de détecter ses signatures infrarouges. Le spectre obtenu entre 5 et 10 μm, présenté en figure G, montre clairement la superposition des bandes d'absorption observées et les données de transmission du composé répertoriées dans la littérature scientifique.

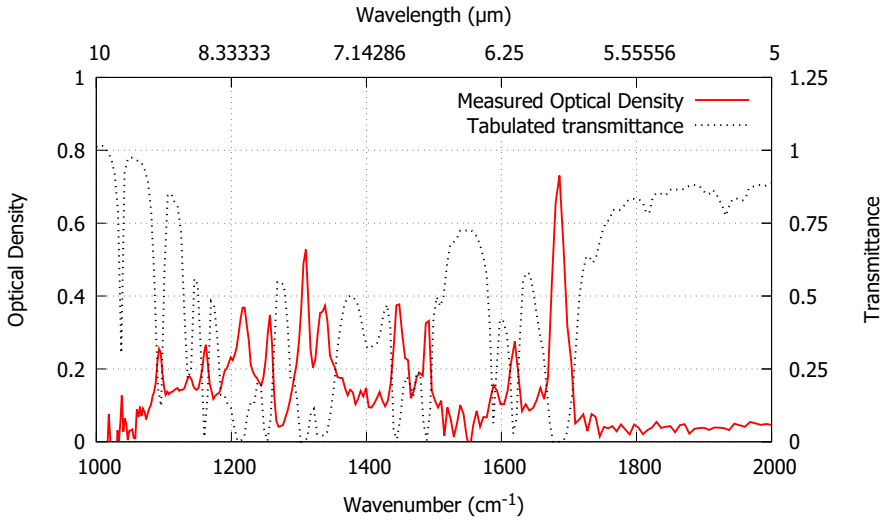

Figure G: *Détection des bandes d'absorption du méthyl salicylate à l'aide d'un supercontinuum obtenu par concaténation: fibre silice - fibre fluorée - fibre de chalcogénures.*

Chapitre 4 : Fabrication de fibres en verres de chalcogénures à gradient d'indice

Le contrôle du profil de dispersion dans les fibres est un élément important dans la génération de supercontinuum. Dans le chapitre 3 la dispersion des fibres est contrôlée, gérée par la géométrie des fibres microstructurées: taille du cœur, taille des trous et valeur du rapport entre la taille des trous et la distance entre les trous. Les fibres classiques à saut d'indice offrent peu de possibilités de contrôle de la dispersion si on excepte la taille du cœur et la différence d'indice entre le cœur et la gaine. Une possibilité de contrôle de la dispersion et notamment de la forme de la dispersion en fonction de longueur d'onde peut être la réalisation de fibres à gradient d'indice. Cependant la communauté scientifique ne recense aucune réalisation de fibres à gradient d'indice en verre de chalcogénures. C'est dans ce contexte qu'une méthode de fabrication par microstructuration du cœur d'une fibre développée par l'ITME (également partenaire du projet européen SUPUVIR) va être testée avec des verres de chalcogénures.
L'idée est de microstructurer le cœur d'une fibre avec des plots de deux indices différents, et donc des inclusions de haut et bas indices. Le gradient d'indice est obtenu par la présence d'inclusions de bas indice de plus en plus nombreuses lorsque l'on s'éloigne du centre du cœur de la fibre (figure H).

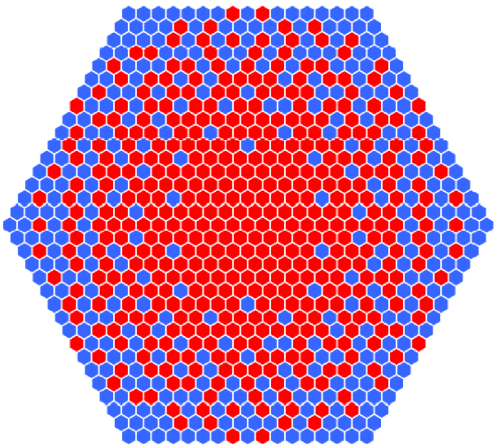

Figure H: *Exemple de géométrie d'un cœur à gradient d'indice (en rouge les inclusions de haut indice, en bleu les inclusions de bas indice).*

En fin de procédé, la taille des inclusions devra être largement inférieure aux longueurs d'onde d'utilisations.
La fabrication d'une telle fibre demande la mise œuvre de plusieurs étapes (figure I) :

- Fabrication des barreaux de verres de chalcogénures de bas indice
- Fabrication des barreaux de verres de chalcogénures de haut indice
- Empilement de la préforme à gradient d'indice
- Manchonnage de la préforme à gradient d'indice
- Etirage de l'empilement en forme de baguette à gradient d'indice
- Fabrication des tubes en verre de bas indice par centrifugation
- Etirage de la fibre à gradient d'indice par la méthode "baguette dans tube"

Un premier essai a été entrepris avec le verre $As_{38}Se_{62}$, pour les inclusions de haut indice et le verre $Ge_{10}As_{22}Se_{68}$ pour les inclusions de bas indice. Un empilement contenant donc 817 barreaux de 450 μm de diamètre a été réalisé (compromis entre taille de la préforme et les performances attendues). Ensuite, des baguettes de 1, 2 et 3 mm ont été fabriquées. Enfin, deux fibres ont été réalisées par étirage d'une baguette insérée dans un tube (de diamètre extérieur de 12 mm et diamètre intérieur de 4 mm fabriqué par centrifugation avec le même verre que les inclusions de bas indice), l'une avec une baguette de 1 mm de diamètre et l'autre avec une baguette 3 mm de diamètre. Dans le cas de la première fibre, avec une baguette à gradient d'indice de 1 mm, le cœur, trop petit, était totalement déformé et aplati. Avec la baguette de 3 mm, il a été possible d'obtenir une fibre dans laquelle le cœur n'était pas déformé et avait gardé parfaitement l'organisation et la structure de la baguette à gradient d'indice. Cependant dans cette fibre, aucun guidage de lumière n'a pu être observé, ni dans le proche infrarouge à la longueur d'onde télécom de 1,55 μm, ni dans le moyen infrarouge. Une étude plus approfondie a mis en évidence la présence de nombreux cristaux dans le cœur de la fibre et plus précisément des cristaux de As_2Se_3. Bien que stable vis-à-vis de la cristallisation, le verre d'$As_{38}Se_{62}$ n'a pas résisté aux multiples traitements thermiques nécessaires à la fabrication de la fibre.
L'ajout de germanium peut permettre d'augmenter la stabilité du verre vis-à-vis de la cristallisation. Pour les essais suivants, le verre de $Ge_{10}As_{22}Se_{68}$ a été conservé pour la réalisation des inclusions de bas indice mais les inclusions de haut indice seront réalisées avec le verre $Ge_5As_{30}Se_{65}$. Avec ce changement de composition il été possible de réaliser de nouvelles fibres à gradient d'indice. Malgré les fortes atténuations des fibres il a été de possible de mesurer leur transmission. La figure

J présente une courbe d'atténuation d'une fibre présentant un cœur à gradient d'indice de 10 μm et un diamètre extérieur de 125 μm. On notera que ce cœur est fait de 817 inclusions de verre d'environ 300 nm de diamètre chacune. Le minimum des pertes a été mesuré à 21 dB/m à 5,5 μm. Des simulations de la courbe de dispersion sur cette fibre avec un cœur de 10 μm, ont montré une dispersion très plate, proche de zéro, et légèrement négative. Ce type de profil appelé ANDi, pour All Normal dispersion, est très recherché pour la génération de supercontinuum très cohérents spatialement et temporellement.

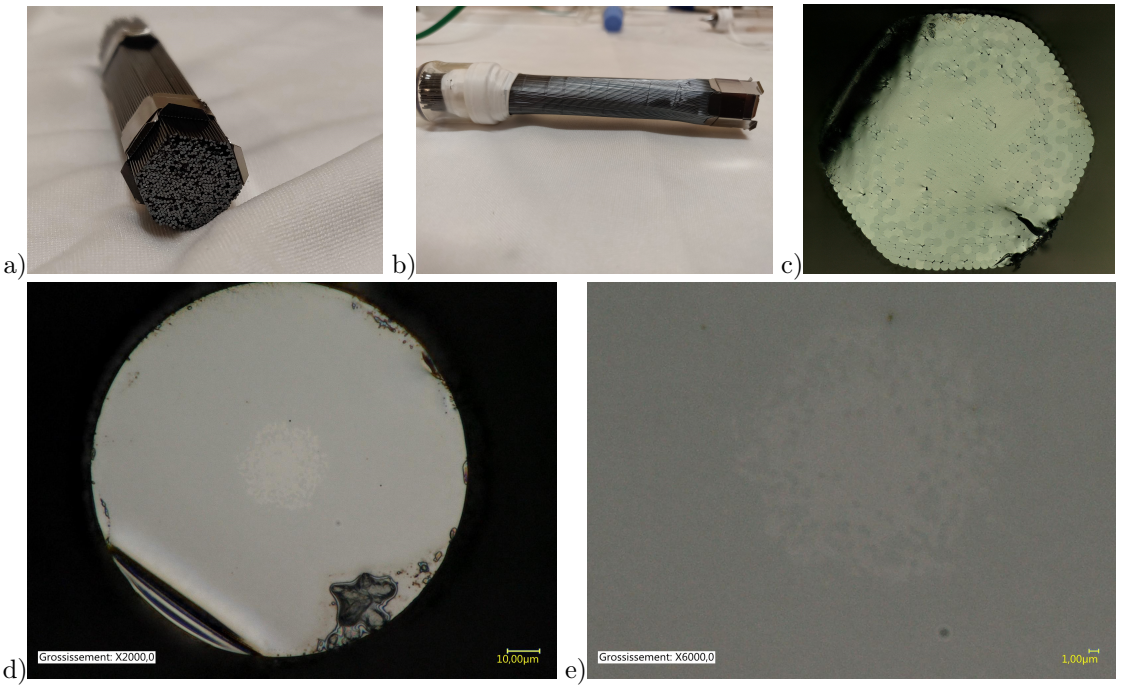

Figure I: *Illustration des différentes étapes de la réalisation d'une fibre à gradient d'indice en verre de chalcogénures. L'empilement (a) , le manchonnage (b), la baguette à gradient d'indice (c), la fibre à gradient d'indice (d), le cœur de la fibre à gradient d'indice (e).*

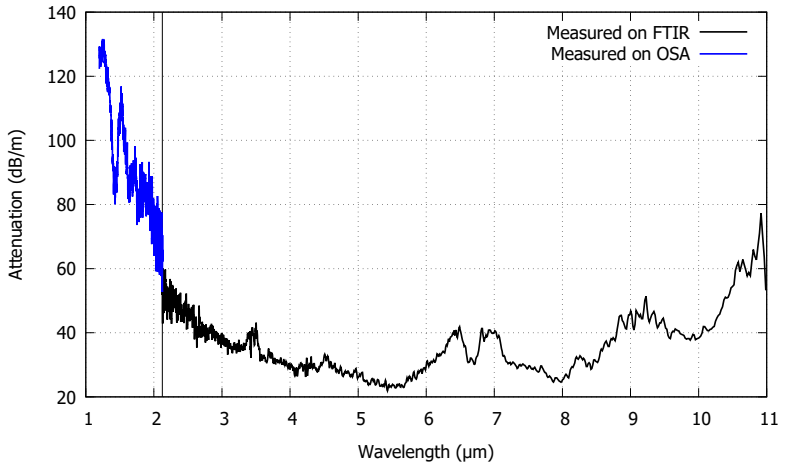

Figure J: *Courbe d'atténuation de la première fibre optique en verres de chalcogénures à gradient d'indice.*

Conclusion

Ce travail de thèse s'est déroulé dans le cadre d'un projet européen, nommé SUPUVIR, dont l'objectif est d'améliorer les sources de supercontinuum de l'ultraviolet ou moyen infrarouge (MIR). Dans ce contexte, le travail de thèse s'est concentré sur le développement et la réalisation de fibres optiques en verres de chalcogénures transparentes dans le moyen infrarouge. Plus précisément, l'objectif était de réaliser des fibres infrarouges transparentes dans la plage de longueurs d'onde allant de 2 à 12 μm avec un profil de dispersion sur mesure en associant la science du verre et des techniques innovantes de mise en forme des fibres afin de les utiliser pour la réalisation de nouvelles sources dans le moyen infrarouge. Afin de convenir à cette application, la fibre optique doit présenter le meilleur compromis entre les paramètres non linéaires (principalement contrôlés par la taille du cœur et la composition du verre), la position de la longueur d'onde de dispersion nulle (en fonction de longueur d'onde souhaitée de la pompe) et la fenêtre de transmission infrarouge. Au cours de ces travaux, des fibres microstructurées avec des verres de haute pureté ont pu être fabriquées. L'utilisation de ces fibres a permis l'obtention de supercontinua étendus de 2 à 10 μm. L'utilisation de cette source a ensuite permis la détection de signatures infrarouges d'un composé chimique et aussi montré le fonctionnement d'un spectromètre original utilisant un supercontinuum. Enfin, au cours de ces travaux de thèse, la première fibre optique à gradient d'indice en verres de chalcogénures a été fabriquée et ses propriétés de transmission et de dispersion ont été mesurées et étudiées.

Publications et communications réalisées au cours des travaux de thèse

Publications dans des journaux à comité de lecture

Amar Nath Gosh, Marcello Meneghetti, Christian Rosenberg Petersen, Ole Bang, Laurent Brilland, Sebastien Venck, Johann Troles, John Michael Dudley, Thibaut Sylvestre: *Chalcogenide Glass Polarization-Maintaining Photonic Crystal Fiber for Mid-Infrared Supercontinuum Generation.* Journal of Physics: Photonics 1.4 (2019): 044003. DOI:10.1088/2515-7647/ab3b1e

Yiming Wu, Marcello Meneghetti, Johann Troles, Jean-Luc Adam: *Chalcogenide Microstructured Optical Fibers for Mid-Infrared Supercontinuum Generation: Interest, Fabrication, and Applications.* Applied Sciences 09/2018; 8(9):1637. DOI:10.3390/app8091637

Marcello Meneghetti, Celine Caillaud, Radwan Chahal, Elodie Galdo, Laurent Brilland, Jean-Luc Adam, Johann Troles: *Purification of Ge-As-Se ternary glasses for the development of high quality microstructured optical fibers.* Journal of Non-Crystalline Solids 09/2018. DOI:10.1016/j.jnoncrysol.2018.09.028

Actes de conférences

Amar Nath Gosh, Marcello Meneghetti, Christian Rosenberg Petersen, Ole Bang, Laurent Brilland, Sebastien Venck, Johann Troles, John Michael Dudley, Thibaut Sylvestre, *Chalcogenide Glass Polarization-Maintaining Photonic Crystal Fiber for Mid-Infrared Supercontinuum Generation*, Conference on Lasers & Electro-Optics / Europe 2019

Marcello Meneghetti, Celine Caillaud, Radwan Chahal, Laurent Brilland, Johann Troles: *Fabrication of high optical quality Ge-As-Se glasses for the development of low-loss microstructured optical fibers.* Optical Components and Materials XVI (Vol. 10914, p. 109140X). International Society for Optics and Photonics; 2019, DOI:10.1117/12.2506267

Communications orales

Johann Troles, Marcello Meneghetti et. al: *Mid-infrared detection of organic compounds with a 2-10 μm supercontinuum source generated from concatenated fluoride and chalcogenide fibers*, SPIE Photonics West 2020 – BIOS, 1-7 February 2020, San Francisco, USA

Thibaut Sylvestre, Marcello Meneghetti et. al: *2-10 μm Mid-Infrared Supercontinuum Generation in Cascaded Optical Fibers: Experiment and modelling*, SPIE Photonics West 2020 – BIOS, 1-7 February 2020, San Francisco, USA

Johann Troles, Laurent Brilland, Marcello Meneghetti, Radwan Chahal, Catherine Boussard, Bruno Bureau, Sebastien Venck, Jean-Luc Adam, *Chalcogenide microstructured optical fibers for optical sensing*, Invited talk at 25th International Congress on Glass (ICG 2019), 9-14 June 2019, Boston, USA

Johann Troles , Marcello Meneghetti, Celine Caillaud, Laurent Brilland, Sébastien Venck, Jean-Luc Adam, Maxime Duris, Damien Deubel, Loïc Bodiou, Joel Charrier, Mathieu Carras, Mickael Brun, *Fabrication of low loss chalcogenide microstructured optical fibers for Mid-IR QCL pigtailing*, Invited talk at 25th International Congress on Glass (ICG 2019), 9-14 June 2019, Boston, USA

Amar Nath Gosh, Marcello Meneghetti, Christian Rosenberg Petersen, Ole Bang, Laurent Brilland, Sebastien Venck, Johann Troles, John Michael Dudley, Thibaut Sylvestre, *Chalcogenide Glass Polarization-Maintaining Photonic Crystal Fiber for Mid-Infrared Supercontinuum Generation*, Conference on Lasers & Electro-Optics / Europe, 23-27 June 2019, Munich, Germany

Marcello Meneghetti, Céline Caillaud, Radwan Chahal, Laurent Brilland, Johann Troles: *Fabrication of high optical quality Ge-As-Se glasses for the development of low-loss microstructured optical fibers*, SPIE Photonics West 2019 – OPTO, 2-7 February 2019, San Francisco, USA

Johann Troles, Marcello Meneghetti, Laurent Brilland, Celine Caillaud, Sebastien Venck, Yiming Wu, Jean-Luc Adam: *Fabrication of chalcogenide microstructured optical fibers for the 2-10 μm Mid-IR window*, Invited talk at Advanced architectures in photonics 2018, 2-5 September 2018, Cambridge, UK

Johann Troles , Celine Caillaud, Marcello Meneghetti, Yiming Wu, Christian Rosenberg Petersen , Ole Bang , Jean-Luc Adam, Laurent Brilland: *Fabrication of tapered chalcogenide microstructured optical fibers for enhancing the non linear properties*, ACERS GOMD 2018, May 20-24 2018, San Antonio, USA

Johann Troles, Celine Caillaud, Marcello Meneghetti, Christian Rosenberg Petersen, Ole Bang, Jean-Luc Adam, Laurent Brilland: *Elaboration of chalcogenide microstructured optical fibers for generation of mid-IR supercontinuum*, Invited talk at 5th Workshop on Speciality Optical Fibers and Their Applications, 11-13 October 2017, Limassol, Cyprus

General introduction

This thesis is the final product of a 3 years PhD funded by the Marie Curie action as a part of the SUPUVIR European project.
SUPercontinuum broadband light sources covering UV to IR applications (SUPUVIR) combined the efforts of 6 academic and 4 non-academic beneficiaries to train 15 early stage researchers (ESRs) for the growing industry within supercontinuum (SC) broadband light sources, giving them extensive knowledge in silica and soft-glass chemistry, preform design and fiber drawing, linear and nonlinear fiber and waveguide characterization, nonlinear fiber optics, SC modeling, SC system design, patent protection, development of new applications and gain and in-depth knowledge of a broad range of the main current applications of SC sources.
The scientific challenge addressed in SUPUVIR is to overcome the shortcomings of current SC sources in the various wavelength ranges. In the UV range we address the 200-400 nm range to achieve brighter SC sources extending further into the UV (down to 200 nm) and with better noise properties. In the visible and near-IR range, in which SC sources are most mature, the key aspects are to improve them and optimize them for different applications which might open new markets: this concerns topics like stability, coherence, noise, fiber lifetime and pulse energy. The mid-IR range is instead an emerging scientific area, so many aspects need to be addressed, including nonlinear host material issues, fiber fabrication, durability of fiber materials, alternatives to fibers represented here by waveguides in quadratic nonlinear crystals, proof-of-principle supercontinuum generation (SCG) experiments to achieve as broadband SCG as possible and to push the average power as high as possible. Also novel SC applications will be investigated across the three ranges, e.g. drug screening, photoacoustic imaging, food quality monitoring, multi-modal spectroscopy and Lidar-based process monitoring. Such novel applications are currently driving the research and development of SC sources.
SUPUVIR aims to solve these challenges by advancing current SCG techniques, which requires highly nonlinear PCFs or waveguides specifically tailored or developed for the purpose, and improving current applications and developing novel applications, enabled by the advances in SC sources in the project.

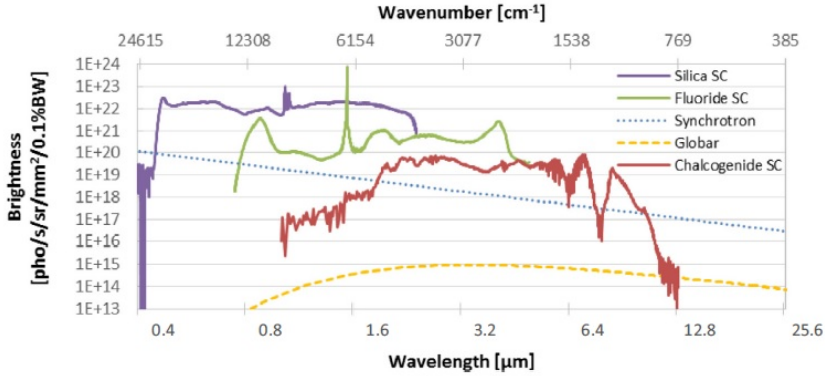

Figure I: *Brightness of silica, fluoride, and chalcogenide fiber-based SC sources compared to a synchrotron and a Globar (1500 K blackbody). Image from Petersen, C.R. et al, "Towards a table-top synchrotron based on supercontinuum generation", 2018.*

In the framework of this project, the work reported in this document was focused on two work packages: the development of mid-IR materials and the realization of optical fiber based on them, to be applied to expand the capabilities of SC sources at long wavelengths. As of now, no supercontinuum sources reaching far in the mid infrared are commercially available. Indeed, black body radiation sources (free space, low brightness), quantum cascade lasers (free space, very narrow bandwidth) and synchrotrons (free space, extremely bulky and expensive) are the only available solutions for broadband light in this spectral range. Thanks to their high compactness, brightness (see Figure I) and spatial coherence, as well as to the versatility of use typical of fibers, mid infrared supercontinuum fiber sources could enable progress in many fields, such as spectroscopy, remote sensing, microscopy and tomography, to name a few.
More specifically the objective of the research was to realize high quality infrared (in the 2-12 μm wavelength range) fibers based on chalcogenide glasses, with a dispersion profile tailored by combining glass sciences and innovative fiber shaping techniques. The fiber design needed be a best compromise between nonlinear parameters (mainly controlled by the core size and chalcogenide composition), position of the zero dispersion wavelength (depending on desired pump wavelength), power handling properties and breadth of the transmission window. The fibers fabricated were to be be tested and used for supercontinuum generation in cooperation with different members and partners of the SUPUVIR project. The work here presented was done in a close collaboration with Selenoptics (partner organization), in particular for the microstructured fiber shaping and drawing.
In order to encourage a closer cooperation between different laboratories and companies in the SUPUVIR consortium, two secondment periods of two weeks each were introduced in the plan for the PhD. The first period was spent in Instytut Technologii Materiałów Elektronicznych (ITME), in Warsaw, in the context of the production of chalcogenide graded index fibers by stack and draw technique. Afterwards, a student from that institute had his secondment period in the University of Rennes 1, to work on the same project. The second period was spent in the FEMTO-ST institute in Besançon, measuring the power handling properties of chalcogenide index guiding PCFs; previously, a student from there had spent two weeks at Selenoptics, working on the development of arsenic selenide polarization maintaining fibers.
This thesis was separated into 4 main chapters. Chapter 1 was written to offer a concise introduction of the main concepts used in the remainder of the work, acting a base for the other chapters, as well as an account of the current status of mid infrared SCG generation. In Chapter 2, a detailed report of the synthesis and distillation techniques used to produce high purity chalcogenide glasses is given, together with an explanation of the characterization techniques used and a list of properties for the different glass compositions obtained. Chapter 3 is focused on chalcogenide index-guiding PCFs, starting with a general overview of the state of the art to move after into a description of how such fibers were produced, tested and used for supercontinuum generation during this PhD. In Chapter 4 the development of the first chalcogenide graded index (Grin) fibers reported in literature is detailed, together with their characterization and the application of their production technique to the fabrication of Grin microlenses.

Chapter 1

Theoretical introduction and state of the art

1.1 General introduction on the glassy state of matter

1.1.1 Definition of "glass"

Despite having a long history, with the first archaeological evidence of man-made glass dating as early as 3500 BC, materials in the glassy, or vitreous, state represent even today a constantly developing field of research, thanks to their optical, mechanical and structural properties.
During the last century, a wide range of different definitions have been given for this state of matter; a comprehensive list of them can be found in [1]. It is interesting to notice that most of them are centered on the lack of long range order in the atomic structure of glasses, which is similar to the one of liquids (e.g. *A glass has an extended three-dimensional network and its energy content is comparable to that of the corresponding crystal but without periodicity and symmetry* [2] or *Glass is a noncrystalline or simple amorphous solid with a liquid-like structure* [3]). While intrinsic disorder is indeed one of the main characteristics of vitreous materials, it has to be noticed that definitions only based on it can sometimes lead to poor distinction between glasses and other non-crystalline materials, such as gels or some types of nanostructured materials. For this reason, more recent definitions (e.g. *A glass is an amorphous solid completely lacking in long range, periodic atomic structure, and exhibiting a region of glass transformation behavior. Any material, inorganic, organic, or metallic, formed by any technique, which exhibits glass transformation behavior is a glass* [4] or *Glass is a noncrystalline solid which exhibits the glass transformation range in the volume or enthalpy-temperature relationship* [1]) put together the structural disorder and the behavior in the transition between liquid and solid state, which is typical of glasses and usually addressed as "glass transition".

1.1.2 Glass transition

The transformation of a liquid into a glass is usually obtained trough fast cooling of the molten mass. With a low enough cooling rate, any liquid will reach the melting temperature T_m and pass to its crystalline phase, corresponding to the global minimum of free energy in the configurations space. This process is defined, as visible in Figure 1.1, by a discontinuity in the variation over temperature of first order derivatives of the Gibbs free energy (such as volume or enthalpy), classifying it as a first order phase transition in the Ehrenfest's classification scheme [5].
If not enough time is given to the atoms to reorganize into the configuration corresponding to the crystal, a supercooled liquid will be obtained instead, and at low enough temperature the increase in viscosity will forbid any further reconfiguration, de facto "freezing" the system in one of many local minima of the free energy (metastable state). In this case there will be no discontinuities in the V/T or H/T plots, but the slope will change sharply (second order phase transition) from being the same as the case of liquid to be similar to the one of the crystalline phase.

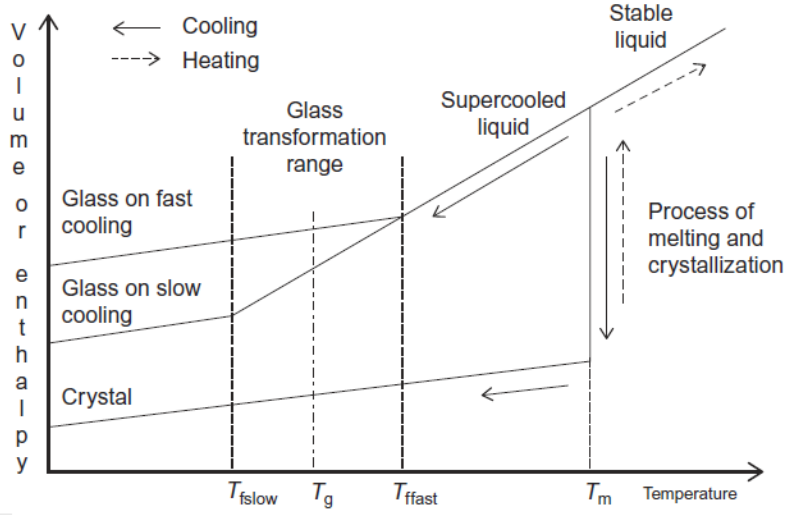

Figure 1.1: *Volume and enthalpy behavior of a material in the transition between melt and solid, for the formation of both crystal and glass [1].*

The temperature at which this change happens, defined as fictive temperature (T_f), can vary into a range depending on the cooling rate and contains information on the configuration in which the system is frozen. It is therefore necessary to define a more general parameter, independent on the thermal history of the glass: the glass transition temperature (T_g). T_g is often chosen as the onset of the glass transition range during heating, and can be determined by thermal analysis measurements such as differential scanning calorimetry or differential thermal analysis (Figure 1.2)

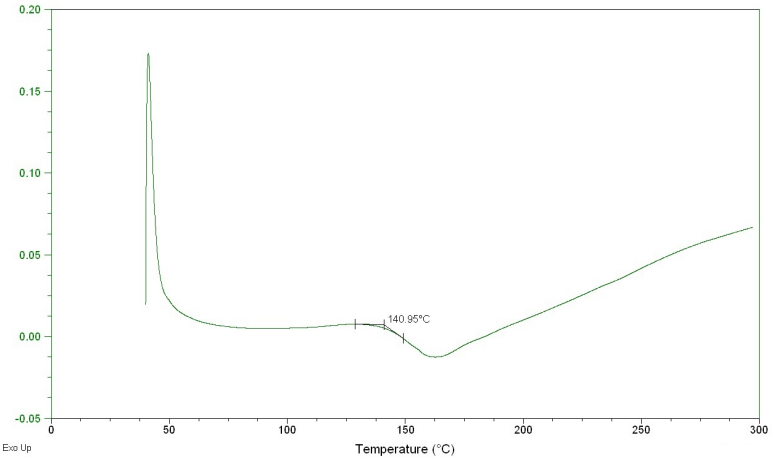

Figure 1.2: *Differential scanning calorimetry measurement of one of the glass compositions produced for this research ($Ge_5As_{25}Se_{70}$), with the value of T_g shown as the onset of the glass transition endothermic peak.*

1.1.3 Structure of glasses

The atomic structure of a material is strongly related to its macroscopic properties, and can be used to interpret or even predict them to some extent. A formal description of the atomic structure, based on the Miller indices, is available for crystals. However, due to the lack of long range order and periodicity, to obtain an equivalent description for glasses is not straightforward.

A first candidate as basic description of the glass structure can be the radial distribution function

$$g(r) = \frac{\rho^{(2/N)}(0, r)}{\rho^2}$$

where $\rho^{(2/N)}(0, r)$ represents the probability of finding a particle in a shell of infinitesimal thickness and radius r in a coordinate system centered on an arbitrary particle and $\rho = N/V$ is the average number density of a system of N particles and volume V [5, 6]. As shown in the example in Figure 1.3, a perfect crystal will have a g(r) represented as a series of Dirac's delta functions, whose position can be calculated from the Miller indexes of the lattice. On the other side, in the case of a glass a broadening of the lines corresponding to the different coordination shells will be observed, caused by the intrinsic disorder of the system. It is important to notice that the broadening is more accentuated for the shells that are more distant from the center of the coordinate system, implying that some order is conserved at short and mid range even in the vitreous state, while there is no long range order.

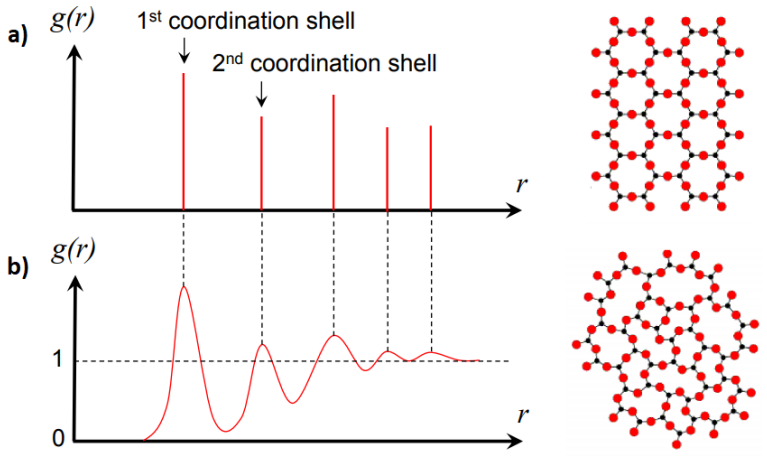

Figure 1.3: *Comparison between the calculated radial distribution functions for an a fictitious* A_2O_3 *2-D compound crystal (a) and the correspective glass (b) [7].*

The g(r) of a material can be experimentally measured via X-Ray, electron or neutron scattering [8], and can be used for the determination of both structural parameters like the average coordination number and, given a pair potential energy function u(r), macroscopic thermodynamic properties [5] like the potential energy

$$U = \frac{N}{2} 4\pi\rho \int_0^\infty r^2 u(r) g(r) dr \quad .$$

It has to be understood, however, that the radial distribution function is an incomplete model, especially because due to its averaging nature it fails to give an appropriate estimation of the amount of void spaces in the network. This is an extremely important structural property, having high impact on macroscopic properties such as example thermal and ionic conductivity.

1.1.4 Viscosity behavior of glasses

As described in Section 1.1.2, in the transition between a glass and a melt, unlike the corresponding situation for crystals, there are no discontinuities in first order derivatives of the Gibbs free energy. One of the most important consequences of this is the continuous behavior of the viscosity η during heating of a glass. This gives to materials in the vitreous state one of their most important characteristics for many applications: the possibility to easily shape them through the use of heat. It is in fact possible to define different regimes of viscosity in the aforementioned continuum, separated by reference values of temperature defined as a standard (see Table 1.1).

Table 1.1: *List of viscosity reference temperatures [4].*

Name of Reference Temperature	Viscosity (Pa·s)
Practical Melting Temperature	$\simeq 1$ to 10
Working Point	10^3
Littleton Softening Point	$10^{6.6}$
Dilatometric Softening Temperature	10^8 to 10^9
Glass Transformation Temperature	$\simeq 10^{11.3}$
Annealing Point	10^{12} or $10^{12.4}$
Strain Point	$10^{13.5}$

In the temperature range between the working point and the Littleton softening point, also known as working range, a glass will be soft enough to be easily deformed while being viscous enough to keep the deformation under control. This allows for many different shaping techniques, as press shaping, glass blowing, fiber drawing and many others.

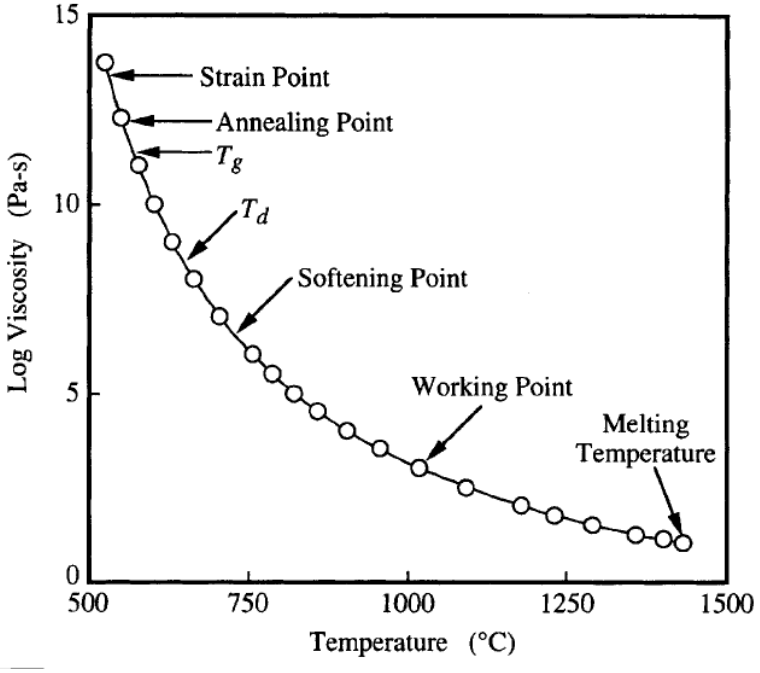

Figure 1.4: *Typical curve for viscosity as a function of temperature for a soda-lime-silica melt (NIST Standard No. 710). Defined viscosity points are indicated on the plot [4].*

1.2 Background on chalcogenide glasses

Between the great variety of glass families, a great interest has been shown in the last twenty years or so in the one of chalcogenide glasses. With this term we refer to non-oxide glasses based on chalcogen elements of the VI group of the periodic table of elements, namely sulfur, selenium and tellurium, combined with other elements, usually from the III-V groups.
Being low phonon energy materials, these glasses can be transparent from the visible up to the mid-infrared [9], therefore being viable for many applications for which transmission between 4 and 20 μm is needed. Despite the great amount of literature regarding rare earth doped chalcogenide glasses, the focus of this section will be to explore the structure and properties of undoped chalcogenide glasses.

1.2.1 Structure of chalcogenide glasses

Chalcogenide glasses are mostly covalently bonded glasses [10] with a wide range of structural configurations, depending on their composition.
For a better understanding of the structure of chalcogenide glasses, a good approach is to start from the elements that define this class of materials: chalcogens S, Se and Te. All of these elements, being 2-coordinated, can form complex structures only in the form of chains. In particular, sulfur melts, at temperatures above 160°C can form extremely long chains, exceeding 10^6 atoms, that when cooled can give rise to a vitreous solid. Selenium forms somewhat shorter chains, and even shorter ones are formed by tellurium, causining the formation of glass from a pure melt of the latter to be a quite difficult task. The addition of elements from the III-V groups of the periodic table to these chalcogens results in the crosslinking of the chains to form structures with higher coordination (see Figure 1.5) [4].

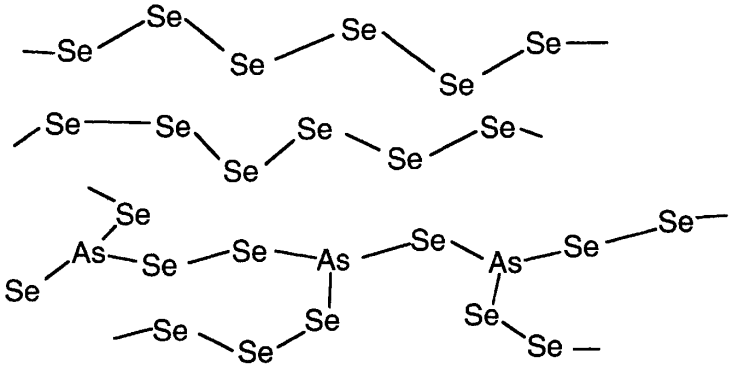

Figure 1.5: *Schematic representation of the structure of vitreous selenium and of an arsenic selenide glass. [4]*

1.2.2 Optical properties of chalcogenide glasses

1.2.2.1 Transparency window

The spectral region of transparency is arguably the most defining property of chalcogenide glasses, with the blue edge, corresponding to bandgap absorption, in the visible or near infrared and the red edge due to multiphonon absorption well in the mid-infrared. The transparency windows of different chalcogenide glasses are shown as an example in Table 1.2.

Table 1.2: *Approximate transmission windows of some chalcogenide bulk glasses [14].*

Glass-forming system	Transmission window (μm)	Reference
Ga-La-S	0.57-9.5	[11]
As-S	0.6-10	[12]
Ge-Sb-S	0.64-11	[13]
As-S-Se	0.75-12.5	[13]
Ge-As-Se	0.84-16	[11]
As-Se	0.85-17.5	[13]
Ge-As-Se-Te	1.0-17	[12]
As-Se-Te	1.23-18.52	[13]
Ge-Se-Te	1.7-17	[11]

This property makes these glasses way more suitable for mid-infrared applications than other common glasses, as shown in Figure 1.6. This is an extremely interesting region of the light spectrum,

with applications in many fields like nocturnal vision cameras, medical imaging and others. It is also important for spectroscopy: many common chemical groups have their fingerprint signature absorption peaks in this wavelength window (see Table 1.3). More to the point of this thesis, chalcogenide fibers can have transmission up to 14 μm, as shown in Figure 1.7. In particular selenide fibers transmitting in the $1-12$ μm range [15], can be especially suitable for telecommunications, sensing, imaging and spectroscopy [12, 16].

Table 1.3: *Infrared absorption peaks locations for common functional groups.*

Group	Wavelength (μm)	Group	Wavelength (μm)
C—O—H	2.9-3.3	—C≡N—	4.3-4.5
R—N—H	2.9-3.3	—C≡C—	4.3-4.5
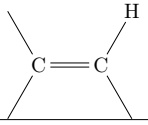	3.0-3.3	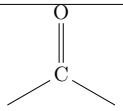	5.4-5.9
—C≡C—H	3.0-3.3	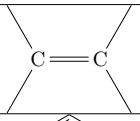	5.9-6.5
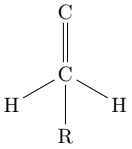	3.3-3.5	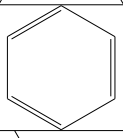	5.9-6.5
		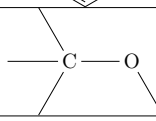	8.3-9.4

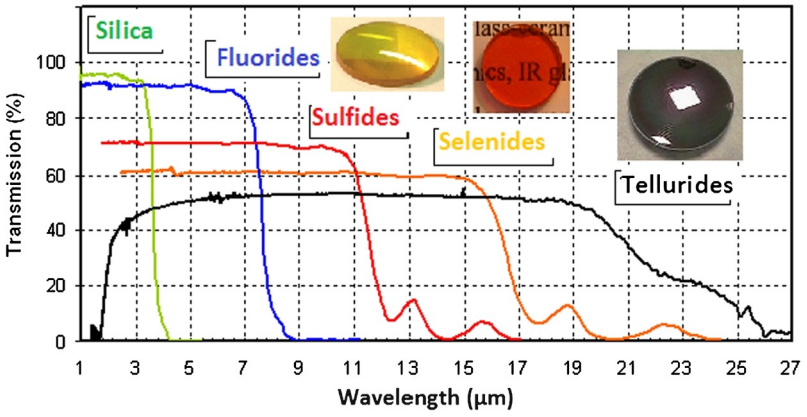

Figure 1.6: *Example of transmission spectra of different chalcogenide bulk glasses, compared to other common systems (silica and fluoride glasses) [17].*

It is important to notice that a large mismatch exists between the widths of the transparency windows in bulk glasses and the ones in fibers. This is due to the difference in the length of material through which the light needs to propagate, which is usually around few millimeters for applications needing bulk glasses and in the order of few meters for what concerns fibers. Considering that the percentage of incident light that gets transmitted through a medium $T_{\%} = \frac{I_{trans}}{I_{inc}} \cdot 100$ is dependent on the length l of medium through which the light travels in an exponential relationship defined by the Beer-Lambert law

$$I_{trans} = I_{inc} e^{-\alpha l}$$

it's easy to see that a small variation in α can correspond to almost no difference in $T_{\%}$ when measured on a bulk, but to a huge one over few meters of fiber, making the latter opaque in spectral regions in which the bulk is transparent.

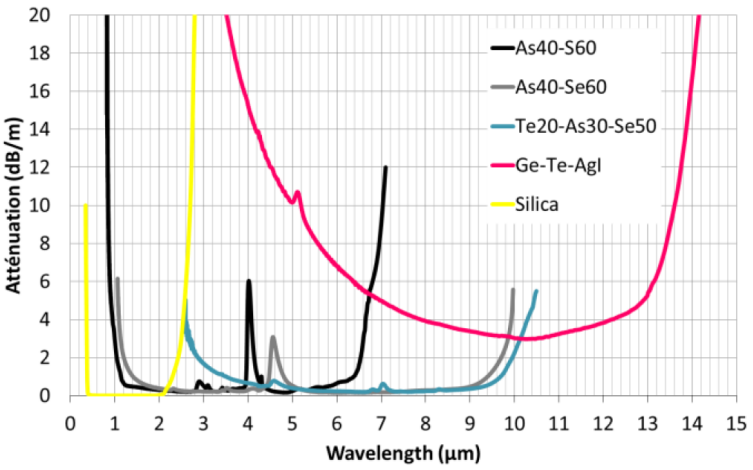

Figure 1.7: *Example of attenuation spectra of different chalcogenide fibers, compared to the common silica fibers used in telecommunications [18].*

1.2.2.2 Linear and nonlinear refractive indices

Chalcogenide glasses have high magnitudes of refractive index (n), in the order of 2.5-3 [19] (as a comparison, silica has a refractive index in the order of 1.5). In this work the dependence of refractive index on the light wavelength λ will be described via the Sellmeier equation,

$$n^2(\lambda) = 1 + \sum_i \frac{a_i \lambda^2}{\lambda^2 - b_i}$$

with each term of the sum representing an absorption resonance of strength a_i at a wavelength $\sqrt{b_i}$. This is the same equation that could be obtained from the electromagnetic theory, with certain simplifying assumptions. Its derivation, however, is far from the goals of this work. It is interesting to notice that reducing the number of poles to one and expanding by the binomial theorem, the less precise but still widely used Cauchy equation can be obtained [20].

$$n^2(\lambda) = 1 + \frac{a\lambda^2}{\lambda^2 - b} = 1 + \frac{a}{1 - (\frac{b}{\lambda^2})} = 1 + a(1 + \frac{b}{\lambda^2} + \frac{b^2}{\lambda^4} + ...) \simeq (1 + a) + \frac{ab}{\lambda^2}$$

Usually a quite complete description of the dispersion curve can be obtained using three poles

$$n^2(\lambda) = 1 + \sum_{i=1}^{3} \frac{a_i \lambda^2}{\lambda^2 - b_i}$$

where $a_{1,2,3}$ and $b_{1,2,3}$ are obtained fitting experimental data. This relation has been shown to hold well in the spectral regions far from the $\lambda = \sqrt{b_i}$ poles, including the infrared region, where Cauchy equation doesn't hold.
In literature many forms of this equation are found, relying on various approximations; one of the most general ones is the two-poles expression

$$(n^2(\lambda) - 1) = A_0 + \frac{A_1 \lambda^2}{\lambda^2 - a_1^2} + \frac{A_2 \lambda^2}{\lambda^2 - a_2^2} \quad [21]$$

where the contributions given from plasmons in the far UV to higher wavelengths is approximated as a constant. This particular formulation is the one that will be used throughout this thesis.

An important property of a material is the dispersion $D(\lambda) = \frac{\partial^2 n}{\partial \lambda^2}$, and more specifically the wavelength for which $D(\lambda) = 0$ (zero dispersion wavelength, usually abbreviated as ZDW). The dispersion profile and the position of the ZDW are fundamental for many applications, especially in nonlinear optics, as will be seen through the remainder of this work. The ZDW of chalcogenide glasses is usually in the mid-IR. In particular, for the glasses in the As-Se and Ge-As-Se systems studied in this thesis, its value is around $7-8$ μm.
For what concerns the nonlinear refractive index n_2, another value of great importance as it can be seen as an indicator of how much a material is suited for nonlinear applications (the higher the better), chalcogenides exhibit high values that can be as much as three orders of magnitude larger in chalcogenides with respect to silica. The values of n, n_2 and ZDW for some example chalcogenide systems (and for other glasses as a comparison) are listed in Table 1.4.

Table 1.4: *Values of n, n_2 and ZDW for some example chalcogenide systems (and for other glasses as a comparison) [14].*

Glass	**n**	**n_2 ($10^{-20}\frac{m^2}{W}$)**	**ZDW (μm)**	**Reference**
SiO_2	1.44	2.2	1.26	[22, 23]
TeO_2	2.10	25-59	2.24	[23–25]
ZBLAN	1.45	2.1	1.6	[26, 27]
As_2S_3	2.44	480	4.8	[28, 29]
As_2Se_3	2.81	1450	7.2	[28]
$Ge_{11}As_{22}Se_{67}$	2.6	1160	> 6	[30]

1.2.3 Thermal properties of chalcogenide glasses

Chalcogenide glasses are a part of the class of materials called soft glasses. This term commonly refers tho glasses which start to soften (viscosity$< 10^7$ Pa $\cdot$ s) at lower temperatures with respect to the one of soda-lime-silica [4], for which this happens at ~ 700℃ [31].

1.2.3.1 Thermal stability

For most applications, chalcogenide glasses need to be shaped after synthesis, a process that usually involves heating them above the glass transition temperature. To avoid crystallization during the shaping, it is of great importance to know at which temperature the onset of the crystallization peak (T_c) is. The difference between T_c and T_g is an indicator defining the so-called thermal stability of glasses. As a rule of thumb, this difference should be no lower than 100℃ to provide enough window for most shaping techniques [14]. In general, germanium-containing chalcogenide glasses seem to exhibit higher thermal stability than the counterpart compositions without germanium, fact that will be important in this work when having to choose between As-Se and Ge-As-Se glasses for different applications. Examples of values of T_g and T_c for different glasses are provided in table 1.5.

Table 1.5: *Glass transition and crystallization temperatures for some example chalcogenide systems [14, 32].*

Glass	**T_g (℃)**	**T_c (℃)**	**$T_c - T_g$ (℃)**
As_2S_3	185	-	-
As_2Se_3	170	298	128
$GeSe_2$	380	580	200
$As_2Se_{1.5}Te_{1.5}$	150	231	81
$Ge_{25}Sb_{10}S_{65}$	315	> 515	> 200
$Ge_{30}As_{10}Se_{30}Te_{30}$	260	485	225
$Ge_5As_{30}Se_{65}$	165	-	-
$Ge_{10}As_{22}Se_{68}$	175	-	-

1.2.3.2 Viscosity

Another important property for the shaping of chalcogenide glasses is the viscosity behavior during heating. An in-depth discussion of the modelization of this behavior is presented in Section 2.1.3.2. The viscosity needed for fiber drawing, which is the main focus of this work, is of about 10^5 Pa · s. This value can be reached at temperatures below 300°C for glasses in the binary As-Se and As-S systems [14]. According to the models used in Section 2.1.3.2, this holds true also for most of the glasses in the Ge-As-Se system prepared during the development of this thesis.
A relevant parameter related to the temperature dependence of viscosity is the fragility parameter m, defined as the slope at T_g of the viscosity when plotted in an Angell plot [33] ($\log_{10}\eta$ against T_g/T).

$$m = \frac{\partial \log_{10} \eta(T)}{\partial(T_g/T)}\Big|_{T=T_g}$$

Glasses with a low value of m are deemed to be "strong", and exhibit an Arrhenius-like behavior of viscosity above T_g (meaning they appear as straight lines on Angell plots), while glasses with high m are called "fragile" and have a super-Arrhenius behavior of viscosity. Figure 1.8 shows a schematic representation of how strong and fragile glasses appear on an Angell plot.

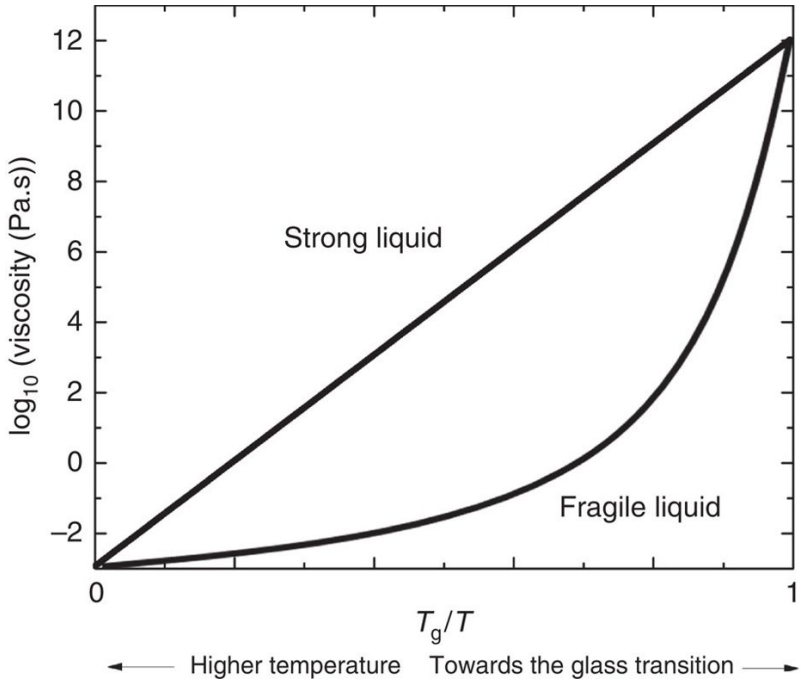

Figure 1.8: *Appearance on an Angell plot of Arrhenius and super-Arrhenius behaviors of the viscosity in glass-forming liquids [34].*

Structurally speaking, fragility is related to the disorder in the glass, with an high degree of short range order corresponding to a lower m. A large value of m corresponds to a large variation of thermodynamic properties during the glass transition [33]. The prototypical strong glass, silica, has an m of 17, while more fragile polymeric glass formers have values of m around 200. In this context, chalcogenide result to be quite strong glasses, with values of m in the 20 – 40 range [14].

1.3 Introduction to fiber optics

1.3.1 A brief history of fiber optics

Nowadays optical fibers are a common, widespread technology, carrying enormous amounts of data through the world up to our houses and working places. The fibers used for telecommunication

are, however, based on a relatively new technology, dating less than 50 years ago.
The idea of transmitting information of some kind using light is actually an historically really old one: since ancient times open fires, lanterns and lighthouses were used for signaling. There was, however, a great limitation to that: in air, light travels in a straight line, thus needing a clear path between the transmitter and the receiver of the signal. It wasn't until the 19th century that the possibility of bending light was taken into consideration.
Between the 1840s and 1870s, experiments were performed by different scientists around the world showing that light, if focused into water, was following the flow of the liquid, even when its path was curved. The most famous of such experiments was performed by John Tyndall in 1870 [35]. This was the beginning of the concept of light guiding by total internal reflection. In the wake of these experiments, in the following years light focused into curved glass rods started to be used by medical doctors to illuminate body cavities.
In order to move from the concept of light guiding to optical fibers similar to the modern ones, however, another century had to pass by. The problems in using guided light for long-range communication were fundamentally two: the lack of a suitable light source and the high power losses during the guiding. The first problem ceased to exist in the 1950s with the birth of laser sources; the second one was addressed in the 1970s with the production of low loss silica, first from Corning Glass Works (<20 dB/km in titanium doped silica in 1970) and then from Bell Laboratories (ultra-transparent glass mass-produced by modified chemical vapor deposition in 1973, a technique which still is the standard in industry these days). Thanks to these discoveries, fiber optics for telecommunications became a thriving industry and a major research field.
Alongside the most common use of just transmitting light, the need for various specific applications made the field of specialty optical fiber prosper, bringing with it fiber designs different from the standard step index fiber. In the late sixties, graded index core optical fibers were introduced as a way to reduce intermodal dispersion in multimode fibers [36, 37]. In the 1990s, the work of Russel, Birks and Knight [38–40] brought to the limelight the idea of silica-air microstructures as a mean to achieve light confinement. Then, this new fiber design has spread over other glassy matrices, and since 2000 to chalcogenide glasses [41]. The development of holey and graded index chalcogenide fibers represents the main goal of this thesis.

1.3.2 Ray optics approach to light guiding in optical fibers

The simplest example of optical fiber is a long and thin thread of transparent material, usually glass. The reason why it's possible to force light to travel enclose inside the boundaries of a fiber, namely "guiding" light, lies in the Snell-Descartes law, which describes the refraction of light at the boundary between two different media. This law states that a ray of light propagating through a material of refractive index n_1 and reaching the interface with a material of refractive index n_2 with an impinging angle θ_1 with respect to the axis normal to the interface, will then propagate through the second medium with an angle θ_2 with respect to the same axis such that

$$n_1 \sin\theta_1 = n_2 \sin\theta_2 \quad .$$

Reformulating this law as $\sin\theta_2 = \frac{n_1}{n_2}\sin\theta_1$, it can be seen that, when $n_1 > n_2$, for high enough values of θ_1 we obtain $\sin\theta_2 > 1$. This condition is of course impossible, and in this case there is no propagation at all in the second medium, with the light being completely reflected at the interface. It is therefore possible in this situation to define an impinging critical angle $\theta_c = \sin^{-1}(\frac{n_2}{n_1})$ and stating that all light reaching the interface at an angle $\theta_1 > \theta_c$ will be completely reflected.
This particular simple case of optical fiber can be approximated as a cylinder of glass or polymer with refractive index higher than the one of air, as depicted in 1.9. Light reaching its face at an angle θ_{in} will start traveling inside the fiber with an angle θ' with respect to the fiber axis until reaching the side of the fiber. Here, if the angle between the light and the normal to the lateral surface of the fiber (θ'') is higher than the critical angle, light will be completely reflected inside the fiber. The reflected light will reach the glass/air interface again, after traveling more in the cylinder, with the same angle θ'', and will be thus reflected again. Thanks to this phenomenon, called total internal reflection, light is confined to propagate inside the fiber. The sine of the largest angle θ_{in} for which $\theta'' > \theta_c$ is named numerical aperture (NA) and can be defined also as

NA $= \sqrt{n_1^2 - n_2^2}$ with n_1 and n_2 being in this case the refractive index of the glass and the air respectively.

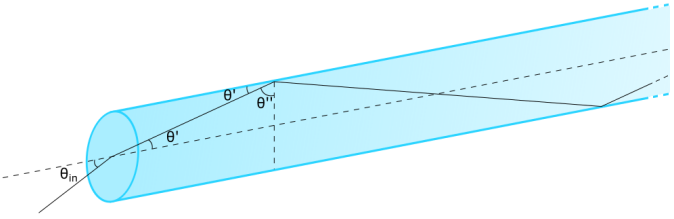

Figure 1.9: *Propagation of light into an single index optical fiber by total internal reflection.*

In the case of the simple thread of glass, the critical angle for total internal reflection is dependent on the refractive index difference between the glass and the surrounding air. Because of this, the presence of dirt or humidity (whose refractive index is higher than the one of air) on the fiber surface can induce a local reduction of θ_c, and the subsequent leakage of part of the light outside the fiber. In order to avoid this source of optical losses usually a step-index design is used for optical fibers: a central cylindrical core surrounded by glass (cladding) of lower refractive index. This design also allows to obtain small cores without increasing the fiber's fragility.
Another typical problem of glass fibers is their fragility, due to the fact that even a small nick on the surface can spread very fast upon bending of the fiber, eventually causing it to break. This problem is usually solved by covering the fiber with a layer of polymer, which provides mechanical protection without being involved in the process of light guiding. This layer is named coating or primary buffer, and with its addition we obtain the standard configuration for commercial fibers used in telecommunications, schematized in Figure 1.10.

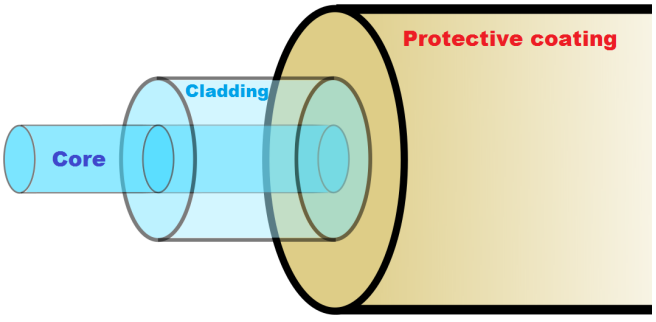

Figure 1.10: *Classic design of a step index optical fiber.*

1.3.3 Wave optics approach to light guiding in optical fibers

When treating light propagation in optical fibers, using geometrical optics as in Section 1.3.2 has the advantage of simplicity and immediateness. However, an approach based on wave optics is needed for the correct understanding of the phenomenon, and absolutely necessary for the treatment of nonlinear optics, which is a fundamental part of this thesis.

1.3.3.1 Light propagation in materials according to Maxwell's equations

For a treatment of optics from the point of view of electromagnetics, it is necessary to start with the general case of the Maxwell's equations, describing the behavior of the electric and magnetic fields in a medium different from vacuum:

$$\nabla \cdot \vec{D} = \rho$$
$$\nabla \cdot \vec{B} = 0$$
$$\nabla \times \vec{H} = \vec{J} + \frac{\partial \vec{D}}{\partial t}$$
$$\nabla \times \vec{E} = -\frac{\partial \vec{B}}{\partial t}$$

where

- $\vec{E}$ is the electric field vector;
- $\vec{H}$ is the magnetic field vector;
- $\vec{D}$ is the electric displacement;
- $\vec{B}$ is the magnetic induction;
- $\vec{J}$ is the current density;
- ρ is the charge density.

This formulation of the equations is implicitly dependent on the properties of the material, namely the electric polarization density $\vec{P}$, the magnetic polarization density $\vec{M}$ and the conductivity σ. The dependence of the electric and magnetic fields behaviors on these physical characteristic of the medium is made explicit by the following relations:

$$\vec{D} = \epsilon_0 \vec{E} + \vec{P} \simeq \epsilon_0 (1 + \chi^{(1)}) \vec{E}$$
$$\vec{B} = \mu_0 (\vec{H} + \vec{M})$$
$$\vec{J} = \sigma \vec{E}$$

The approximated term to the right of the first equation is true in the so-called linear approximation. The correct expression for the polarization density is

$$\vec{P} = \epsilon_0 (\chi^{(1)} \vec{E} + \chi^{(2)} \vec{E}^2 + \chi^{(3)} \vec{E}^3 + ...) \ ,$$

but for not exceedingly high magnitudes of $\vec{E}$ this series can be truncated at the first (linear) term. Another approximation that can be safely done when speaking of optical fibers (which are made of dielectric materials) is the negligible contribution of free charges, electrical current and magnetization. In these approximation, polarization density stays as the only relevant material characteristic in the calculations, and the Maxwell equations can be rewritten as

$$\nabla \cdot \vec{D} = 0$$
$$\nabla \cdot \vec{B} = 0$$
$$\nabla \times \vec{B} = \mu_0 \frac{\partial \vec{D}}{\partial t}$$
$$\nabla \times \vec{E} = -\frac{\partial \vec{B}}{\partial t}$$

From this approximated formulation we can finally derive the expression for light propagation in a material: the wave equation. Taking the curl of the 4th equation and applying the proper theorems to simplify the expression, the following relation is obtained

$$\nabla(\nabla \cdot \vec{E}) - \nabla^2 \vec{E} = -\frac{\partial}{\partial t}(\nabla \times \vec{B})$$

Now, substituting $\nabla \times \vec{B} = \mu_0 \frac{\partial \vec{D}}{\partial t}$ and $\vec{D} = \epsilon_0 \vec{E} + \vec{P}$ into this relation, the result is

$$\nabla(\nabla \cdot \vec{E}) - \nabla^2 \vec{E} = -\mu_0 \epsilon_0 \frac{\partial^2 \vec{E}}{\partial t^2} - \mu_0 \frac{\partial^2 \vec{P}}{\partial t^2} \ .$$

From now on only equations concerning the electric field will be treated. It is, however, important to remember that in a way analogous to the one used to retrieve the wave equation for $\vec{E}$, one for $\vec{H}$ can be obtained which holds the same form. Therefore, all the results below can be applied to the magnetic field too, with the appropriate corrections.

1.3.3.2 Propagation modes in a optical fiber

The wave equation at the end of the section above is mathematically complex, and describes a quite general case of light propagation in matter. However, speaking of light propagation in fibers, their specific geometrical and physical features can be used to simplify the problem. In this section, the case of low intensity light propagating in a cylindrically symmetric fiber made of a low losses, isotropic dielectric will be treated.
By assuming low intensity, and therefore low magnitude of $\vec{E}$, the linear approximation $\vec{P} = \epsilon_0 \chi^{(1)} \vec{E}$ can be used. By assuming low losses the imaginary part of the refractive index can instead be deemed to be negligible, and therefore the $n^2 = \epsilon = 1 + \chi^{(1)}$ approximation can be used. In the case of an isotropic material, which is a fair approximation for glass, the polarization vector and the electric field are always parallel, and this implies for $\vec{D}$ and $\vec{E}$ to be parallel too, guaranteeing that $\nabla \cdot \vec{E} = \nabla \cdot \vec{D}$; the term to the right is known to be 0 from the first Maxwell equation, meaning that in the treated case $\nabla \cdot \vec{E} = 0$.
When the approximations above are all inserted in the wave equation, the latter can be written in a fairly simplified form:

$$\nabla^2 \vec{E} = \frac{n^2}{c^2} \frac{\partial^2 \vec{E}}{\partial t^2} \ ,$$

where the well known relation $c^2 = \frac{1}{\sqrt{\mu_0 \epsilon_0}}$ has been implemented too.
Coming to the geometrical features of the fiber, the first one to be used is the fact that one of its dimensions is way more extended than the other two. Thanks to this, light propagation in the fiber can be modeled as parallel to its length, direction that will be here defined as z. This allows for the separation of coordinates in the general solution of the wave equation, splitting it into the transverse components, the one along z and the temporal one, and thus obtaining the form

$$E = E_0 A(x, y) e^{-i\beta z} e^{i\omega t} \ ,$$

where ω is the angular frequency of the light and β its propagation constant inside the fiber. In the geometrical optics treatment of light propagation, β would correspond to the component along z of the wavevector $k = n\frac{2\pi}{\lambda}$ of light traveling in the fiber at a certain angle.
Focusing on the transverse component A(x,y), the circular symmetry that most fibers exhibit allows to move from cartesian to cylindrical coordinates and perform a further separation:

$$A(x, y) \rightarrow A(r, \phi) = \mathcal{R}(r) \mathbf{\Phi}(\phi) \ .$$

Applying this separation into the wave equation, rewritten with the Laplacian operator in cylindrical coordinates, a couple of equations describing $A(r,\phi)$ is obtained:

$$\frac{\partial^2 \mathbf{\Phi}}{\partial \phi^2} + m^2 \mathbf{\Phi} = 0$$

$$r^2 \frac{\partial^2 \mathcal{R}}{\partial r^2} + r \frac{\partial \mathcal{R}}{\partial r} + (\kappa^2 r^2 - m^2) \mathcal{R} = 0$$

with $\kappa^2 = k^2 - \beta^2$ and m is a constant.
It can be demonstrated that the m can only be an integer number, and therefore a discrete set of transverse field distribution profiles for light propagating through a fiber exists. These profiles are called modes. To each mode corresponds a different propagation constant β. The set of modes is

not only discrete, but finite: only a limited number of them can propagate in a fiber. This number is approximately proportional, in a step index fiber, to the square of the normalized frequency V, defined in terms of the numerical aperture NA as

$$V = \frac{2\pi a}{\lambda} NA \ .$$

For $V < 2.405$, only one propagating mode exists, and the fiber is defined to be single mode. It is important to notice here that V is a function of the wavelength, so that normally a fiber can be single mode for some wavelengths and multimode for others. The wavelength above which a particular mode ceases to exist is called the cut-off wavelength of that mode. Commonly people refer more generally to a cut-off wavelength of the fiber, instead of the ones of the different modes, meaning the wavelength above which all modes apart from one cease to exist, making the fiber effectively single mode.
Modes are usually classified using the LP_{lm} scheme, where l represents the number of node pairs in the angular profile while m represents the number of lobes in the radial profile. LP_{01} is the lowest order mode that can be defined in this classification, as well as the only one propagating in single mode fibers, and is usually named fundamental mode. A more detailed description of LP classification and of the calculations performed in this section can be found in [42].

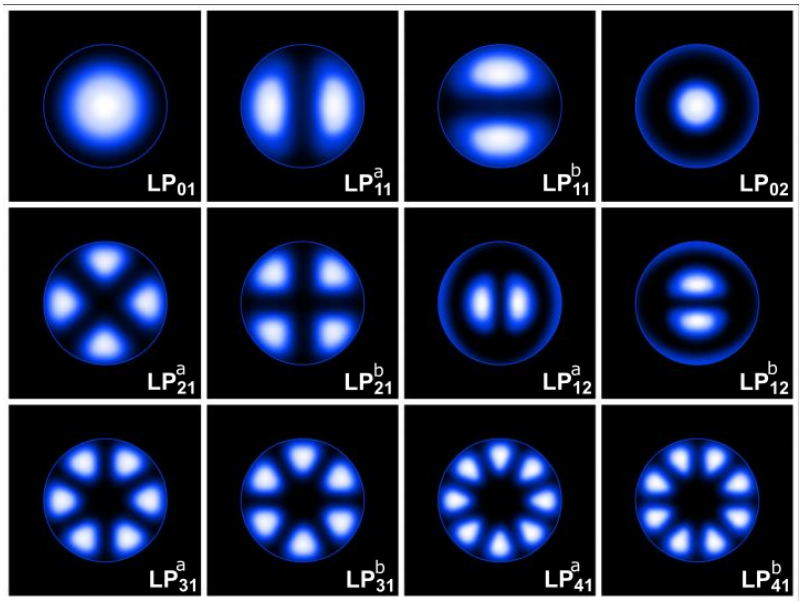

Figure 1.11: *Transverse field distribution profile of some LP_{lm} modes in a fiber with circular core [43].*

1.3.3.3 Intermodal and chromatic dispersion in fibers

As explained in the previous section, the different modes in a fiber are defined by different propagation constants. It is important to remind here that these propagation constants are also a function of the wavelength. Keeping the LP_{lm} classification for modes, this fact can be stated as $\beta_{l,m} := \beta_{l,m}(\lambda)$.
For light propagating in a material without constraint, the part of the solutions of the wave equation relative to the propagation direction, here once again defined as z, can be written as $e^{n(\lambda)\frac{2\pi}{\lambda}z}$, meaning that in absence of a confinement of light $\beta(\lambda) = n(\lambda)\frac{2\pi}{\lambda}$. Knowing this, it is possible to define an effective refractive index $n_{eff}^{l,m}(\lambda) = \beta_{l,m}(\lambda)\frac{\lambda}{2\pi}$, which at a fixed value of λ will be different for every mode. This difference in effective refractive index between modes, usually called intermodal or modal dispersion, means that each mode will propagate in the fiber with a different speed. An intuitive way to understand this phenomenon is to make a parallel with geometrical optics: imagining the different modes as different entrance angles for the light in the fibers, it's

easy to imagine the rays traveling through paths of different length during the process of total internal reflection, causing time delays at the fiber output.
It is important to notice that, even for the fundamental mode, in general $n_{eff}(\lambda) \neq n(\lambda)$. Moving from the refractive index to the dispersion defined in Section 1.2.2.2, which is a more important property for the goals of this thesis, this means that fiber geometry acts as a modifier of material dispersion. This is a matter of great importance because it means that fiber design can be tailored to some extent in order to to obtain the dispersion profiles and positions of the zero dispersion wavelength most suitable for different applications, as visible in the example in Figure 1.12. Considering the difference between the total dispersion $D_{tot}(\lambda) = \frac{\partial^2 n_{eff}}{\partial \lambda^2}$ and the material dispersion $D_{mat}(\lambda) = \frac{\partial^2 n}{\partial \lambda^2}$, a waveguide dispersion can be defined as $D_{WG}(\lambda) = D_{tot}(\lambda) - D_{mat}(\lambda)$. Through the remainder of this thesis, if not otherwise specified, the term "dispersion" (D) will refer to the total dispersion.

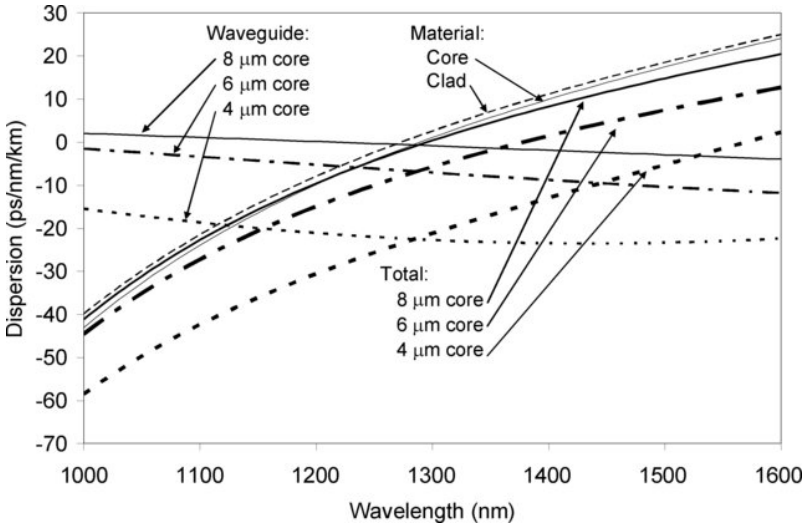

Figure 1.12: *Material, waveguide dispersion, and total dispersion of step index fibers doped with GeO. Three core diameters, 4, 6, and 8 m are compared to illustrate the waveguide dispersion effect [44].*

1.3.4 Causes of optical losses in fibers

A fundamental topic that needs to be addressed when discussing fiber optics is the one of optical losses: not all of the light that is fed in the input end of a fiber will travel all the way to the output end. This is caused by the contributions from a series of different mechanisms; the goal of this section is to introduce the most important ones.

1.3.4.1 Material-related attenuation

As introduced in Section 1.2.2.1, optical fibers can only transmit light whose wavelength is inside a defined spectral window, the transparency window, whose position and bandwidth are dependent on the material the fiber is composed of. This window is limited on the short wavelength side by absorption due to electronic phenomena, and on the long wavelength side by absorption related to vibrational mechanisms. Inside the transparency window, optical losses are not equal to zero, even in the ideal case of a perfectly pure and homogeneous material: there is a theoretical lower limit, sum of the contributions of the tails from the bandgap and multiphonon absorption and of the Rayleigh scattering from atoms and molecules in the material structure. It has to be noticed here that scattering is a completely different mechanism from absorption: light is not converted to another form of energy, but rather it merely changes direction. This change of direction can cause the light to cease to be guided or to propagate in the wrong direction.
The theoretical lower limit of attenuation, however, has been neared (but never reached) only for silica fibers, which are by far the most studied for telecommunications applications. One of the

factors causing the impossibility up to now to reach these limits is the presence of impurities: no material is 100% pure, and even concentrations of unwanted atoms in the order of magnitude of parts per billion can create a significant increase in losses, when they have absorption peaks (electronic or vibrational) inside the transparency window. A schematic representation of how the contributions mentioned up to now can affect the attenuation of an optical fiber is shown in Figure 1.13.

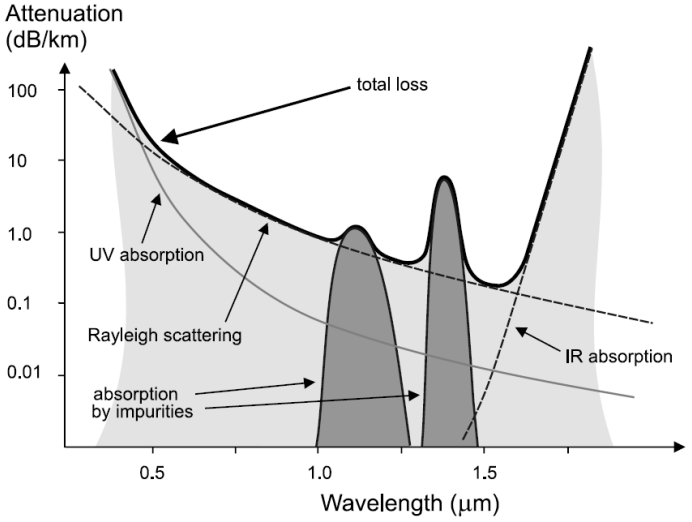

Figure 1.13: *Different contributions to material-related attenuation in a homogeneous optical fiber [42]. The UV absorption contribution is related to the material bandgap, while the IR one to multiphonon absorption processes.*

Finally, inhomogeneities in the material, such as the presence of particles, crystals or difference glass domains can be another source of scattering-related losses. Normally these inhomogeneities have sizes $> \frac{\lambda}{10}$, so that they cause a phenomenon called Mie scattering, following physical laws different from the ones regulating Rayleigh scattering.

1.3.4.2 Confinement losses

For most applications of fiber optics, only light guided in the core is useful. This might be either because some particular properties need to be well defined during propagation (for example the time profile of a modulated beam, or the intermodal dispersion, which are different when light is guided in the cladding because of the difference in refractive index) or because a small modal area is needed, like in the case of nonlinear applications, which require high power density. Moreover, the cladding could have higher material-related losses than the core. Due to all this reasons, all light moving from modes guided in the core to modes guided in the cladding is usually considered as lost. In some cases, a coating with extremely high absorption in the wavelength used is applied on the cladding, so that all cladding-guided light is absorbed at the interface and only core-guided light can actually propagate.
From a purely theoretical point of view, the LP_{01} mode is guided independently on the core diameter, even if with decreasing core diameter a larger part of the energy propagates in the area surrounding the core instead of being strictly confined inside it [45]. This, however, is true only for perfectly straight fibers, which is not a realistic situation. When fibers experience some degree of bending, even the fundamental mode can couple with cladding modes and transfer part of its power to them, therefore exhibiting confinement losses. These losses decrease when more light is confined into the core (larger core diameter) and increase when the bend radius is smaller.
In the case of multimode fibers, the non-fundamental modes can have confinement losses even in the case of a perfectly straight fiber. This is due to their field being distributed further from the center as the order of the mode increases, causing them to couple with cladding modes. The

considerations about the influence of core diameter and bending radius on confinement losses made for the fundamental mode apply to higher order modes too.

1.3.4.3 Fresnel losses at fiber ends

All sources of optical losses discussed up to now are caused by phenomena happening diffusely along the path through which light propagates. There is, however, also an often non-negligible localized effect to take into account as a contribution to the total losses: Fresnel reflections at the input and output ends of the fiber. The amount of incident intensity that is reflected at the interface between two media with different refractive indices depends on both incidence angle and polarization of light. In the simplified case of normal incidence, however, it is a function only of the two refractive indices:

$$I_{ref} = \left| \frac{n_1 - n_2}{n_1 + n_2} \right|^2 I_{inc} \ .$$

A way to minimize optical losses due to Fresnel reflections is to coat the fiber ends with anti-reflective or anti-glare coatings. Anti-reflective coatings reduce the total reflectance R by adding one or more layers of materials with intermediate refractive indexes between the one of the air and the one of the fiber core. Anti-glare coatings, on the other side, use high roughness at the nanoscale or microscale levels to reduce reflectance by scattering-based light diffusion.

1.4 Different designs for optical fibers

While Section 1.3 has been focused on step index fibers, which are the most common design thanks to their diffusion in telecommunications networks as well as one of the simplest cases to treat, the goal of this section is to elaborate on the more exotic fiber designs around which the experimental work for the realization of this thesis revolves.

1.4.1 Photonic crystal fibers

The name "photonic crystal fibers" (PCFs) is commonly used to denote fibers designed with a periodic structure of materials with different refractive indexes across their section, often created by the presence of air holes along the fiber. They can be classified in two main groups, depending on the mechanism they rely on to guide light [45]:

- **Photonic bandgap-guiding fibers:** in these fibers, light is confined in the core thanks to a phenomenon analogous to the presence of an electronic bandgap in materials. In a way similar to the one in which the periodicity of the atomic distribution in a semiconducting crystal induces a forbidden band in the electronic density of states, carefully calibrated periodic modulations of the refractive index can create a band of light wavelengths that cannot propagate in the structure. Introducing a defect in the periodicity, for example a missing hole in the case of air-hole PCFs, will force light having a wavelengths that falls in the bandgap to travel confined in the defect, that will thus act as the fiber core. An interesting property related to this guiding mechanism is that there is no more need for the refractive index of the clad to be lower than the one of the core, as long as the wavelength is proper.
- **Index-guiding PCFs:** in these fibers, light is confined in the core by the mechanism of modified total internal reflection, which instead of a cladding of another material uses a periodic structure of lower refractive index inclusions (often holes) to create the refractive index contrast needed for guiding light in the core. As visible in Figure 1.14, the average refractive index is indeed lower in the periodic structure area than in the core area, allowing for a guiding mechanism similar to the one of step index fibers. This configuration, however, allows for a tailoring of characteristics like the dispersion profile and number of modes that would be impossible in step index fibers.

As they are not the focus of this work, from here on the discussion on photonic bandgap-guiding fibers will be neglected, and only index-guiding PCFs having air-filled holes as low refractive index inclusions will be discussed further in this section.

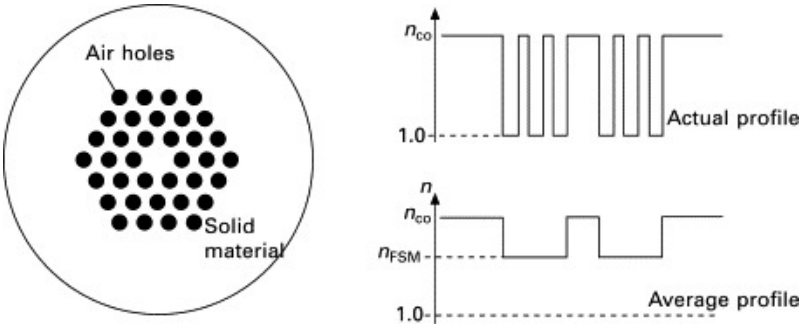

Figure 1.14: *Real and average refractive index profiles in an air-hole index-guiding PCF [46].*

1.4.1.1 Fabrication methods for air-hole PCFs

The most common technique for the fabrication of fibers with holey structures is the one of stack and draw: rods and capillaries of the core material are stacked in an exagonal structure, which is then jacketed with a tube of the same material. The jacketed structure can then be drawn either directly into a fiber or into a cane to be re-jacketed and re-drawn, depending on the desired final size of the core. After the final drawing, the fiber will have holes where the capillaries were placed in the structure. A schematic representation of the different steps of the technique are shown in Figure 1.15. This technique is nowadays a well-established one, and its high versatility is exploited to develop all kinds of exotic designs.

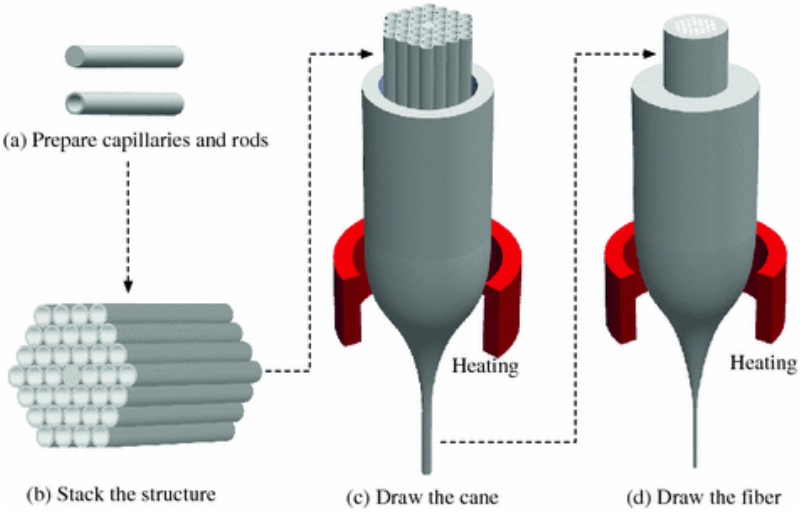

Figure 1.15: *Schematics of the stack and draw technique for the fabrication of air-hole PCFs [47].*

Other techniques used for the fabrication of preforms with holes to be drawn into PCFs include the mechanical drilling of holes into a solid cylinder, producing the glass by sol-gel in a cast, extruding the materials through a die and injection molding [48].
In the case of chalcogenide glasses, the casting technique described in [49] has been shown to particularly promising, and as such is the one used in the experimental part of this work regarding index-guiding PCFs(see Section 3.2.4).

1.4.1.2 Guiding mechanism and confinement losses

The index-guiding PCFs that will be treated in the remainder of this thesis have one of the most common structures, the same depicted in Figure 1.14: an hexagonal periodic series of holes in the fiber, with the central one missing. The area surrounding the central missing hole acts as the core

of the fiber. The fiber's geometrical structure is, in this case, entirely defined by three parameters: the hole diameter d, the pitch (distance between the centers of two neighboring holes) Λ and the number of hole rings surrounding the core N_r. The largest cylindrical area without holes, which has diameter equal to $2\Lambda - d$, is considered as the core of the fiber.
Having the same refractive index in the core and in the circular crown surrounding the holey part, this kind of index-guiding PCF can be modeled, at a first approximation, as a w-type fiber. The name w-type fibers is normally used to define all-solid fibers having two claddings, as opposed to the single cladding of step index fibers, with the outer cladding having higher refractive index than the inner one. Due to this last characteristic, in w-type fiber modes having tails of their transverse field profile larger than the inner cladding will leak energy from the core to the outer cladding, causing confinement losses. The same applies to the PCFs that are object of this section. These confinement losses can be decreased modifying the geometry in two ways: increasing N_r or increasing the $\frac{d}{\Lambda}$ ratio (see Figure 1.16). In the w-type fiber model, those modifications would correspond to increasing the diameter of the inner clad and increasing the refractive index contrast between core and inner clad respectively.

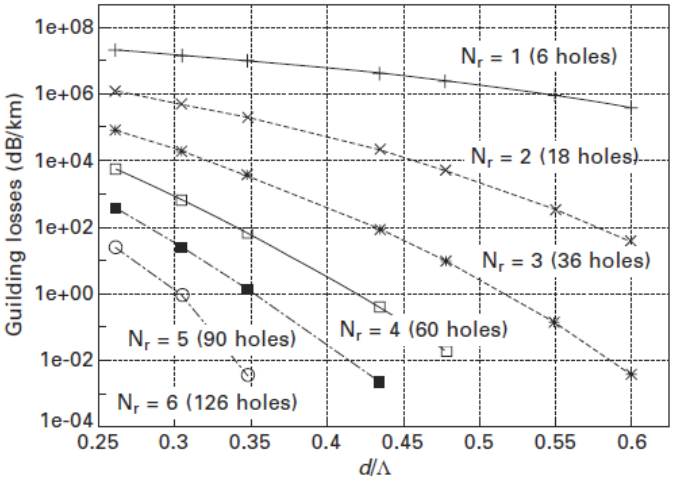

Figure 1.16: *Fundamental mode losses as function of number of air hole ring* N_r *and the ratio* $\frac{d}{\Lambda}$ *for index-guiding PCFs with* $n_{core} = 2.5$, $\Lambda = 1.55$ μm, *calculated at a wavelength of* 1.55 μm *[14, 50].*

The tunability of confinement losses allows for a behavior typical of this kind of fibers: the endlessly single mode regime. Higher order modes exhibit higher confinement losses, so the structure can be engineered to have confinement of the fundamental mode and total leakage of the higher order ones, independently on the light wavelength. Theoretically, this happens for $\frac{d}{\Lambda} < 0.4$, regardless of the material refractive index or number of rings [45]. Endlessly single mode behavior can have wide applications, allowing to avoid modal interference even in large core fibers, thus increasing the power that can be injected without having detrimental thermal effects and nonlinear behavior.

1.4.1.3 Dispersion

Another property that increased the interest in solid core index-guiding PCFs as a possible solution for many scientific challenges is the possibility of tailoring the dispersion profile. For applications involving pulsed light, such as telecommunications and nonlinear optics, dispersion management can be extremely important, as the position of the zero dispersion wavelength influences nonlinear phenomena and, more in general, dispersion modifies the time profile of pulses during propagation. In the case of single mode step-index fibers, the waveguide contribution to the total dispersion, D_{wav}, is generally negative, meaning that the zero dispersion wavelength can only be redshifted by changing the only relevant geometrical parameter in this kind of fibers, the core diameter. The smaller the core, the stronger the ZDW redshifting effect.
In index-guiding PCFs, instead, using the appropriate geometrical parameters the ZDW can be

blueshifted (see Figure 1.17). Furthermore, this effect can be significantly stronger than the red-shifting in step-index fibers. Once again, the main parameter to be adjusted in order to tailor the dispersion is the core diameter, that in this kind of fibers is determined by both the holes' diameter and pitch.

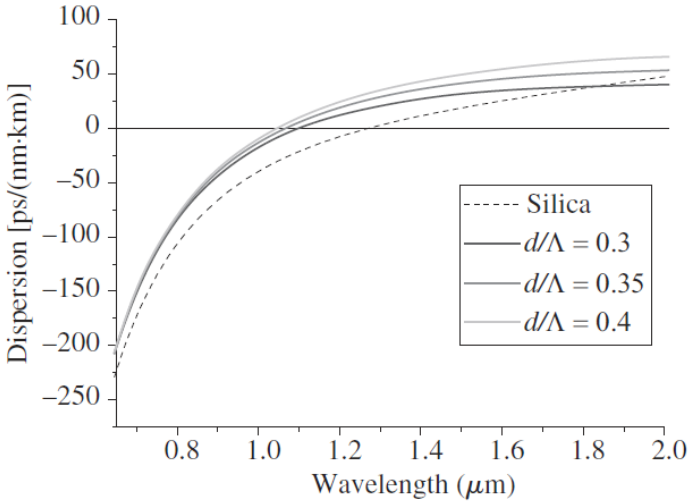

Figure 1.17: *Dispersion curves for an air-silica PCF with* $\Lambda = 3$ μm *and* $\frac{d}{\Lambda}$ *varied from 0.3 to 0.4 [45].*

1.4.2 Graded index fibers

A typical problem encountered in applications requiring multimode fibers is the one of excessive intermodal dispersion disrupting the time profile of the beam. A possible solution that has been found to reduce the time delay $\delta\tau$ between modes is using graded index fibers. These, as the name suggests, are fibers in which the refractive index in the core has a gradual radial variation from its maximum to the cladding refractive index, in opposition to the sharp variation typical of step-index fibers and index-guiding PCFs (see Figure 1.18). While being mostly used in multimode applications, these kind of smoother refractive index profiles can also be exploited for chromatic dispersion tailoring in single mode fibers.

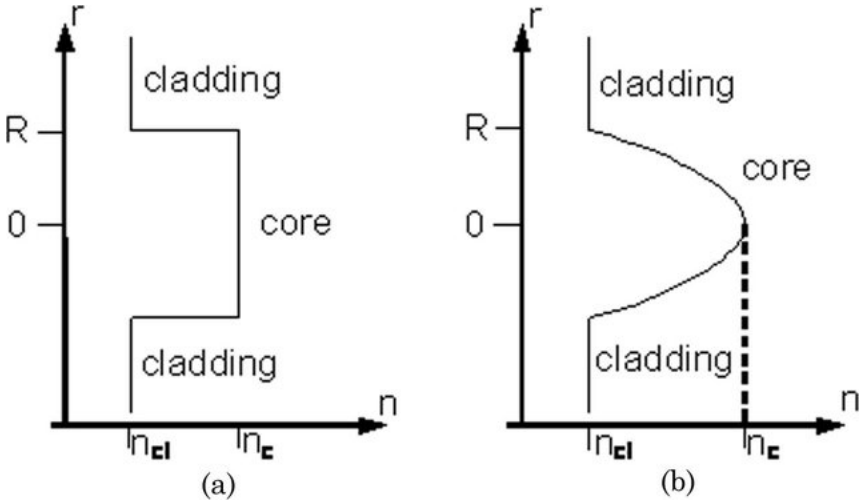

Figure 1.18: *Refractive index distribution in (a) step-index fibers and (b) graded index fibers [51].*

1.4.2.1 Fabrication

The most common way to fabricate graded index preforms to be drawn into fibers, especially silica-based ones to be used in telecommunications, is to use modified chemical vapor deposition (MCVD). This technique is based on thermally-induced reaction between gases at a surface. A mixture of oxygen, $SiCl_4$ and a refractive index modifier, usually $GeCl_4$, is flowed through a rotating silica tube, while an external burner is moved back and forth along it. Where the silica is heated by the burner, the gases react forming on the tube surface a fine of SiO_2 and, in the case of $GeCl_4$ gas being present, GeO_2. This soot is sintered by the heat into a thin glass layer. Controlling the speeds of the tube rotation and burner movement allows the formation, layer after layer, of uniform glass through the tube. At the end of the process, the remaining central hole is collapsed by heat. Changing the concentration ratios of the different gases inside the tube during the process allows for a fine control of the radial refractive index profile of the preform, and thus this technique is well suited for producing graded index preforms of various kinds.
Another technique for the manufacturing of graded index preforms is ion exchange [52, 53]. It consists of immersing a glass rod in a molten salt bath, creating the conditions for atomic exchange between the cations in the glass structure and the ones in the salt. This locally affects, usually by decreasing it, the refractive index of the glass at the exchange sites, due to the combined effects of the difference in polarizability and the structural strains created by the difference in size between the salt cations and the glass ones. Leaving the glass in the salt bath for an appropriate amount of time will induce the creation of the desired graded radial profile of refractive index by diffusion of the exchanged ions towards the center of the rod.
Other common techniques to obtain refractive index gradients in glasses are: irradiation by neutrons of glasses with large boron content, partial polymerization by UV irradiation (for plastic materials), ion leaching or stuffing in sol-gel formed glasses, partial crystallization of the glass [52–54]. It has to be noticed, though, that not all of these techniques are suitable for fiber drawing after the gradient formation.
A technique that has only recently been applied to graded index optics production is the one of stack and draw [53], already described in Section 1.4.1.1 for PCFs fabrication. Using rods of glasses with different refractive indexes a graded index profile can be obtained, with great versatility in both profile design and refractive index contrast. This last technique is the one used for the production of graded index chalcogenide optical fibers in this thesis.

1.4.2.2 Optimal refractive index profile

As already mentioned, nowadays the main use of graded index fibers is the minimization of intermodal dispersion during multimode light propagation. In order to achieve this goal, a proper refractive index profile of the core must be chosen.
A roughly approximated way to take on this optimization problem starts by using geometrical optics to estimate the maximum delay between modes in a step index fiber, which is a good indicator of the magnitude of intermodal dispersion, and then trying to minimize it, as described in [42]. Being the shortest possible path to travel an optical fiber of length L the one along the axis, the shortest possible travel time for light can be written as

$$\tau_{\min} = \frac{n_{core} L}{c} \ .$$

Meanwhile, the longest path for propagation inside the fiber is the one taken by light entering the fiber at the maximum possible incidence angle, which is defined by the numerical aperture NA. The travel time for such a path will be

$$\tau_{\max} = \frac{n_{core} L}{c}(1 + \Delta) \ ,$$

where $\Delta = \frac{NA^2}{2n_{core}^2}$ represents the refractive index contrast between core and cladding. Often this contrast is small, and in that case the approximation $\Delta = \frac{n_{core} - n_{clad}}{n_{core}}$ is used. From the relations above, the maximum possible delay between modes can be estimated as

$$\delta\tau = \frac{n_{core} L}{c}\Delta \ .$$

A commonly used description for the refractive index profile of graded index fibers [42, 55] is:

$$\begin{cases} n = n_{core}\sqrt{1-2\Delta(\frac{r}{\varnothing_{core}})^{\alpha}} & \text{for } |r| \leq \varnothing_{core} \\ n = n_{clad} & \text{for } |r| > \varnothing_{core} \end{cases}$$

where r is the distance from the center of the fiber and n_{core} indicates here the maximum of the refractive index, at the core center. The value of α here defines the profile shape, which can be approximated as triangular for $\alpha = 1$, as parabolic for $\alpha = 2$, and which tends to the step index profile for $\alpha \to \infty$.
Calculating the time delay for $\alpha = 2$, it is found that

$$\delta\tau = \frac{n_{core} L}{c}\frac{\Delta^2}{2} ,$$

which, considering that for the most common fibers $\frac{\Delta}{2} \simeq 10^{-3}$, is a strong improvement with respect to the step index fiber case.
The optimum value is of α to minimize $\delta\tau$ is, however, not exactly 2. Calculating it precisely is an involved matter, as it depends on the composition of the glasses used to produce the fiber and on its intended operational wavelength range (as the refractive indexes are functions of the wavelengths, and therefore $\Delta := \Delta(\alpha)$).
Another interesting property of graded index fibers is the cut-off wavelength: these fibers have wider single mode operation ranges with respect to their step-index counterparts. While step index fibers are single mode for values of the normalized frequency $V < 2.405$, for graded index fibers this range increases to $V < 3.518$ when $\alpha = 2$, and is even larger when $\alpha = 1$. As a rule of thumb, for graded index fibers the cutoff occurs at $V \simeq 2.405\sqrt{1+\frac{2}{\alpha}}$.

1.5 Elements of nonlinear optics

The final goal of this thesis is the development of chalcogenide microstructured fibers suitable for supercontinuum generation, meaning for the conversion of laser light to broadband light while maintaining an high spatial coherence, in the mid-infrared. For a better understanding of the topic at hand, in this section a brief introduction of the physical phenomena underlying supercontinuum generation is given, with a special focus on nonlinear optics.

1.5.1 From linear to nonlinear optics

In Section 1.3.3.2, a simplified form of the wave equation has been derived from Maxwell equations using a number of approximations. One of them was the low power, or linear, approximation:

$$\vec{P} = \epsilon_0 \chi^{(1)} \vec{E} .$$

In cases in which the power density of light inside a material is high, like for example a high-peak-power pulsed laser propagating through a small core fiber, this approximation ceases to hold. When this happens, some of the higher order components of the polarization density vector cease to be negligible, and the full formulation needs to be used:

$$\vec{P} = \epsilon_0(\chi^{(1)}\vec{E} + \chi^{(2)}\vec{E}^2 + \chi^{(3)}\vec{E}^3 + ...) := \vec{P} + \vec{P}^{NL} .$$

Here the sum of all terms of order higher then one is defined as $\vec{P}^{NL}$.
Using this redefinition of the polarization density vector to derive once again the wave equation, an inhomogeneous differential equation is obtained:

$$\nabla^2\vec{E} - \frac{n^2}{c^2}\frac{\partial^2\vec{E}}{\partial t^2} = \frac{1}{\epsilon_0 c^2}\frac{\partial^2\vec{P}^{NL}}{\partial t^2} ,$$

where the term on the right is the one responsible for nonlinear phenomena.
The appearance of $\vec{P}^{NL}$ is strictly connected with the generation of new frequencies, which is the

basis of supercontinuum generation. Considering only the temporal component of the electric field, $E(t) = Ee^{-i\omega t}$, one can immediately see that the presence of higher order terms like $\vec{E}^2$ and $\vec{E}^3$ will correspond to the appearance of frequencies equal to 2ω and 3ω respectively (second and third harmonic generation). Furthermore, in reality the spectral profile of light is never a Dirac delta, as even a laser has a finite bandwidth. When more than one frequency is present, the inhomogeneous term in the nonlinear wave equation gives rise to frequency mixing. Even in the simplest case of nonlinearity ($\vec{P} = \epsilon_0(\chi^{(1)}\vec{E}+\chi^{(2)}\vec{E}^2$) in which all the terms of order higher than 2 are negligible, the presence of two different frequencies ω_1 and ω_2 will give rise to terms with different frequencies, corresponding to different phenomena: $2\omega_1$ and $2\omega_2$ (once again second harmonic generation), $\omega_1 + \omega_2$ (sum frequency generation), $|\omega_1 - \omega_2|$ (difference frequency generation) and a term at 0 frequency (optical rectification).
The nonlinear refractive index defined in Section 1.2.2.2 as an indicator of how much a material is suitable for nonlinear applications is directly proportional to the real part of $\chi^{(3)}$. For fibers, the overall capability of exhibiting nonlinear behavior is quantified by the nonlinear parameter

$$\gamma = \frac{2\pi}{\lambda}\frac{n_2}{A_{eff}}$$

where A_{eff} is the effective mode area, which is linked to the core size of the fiber.

1.5.2 Nonlinear optical phenomena involved in supercontinuum generation

1.5.2.1 Optical Kerr effect

The name "Kerr effect" refers in general to a change in the refractive index of a material in response to an applied electric field. The magnitude of this variation is directly proportional to the square of $\vec{E}$.
When the source of the electric field is the light propagating through the material itself, this phenomenon takes the name of "optical Kerr effect" (in opposition to the electro-optical Kerr effect, in which the field is applied externally). In this case, being the light intensity proportional to the square of $\vec{E}$ too, the refractive index variation is usally expressed in terms of I as

$$\Delta n = n_2 \cdot I \ ,$$

where n_2 is the nonlinear refractive index mentioned at the end of Section 1.5.1.
It needs to be mentioned that the relation above is not true for all materials. Indeed, some materials exist which are said to be "non-Kerr" [56], in which the dependence of the refractive index variation on intensity follows more complex laws, in general

$$\Delta n = f(I) \ .$$

While the optical Kerr effect doesn't directly generate any new light wavelength, it is the foundation of many of the nonlinear effects described in this section.

1.5.2.2 Self- and cross-phase modulation

When light propagates through a nonlinear medium with a time-dependent intensity, like in the case of short or ultrashort pulses, the variation of refractive index induced by the Kerr effect can be expressed as $\Delta n := \Delta n(t) = n_2 I(t)$. This in turn causes a time-dependent phase delay $\phi_{NL}(t)$ to the pulse itself (self-phase modulation) or to a co-propagating pulse (cross-phase modulation) [57].
To this phase shift corresponds, if the pulse envelope is slowly varying, an instantaneous frequency shift

$$\delta\omega(t) = \frac{d\phi_{NL}(t)}{dt} \ .$$

At the peak of the pulse, both $\Delta n(t)$ and $\phi_{NL}(t)$ exhibit a maximum, meaning that $\delta\omega(t) = 0$. Meanwhile on the leading edge of the pulse $\delta\omega(t) < 0$ (red-shift) and on the trailing edge $\delta\omega(t) > 0$

(blue-shift) [56] (see Figure 1.19). This corresponds to applying a chirp to the pulse (a pulse is called chirped if the frequency depends on time, namely upchirped if frequency increases in time and down-chirped if it decreases). If the starting pulse was down-chirped, this ulterior chirp causes spectral compression of the pulse. If it was unchirped or upchirped instead, self- or cross-phase modulation induces a spectral broadening, leading to the generation of new wavelengths in the pulse.

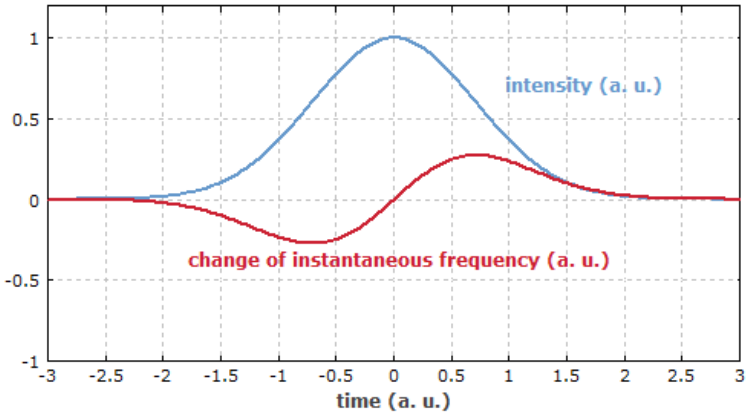

Figure 1.19: *Instantaneous frequency of an initially unchirped pulse which has experienced self-phase modulation [58].*

1.5.2.3 $\chi^{(n)}$-related new frequencies generation

As described in Section 1.5.1, when $\chi^{(n)}$ terms with n>1 in the expression of the polarizability vector cease to be negligible new terms appear in the solutions of the wave equation.
One of these corresponds to the generation of light having a frequency $\omega = n\omega_0$, where ω_0 is the frequency of the original signal and n corresponds at a non-negligible term $\chi^{(n)}$ in the decomposition of $\vec{P}^{NL}$. This phenomenon is called "high harmonic generation" (HHG). Due to phase matching conditions, the original signal and the newly generated one will propagate in the same direction. It is important to notice here that the HHG with n=2, named "second harmonic generation" (SHG), is irrelevant in fiber-based nonlinear optics. Indeed, being fibers normally made of isotropic materials such as glasses or polymers, $\chi^{(2)}$-related phenomena, which are by nature directional, do not take place. However, SHG, as other second order nonlinear effects, can be of great importance for new frequencies generation in crystal-based devices.
Another $\chi^{(2)}$ based effect leading to the appearance of new wavelengths is the one of sum and difference frequencies generation: when two signals of frequencies ω_1 and ω_2 copropagate through the non linear medium in exam, light will be generated at $\omega = \omega_1 + \omega_2$ and $\omega = |\omega_1 - \omega_2|$. However, due to issues related to phase matching, normally only one of the two new frequencies will experience efficient conversion from the signals. Interestingly, sum frequency generation can happen between a signal and its abovementioned second harmonic, leading to generation of light at $\omega = 3\omega_0$ in a way that is often more efficient than the one relying on $\chi^{(3)}$.

1.5.2.4 Raman and Brillouin scattering

Light propagating through a material can cause its molecules or its lattice to change their vibrational state. This phenomenon is called Raman scattering if it involves optical phonons and Brillouin scattering if it involves acoustical ones. Unlike IR absorption, where the energy of the photons absorbed by the material have to match the energy of the created phonon, Raman and Brillouin scattering can happen at every wavelength. This is due to the fact that these are two-photon processes: a photon is depleted from the signal (from now on named pump) to send the material to a high energy virtual state, and afterwards the material falls down to a state different from the original one by emitting a photon. If the material moves by this process from ground state

to an excited state, the frequency of the emitted photon will be lower than the one of the absorbed one and the new spectral band appearing is named "Stokes band". If, instead, the material was already in an excited state (for example because of thermal effects) and reverts to ground state, an "anti-Stokes" band will appear at frequencies higher than the one of the original signal. Usually the Stokes band is more intense than the anti-Stokes one.
Photons generated by spontaneous Raman scattering have no constraints in terms of propagation direction or phase, and they aren't therefore of great interest for the generation of supercontinuum. The interesting phenomenon for this application is stimulated Raman scattering: if a signal with frequency falling in a Raman band generated by the pump co-propagates with it, the generated photons have an high probability to have the same frequency, phase and direction as the signal. This causes an amplification of the signal by depletion of the pump, preserving the spatial coherence.

1.5.2.5 Solitons generation, fission and new frequencies generation

When an intense pulse is injected into a nonlinear medium under the right conditions, and his wavelength falls in the anomalous dispersion regime of the material, Kerr effect can balance out dispersion. This will cause the temporal and spectral profiles of the pulse to be either constant (fundamental soliton) or periodically evolving (higher order soliton) during propagation. The order of a soliton, which is identified as N and equal to 1 for fundamental ones, is depending on the peak power P_0 of the pulse once the material properties are fixed. This dependence can be expressed as $N^2 \propto P_0$.
For higher order solitons, the way they evolve periodically depends on a number of conditions, but it always starts with a phase of spectral broadening and temporal compression, which can be exploited for the generation of new frequencies. Also, higher order solitons are inherently unstable, and if perturbed they can split into a number of lower order ones. This phenomenon is known as soliton fission, and it is of great importance in supercontinuum generation. The other two ways soliton propagation can lead to the rise of new wavelengths are the generation of dispersive waves and the solitons self-frequency shifting.
When solitons with a peak wavelength close to ZDW are propagating, part of their energy can be transferred to the normal dispersion regime region of the spectrum, either during propagation or fission. Under proper phase matching conditions, the light generated this way will co-propagate with the solitons themselves, and take the name of dispersive wave. This phenomenon can lead to the broadening of the overall spectrum in the region with wavelengths shorter than the one of the pump.
Soliton self-frequency shifting is a phenomenon happening when the spectral profile of a soliton is overlapping with its Raman band, usually the Stokes one. In this condition, the long wavelength tail of the soliton can be amplified by stimulated Raman scattering during propagation, depleting the short wavelength one, causing an overall red-shift of the soliton spectral profile. As the Raman band shifts together with the soliton, this process can potentially continuously go on during the propagation, moving the soliton further and further towards wavelengths longer than the one of the pump.

1.5.2.6 Four-wave mixing

Four-wave mixing is a $\chi^{(3)}$-related nonlinear process leading to the generation of new wavelengths during light propagation in a material.
In its non-degenerate form it involves four different frequencies interacting, two pumps being depleted and two signals being generated. Defining the frequencies of the pumps as ω_1 and ω_2, with $\omega_2 > \omega_1$, this process leads to the generation of a short wavelength sideband with frequency $\omega_3 = 2\omega_2 - \omega_1$ and of a long wavelength one with frequency $\omega_4 = 2\omega_1 - \omega_2$. This is due to refractive index modulation, in a way analogous to self- and cross-phase modulation but with different wave degeneracy [59]. As in Raman scattering, this process favors stimulated emission with respect to spontaneous one, leading to the amplification of eventual signals propagating at ω_3 or ω_4. Phase matching conditions are of fundamental importance for four-wave mixing, and cumulative effects along propagation can be observed only if the dispersion allows those conditions to hold.

Degenerate four-wave mixing, in which the two pump frequencies are coincident, can also happen. In this case, a signal (or noise) is amplified through the depletion of two photons from the pump and the emission of one at its frequency. The remaining energy is dispersed through the emission of a second photon at the frequency equal to $2\omega_p - \omega_s$, with ω_p and ω_s the frequencies of the pump and amplified signal respectively. Thus, this amplification process leads to the rise of a sideband, called idler, at a frequency shifted with respect to the pump one symmetrically to the signal.

1.5.2.7 Two-photons absorption

The spectral position of the blue edge of the transparency window of a material is, in the linear approximation, correlated to the material's bandgap. Photons with high enough energy (i.e. short enough wavelength) to surpass the bandgap are absorbed by the material, with the result of sending electrons from the valence band to the conduction band.
When the phenomenon of many-photon absorption happens, a number $n > 1$ of photons, with total energy equal or greater to the one needed for an electron to cross the bandgap, is absorbed instead to obtain the same result. The probability of many-photons absorption, however, decreases rapidly when n increases, and for low light intensities this phenomenon is negligible with respect to single-photon absorption, even for $n = 2$.
With high enough light intensity, two-photon absorption can become relevant. This effect is also known as nonlinear absorption, because the magnitude of its impact is directly proportional to I. Its contribution to the total absorption coefficient is in fact expressed as

$$\alpha_{NL} = \beta I \ .$$

It's important to not confuse the two-photon absorption coefficient β above with the light's propagation constant, which shares the same Greek letter for notation.
Nonlinear absorption can be a relevant effect for supercontinuum generation in optical fibers: allowing photon absorption at wavelengths longer than the linear blue edge, it can reduce the bandwidth of the spectral window in which pulse broadening can be efficiently achieved.

1.6 State of the art of supercontinuum generation in the mid-infrared

1.6.1 Mid-IR supercontinuum generation in optical fibers

While supercontinuum sources in the visible and near infrared ranges are, thanks to the maturity of silica fiber technology, already well established, highly efficient and widely commercially available, the same cannot be said for the mid-IR region. Being the latter a spectral region of great interest for many applications, as will be explained more in detail in Section 1.6.2, the broadening of supercontinuum sources' spectral range towards longer wavelengths is nowadays a thriving research field.
Being supercontinuum generation a sum of nonlinear processes, optical fibers are an ideal medium for it. Indeed the small mode area, large interaction length and, for some fiber designs, highly tunable dispersion can strongly increase the effectiveness of these processes. In addition to this, fiber-based light sources have huge advantages in terms of compactness, ease of use and versatility.
The most common glasses used to produce fibers for mid-IR supercontinuum generation are GeO_2 doped silica, fluorides, heavy metal oxides and chalcogenides, each of them having different strong and weak points.
GeO_2 doped silica and fluoride glasses, especially the most commonly used $ZrF_4 - BaF_2 - LaF_3 - AlF_3 - NaF$ (ZBLAN), both have a quite mature technological development and very low losses in their transparency windows. Germanium-oxide-doped silica fibers have reduced losses up to about $3 - 3.3$ μm [60], and the transparency windows extends to 4.5 μm for ZBLAN and to 5.5 μm for fluoroindate, another fluoride system that has been considered attractive for supercontinuum generation [61]. Regarding the nonlinear refractive index n_2, both these glass systems exhibit values on the same order of magnitude of the one of pure silica ($2.2 \cdot 10^{-20}$ m^2/W [22]). More specifically ZBLAN and fluoroindate have n_2 values of about $2.1 \cdot 10^{-20}$ m^2/W and $3.2 \cdot 10^{-20}$ m^2/W

respectively [26, 62], while GeO_2-doped silica can reach values as high as $5 \cdot 10^{-20}$ m^2/W for a GeO_2 concentration of 97% [63]. In this section even fibers with a 100% germania core, which can reach values of n_2 of 4.5 times the one of silica [64], will be referred to as $GeO_2 - SiO_2$ fibers. The ZDW for both these systems allow pumping with common near infrared lasers. A pump power limitation exists for fluoride glasses due to the thermal stability of splicing between fluoride and silica fibers, in setups where such splicing is necessary [61].
Among the heavy metal oxide glasses, tellurites are probably the most interesting ones for mid infrared applications, more specifically fluorotellurites with low OH content. Their transparency window can reach up to around 5 μm [65], making them attractive as substitutes for fluorides. The optical losses are higher with respect to the systems discussed above, but the value of n_2 can be up to 15 times larger than the one of silica [61], allowing for shorter fibers and thus effectively compensating the problem of attenuation. The ZDW of tellurites, however, is at longer wavelengths compared to the ones of silica or fluorides [23], a fact that may limit the laser sources available for pumping. This last issue can be solved by blue-shifting the ZDW with proper fiber design [24].
Chalcogenide fibers can be transparent up to 15 μm, and their nonlinear refractive index can reach values as high as 1000 times the one of silica. This makes them the natural candidates for supercontinuum generation further extended in the mid-IR with respect to the other materials discussed in this section. The main drawbacks in the use of chalcogenide fibers are the low power damage threshold limiting the intensity of the pumps, and subsequently the output powers, and the ZDW being usually placed at more than 4 μm, which requires bulky and expensive laser sources such as OPOs and OPAs to be used as pumps [61]. The last problem has been recently addressed using cascaded pumping schemes such as the one described in [66].
Some of the best results as of now in terms of broadness and average output power for supercontinua generated in the mid infrared using fibers produced with the different glass systems discussed above can be found in Table 1.6.

Table 1.6: *State of the art of mid-IR supercontinuum generation in different fibers.*
(MOPA: Master Oscillator Power Amplifier; TDF: Thulium Doped Fiber; TDFL: Thulium Doped Fiber Laser; TDFA: Thulium Doped Fiber Amplifier; EDFA: Erbium Doped Fiber Amplifier; EYDFA: Erbium Ytterbium Doped Fiber Amplifier; OPG: Optical Parametric Generator; OPO: Optical Parametric Oscillator; OPA: Optical Parametric Amplifier; NDFG: Noncollinear Difference Frequency Generator; SPPG: Single-Pass Parametric Generation.)

Glass system	Type of fiber	Pumping	Output spectral range	Output power	Reference
$GeO_2 - SiO_2$	Graded index	MOPA	0.7 μm – 3.2 μm	1.44 W	[67]
$GeO_2 - SiO_2$	Step index	TDFL + TDFA	2 μm – 3 μm	30 W	[64]
ZBLAN	Step index	1550nm + TDF	1.75 μm – 4.75 μm	1.2 W	[68]
ZBLAN	Step index	1550nm + EDFA + EYDFA + TDFA	1.9 μm – 4.2 μm	15.2 W	[69]
Fluoroindate	Step index	OPG + EDFA	2.4 μm – 5.4 μm	10 mW	[70]
Fluoroindate	Step index	Tm-doped MOPA	0.8 μm – 4.7 μm	11.3 W	[71]
Tellurite	Step index	Post-amplified OPO	1.3 μm – 5.3 μm	150 mW	[72]
Chalcogenide	Step index	OPA + NDFG	1.4 μm – 13.3 μm	150 μW	[73]
Chalcogenide	Tapered PCF	SPPG	1 μm – 11.5 μm	35.4 mW	[74]
Chalcogenide	Step index	Cascaded	2 – 11 μm	417 mW	[75]

1.6.2 Applications of mid infrared supercontinuum sources

Thanks to their broad mid-IR spectral coverage, high coherence, and good beam quality, mid-IR supercontinuum sources are potential candidates for a variety of applications in domains such as spectroscopy, sensing, biology, metrology, and spectral imaging [76, 77].
As an example of this, the IR signature of propanol and acetone has been detected by fibers evanescent wave spectroscopy (FEWS) using a chalcogenide index guiding PCF [77]. In this experiment, it was demonstrated that an exposed-core chalcogenide PCF, as the one shown in Figure 1.20, can be more sensitive to the environment than classical single-index fibers, such as those used in [78].
Mid-IR spectral imaging, combined with data mining algorithms, has also been utilized as an aid for diagnosing some types of cancers [79–82]. The acquisition speed and penetration depth of traditional mid-IR spectral imaging is subject to low brightness and lack of flexibility for the delivery and detection of light [83], making intense laser sources with high signal-to-noise ratios an ideal choice for rapid acquisition through the mid-IR range. Quantum cascade lasers (QCL) were once

used in mid-IR spectral imaging systems to reduce the acquisition time, but the limited frequency coverage of QCLs cannot satisfy the diagnostic requirements and maintain, at the same time, the simplicity of the system at a reasonable cost. Thus, supercontinuum sources are the most suitable ones for broadband mid-IR spectral imaging. For example, ZBLAN-fluoride-fiber-based supercontinuum sources, with a 2–4.5 μm spectral range, were selected to be integrated into mid-IR spectral imaging systems demonstrated in the past few years [84–86].

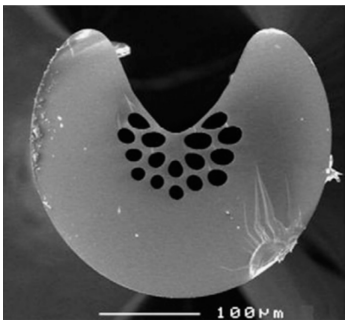

Figure 1.20: *Scanning electron microscope image of an exposed-core chalcogenide index guiding PCF [77].*

In 2012, Dupont et al. presented, for the first time, a high-resolution contact-free infrared microscope, based on a supercontinuum spanning from 1.4 to 4.0 μm generated by using a 1900 nm fiber laser to pump 10 m of ZBLAN fiber. The system was tested by a mixture of oil and water and resolutions of 35 μm and 25 μm for the water absorption image and oil absorption image were obtained, respectively, as shown in Figure 1.21 [84].
In 2017, Farries et al. reported a mid-infrared spectral imaging system for the rapid assessment of cells to be used cytological diagnosis, consisting of a ZBLAN-fiber-based supercontinuum source, a fast acousto-optic tunable filter (AOTF), and a high-resolution thermal camera. The AOTF enables the system to record a 100-wavelengths image cube and 300 k pixels in 2 s, so that it can be used to test the cells of a living person. By comparison, the system proved to have a higher spectral resolution than a Fourier transform infrared (FTIR) system. Despite the restrictions imposed by the filter inside the thermal camera and the range of the supercontinuum source, samples of colon cells could be imaged in the 2.87–3.7 μm spectral range [85]. In order to improve the spectral range, in later studies, chalcogenide MOFs were chosen to replace ZBLAN fibers.

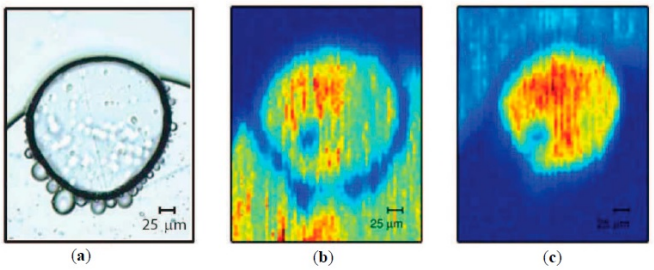

Figure 1.21: *(a) Optical microscope image of oil–water mixture; (b,c) IR microscope image obtained at wavelengths corresponding to high absorption of water and oil, respectively [84].*

In 2018, Petersen et al. designed the first mid-IR spectral imaging system in the long-wavelength region using SC generation [83]. The system consisted of a point scanning device and a chalcogenide fiber-based supercontinuum. The supercontinuum source could deliver light from 2 to 7.5 μm with an output power of 25 mW, which enabled the system to collect sample information from 5.7 to 7.3 μm, in the diagnostic fingerprint region [83]. Figure 1.22 presents the first mid-IR spectral

image obtained with a supercontinuum source emitting wavelengths longer than 4 μm. The mid-IR image obtained at 6.03 μm (Figure 1.22.c) held interesting information on the position of specific molecules that could be integrated with classical histologic analysis (visible images, Figure 1.22a,b) [83].

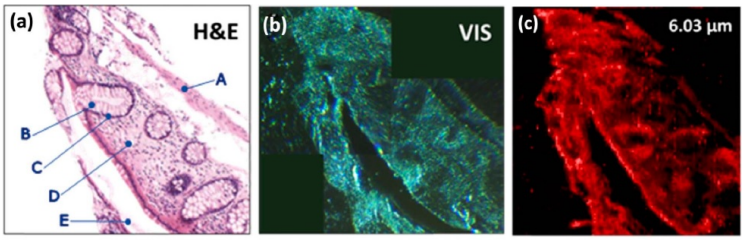

Figure 1.22: *(a) Confocal image from histological analysis using gold standard hematoxylin and eosin (H&E); (b) visible light transmission image of the sample; (c) mid-IR absorbance image [83].*

Bibliography

[1] Basudeb Karmakar, Klaus Rademann, and Andrey Stepanov. *Glass nanocomposites: synthesis, properties and applications*. William Andrew, 2016.

[2] William Houlder Zachariasen. "The atomic arrangement in glass". In: *Journal of the American Chemical Society* 54.10 (1932), pp. 3841–3851.

[3] Arun K Varshneya. *Fundamentals of inorganic glasses*. Elsevier, 2013.

[4] James E Shelby. "Introduction to glass science and technology, Royal Soc". In: *Chem., Cambridge* (1997), p. 20.

[5] Ioannis M Kalogeras and Haley E Hagg Lobland. "The nature of the glassy state: structure and glass transitions". In: *Journal of Materials Education* 34.3 (2012), p. 69.

[6] David Chandler. "Introduction to modern statistical mechanics". In: *Introduction to Modern Statistical Mechanics, by David Chandler, pp. 288. Foreword by David Chandler. Oxford University Press, Sep 1987. ISBN-10: 0195042778. ISBN-13: 9780195042771* (1987), p. 288.

[7] Juejun Hu. *MIT 3.071 Amorphous Materials*. URL: https://ocw.mit.edu/courses/materials-science-and-engineering/3-071-amorphous-materials-fall-2015/lecture-notes/MIT3_071F15_Lecture1.pdf.

[8] CNJ Wagner. "Direct methods for the determination of atomic-scale structure of amorphous solids (X-ray, electron, and neutron scattering)". In: *Journal of Non-Crystalline Solids* 31.1-2 (1978), pp. 1–40.

[9] A Zakery and SR Elliott. "Optical properties and applications of chalcogenide glasses: a review". In: *Journal of Non-Crystalline Solids* 330.1-3 (2003), pp. 1–12.

[10] James A Savage. "Optical properties of chalcogenide glasses". In: *Journal of Non-Crystalline Solids* 47.1 (1982), pp. 101–115.

[11] DJ Brady. "Dl. 1 Transmission of chalcogenide glass". In: *Properties, Processing and Applications of Glass and Rare Earth-doped Glasses for Optical Fibres* 22 (1998), p. 283.

[12] JS Sanghera and ID Aggarwal. "Active and passive chalcogenide glass optical fibers for IR applications: a review". In: *Journal of Non-Crystalline Solids* 256 (1999), pp. 6–16.

[13] GE Snopatin, VS Shiryaev, VG Plotnichenko, EM Dianov, and MF Churbanov. "High-purity chalcogenide glasses for fiber optics". In: *Inorganic materials* 45.13 (2009), p. 1439.

[14] Jean-Luc Adam and Xianghua Zhang. *Chalcogenide glasses: preparation, properties and applications*. Woodhead publishing, 2014.

[15] Johann Troles, Vladimir Shiryaev, Mikhail Churbanov, Patrick Houizot, Laurent Brilland, Frédéric Désévédavy, Frédéric Charpentier, Thierry Pain, G Snopatin, and Jean-Luc Adam. "GeSe4 glass fibres with low optical losses in the mid-IR". In: *Optical Materials* 32.1 (2009), pp. 212–215.

[16] Julie Keirsse, Catherine Boussard-Plédel, Olivier Loreal, Olivier Sire, Bruno Bureau, Bruno Turlin, Patricia Leroyer, and Jacques Lucas. "Chalcogenide glass fibers used as biosensors". In: *Journal of non-crystalline solids* 326 (2003), pp. 430–433.

[17] Laurent Calvez. "Chalcogenide glasses and glass-ceramics: Transparent materials in the infrared for dual applications". In: *Comptes Rendus Physique* 18.5–6 (2017), pp. 314–322.

[18] Johann Troles, Jean-Luc Adam, Laurent Brilland, Catherine Boussard-Plédel, Bruno Bureau, Virginie Nazabal, Céline Caillaud, Frédéric Charpentier, Hugues Tariel, Samuel Poulain, Solenn Cozic, and Marcel Poulain. "Mid-infrared glass optical fibers: tools for versatile, robust and compact spectroscopic systems". In: *Proceeding of the 8th International Symposium on Optronics in Defence and Security* (2018).

[19] Robert Fairman and Boris Ushkov. *Semiconducting Chalcogenide Glass II: Properties of Chalcogenide Glasses*. Academic Press, 2004.

[20] FA Jenkins and HE White. "Fundamentals of optics". In: (1976).

[21] Gorachand Ghosh. *Handbook of optical constants of solids: Handbook of thermo-optic coefficients of optical materials with applications*. Academic Press, 1998.

[22] A Boskovic, SV Chernikov, JR Taylor, Lars Gruner-Nielsen, and OA Levring. "Direct continuous-wave measurement of n2 in various types of telecommunication fiber at 1.55 μm". In: *Optics letters* 21.24 (1996), pp. 1966–1968.

[23] Shigeru Fujino and Kenji Morinaga. "Material dispersion and its compositional parameter of oxide glasses". In: *Journal of non-crystalline solids* 222 (1997), pp. 316–320.

[24] P Domachuk, NA Wolchover, M Cronin-Golomb, A Wang, Alan K George, CMB Cordeiro, Jonathan C Knight, and FG Omenetto. "Over 4000 nm bandwidth of mid-IR supercontinuum generation in sub-centimeter segments of highly nonlinear tellurite PCFs". In: *Optics Express* 16.10 (2008), pp. 7161–7168.

[25] Meisong Liao, Chitrarekha Chaudhari, Guanshi Qin, Xin Yan, Chihiro Kito, Takenobu Suzuki, Yasutake Ohishi, Morio Matsumoto, and Takashi Misumi. "Fabrication and characterization of a chalcogenide-tellurite composite microstructure fiber with high nonlinearity". In: *Optics express* 17.24 (2009), pp. 21608–21614.

[26] Chenan Xia, Malay Kumar, Ojas P Kulkarni, Mohammed N Islam, Fred L Terry Jr, Mike J Freeman, Marcel Poulain, and Gwenael Mazé. "Mid-infrared supercontinuum generation to 4.5 μm in ZBLAN fluoride fibers by nanosecond diode pumping". In: *Optics letters* 31.17 (2006), pp. 2553–2555.

[27] CR Day, PW France, SF Carter, MW Moore, and JR Williams. "Fluoride fibres for optical transmission". In: *Optical and quantum electronics* 22.3 (1990), pp. 259–277.

[28] JM Harbold, FÖ Ilday, FW Wise, JS Sanghera, VQ Nguyen, LB Shaw, and ID Aggarwal. "Highly nonlinear As–S–Se glasses for all-optical switching". In: *Optics Letters* 27.2 (2002), pp. 119–121.

[29] Mohammed El-Amraoui, Julien Fatome, Jean-Charles Jules, Bertrand Kibler, Grégory Gadret, Coraline Fortier, Frédéric Smektala, Igor Skripatchev, CF Polacchini, Younes Messaddeq, et al. "Strong infrared spectral broadening in low-loss As-S chalcogenide suspended core microstructured optical fibers". In: *Optics express* 18.5 (2010), pp. 4547–4556.

[30] Jeffrey M Harbold, F Omer Ilday, Frank W Wise, and Bruce G Aitken. "Highly nonlinear Ge-As-Se and Ge-As-S-Se glasses for all-optical switching". In: *IEEE Photonics Technology Letters* 14.6 (2002), pp. 822–824.

[31] SM Karazi, IU Ahad, and KY Benyounis. *Laser Micromachining for Transparent Materials*. Elsevier, 2017.

[32] Adalbert Feltz. *Amorphous inorganic materials and glasses*. VCH, 1993.

[33] Qiuju Zheng and John C Mauro. "Viscosity of glass-forming systems". In: *Journal of the American Ceramic Society* 100.1 (2017), pp. 6–25.

[34] NA Mauro, M Blodgett, ML Johnson, AJ Vogt, and KF Kelton. "A structural signature of liquid fragility". In: *Nature communications* 5 (2014), p. 4616.

[35] John Crisp. *Introduction to fiber optics*. Elsevier, 2005.

[36] So Kawakami and J Nishizawa. "An optical waveguide with the optimum distribution of the refractive index with reference to waveform distortion". In: *IEEE Transactions on Microwave Theory and Techniques* 16.10 (1968), pp. 814–818.

[37] Teiji Uchida, Moatoaki Furukawa, Ichiro Kitano, K Koizumi, and Hiroyoshi Matsumura. "Optical characteristics of a light-focusing fiber guide and its applications". In: *IEEE Journal of Quantum Electronics* 6.10 (1970), pp. 606–612.

[38] TA Birks, PJ Roberts, P St J Russell, DM Atkin, and TJ Shepherd. "Full 2-D photonic bandgaps in silica/air structures". In: *Electronics letters* 31.22 (1995), pp. 1941–1943.

[39] Tim A Birks, Jonathan C Knight, and P St J Russell. "Endlessly single-mode photonic crystal fiber". In: *Optics letters* 22.13 (1997), pp. 961–963.

[40] JC Knight, TA Birks, BJ Mangan, and P St J Russell. "Microstructured silica as an optical-fiber material". In: *Mrs Bulletin* 26.8 (2001), pp. 614–617.

[41] Tanya M Monro, Yvonne D West, Daniel W Hewak, NGR Broderick, and DJ Richardson. "Chalcogenide holey fibres". In: *Electronics Letters* 36.24 (2000), pp. 1998–2000.

[42] Fedor Mitschke and Fedor Mitschke. *Fiber optics*. Springer, 2016.

[43] Moscow Institute of Physics and Technology. *Patterns of transverse distribution of optical radiation intensity in the output beam*. URL: https://www.photonics.com/Articles/Large-Mode-Area_Optical_Fibers_Maintain/a62269.

[44] Ming-Jun Li and Daniel A Nolan. "Optical transmission fiber design evolution". In: *Journal of Lightwave Technology* 26.9 (2008), pp. 1079–1092.

[45] Luc Thévenaz. *Advanced fiber optics*. EPFL press, 2011.

[46] A Argyros. "Structure, properties and characteristics of optical fibres". In: *Handbook of textile fibre structure*. Elsevier, 2009, pp. 458–484.

[47] Zhengyong Liu and Hwa-Yaw Tam. "Photonic Crystal Fiber Pressure Sensors". In: *Computational Photonic Sensors*. Springer, 2019, pp. 261–285.

[48] Desmond M Chow, SR Sandoghchi, and FR Mahamd Adikan. "Fabrication of photonic crystal fibers". In: *2012 IEEE 3rd International Conference on Photonics*. IEEE. 2012, pp. 227–230.

[49] Quentin Coulombier, Laurent Brilland, Patrick Houizot, Thierry Chartier, Thanh Nam N'guyen, Frédéric Smektala, Gilles Renversez, Achille Monteville, David Méchin, Thierry Pain, et al. "Casting method for producing low-loss chalcogenide microstructured optical fibers". In: *Optics Express* 18.9 (2010), pp. 9107–9112.

[50] Johann Troles, Laurent Brilland, Frédéric Smektala, P Houizot, Frédéric Désévédavy, Quentin Coulombier, N Traynor, Thierry Chartier, Thanh Nam Nguyen, Jean-Luc Adam, et al. "Chalcogenide microstructured fibers for infrared systems, elaboration modelization, and characterization". In: *Fiber and Integrated Optics* 28.1 (2009), pp. 11–26.

[51] Hamdy H Wahba and Thomas Kreis. "Characterization of graded index optical fibers by digital holographic interferometry". In: *Applied optics* 48.8 (2009), pp. 1573–1582.

[52] Duncan T Moore. "Gradient-index optics: a review". In: *Applied Optics* 19.7 (1980), pp. 1035–1038.

[53] F Hudelist, R Buczynski, AJ Waddie, and MR Taghizadeh. "Design and fabrication of nanostructured gradient index microlenses". In: *Optics express* 17.5 (2009), pp. 3255–3263.

[54] Myungkoo Kang, Laura Sisken, Justin Cook, Cesar Blanco, Martin C Richardson, Ilya Mingareev, and Kathleen Richardson. "Refractive index patterning of infrared glass ceramics through laser-induced vitrification". In: *Optical Materials Express* 8.9 (2018), pp. 2722–2733.

[55] B Ainslie and C Day. "A review of single-mode fibers with modified dispersion characteristics". In: *Journal of lightwave technology* 4.8 (1986), pp. 967–979.

[56] Richard L Sutherland. *Handbook of nonlinear optics*. CRC press, 2003.

[57] John M Dudley and James Roy Taylor. *Supercontinuum generation in optical fibers*. Cambridge University Press, 2010.

[58] RP Photonics Consulting GmbH. *Self-phase Modulation*. URL: https://www.rp-photonics.com/self_phase_modulation.html.

[59] RP Photonics Consulting GmbH. *Four-wave Mixing.* URL: https://www.rp-photonics.com/four_wave_mixing.html.

[60] Shigeki Sakaguchi and Shin-ichi Todoroki. "Optical properties of GeO 2 glass and optical fibers". In: *Applied optics* 36.27 (1997), pp. 6809–6814.

[61] Deepak Jain and Ole Bang. "High Power mid-infrared fiber based supercontinuum sources: current status and future perspectives". In: *2018 Conference on Lasers and Electro-Optics Pacific Rim (CLEO-PR)*. IEEE. 2018, pp. 1–2.

[62] Isaac Basaldua, Robinson Kuis, Paul Burkins, Zack Jiang, and Anthony M Johnson. "Measurements of the Nonlinear Refractive Index (n2) for Indium Fluoride (InF3) Bulk Glass and Fiber". In: *Frontiers in Optics*. Optical Society of America. 2018, JTu3A–38.

[63] Yuri Yatsenko and Alexei Mavritsky. "D-scan measurement of nonlinear refractive index in fibers heavily doped with GeO 2". In: *Optics letters* 32.22 (2007), pp. 3257–3259.

[64] Ke Yin, Bin Zhang, Linyong Yang, and Jing Hou. "30 W monolithic 2–3 μm supercontinuum laser". In: *Photonics Research* 6.2 (2018), pp. 123–126.

[65] Mariusz Klimczak, Damian Michalik, Grzegorz Stępniewski, Tanvi Karpate, Jarosław Cimek, Xavier Forestier, Dariusz Pysz, Ryszard Stępień, Ryszard Buczyński, et al. "Coherent supercontinuum generation in tellurite glass regular lattice photonic crystal fibers". In: *JOSA B* 36.2 (2019), A112–A124.

[66] Christian Rosenberg Petersen, Peter M Moselund, Christian Petersen, Uffe Møller, and Ole Bang. "Spectral-temporal composition matters when cascading supercontinua into the mid-infrared". In: *Optics Express* 24.2 (2016), pp. 749–758.

[67] Deepak Jain, R Sidharthan, Peter M Moselund, S Yoo, D Ho, and Ole Bang. "Record power, ultra-broadband supercontinuum source based on highly GeO 2 doped silica fiber". In: *Optics express* 24.23 (2016), pp. 26667–26677.

[68] Peter M. Moselund, Christian Petersen, Lasse Leick, Jeppe Seidelin Dam, Peter Tidemand-Lichtenberg, and Christian Pedersen. "Highly Stable, All-fiber, High Power ZBLAN Supercontinuum Source Reaching 4.75 µm used for Nanosecond mid-IR Spectroscopy". In: Optical Society of America, 2013, JTh5A.9.

[69] Ke Yin, Bin Zhang, Linyong Yang, and Jing Hou. "15.2 W spectrally flat all-fiber supercontinuum laser source with> 1 W power beyond 3.8 μm". In: *Optics letters* 42.12 (2017), pp. 2334–2337.

[70] Jean-Christophe Gauthier, Vincent Fortin, Jean-Yves Carrée, Samuel Poulain, Marcel Poulain, Réal Vallée, and Martin Bernier. "Mid-IR supercontinuum from 2.4 to 5.4 μm in a low-loss fluoroindate fiber". In: *Optics letters* 41.8 (2016), pp. 1756–1759.

[71] Tianyi Wu, Linyong Yang, Zhiyuan Dou, Ke Yin, Xuan He, Bin Zhang, and Jing Hou. "Ultra-efficient, 10-watt-level mid-infrared supercontinuum generation in fluoroindate fiber". In: *Optics letters* 44.9 (2019), pp. 2378–2381.

[72] Stefan Kedenburg, Clément Strutynski, Bertrand Kibler, Paul Froidevaux, Frédéric Désévédavy, Grégory Gadret, Jean-Charles Jules, Tobias Steinle, Florian Mörz, Andy Steinmann, et al. "High repetition rate mid-infrared supercontinuum generation from 1.3 to 5.3 μm in robust step-index tellurite fibers". In: *JOSA B* 34.3 (2017), pp. 601–607.

[73] Christian Rosenberg Petersen, Uffe Møller, Irnis Kubat, Binbin Zhou, Sune Dupont, Jacob Ramsay, Trevor Benson, Slawomir Sujecki, Nabil Abdel-Moneim, Zhuoqi Tang, et al. "Mid-infrared supercontinuum covering the 1.4–13.3 μm molecular fingerprint region using ultra-high NA chalcogenide step-index fibre". In: *Nature Photonics* 8.11 (2014), p. 830.

[74] Christian Rosenberg Petersen, Rasmus D Engelsholm, Christos Markos, Laurent Brilland, Céline Caillaud, Johann Trolès, and Ole Bang. "Increased mid-infrared supercontinuum bandwidth and average power by tapering large-mode-area chalcogenide photonic crystal fibers". In: *Optics express* 25.13 (2017), pp. 15336–15348.

[75] Ramon A Martinez, Genevieve Plant, Kaiwen Guo, Brian Janiszewski, Michael J Freeman, Robert L Maynard, Mohammed N Islam, Fred L Terry, Oseas Alvarez, Francois Chenard, et al. "Mid-infrared supercontinuum generation from 1.6 to> 11 μm using concatenated step-index fluoride and chalcogenide fibers". In: *Optics letters* 43.2 (2018), pp. 296–299.

[76] O Mouawad, J Picot-Clémente, F Amrani, C Strutynski, J Fatome, B Kibler, F Désévédavy, G Gadret, J-C Jules, D Deng, et al. "Multioctave midinfrared supercontinuum generation in suspended-core chalcogenide fibers". In: *Optics letters* 39.9 (2014), pp. 2684–2687.

[77] Perrine Toupin, Laurent Brilland, Catherine Boussard-Plédel, Bruno Bureau, David Mechin, Jean-Luc Adam, and Johann Troles. "Comparison between chalcogenide glass single index and microstructured exposed-core fibers for chemical sensing". In: *Journal of Non-Crystalline Solids* 377 (2013), pp. 217–219.

[78] Sandrine Hocdé, Catherine Boussard-Plédel, Gilles Fonteneau, and Jacques Lucas. "Chalcogens based glasses for IR fiber chemical sensors". In: *Solid State Sciences* 3.3 (2001), pp. 279–284.

[79] R Baker, KD Rogers, N Shepherd, and N Stone. "New relationships between breast microcalcifications and cancer". In: *British journal of cancer* 103.7 (2010), p. 1034.

[80] Jin Tae Kwak, André Kajdacsy-Balla, Virgilia Macias, Michael Walsh, Saurabh Sinha, and Rohit Bhargava. "Improving prediction of prostate cancer recurrence using chemical imaging". In: *Scientific reports* 5 (2015), p. 8758.

[81] Daniel C Fernandez, Rohit Bhargava, Stephen M Hewitt, and Ira W Levin. "Infrared spectroscopic imaging for histopathologic recognition". In: *Nature biotechnology* 23.4 (2005), p. 469.

[82] Jayakrupakar Nallala, Marie-Danièle Diebold, Cyril Gobinet, Olivier Bouché, Ganesh Dhruvananda Sockalingum, Olivier Piot, and Michel Manfait. "Infrared spectral histopathology for cancer diagnosis: a novel approach for automated pattern recognition of colon adenocarcinoma". In: *Analyst* 139.16 (2014), pp. 4005–4015.

[83] Christian Rosenberg Petersen, Nikola Prtljaga, Mark Farries, Jon Ward, Bruce Napier, Gavin Rhys Lloyd, Jayakrupakar Nallala, Nick Stone, and Ole Bang. "Mid-infrared multispectral tissue imaging using a chalcogenide fiber supercontinuum source". In: *Optics letters* 43.5 (2018), pp. 999–1002.

[84] Sune Dupont, Christian Petersen, Jan Thøgersen, Christian Agger, Ole Bang, and Søren Rud Keiding. "IR microscopy utilizing intense supercontinuum light source". In: *Optics express* 20.5 (2012), pp. 4887–4892.

[85] Mark Farries, Jon Ward, Ian Lindsay, Jayakrupakar Nallala, and Peter Moselund. "Fast hyper-spectral imaging of cytological samples in the mid-infrared wavelength region". In: *Optical Biopsy XV: Toward Real-Time Spectroscopic Imaging and Diagnosis*. Vol. 10060. International Society for Optics and Photonics. 2017, 100600Y.

[86] F Borondics, M Jossent, C Sandt, Laure Lavoute, Dmitry Gaponov, Ammar Hideur, Paul Dumas, and S Février. "Supercontinuum-based Fourier transform infrared spectromicroscopy". In: *Optica* 5.4 (2018), pp. 378–381.

Chapter 2

Synthesis of high purity chalcogenide glasses

2.1 Fabrication and characterization of Ge-As-Se glasses

2.1.1 Different compositions of glass used in this work

On the road to develop optical fibers to be used for mid-IR supercontinuum generation, the starting point is to choose a proper glass for their fabrication. Between the glassy systems exhibiting transmission in the mid infrared range, chalcogenides have the broadest transparency window and are highly promising for nonlinear applications because of their nonlinear refractive index n_2, which is 2 to 3 orders of magnitude higher than the ones of silica or ZBLAN. In the class of chalcogenide glasses, Ge-As-Se ternary systems were chosen to be studied in this work because they represent a good compromise between the position of the transparency window (which includes both the telecommunication C-band, around 1.55 μm, and mid-IR wavelengths, up to $10-12\mu$m for fibers), the nonlinear refractive index and the improved thermal and mechanical properties given by the addition of germanium to the composition.

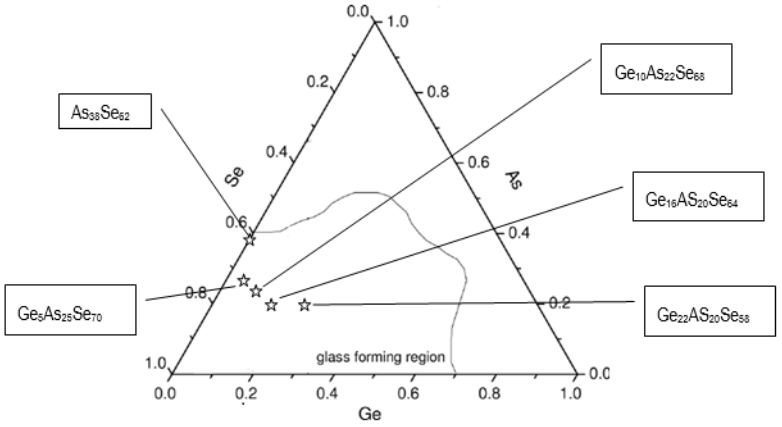

Figure 2.1: *Ternary diagram showing the glass-forming region of Ge-As-Se ternary systems. The compositions used in this work are highlighted.*

The glass-forming region for Ge-As-Se is quite large (Figure 2.1), granting room for maneuver in the variation of the composition for pursuing the best properties for the target applications of this work.

The different compositions studied in this work are listed below:

- $As_{38}Se_{62}$
- $Ge_5As_{25}Se_{70}$
- $Ge_5As_{30}Se_{65}$
- $Ge_{10}As_{22}Se_{68}$
- $Ge_{16}As_{20}Se_{64}$
- $Ge_{22}As_{20}Se_{58}$

2.1.2 Glass synthesis

The route chosen for the preparation of the samples presented in this work is the one of melt-quenching: the rapid cooling of a melt of the desired stoichiometry, followed by a thermal annealing in order to reduce the internal mechanical stress of the obtained glass. A detailed description of its procedural steps is given in this section.

2.1.2.1 Charge preparation

The preparation of the initial set of elements to be melted, named charge, is performed in a glovebox under controlled argon atmosphere, with amounts of both O_2 and H_2O below 1 ppm. Inside it the elements (Ge, As and Se in this work), all of 5N purity, are weighted and inserted in a silica tube with low amount of surface OH, which will act as a crucible for the melting. These tubes, whose internal diameter is 12 mm and external one is 16 mm, are previously etched with HF for removal of surface impurities, washed with distilled water and dried under vacuum. Once the charge is inside the tube, the latter is connected to a condensation trap cooled with liquid nitrogen, which is in turn linked to a two stages (oil and turbomolecular) vacuum pump (see schematics in Figure 2.2). The oil pump, or primary pump, is then used to reach a preliminary vacuum of about 10^{-3} mbar before using the turbomolecular, or secondary, pump to achieve a final vacuum of 10^{-5} mbar. After this, the silica tube is flame-sealed in order to obtain a closed crucible containing the charge under high vacuum. For the glasses fabricated in this work, charges with mass between 60 and 90 g were used.

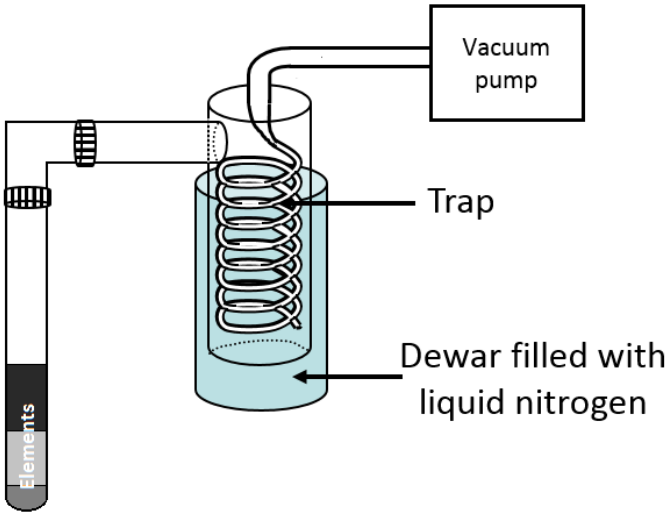

Figure 2.2: *Schematics of the setup to put the charge under high vacuum.*

2.1.2.2 Melting and homogenization

The crucible containing the charge, once ready, is put into a rocking tubular furnace preheated at 450℃. The melt is then obtained by following a thermal treatment which is dependent on the glass components (the thermal treatments for arsenic selenide and germanium arsenic selenide glasses are presented in Figure 2.3). The presence of germanium in the glass increases the peak temperature needed in the treatment to achieve complete melting of all the glass component, due to the higher melting temperatures of $GeSe_2$ and Ge with respect to As_2Se_3. This high temperature, however, can cause strong interaction between the germanium in the melt and the silica of the crucible, leading to the inclusion of silicon or silica particles in the chalcogenide glass. To reduce as much as possible this effect, the duration of the plateau at high temperature is shorter for germanium-containing glass. For the same reason, after 30 minutes the temperature is moved to a slightly lower temperature.

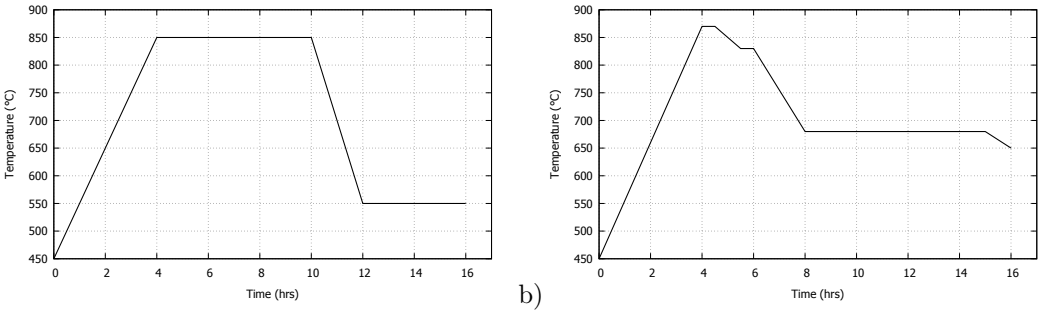

Figure 2.3: *Thermal treatment for the melting of arsenic selenide (a) germanium arsenic selenide (b) charges.*

2.1.2.3 Quenching

After the thermal treatment, the melt is rapidly cooled (quenched) in water at room temperature, in order to have the transition from liquid to glassy state. The cooling rate with this method has been estimated to be around 80 – 100 ℃/s, and has been shown to be sufficient to avoid crystallization in both As-Se and Ge-As-Se systems. The needed duration of the quenching can be empirically determined by observing the contraction of the material inside the silica tube.

2.1.2.4 Annealing

Fast cooling of the melt is fundamental for the formation of a glass, but it can induce strong internal stress due to the different cooling rate between the center and external surface of the melt. To reduce this stress, after the quenching a thermal treatment for the annealing of the glass must be performed. The glass is placed into a stove at a temperature equal to $(T_g - 5)$℃, deemed sufficient to allow a partial relaxation of the atomic network, for 30 minutes, and then slowly cooled to room temperature over 6 hours.

2.1.3 Optical and mechanical caracterization of the bulks

2.1.3.1 Glass transition temperature

When developing a new glass composition, the first parameter to be measured is T_g, which is needed also to determine the proper annealing temperature and thus being able to produce higher quality glasses. In order to do so, a first sample is produced inferring an approximate T_g from the behavior of glasses with similar composition, and a differential scanning calorimetry (DSC) measurement is performed on it using a Q20 DSC module from TA instruments (the first guess of T_g is determined assuming in Ge-As-Se systems a linear relation between the average coordination number and the glass transition temperature, which seems to be a reasonable even if crude approximation for most chalcogenide glasses [1]).

DSC measurements are performed by heating separately the sample and a reference sample of comparable size, both placed in crucibles made of aluminum, which is a material thermodynamically stable in the temperature range in which the measurement will be done. The apparatus operates to maintain the difference in temperature between them equal to zero, and measures the difference in the amount of power that the two heaters have to use to reach that goal. If endothermic processes happen in the sample, the respective heater will have to input more power in order to compensate for the energy that is consumed by them; exothermic processes, instead, will force it to have to input less power. This will cause characteristic variations in the otherwise approximately constant difference in power consumption.

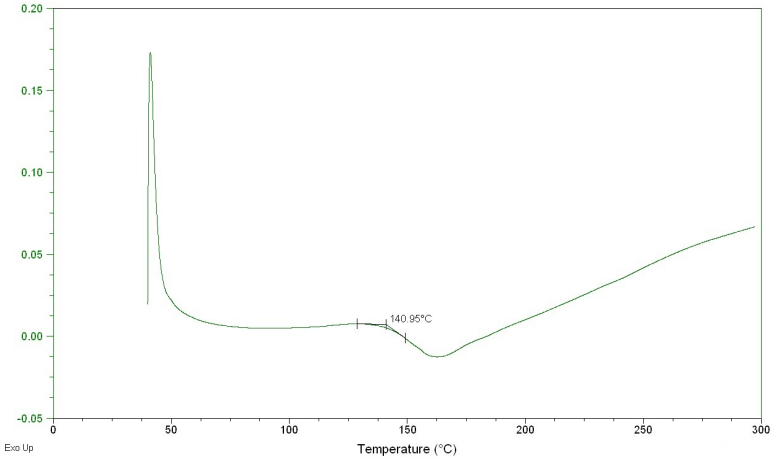

Figure 2.4: *Typical heat flow vs temperature plot resulting from a DSC measurement, in the case of this example performed on* $Ge_5As_{25}Se_{70}$ *glass.*

Measurements are usually performed heating the sample, of about 10 mg in weight, from room temperature to $\sim$ 150°C above the inferred value of T_g. This range has been chosen to avoid the risk of melting the glass and contaminating the apparatus with vapors. In the resulting plot of heat flow difference versus temperature (example in Figure 2.4), a negative (endothermic) peak of characteristic shape corresponding to the glass transition should be individuated. Its onset corresponds to the value of T_g. Depending on the glass, in some cases a positive (exothermic) peak can also be individuated at $T>T_g$, indicating the crystallization of the glass. The difference between the onset temperature of this peak (T_x) and T_g is defined as the stability parameter ΔT, and is of high importance for fiber production: if the temperature needed to reduce viscosity enough to draw a fiber is higher than T_x, the fabrication of good quality fibers is not possible due to crystallization during the drawing process. In the studied glasses no crystallization peak was observed in the measured temperature range.

2.1.3.2 Viscosity behavior during heating

Another fundamental property of glass, especially when it is produced for fiber optics applications, is its viscosity behavior when heated. Measurements of viscosity can be used to have an approximate idea of the temperature to be reached to bring the glass to the drawing point (generally 10^3 Pa·s $\leq \eta \leq 10^{6.6}$ Pa · s, it is usually considered as $\eta \simeq 10^5$ Pa · s for chalcogenide glasses [2]).
The technique used to measure viscosity in this work was parallel plate viscometry, in which a bulk sample of known volume (a polished cube with a 5 mm edge in this case) is placed between two plates compressing it with known constant force during heating. The viscosity behavior is calculated from the variation in distance between the two plates. The temperature range used was between room temperature and (T_g + 100)°C. The viscosity behavior was measured for all the produced compositions apart from $Ge_5As_{25}Se_{70}$ and $Ge_{22}As_{20}Se_{58}$, which were deemed not feasible as candidates for the production of microstructured fibers. A formal description of this technique is given in [3], and an example of data obtained with this method is given in Figure 2.5.

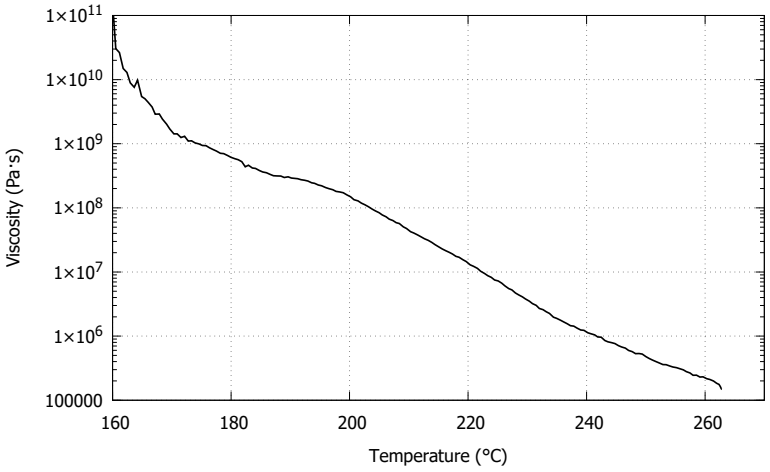

Figure 2.5: *Typical viscosity behavior of chalcogenide glass when heated above* $\mathrm{T_g}$*, in the case of this example performed on* $\mathrm{Ge_5As_{30}Se_{65}}$ *glass (having a* $\mathrm{T_g}$ *of* 165°C*).*

In order to better understand the physical behavior of our system under heating, a fit of a viscosity with semiempirical models was attempted. Three different models were considered, in order to find the one giving the best fit:

Vogel-Fulcher-Tammann (VFT) [2]

$$\log_{10}\eta(\mathrm{T}) = \log_{10}\eta_\infty + \frac{\mathrm{A}}{\mathrm{T}-\mathrm{T_0}}$$

Avramov-Milchev (AM) [4]

$$\log_{10}\eta(\mathrm{T}) = \log_{10}\eta_\infty + \left(\frac{\tau}{\mathrm{T}}\right)^{\alpha}$$

Mauro, Yue, Ellison, Gupta and Allan (MYEGA) [5]

$$\log_{10}\eta(\mathrm{T}) = \log_{10}\eta_\infty + \frac{\mathrm{K}}{\mathrm{T}}\cdot \mathrm{e}^{\frac{\mathrm{C}}{\mathrm{T}}}$$

The attempt to fit these models to the measured data, however, had to be considered unsuccessful, probably due to either noise or lack of a sufficient amount of data to estimate independently the three parameters needed for each model: despite the accordance of the curve with the data, the results for some of the fitting parameters were non-physical.

Table 2.1: *Results of the viscosity behavior fits for different compositions, using the three models described in this section.*

Parameter	$\mathrm{As_{38}Se_{62}}$	$\mathrm{Ge_5As_{30}Se_{65}}$	$\mathrm{Ge_{10}As_{22}Se_{68}}$	$\mathrm{Ge_{16}As_{20}Se_{64}}$
VFT				
$\log_{10}\eta_\infty$	-100	-127	-48	-13
A	241988	398830	76420	10740
$\mathrm{T_0}$	-1765	-2481	-870	52
AM				
$\log_{10}\eta_\infty$	-9.4	-8.6	-9	-11
τ	3567	3050	4366	6522
α	1.4	1.5	1.3	1.2
MYEGA				
$\log_{10}\eta_\infty$	-245	-137	-75	-14
K	305653	161747	88276	11267
C	-442	-404	-375	42

It is known, for example, that $\log_{10}\eta_\infty$ should be negative, with the absolute value having an order of magnitude of $10^0 - 10^1$ ($\log_{10}\eta_{T_g} - \log_{10}\eta_\infty \simeq 17$ according to [6], $\log_{10}\eta_\infty \simeq -5.5$ according to [7]), and that $0 < T_0 < T_g$ when expressing the temperature in Kelvin in the VFT model. The first performed fits were far for respecting these conditions for almost all samples, with the only exception of the Avramov-Milchev model, as visible in Table 2.1. Therefore, no extrapolation of data outside the measured range should be performed using the fits of VFT and MYEGA models as formulated above. As a first attempt to solve this problem for the VFT and MYEGA models, a parameter restriction was included in the fit to force the values in a reasonable range. This was done by substituting the parameters with limited functions, and then fitting via the arguments of those functions. Supposing, as an example, that a parameter K has to be fitted, and that $K_{min} < K < K_{max}$ needs to be imposed, this can be achieved by using the substitution below, fitting via k and obtaining the parameter as $K = K(k_{fit})$.

$$K \to K(k) := \frac{K_{max} - K_{min}}{\pi}(\arctan(k_{fit}) + \frac{\pi}{2}) - K_{min}$$

This method, however, didn't prove to be viable in the case in exam, as it produced an enormous error on k_{fit}.
As a second approach to the fit of viscosity data, a reformulation of the models was used to reduce the number of parameters from three to two. As described in [8], the three models above can be rewritten as functions of $\log_{10}\eta_\infty$, the fragility parameter $m = \frac{\partial \log_{10}\eta(T)}{\partial(T_g/T)}\big|_{T=T_g}$ and T_g, obtaining the forms below:

VFT

$$\log_{10}\eta(T) = \log_{10}\eta_\infty + \frac{(\log_{10}\eta(T_g) - \log_{10}\eta_\infty)^2}{m(T/T_g - 1) + (\log_{10}\eta(T_g) - \log_{10}\eta_\infty)}$$

AM

$$\log_{10}\eta(T) = \log_{10}\eta_\infty + \left(\frac{T_g}{T}\right)^{m/(\log_{10}\eta(T_g) - \log_{10}\eta_\infty)}$$

MYEGA

$$\log_{10}\eta(T) = \log_{10}\eta_\infty + (\log_{10}\eta(T_g) - \log_{10}\eta_\infty)\frac{T_g}{T} \cdot e^{\left[\left(\frac{m}{\log_{10}\eta(T_g) - \log_{10}\eta_\infty} - 1\right)\left(\frac{T_g}{T} - 1\right)\right]}$$

Being T_g (and subsequently $\log_{10}\eta(T_g)$) known for the studied systems, using these reformulations only m and $\log_{10}\eta_\infty$ need to be fitted. Furthermore, the fact that the fitted parameters are the same for all the considered models allows for a direct comparison. Fits performed using these formulations of the three models all gave physically reasonable estimations of the parameters for the compositions under study. Moreover all models returned the same value of m for a given composition, hinting to a strong reliability of its estimation. When inverting the obtained functions to obtain $T(\eta = 10^5\ \text{Pa}\cdot\text{s})$, the different models lead to the same result too, as shown in Table 2.4. The parameters fitted using the reformulated models are shown in Table 2.2, where also the fact that the AM model seems to underestimate the absolute value of $\log_{10}\eta_\infty$ can be noticed.
The values obtained for the fragility parameter are $m \simeq 32$ for $As_{38}Se_{62}$ and $m \simeq 27$ for compositions containing germanium, values well compatible with the literature assigning a value of 20-30 to chalcogenide glasses [9]. A trend would seem to emerge showing a slight decrease of m when increasing T_g, but the error in the fitted values (± 1) is too high to confirm it. In the future, measurements with an extended temperature range could be performed in order to increase the precision of the fit and confirm this trend. When comparing these values with the tabulated ones for a quite extensive list of oxide glasses in [7], it can be noticed that composition in our system appear to have m larger than SiO_2, which is considered to be a limit case for glass strength, but equal or lower than most common oxide glasses.

Table 2.2: *Results of the viscosity behavior fits for different compositions, using the reformulations of the three models described in this section. The error on the values of m has been estimated to be ±1.*

Parameter	$As_{38}Se_{62}$	$Ge_5As_{30}Se_{65}$	$Ge_{10}As_{22}Se_{68}$	$Ge_{16}As_{20}Se_{64}$
VFT				
$\log_{10}\eta_\infty$	-8.7	-11.4	-6.5	-13.0
m	32.0	27.5	27.5	26.5
AM				
$\log_{10}\eta_\infty$	-5.5	-8.6	-3.5	-11.0
m	31.4	27.4	27.1	26.5
MYEGA				
$\log_{10}\eta_\infty$	-8.1	-11.1	-5.8	-13
m	31.6	27.5	27.3	26.5

As visible in Figure 2.6 the three models keep being consistent when going further from the measured range, with only the MYEGA model diverging from the others at low viscosities, and only by a few degrees. After refining the fitted parameters with measurements at higher temperature, these models could be used to extrapolate data on the vicosity behavior of chalcogenide glasses.

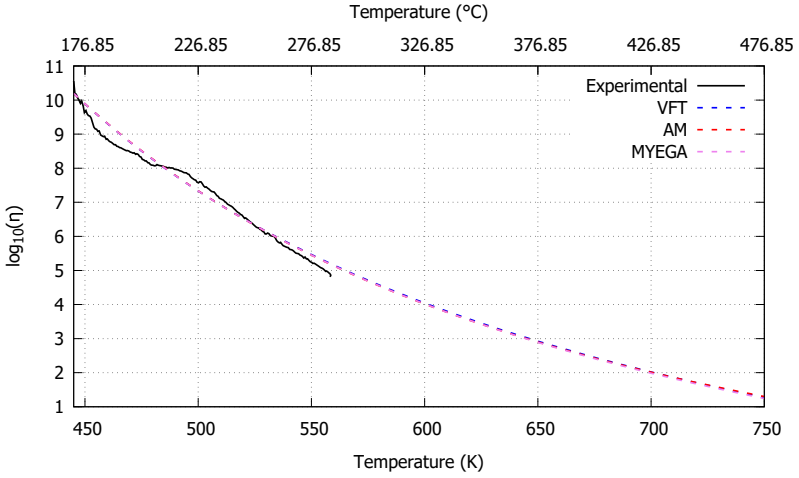

Figure 2.6: *Experimental viscosity behavior of* $Ge_{10}As_{22}Se_{68}$*. As dashed lines, the fitted curves for the three different models, obtained using the two parameters formulation.*

2.1.3.3 Refractive index measurement and Sellmeier parameters estimation

Refractive index and material dispersion are quantities of great importance for fiber optics, allowing to calculate confinement, dispersion and modal behavior for a given fiber geometry. In this work, refractive index measurements were performed at the wavelengths of 1.55 and 1.33 μm for each of the compositions produced, once again with the exception of $Ge_5As_{25}Se_{70}$.
In order to perform this measurement, discs of about 1 mm thickness were cut and polished to optical quality, and their refractive index was determined by prism coupling technique using a Metricon 2010/M Prism Coupler instrument. The basic concept behind this technique is quite simple: the sample to be measured is put in contact with a prism of known refractive index, a laser at the needed wavelength is shone on one side of the prism and the intensity of the reflected light is detected on the other side, as shown in Figure 2.7. The sample+prism system is then rotated, in order to obtain a curve of intensity vs incidence angle θ. According to standard geometrical optics, at the critical incidence angle ϑ_c the light will pass from being totally reflected at the prism-sample interface to being partially propagated inside the sample, causing a sharp decrease in the detected intensity. Being ϑ_c only dependent on the known values of the prism refractive index n_p and of the laser wavelength, and on the unknown sample refractive index n, its value can be used to determine the latter. A more formal discussion of this technique can be found in [10].

Concerning the material dispersion, in this work the semiempirical Sellmeier equation shown below is used to describe it. The 2 poles approximation (m = 2) has been found sufficient to describe the studied systems [11].

$$n^2 - 1 = A_0 + \sum_{i=1}^{m} \frac{A_i \lambda^2}{\lambda^2 - a_i^2}$$

For the $As_{38}Se_{62}$ composition, the refractive index data measured prior to this work and published in [12] was used for fitting the equation. Concerning Ge-As-Se glasses, a different approach was used to obtain a dispersion curve: the curve described by the Sellmeier coefficients reported in [11] for this system was shifted in order to match the values measured with prism coupling for the composition in exam, and new Sellmeier coefficients were then calculated. The reasonable agreement of this approximation with measured data is shown in [13]. The calculated Sellmeier coefficients are shown in Table 2.3, and an example curve can be found in Figure 2.8.

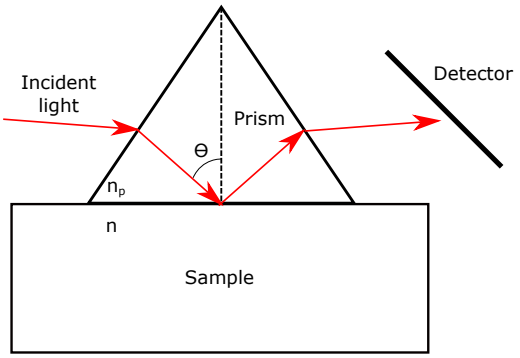

Figure 2.7: *Schematics of the prism coupling setup for the determination of refractive index.*

Table 2.3: *Sellmeier coefficients estimated for the different glass compositions produced.*

Coefficient	$As_{38}Se_{62}$	$Ge_5As_{30}Se_{65}$	$Ge_{10}As_{22}Se_{68}$	$Ge_{16}As_{20}Se_{64}$	$Ge_{22}As_{20}Se_{58}$
A_0	2.7135	3.0841	2.8060	2.6886	2.5463
A_1	3.9387	3.0082	2.7938	2.7579	2.7137
a_1	0.40574	0.40385	0.41025	0.41049	0.41080
A_2	1.0693	0.74782	0.77098	0.76222	0.75143
a_2	42.395	38.451	39.463	39.470	39.478

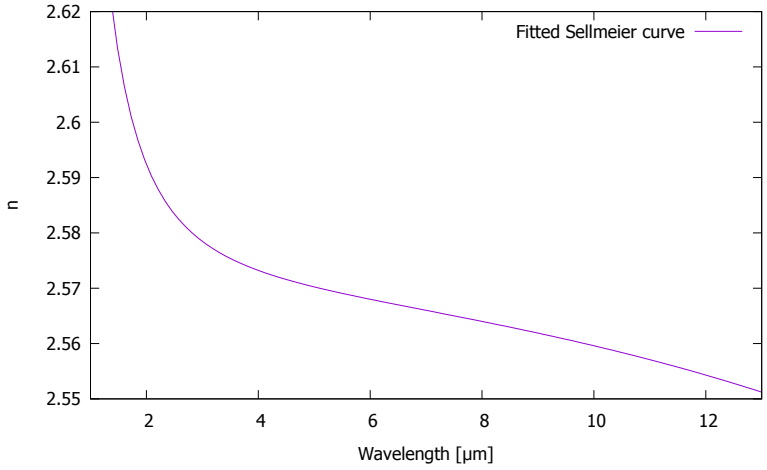

Figure 2.8: *Sellmeier curve for $Ge_{10}As_{22}Se_{68}$, obtained by shifting the one in [11].*

2.1.3.4 Summary of the main properties of the studied compositions

The main characteristics of Ge-As-Se bulk glasses are summarized in the table below for the different compositions examined in this study. It can be noticed that not all the slots of the table are filled: $Ge_5As_{25}Se_{70}$ and $Ge_{22}As_{20}Se_{58}$ were indeed discarded partway through the work, the first because of the too low T_g and the second because of the too high network rigidity. When using the glasses to produce index-guiding PCFs fibers by molding technique (see Section 3.2.4), in fact, those properties would prove the compositions not to be proper candidates.

Table 2.4: *Summary of the characteristics measured on bulk samples of different attempted compositions.*

Composition	$As_{38}Se_{62}$	$Ge_5As_{25}Se_{70}$	$Ge_5As_{30}Se_{65}$	$Ge_{10}As_{22}Se_{68}$	$Ge_{16}As_{20}Se_{64}$	$Ge_{22}As_{20}Se_{58}$
Average coordination number	2.38	2.35	2.40	2.42	2.52	2.64
T_g(℃, ±2℃)	165	139	165	175	235	292
T($\eta = 10^5$ Pa · s) (℃, ±5℃)	258	-	269	291	357	-
Refractive index @1.55μm	2.808	-	2.704	2.618	2.579	2.542

2.2 Drawing of single index fibers and estimation of losses

In order to estimate the optical attenuation of the prepared glasses in the mid infrared, they were drawn into single index fibers with a diameter of 125 μm. The attenuation of these fibers was then measured with a FTIR spectrometer using a standard cut-back technique. The experimental details of this procedure in its whole are described below.

2.2.1 Drawing process for chalcogenide single index fibers

The most common method to draw optical fibers is the elongation of a bulk glass sample of cylindrical shape, using heat to decrease the viscosity of the material to the point of deformability. This process is usually executed on a drawing tower, that is to say a structure which is in its simplest form composed by a moving preform holder surrounded by a furnace placed at a suitable height and a pulling device below it. By suitable height it is meant that the distance between the furnace and the pulling device should be long enough to allow for the fiber to cool down to high viscosity regime before it touches the pulling device.
The drawing towers used in this work have a slightly more complex structure, due to the addition of sensors in order to keep the process under control, as shown in the schematics in Figure 2.9. In their top part the preform and furnace supports can be found. The preform support is connected to a motor allowing for vertical motion, controlled with a precision of 0.1 mm/min, and to a gas injection system used to flow gas through the holes of microstructured preforms or, if needed, to apply vacuum. The furnace support is also connected to a gas injection system for purging the atmosphere inside the furnace, and allows for the use of different furnaces. The furnaces used are made of tubular silica bodies with an annular heating piece and a thermocouple for temperature feedback. Directly below the preform holder, a laser diameter control unit with a precision of 1 μm is placed to keep in check diameter and ellipticity of the fiber during drawing. Further below is the tension control unit, consisting by a pulley around which the fiber has a 90° change of direction, connected to a electronic dynamometer relaying the information about tension. Finally the motor for the rotating drum is present. Drums with a standard diameter of 40 cm are always used, with which a control of the drawing speed of 0.01 m/min can be kept.
For the drawing of the glasses described in this work, a particular care must be taken, due to their strong susceptibility to environmental pollution once heated. For this reason, the furnace needs to be under inert gas flux during the whole process.
After the installation of the preform, the furnace is purged with argon gas for about 30 minutes. Once this time has elapsed, argon is substituted with helium, and the furnace is started. In order to avoid thermal shock to the glass, the drawing temperature is reached quite slowly, in about

15-20 minutes. The heat causes the glass to soften in the area within the heat blade generated by the annular heating piece, and the weight of the glass below this area causes the formation of a drop, which starts falling, elongating the hot part of the preform. In this moment the preform motion is started, the drop is broken off and the piece of fiber connected to it is attached to the rotating drum, passing through the diameter measurement setup and around the wheel of the tension sensor.

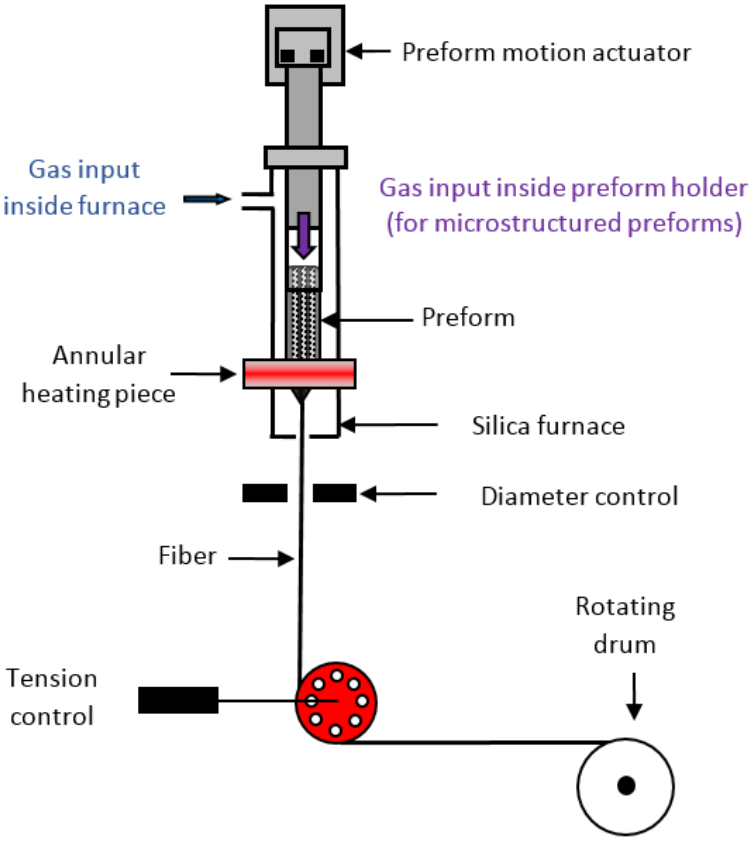

Figure 2.9: *General schematics of the drawing towers used in this work.*

The diameter of the fiber is controlled by modifying the preform motion and drum rotation speeds: due to the fact that the volume flow of glass before the deformation area must be equal to the one after, the following relation holds:

$$S_p \cdot v_p = S_f \cdot v_f$$

With S_p, v_p respectively the section area and speed of the preform and S_f, v_f the ones of the fiber. Assuming the fiber and preform to have circular section of diameters $\varnothing_f$ and $\varnothing_p$, the equation for the determination of fiber diameter when both the speeds and the preform diameter are fixed is obtained:

$$\varnothing_f = \varnothing_p \sqrt{\frac{v_p}{v_f}}$$

Conversely, when the desired final diameter of the fiber and the initial diameter of the preform are known, the speeds during the drawing must be set so that

$$v_f = v_p \frac{\varnothing_p^2}{\varnothing_f^2}$$

The tension of the fiber during the drawing is instead regulated by changing the temperature of the furnace. This is a fundamental parameter, because an excessive tension will cause the fiber to

break during the drawing, while a too low one will cause the glass to be in a free flowing state, impairing an optimal control of the fiber diameter. For chalcogenide glasses, the optimal drawing tension has been found to be of about 20-25 grams.

2.2.2 Attenuation measurements

Once the fibers were drawn, they were used to perform attenuation measurements. Considering that the range of wavelengths studied is between 1.5 and 12 μm microns, in a single index fiber with a diameter of 125 μm confinement losses can be considered to be negligible. Being this the case, apart from the input and output losses caused by Fresnel reflections and bad surface quality of the end facets of the fiber, the attenuation of the intensity of light traveling in the fiber can be assumed to follow a generalized Beer-Lambert law

$$I(z) = I_{in} e^{-K \cdot z}$$

where I_{in} is the light intensity at the input, I(z) is the light intensity after propagation in the fiber for a distance z, and K is a generalized attenuation coefficient given by the combination of absorption and scattering losses

$$K = \alpha + k_{scatt}$$

In this work attenuation is studied using the so-called cut-back technique: the intensity of light transmitted through a relatively long piece of fiber, which length will be defined as L_0, is measured. The fiber is then cut to a length L_1, and the measurement repeated. The attenuation in units of dB/m is then obtained as

$$\text{Attenuation} = \frac{10}{L_0 - L_1} \log\left(\frac{I(L_1)}{I(L_0)}\right)$$

This value is connected to the above defined attenuation coefficient K by

$$\text{Attenuation} = 10 \cdot \log(e) \cdot K$$

Using this technique, the input end of the fiber is the same for the two lengths, causing the input losses to be the same for L_0 and L_1, and therefore for them to be eliminated when the ratio between $I(L_1)$ and $I(L_0)$ is taken in the formula for the attenuation.

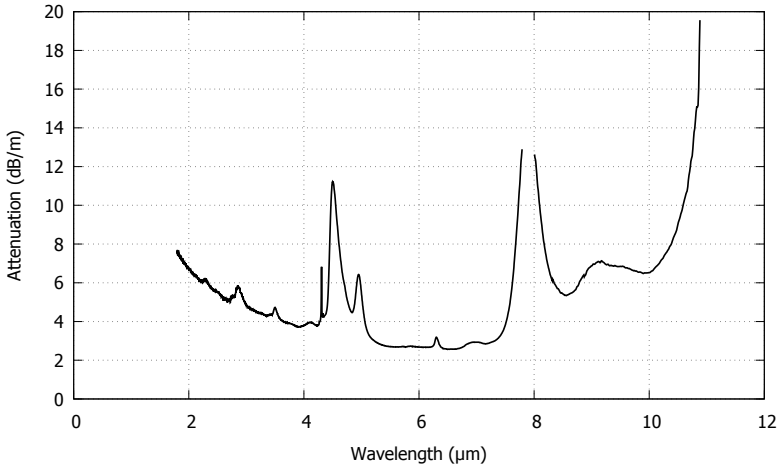

Figure 2.10: *Typical attenuation of a Ge-As-Se ternary glass, measured by cutback technique.*

For the chalcogenide fibers here studied, measurements by cut back technique were performed both in the mid-infrared range and at the main telecommunications wavelength (1.55 μm). For the mid infrared range, a measurement spanning the whole transparency window of the fiber using a Bruker Tensor 37 FTIR spectrometer, with a standard black body infrared source and an external

liquid nitrogen cooled D316/6 MCT detector from InfraRed Associates, Inc. This setup allows to obtain a full attenuation curve, as the one shown in Figure 2.10. The measurement at 1.55 μm is performed separately, using a Thorlabs S1FC1550 Benchtop Laser as a source and a Enertec 7741 Radiometer photodiode as a detector. This is done because the great importance of that wavelength for numerous application asks for precise measurements, and the low signal-to-noise ratio for wavelengths below 2 μm of the MCT detector doesn't allow that.
For each measurement two cut-backs are usually performed when using the spectrometer: one with a long part of fiber for the measurement of the low (background) attenuation and one with a short length of fiber for the measurement of the high (peaks) attenuation. The results of the two measurements are then combined into complete spectra. The error on the obtained values has been estimated by comparison of repeated measurements on the same fiber, and like the experiment can be separated in two regimes: an error of about 0.1 dB/m for the background, where detection-related sources of error are dominant, and an error of about 5% for the intensity of the peaks, where because of the short length of fiber random errors related to the cleaving of the output end the fiber are dominant.

2.2.3 Causes of high attenuation in the transparency window for Ge-As-Se systems

As visible in Figure 2.10, Ge-As-Se glasses prepared by the method described in Section 2.1.2 exhibit a strong attenuation even in their transparency window. The background attenuation is of few dB/m, with peaks of more than 10 dB/m. This is caused by the presence of impurities in the glasses, that can lead both to additional absorption losses due to their mid-infrared vibrational bands and to scattering losses given by pollutants in particle form or apt to act as crystallization nuclei.
It was empirically found that in the system here treated the most common impurities leading to absorption are O, H, H_2O and CO_2, while the most common one in the form of particles are carbon and silica. The most common absorption bands appearing in the attenuation spectra of Ge-As-Se systems are listed in Table 2.5. The impact of even small amounts of impurity on the optical quality of the fibers can be very high, with one ppm of them able to induce additional absorption losses from 1 up to tens of dB/m, depending of their chemical nature [14].

Table 2.5: *List of the most common absorption bands appearing in the attenuation spectra of Ge-As-Se systems and of their spectral position [9, 15].*

Component or functional group leading to absorption	**Position of the maximum of absorption band [μm]**
O – H	2.92
Se-H	4.57; 4.12
H_2O	6.31
Ge-O	7.9
CO_2	4.28; 4.23
As-O	8.9

In order to reduce the level of optical losses to a more suitable level for the intended applications, the simple melt quenching method is substituted by the double distillation method described in Section 2.3.1.

2.3 Purification of chalcogenide glasses for the development of low-loss fibers

2.3.1 Double distillation method for the removal of loss-inducing impurities

As shown in the previous section, chalcogenide glasses prepared using the route described in Section 2.1.2 contain various impurities, coming from both the starting materials and the procedure used

to synthesize them into a glass. While this is not an issue for most applications pertaining bulk glasses or thin films, it can be a serious impairment for any application requiring a length of optical fiber.
With the goal of producing high purity glasses with optical losses low enough to render them suitable for fiber application, in this work the double-distillation approach to the purification of chalcogenide glasses was used. This method is based on the addition of chemical getters to the initial charge, which will react with the chemical contaminants in the glass to create compounds that can be removed by distillation.
The getters used for this purpose are halides and metals. As halides, chlorides of elements that are well known to have the ability to enter the network of Ge-As-Se systems in small quantities without inducing additional losses were chosen. During the melting of the charge these compounds can react with hydrogen and carbon to generate volatile chemical species, as shown in the reaction below for the example of $TeCl_4$ [16] (only the initial and final states are shown, as intermediate reaction steps are influenced by a number of variables).

$$\begin{aligned} 4\,Se - H \;+\; TeCl_4 &\rightleftharpoons 4Se \;+\; Te \;+\; 4HCl \\ C \;+\; TeCl_4 &\rightleftharpoons Te \;+\; CCl_4 \end{aligned}$$

Meanwhile metals will react with the oxygen forming thermally refractory compounds, in a way similar to the one shown below for the case of magnesium.

$$As - O \;+\; Mg \rightleftharpoons As \;+\; MgO$$

In order to achieve a good equilibrium for these reactions, the heat treatment of the glass in the syntheses with getters is slightly modified by increasing the temperature of the last plateau to 700°C, as visible in Figure 2.11.

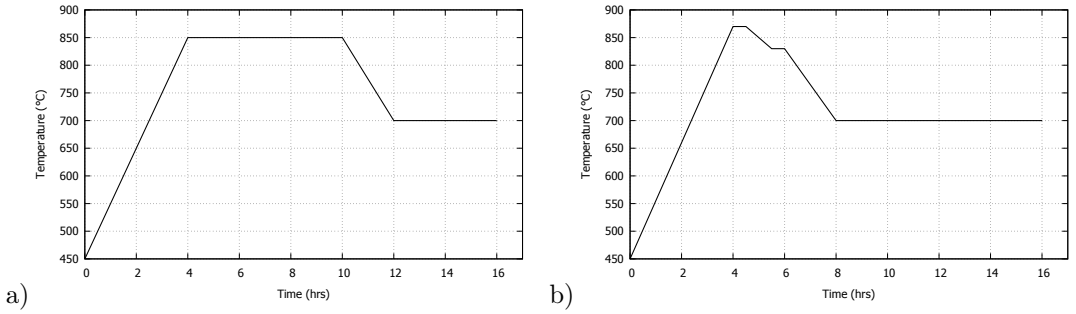

Figure 2.11: *Thermal treatment for the melting of arsenic selenide (a) and germanium arsenic selenide (b) charges during the first synthesis of the double distillation method.*

After the synthesis, quenching and annealing the glass is distilled in two step in order to remove the byproducts of the reaction with the chemical getters.
The first step, or dynamic distillation, is depicted in Figure 2.12.a. The glass is inserted in the first batch of a silica setup with two batches, connected to the system of trap and pumps described in Section 2.1.2.1 and put under high vacuum (10^{-6} mbar). Upon slow heating of the first batch up to 460°C for arsenic selenides or 640°C for germanium arsenic selenides, the glass migrates to the room temperature second batch, leaving behind refractory impurities such as silica particles or metal oxides. During this process, the highly volatile impurities such as hydrochloric acid, water and tetrachloromethane are sucked in by the vacuum pumps and caught in the cooled distillation trap.
For the second step, or static distillation, the setup is reduced by sealing it under vacuum to a single batch and a length of tube, as shown in the schematic in Figure 2.12.b. The batch is then gradually heated until all the glass has moved from the batch to the length of tube, leaving behind residual traces of refractory compounds. These are indeed more difficult to remove than the volatile ones, making this second step necessary to obtain high quality glasses.

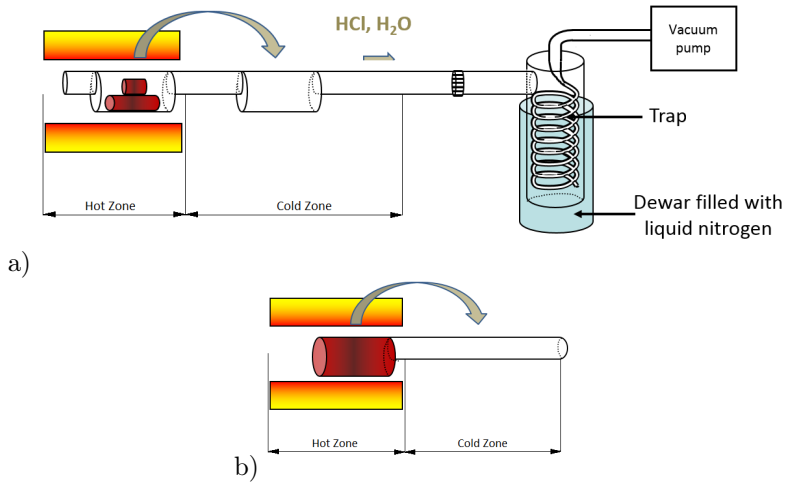

Figure 2.12: *Schematics of the dynamic (a) and static (b) distillation processes.*

When the two steps are completed, the setup for the static distillation is further sealed to remove the batch, leaving a tube containing the purified material. This material is however both inhomogeneous, due to the separation of different compounds during distillation according to their vapor pressures, and partially crystalline, due to the lack of quenching. To overcome this problem, the glass needs to undergo a second process of melting and quenching, exactly as the one described in Section 2.1.2, in order to obtain a finished product.
An example of attenuation spectra to show the difference between purified and non purified germanium arsenic selenide glass is given in Figure 2.13.

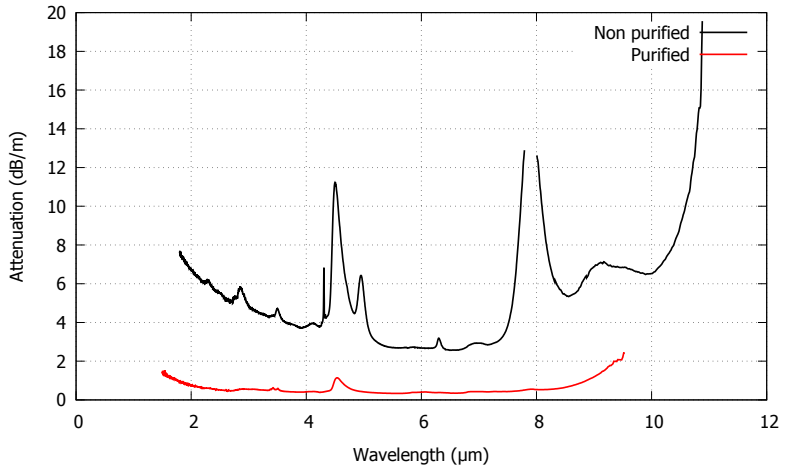

Figure 2.13: *Comparison between the attenuation spectrum in Figure 2.10 and the one of a glass of the same composition obtained via the double distillation purification method.*

2.3.2 Comparison between different getters

In order to optimize the purification process, a comparative study of the efficacy of different getters in removing impurities has been performed. The $Ge_{10}As_{22}Se_{68}$ composition has been chosen for this study, because it has been demonstrated to be stable against crystallization and suitable to develop small core index-guiding PCFs [17]. The results of this study were published in [18].
$TeCl_4$, $SeCl_4$, $SbCl_3$, $GaCl_3$ were chosen as halides, while as metals Mg, Al, Zr and Ni were used. The ratio between the mass of both getters (one halide and one metal for each sample) and the total mass of glass was kept fixed along all the samples. Specifically, each sample contained 2000 ppmw

of hydrogen getter and 200 ppmw of oxygen getter. It has to be noticed that hydrogen getters used are all chlorides of elements that are known to be well compatible with the chalcogenide glass network, and are commonly used as components of selenide glasses. Thanks to this and to the low amounts used, we expect those elements to not affect the optical properties, should they enter the glass during distillation for any reason.

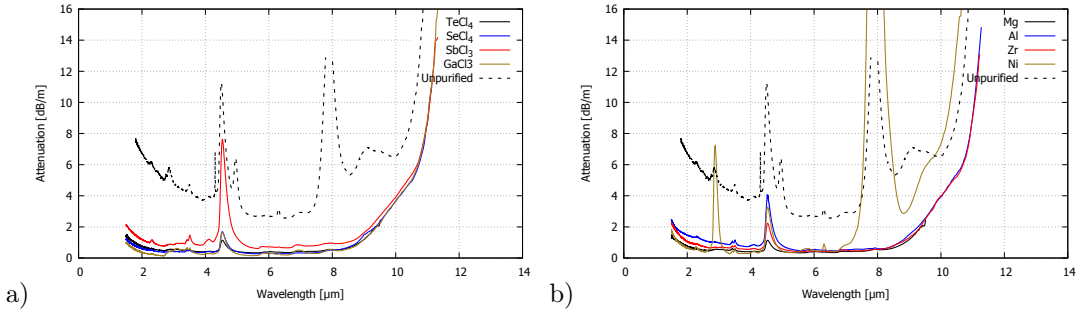

Figure 2.14: *Comparison between the attenuation spectra of* Ge–As–Se *fibers prepared using magnesium in combination with different hydrogen getters (a) and* $TeCl_4$ *in combination with different oxygen getters (b). In both graphs, an example of non purified glass is shown.*

In order to compare the effect of different hydrogen getters on the Se-H absorption peak (4.5 μm), a series of samples was prepared using Mg as the oxygen getter in combination with the different halides listed above. In a similar way, a second series was prepared using $TeCl_4$ as an hydrogen getter and Mg, Al, Zr and Ni as metals, with the intention of studying the Ge-O and As-O peaks (7.9 μm and 8.9 μm respectively). Mg and $TeCl_4$ were chosen as fixed getters for the comparison because their use has already been documented on this composition [17]. The measured losses in the transparency windows for the two series are visible in Figure 2.14, together with the ones of an unpurified glass to show the huge improvements in terms of transmission given by the purification.

2.3.2.1 Effect of the different hydrogen getters

Looking at Figure 2.14.a, it can be seen that $TeCl_4$, $SeCl_4$ and $GaCl_3$ reduce the intensity of the Se-H peak to a level of around 1.5 dB/m. They seem therefore seem to be considerably more efficient than $SbCl_3$.
In order to better understand the reason of this difference, a starting point could be comparing the actual amount of chlorine ions introduced in the melt by the addition of the different halides. Knowing that the mass percentage of all these compounds on the total glass mass was kept constant, a first estimation can be obtained under the assumption of full dissociation, so that the number of moles of chlorine ions inserted in 100 grams of glass (N_{Cl}) will be given, for each distinct getter, by

$$N_{Cl} = n \cdot \frac{m}{M}$$

where n stands for the amount of chlorine atoms in the molecule, m for the mass of the getter inserted in the glass (0.2 grams in the case of 100 grams of glass) and M for the molar mass of the compound. No relation between the theoretical moles of Cl and the efficiency appears to emerge from the values presented in Table 2.6, with $TeCl_4$ resulting to be the most efficient getter despite the relatively low total amount of chlorine it can introduce in the system.

Table 2.6: *Molar content of chlorine per 100 g of glass introduced in the melt by different getters.*

Halide	N_{Cl} $(mol \cdot 10^{-3})$
$TeCl_4$	2.91 ± 0.25
$SeCl_4$	3.5 ± 0.3
$SbCl_3$	2.7 ± 0.2
$GaCl_3$	3.3 ± 0.3

Also, attempts to increase the mass of hydrogen getters inserted in the systems didn't bring to better results in terms of reduction of the Se-H absorption band, further confirming the absence of this relation.

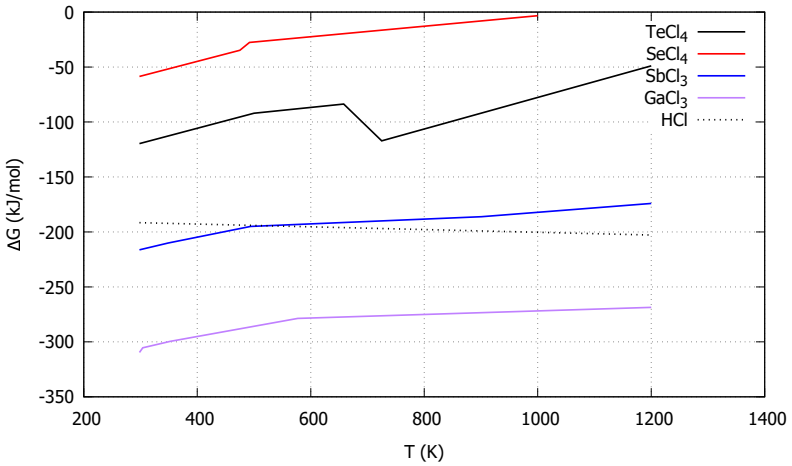

Figure 2.15: *Ellingham diagrams of the different hydrogen getters compared to the one of HCl [19–21].*

Comparing the standard Gibbs free energies of the different getters and of HCl in the range of temperatures used during the synthesis, it seems also impossible to find any trivial correlation between the stability of these chlorides and their efficiency, as visible in Figure 2.15; on the contrary, in a counterintuitive way the most stable compound, nominally $GaCl_3$ gives better results than the less stable $SbCl_3$. This could be due to different elements in the melt acting as catalysts to favor the reaction

$$\mathrm{n\ Se{-\!\!-}H\ +\ XCl_n \rightleftharpoons n\ Se\ +\ X\ +\ nHCl},$$

in a way similar to the one suggested in [22], and acting differently when changing the element X; the individuation of the actual reaction steps is far from the goals of this work, but the fact that the partial elimination of Se−H bonds happens even without the addition of any metal to the melt (Figure 2.17), a cooperative action of the two getters seems less probable with respect to the action of other glass or crucible components as catalysts.

2.3.2.2 Effect of the different oxygen getters

Concerning the removal of oxygen, Figure 2.14.b shows that magnesium, aluminum and zirconium efficiently suppress the Ge-O and As-O bands in the attenuation spectra of the respective samples. Nickel, on the other side, seems to be completely ineffective in this regard: as visible in Figure 2.17, the spectrum of the Ni containing sample is almost perfectly superimposable with the one of a sample prepared with the same amount of $TeCl_4$, but no oxygen getter. This is compatible with the Ellingham diagrams shown in Figure 2.16.a, from which formation of NiO seem less favored than formation of GeO_2, whereas formation of MgO, Al_2O_3 and ZrO_2 appear to be strongly favored against germanium dioxide.
While the choice of the halide doesn't seem to influence the content of oxides in a relevant way, when comparing the Se-H peaks of the samples prepared with different oxygen getters there is a significant difference. In this case too, the explanation from a reaction dynamics point of view is fairly complicated and would require deeper studies to be fully understood. Anyway, given the high absolute value of the formation ΔG of ternary compounds in the form $M_xSi_yO_z$, with M being a metal, as shown in Figure 2.16.b for Al, Zr and Mg, it is reasonable to suppose that the oxygen getters can interact with the silica crucible. This could cause the release of hydrogen from Si−O−H groups at the surface of the crucible, therefore influencing the amount of hydrogen-related impurities in the chalcogenide glass.

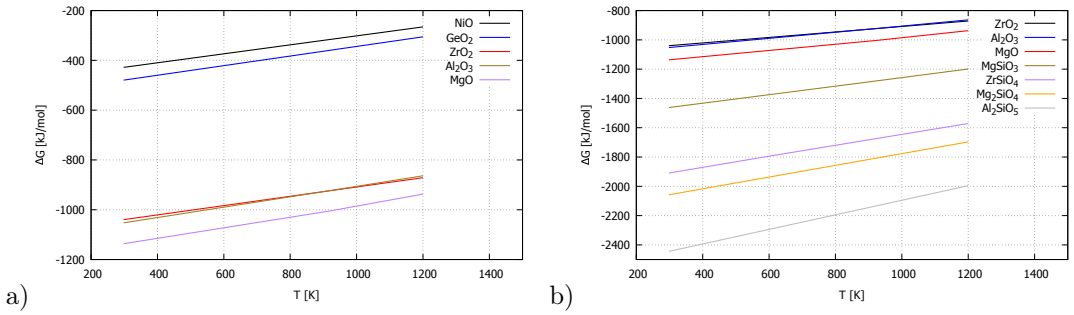

Figure 2.16: *Ellingham diagrams of different oxygen compounds [19, 20].*

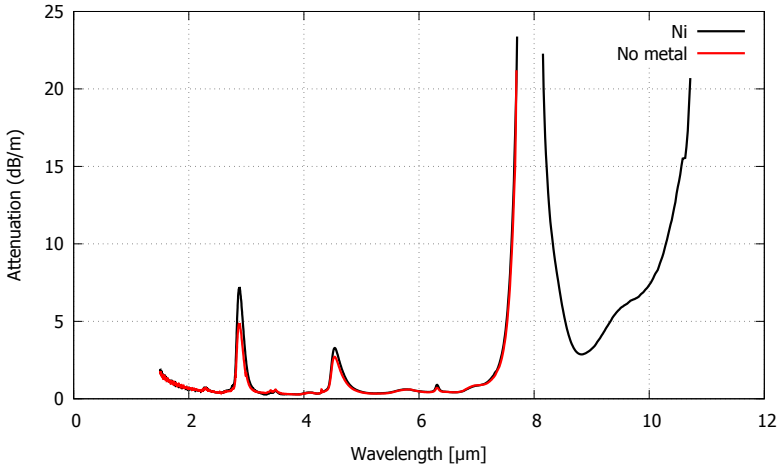

Figure 2.17: *Comparison between the attenuation spectra of a sample with Ni as a metal and a sample with no metal at all. In both samples* $TeCl_4$ *is used as hydrogen getter.*

For all of these reasons, it appears clear that the choice of the getters, as well as the amount of getters used for the reactions, has to be the result of a compromise between the reduction of the bands related to hydrogen and oxygen pollution and the necessity to avoid as much as possible reactions involving the crucible [23–25].

2.3.3 Modification of the quantity of oxygen getter

The main actors in in the crucible-preform interactions, which are a possible explanation to the worse optical quality of the glass, are thought to be the metals used as oxygen getters. Starting from the best getters combination found in Section 2.3.2, namely Mg and $TeCl_4$, two new samples were prepared, keeping the same experimental procedure but changing the quantity of Mg introduced in the charge. The goal in mind here was to further optimize the double distillation route for purification, by adjusting not only the type of getters used but also their quantity.
Keeping the amount of $TeCl_4$ fixed at 2000 ppmw, two samples purified using respectively 100 and 600 ppmw of Mg were produced. The attenuation spectra of the single index fiber obtained from these glasses are shown in Figure 2.18, together with the one of the glass produced with 200 ppmw of Mg already described in the previous section. As visible from the spectra, the glass produced with the highest quantity of Mg shows no oxygen-related peaks, like the one with 200 ppmw of oxygen getter, but a significant increase of the intensity of Se-H peak can be observed. This could be due to the exceeding amount of Mg reacting, once all oxygen is removed, with the crucible or even with the hydrogen getter, having the chlorine atoms from $TeCl_4$ to react with the metal to form $MgCl_2$ instead of binding with hydrogen.

Looking at the sample with less Mg, on the other side, no significant increase in Se-H absorption can be observed (less than 1 dB/m difference between the 100 ppmw and 200 ppmw samples; this kind of relatively small difference cannot be attributed with certainty to the getters quantity). However, a small Ge-O peak does appear in the attenuation spectrum.
Further optimization, as well as a study of the influence of the quantity of halides, will be needed in order to find the best quantity and ratio of getters to be used.

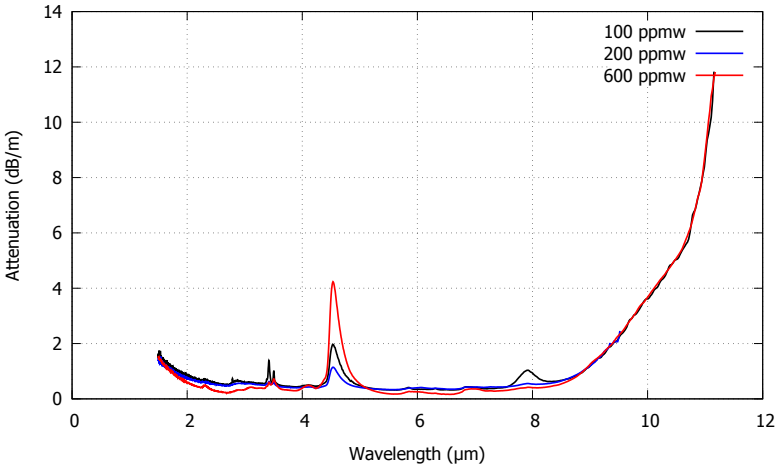

Figure 2.18: *Comparison between the attenuation spectra of a samples containing different amounts of Mg. In all samples* $TeCl_4$ *is used as hydrogen getter.*

2.4 Possible solutions for the reduction of high scattering losses

During the development of this thesis, some of the prepared glasses showed high levels of scattering-related attenuation even after the double distillation process. Due to the high number of variables influencing the reaction, there are many possible causes to this effect. Impurities in the silica tubes and setups could, for instance, enter in the melt, or different impurity levels of the starting materials could throw off the balance of the reactions with getters.
In this section two of the methods attempted to solve this problem are presented: the addition of more distillation steps and the balancing of the ratio between oxygen and hydrogen getters.

2.4.1 Further distillation steps

Upon noticing that some high purity glasses were showing an unusually high attenuation at the wavelength of 1.55 μm, an attempt to reduce it by re-distilling them was done: the part of preform left after the fiber drawing was put into a double-batch silica setup and underwent again the procedure described in Section 2.3.1. As visible from Figure 2.19, this strongly reduced the scattering losses in the fiber without significantly altering the intensity of impurity-related absorption bands. The most likely explanation for the additional losses is the presence of a large amount of particles in the starting batch, too many to be removed by a single purification. In order to understand the nature of those particles, some white residual found on the surface of the silica ampoule used for the first synthesis was analyzed by energy-dispersive spectroscopy. The result of the analysis are shown in Table 2.7.
Apart from the silicon, arsenic and selenium, which are signals to be expected in a SiO_2 crucible used for Ge-As-Se glass synthesis, three other elements were found: calcium, found in trace quantities and of unknown origin, and a considerable amount of magnesium and chlorine, in a nearly 1:2 ratio. The presence and amount of the latter two seem to suggest that, because of an unbalanced reaction equilibrium, $TeCl_4$ and Mg reacted together to form $MgCl_2$, which could be the source

of the additional scattering losses. This kind of reaction can cause a loss of efficacy of one getter when the other one is in excess.

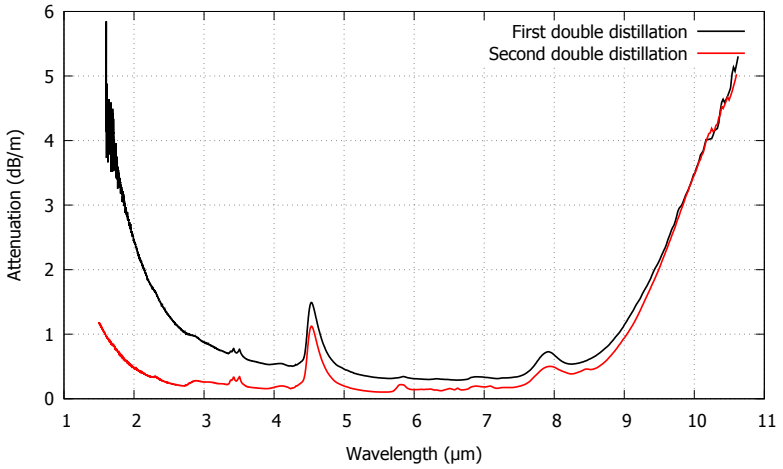

Figure 2.19: *Attenuation spectra of optical fibers obtained by the same* $Ge_5As_{30}Se_{65}$ *batch, before and after performing a second distillation step.*

Table 2.7: *Results of EDS analysis of residuals on the silica ampoule used for the synthesis of a glass exhibiting unusually high scattering losses.*

Element	Mass % (±1)	Atomic % (±1)
Mg	1.5	4.0
Si	5.5	13.0
Cl	5.0	9.0
Ca	0.5	1.0
As	29.5	25.5
Se	58.0	47.5

2.4.2 Balance in the amount of getters

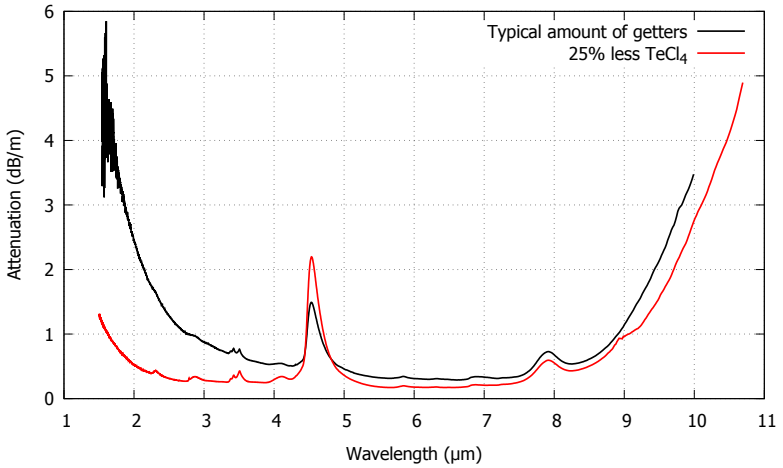

Figure 2.20: *Attenuation spectra of optical fibers obtained by* $Ge_{10}As_{22}Se_{68}$ *batches prepared under the same experimental conditions but with different amounts of* $TeCl_4$.

Following the results from the EDS analysis in Section 2.4.1, an attempt to balance the equilibrium in the reaction was performed by reducing the amount of TeCl4 in the initial charge from 2000 ppm to 1500 ppm, while maintaining the typical Mg amount. As visible in Figure 2.20, this leads to a strong reduction of the scattering losses. The intensity of the Se-H band at 4.56 μm, however, is almost doubled. Despite this being a promising starting point, more experiments well be needed in the future to investigate this route to the solution of the high scattering problem.

2.5 Conclusions

In this chapter, the synthesis and characterization methods used for producing chalcogenide glasses during the development of this thesis have been described, and the characteristics of the different compositions synthesized have been listed. A way to obtain high purity chalcogenide glasses has been detailed, together with the influence of different parameters on the final results of this process. When the standard purification used has proven to not be sufficient to properly reduce scattering-related losses, solutions have been devised to overcome this problem and obtain high quality products.

Bibliography

[1] L Tichỳ and H Ticha. "Covalent bond approach to the glass-transition temperature of chalcogenide glasses". In: *Journal of Non-Crystalline Solids* 189.1-2 (1995), pp. 141–146.

[2] Guang Yang, Tanguy Rouxel, Johann Troles, Bruno Bureau, Catherine Boussard-Plédel, Patrick Houizot, and Jean-Christophe Sangleboeuf. "Viscosity of As2Se3 glass during the fiber drawing process". In: *Journal of the American Ceramic Society* 94.8 (2011), pp. 2408–2411.

[3] AN Gent. "Theory of the parallel plate viscometer". In: *British Journal of Applied Physics* 11.2 (1960), p. 85.

[4] I Avramov and A Milchev. "Effect of disorder on diffusion and viscosity in condensed systems". In: *Journal of non-crystalline solids* 104.2-3 (1988), pp. 253–260.

[5] Ana F Kozmidis-Petrovic. "Equations of viscous flow of silicate liquids with different approaches for universality of high temperature viscosity limit". In: *Processing and Application of Ceramics* 8.2 (2014), pp. 93–99.

[6] Chen-Yang Liu, Jiasong He, Roland Keunings, and Christian Bailly. "New linearized relation for the universal viscosity- temperature behavior of polymer melts". In: *Macromolecules* 39.25 (2006), pp. 8867–8869.

[7] Marcio Luis Ferreira Nascimento and Cristina Aparicio. "Viscosity of strong and fragile glass-forming liquids investigated by means of principal component analysis". In: *Journal of Physics and Chemistry of Solids* 68.1 (2007), pp. 104–110.

[8] John C Mauro, Yuanzheng Yue, Adam J Ellison, Prabhat K Gupta, and Douglas C Allan. "Viscosity of glass-forming liquids". In: *Proceedings of the National Academy of Sciences* 106.47 (2009), pp. 19780–19784.

[9] Jean-Luc Adam and Xianghua Zhang. *Chalcogenide glasses: preparation, properties and applications*. Woodhead publishing, 2014.

[10] Hidetoshi Onodera, Ikuo Awai, and Jun-ichi Ikenoue. "Refractive-index measurement of bulk materials: prism coupling method". In: *Applied optics* 22.8 (1983), pp. 1194–1197.

[11] Harshana G Dantanarayana, Nabil Abdel-Moneim, Zhuoqi Tang, Lukasz Sojka, Slawomir Sujecki, David Furniss, Angela B Seddon, Irnis Kubat, Ole Bang, and Trevor M Benson. "Refractive index dispersion of chalcogenide glasses for ultra-high numerical-aperture fiber for mid-infrared supercontinuum generation". In: *Optical Materials Express* 4.7 (2014), pp. 1444–1455.

[12] Celine Caillaud, Gilles Renversez, Laurent Brilland, David Mechin, Laurent Calvez, Jean-Luc Adam, and Johann Troles. "Photonic bandgap propagation in all-solid chalcogenide microstructured optical fibers". In: *Materials* 7.9 (2014), pp. 6120–6129.

[13] Christian Rosenberg Petersen, Rasmus D Engelsholm, Christos Markos, Laurent Brilland, Céline Caillaud, Johann Trolès, and Ole Bang. "Increased mid-infrared supercontinuum bandwidth and average power by tapering large-mode-area chalcogenide photonic crystal fibers". In: *Optics express* 25.13 (2017), pp. 15336–15348.

[14] Jas S Sanghera and Ishwar D Aggarwal. "Development of chalcogenide glass fiber optics at NRL". In: *Journal of non-crystalline solids* 213 (1997), pp. 63–67.

[15] Frédéric Charpentier, Johann Troles, Quentin Coulombier, Laurent Brilland, Patrick Houizot, Frédéric Smektala, Catherine Boussard-Plédel, Virginie Nazabal, N Thibaud, Karine Le Pierres, et al. "CO2 detection using microstructured chalcogenide fibers". In: *Sensor Letters* 7.5 (2009), pp. 745–749.

[16] Vinh Q Nguyen, Jas S Sanghera, Brian Cole, Pablo Pureza, Frederic H Kung, and Ishwar D Aggarwal. "Fabrication of arsenic sulfide optical fiber with low hydrogen impurities". In: *Journal of the American Ceramic Society* 85.8 (2002), pp. 2056–2058.

[17] Perrine Toupin, Laurent Brilland, Johann Trolès, and Jean-Luc Adam. "Small core Ge-As-Se microstructured optical fiber with single-mode propagation and low optical losses". In: *Optical Materials Express* 2.10 (2012), pp. 1359–1366.

[18] Marcello Meneghetti, Celine Caillaud, Radwan Chahal, Elodie Galdo, Laurent Brilland, Jean-Luc Adam, and Johann Troles. "Purification of Ge-As-Se ternary glasses for the development of high quality microstructured optical fibers". In: *Journal of Non-Crystalline Solids* 503 (2019), pp. 84–88.

[19] Thomas Binnington Reed. *Free energy of formation of binary compounds.* MIT press, 1971.

[20] W Malcolm Jr. *NIST-JANAF thermochemical tables.* American Institute of Physics; The American Chemical Society, 1998.

[21] William M Haynes. *CRC handbook of chemistry and physics.* CRC press, 2014.

[22] Vinh Q Nguyen, Gryphon Drake, Guillermo Villalobos, Daniel Gibson, Shyam Bayya, Woohong Kim, Colin Baker, Geoff Chin, Frederic H Kung, Mikhail I Kotov, et al. "Effect of aluminum and tellurium tetrachloride addition on the loss of arsenic selenide optical fiber". In: *Optical Materials* 64 (2017), pp. 327–333.

[23] VS Shiryaev, SV Mishinov, and MF Churbanov. "Investigation of adhesion of chalcogenide glasses to silica glass". In: *Journal of Non-Crystalline Solids* 408 (2015), pp. 71–75.

[24] SV Mishinov, MF Churbanov, AN Gorokhov, DA Kazakov, VS Shiryaev, AI Suchkov, LA Igumnov, and GE Snopatin. "Adhesion mechanism of destruction of silica-glass surface during the preparation and treatment of optical glassy arsenic Chalcogenides". In: *Inorganic Materials* 52.7 (2016), pp. 716–720.

[25] MF Churbanov, SV Mishinov, VS Shiryaev, and LA Ketkova. "Contamination of glassy arsenic sulfide by SiO2 particles during melt solidification in silica glassware". In: *Journal of Non-Crystalline Solids* 480 (2018), pp. 3–7.

Chapter 3

Chalcogenide index-guiding photonic crystal fibers

3.1 Chalcogenide index-guiding PCFs as a medium for mid-IR supercontinuum generation

3.1.1 Research interest

There are in general two kinds of mid-IR fibers: passive fibers and active fibers. Passive fibers are applied to transmit infrared information, whereas active fibers can generate mid-IR light by using nonlinear effects or rare-earth doping [1]. Active fibers are especially of interest for the generation of supercontinua in the mid infrared region, application for which the conversion medium is of great importance, together with the pump source. Figure 3.1 lists and compares the transmission coverage of several different fibers.

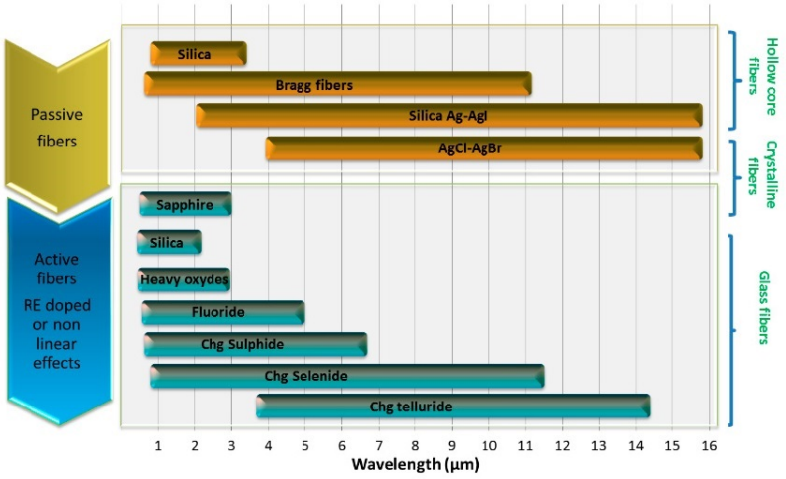

Figure 3.1: *Mid-infrared transmissions of different types of optical fibers [1].*

As can be seen, among glass fibers, only chalcogenide ones have a transparent domain reaching far in the mid-IR region. The transmission window varies with the constituting chalcogen elements, namely sulfur, selenium, and tellurium [2], as shown in Figure 3.2. As–S fibers can transmit from 1 to 6.5 μm [3], As–Se fibers from 1.5 to 10 μm [4], and Te-based fibers, due to heavy atomic weight, can transmit up to 14 μm. In terms of optical nonlinearity, chalcogenide glasses possess a nonlinear refractive index n_2 that is 2 to 3 orders of magnitude higher than the one of silica [2]. These nonlinear optical properties are even more pronounced in small-core single-mode fibers,

thanks to the dependence of nonlinear effects on power density and therefore on the effective mode area.

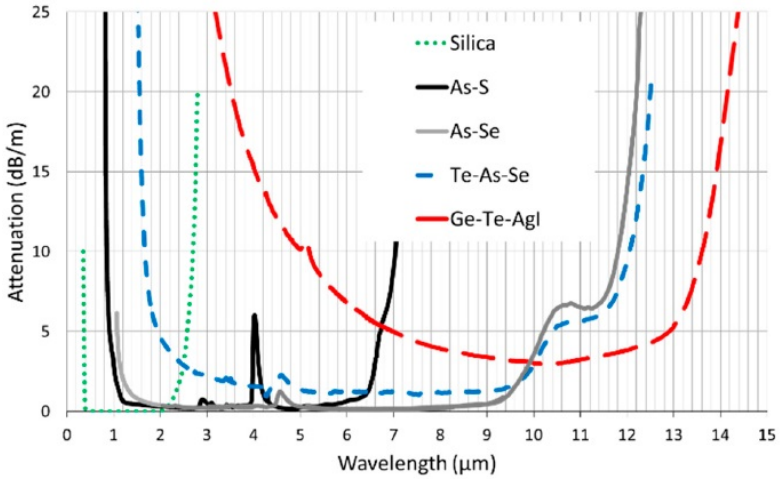

Figure 3.2: *Mid-infrared attenuation of different chalcogenide optical fibers compared to silica ones.*

As already treated in Section 1.4, in index-guiding photonic crystal fibers the light propagation properties are determined by the geometry, that in the case of the classical configuration with hexagonal holes arrangement is entirely defined by the diameter of the air holes (d) and distance between neighboring holes (Λ) depicted in Figure 3.3, and by the number of hole rings (N). By managing the values of d and Λ, the core size can be freely modified while maintaining single-mode guiding regardless of the wavelength, as long as the d/Λ ratio is less than 0.42 [5, 6]. A small core can be used to increase the incidence of nonlinear phenomena, by increasing the value of the nonlinear parameter γ defined in section 1.5.1. Conversely a large core, by decreasing the power density, can increase considerably the amount of power that can be carried without damaging the fiber or triggering nonlinear effect, making these fibers attractive for uses such as telecommunications.

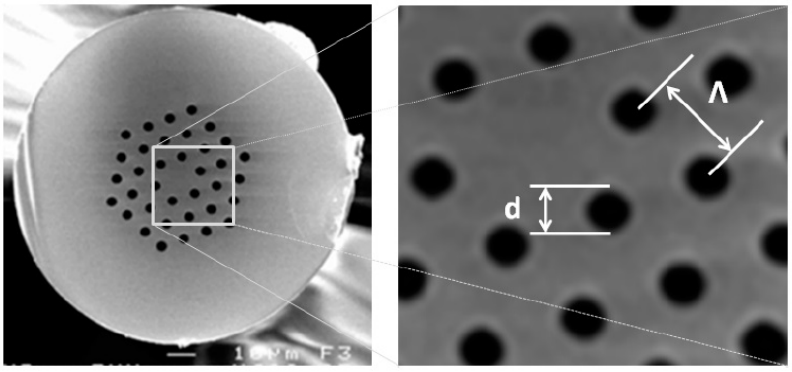

Figure 3.3: *Cross section of a chalcogenide microstructured optical fiber, where the hole size d, and the distance between neighboring holes Λ(also called "pitch") are noted.*

Also, by controlling the fiber geometry, the zero-dispersion wavelength (ZDW) can be controlled over a wide range of wavelengths [7]. Indeed, as in order to obtain an efficient supercontinuum source the fiber has to be pumped close to the ZDW, one of the main advantages of index-guiding PCFs is to obtain strong flexibility in dispersion modification. The intrinsic ZDWs of chalcogenide glasses are normally located beyond 5 μm, where it is difficult to find available powerful laser pump sources (a fact especially true for fiber lasers). Therefore it would be beneficial to shift the ZDW to

a shorter wavelength: 1.55 μm for pumping in the telecom window, or at least less than 4 μm. As an example of how geometrical properties can influence dispersion in a Ge–As–Se system [8], where the ZDW of the bulk material is around 7 μm, a microstructured fiber with a ZDW blue-shifted to 3.6 μm was achieved by tapering it in order to reduce the core diameter from 12 to 6 μm [8]. Once fixed the values of d and Λ, the choice of the correct number of hole rings allows to control confinement losses in the fiber. Such losses would be equal to 0 for of $N \rightarrow \infty$, but this is of course not a case applicable in reality. It is however sufficient for any application to have confinement losses negligible with respect to the intrinsic attenuation losses of the material of which the fiber is constituted. For high refractive index materials such as chalcogenide glasses, this goal can be reached with three or four rings of holes [6, 9]. As a comparison, more than six rings are needed to achieve an analogous result in silica index-guiding PCFs [10].
Other geometries other than the triangular hole lattice can be used to produce index-guiding PCFs. A quite common one is the suspended core geometry, in which a single ring of very large holes is present (see Figure 3.4.b). The glass "bridges" between the holes are very thin, so that the light transmission in the small core has characteristics analogous to what they would be if the core was completely surrounded by air. As an example of dispersion management, a suspended-core chalcogenide As_2S_3 fiber with a ZDW blue-shifted to around 2 μm was realized [11], whereas the ZDW of the bulk glass is around 5 μm. In this study [11] the simulated results were confirmed by experimental measurements.
Another interesting possible structure can be realized by breaking the symmetry along one axis in a common triangular lattice fiber, an effect usually obtained by increasing the size of two opposing holes in the ring closer to the core. By doing this, birefringence can be induced in the fiber, giving it the property of maintaining the light polarization along the propagation length [12].
Summarizing, chalcogenide index-guiding PCFs combine a wide mid-IR transmission, high nonlinearity, single-mode guiding and dispersion tunability, opening up a way for the generation of broad mid-IR supercontinua.

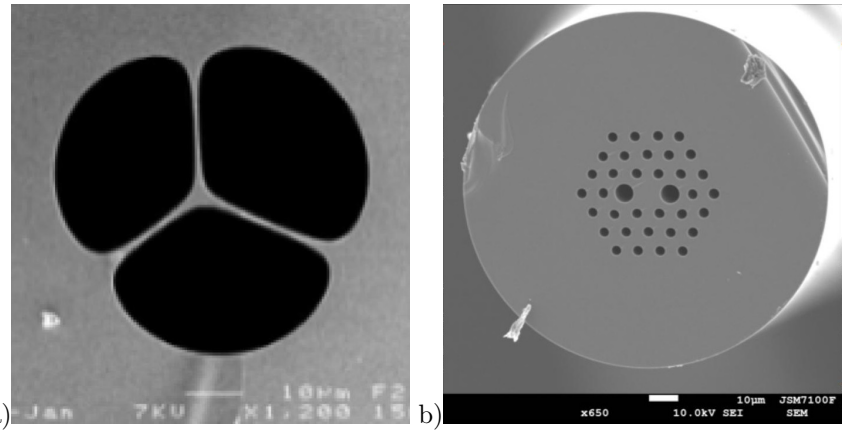

Figure 3.4: *Cross sections of a chalcogenide suspended core fiber (a) and of a chalcogenide polarization maintaining fiber (b).*

3.1.2 State of the art

As one of the most promising applications of chalcogenide fibers, mid-IR supercontinuum generation has been investigated extensively with both step-index and air hole chalcogenide fibers [13–16]. The first generation of supercontinuum was demonstrated in 2006 for chalcogenide index-guiding PCFs [17]. One meter of such a selenide-based chalcogenide fiber was pumped by a Ti:Sapphire laser, with an output wavelength at 2.5 μm and pulse duration and energy of 100 fs and 100 pJ, respectively. The experimental results displayed in Figure 3.5 show that effective wavelength broadening can be achieved through pumping around the ZDW or the anomalous region of the fiber.
In 2010, M. El-Amraoui et al. reported the fabrication of the first As_2S_3 chalcogenide suspended core fiber. Instead of the stack and draw method, mechanical drilling was used to prepare the fiber

preform. By pumping a 45 m-long piece of MOF with an 8-ps mode-locked laser at around 1.55 μm, a continuum covering more than 200 nm from 1450 to over 1700 nm was obtained [11].

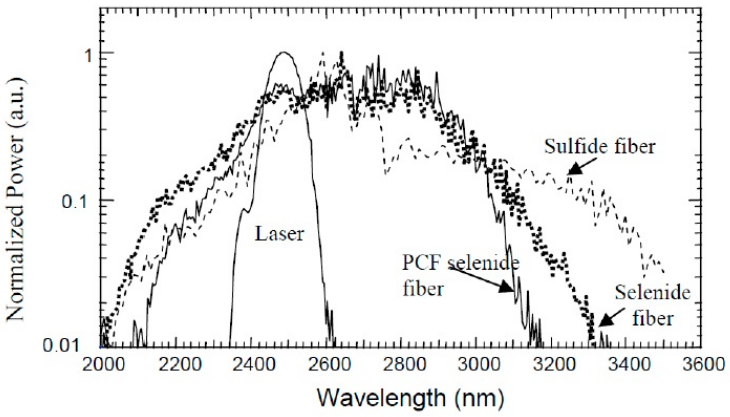

Figure 3.5: *Output spectra of supercontinua generated in chalcogenide microstructured optical fibers produced by stack and draw technique [17].*

Several other pumping schemes have been investigated to generate Mid-IR supercontinua. In 2016, Petersen et al. used a two-cascading configuration, based on a 1.55-μm laser-diode-pumped thulium-doped silica fiber and a ZBLAN fluoride fiber, to pump a chalcogenide air holes fiber [18]. By comparing the output spectra of ZBLAN fibers with different chromatic dispersions, it was concluded that solitons located in the long-wavelength part of the pump are essential for the effective generation of the supercontinuum, and a supercontinuum extending up to 7 μm with a total output power of 6.5 mW was generated at the end of the chalcogenide fiber. In 2017, Mid-IR SC generation from a tapered large-mode-area chalcogenide index-guinding PCF was demonstrated [8]. The Mid-IR pump source utilized in the experiment was achieved by combining a tunable seed laser and a 1.04-μm mode-locked Yb:KYW solid-state laser into periodically-poled MgO:$LiNbO_3$ crystals to obtain quasi-phase-matched parametric anti-Stokes generation from 3.7 to 4.5 μm. Different taper configurations were studied, leading for the best one to an output spectrum from 1 to 11.5 μm with an average output power of 35.4 mW (see Figure 3.6).

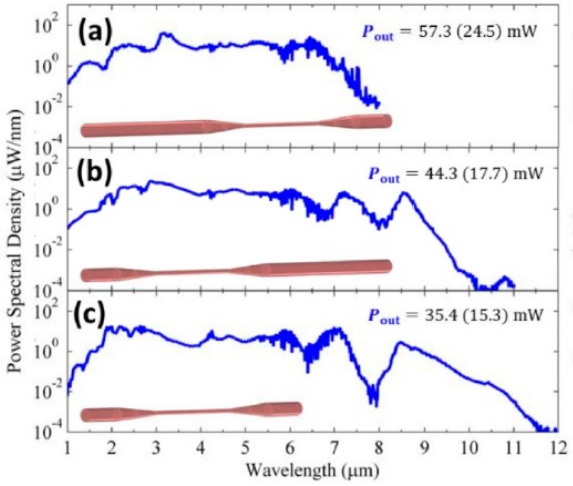

Figure 3.6: *Supercontinuum spectra obtained from a tapered chalcogenide MOF, for three different configurations of lengths of nontapered zones at the input and output of the fiber (in brown color) (a)* L_{bt} = 25 cm, L_{at} = 7.5 cm*; (b)* L_{bt} = 7.5 cm, L_{at} = 25 cm*; (c)* L_{bt} = 7.5 cm, L_{at} = 4 cm. *(*L_{bt}*: length before taper,* L_{at}*: length after taper and* P_{out}*: average integrated out power) [8].*

A summary of the results obtained in supercontinuum generation in chalcogenide index-guiding PCFs, from the experiments discussed in this section, are presented in Table 3.1. The broader supercontinuum spectrum obtained in such fibers presents a spectral coverage from 1 to 11.5 μm with an average output power of 35 mW. The higher output power reaches more than 57 mW, with a spectrum spanning the 1–8 μm wavelength range. Both these results are reported in [8].

Table 3.1: *State of the art of mid-IR supercontinuum generation in chalcogenide index-guiding PCFs.*

Glass composition	Pump wavelength (pulse duration)	Output spectral range	Output average power	Reference
As_2Se_3	2.5 μm (100 fs)	2.1 μm – 3.2 μm	-	[17]
As_2S_3	1.55 μm (8 ps)	1.45 μm– over 1.7 μm	-	[11]
$As_{38}Se_{62}$	Cascading from 1.55 to 4.5 μm (3 ns)	1.9 μm – 7.1 μm	6.5 mW	[18]
$Ge_{10}As_{22}Se_{68}$	4 μm (252 fs)	1 μm – 11.5 μm	35.4 mW	[8]
$Ge_{10}As_{22}Se_{68}$	4 μm (252 fs)	1 μm – 8 μm	57.3 mW	[8]
$Ge_{20}Se_{70}Te_{10}$	8.6 μm (65 fs)	3.25 μm – 13 μm	-	[19]
$Ge_{15}Sb_{15}Se_{70}$	4 μm ($\sim$ 150 fs)	1.5 μm – 12 μm	-	[20]

The supercontinuum obtained by cascading SC in different materials [18] is probably the most promising way for the future. Indeed, this all-fiber approach can lead to more stable, versatile, robust, and compact Mid-IR sources with easy handling. Also, it is well known that more stable and better coupling efficiencies can be obtained with fibers in comparison to free space coupling.

3.2 Fabrication of chalcogenide PCFs

As introduced in Section 1.4.1.1, different methods exist for the fabrication of index-guiding PCFs. Different production techniques, however, are optimal for different glass systems and/ or fiber structures. The goals of this section are to show how different methods have been applied to the production of chalcogenide fibers, as well as to describe the method that has been chosen for the fibers produced during the development of this thesis and how it has been applied.

3.2.1 Stack and draw

Being the most common method for the fabrication of silica index-guiding PCFs, the stack and draw technique described in Section 1.4.1.1 was the first obvious choice for attempting to develop non-silica fibers of this kind. The first reported attempt to do so happened in the year 2000 using chalcogenide glass, more specifically gallium-lantanium-sulphide (GLS) [21]. This first attempt showed the feasibility of the process, although with only one ring of holes and a very irregular fiber cross-section.
In 2006 the possibility of obtaining a well controlled geometry in chalcogenide index-guiding photonic crystal fibers with 3 rings of holes has been demonstrated for the first time using stack and draw [22], apparently opening the way to the development of chalcogenide PCFs fabricated by this technique. The optical losses in these fibers, however, were about 20 dB/m larger than the ones of the materials used for their fabrication [23], strongly limiting their applicability.
As it was determined in [23] using different glass compositions (Ge-Sb-S, As-Se, Te-As-Se), the high losses registered are caused by defects appearing during the collapsing step at the interfaces between rods. These defects seem to be mainly bubbles of micrometric size caused by imperfect collapsing (see Figure 3.7), which can create an high amount of additional losses due to scattering. Furthermore, the presence of a refractive index variation along the interfaces is evidenced by this study, suggesting additional sources of losses other than the already mentioned bubbles, although it is uncertain if the phenomenon is caused by deposition of volatile materials, crystallization or smaller bubbles. In the same study, it was determined that the losses due to the aforementioned problems can be reduced by avoiding a complete collapse of the interstitial holes, and therefore reducing the area of the interfaces between rods. However, even with this device, the losses remained on a level around 4-5 dB/m, well above the intrinsic ones of the materials used.
In conclusion, according to what can be found in literature up to now, the stack and draw technique seems to be difficult to adapt for use in the field of chalcogenide-based index-guiding PCFs, due to

the excessive optical losses. Different fabrication techniques, such as drilling, extrusion or molding, need therefore to be considered for this specific application.

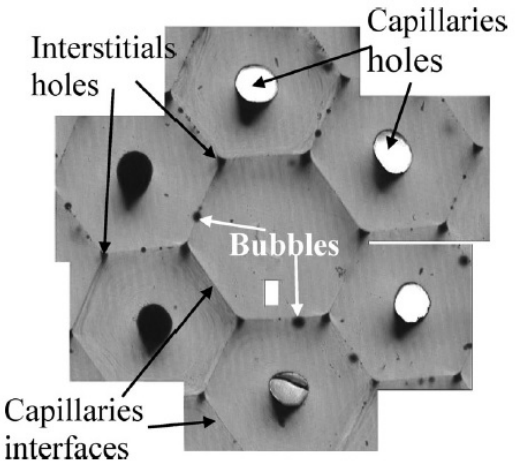

Figure 3.7: *Defects at the interfaces between rods in a pre-collapsed chalcogenide index-guiding PCF preform fabricated by stack and draw technique [23].*

3.2.2 Drilling

Another fabrication technique that can be used for the development of chalcogenide fibers with air holes is to mechanically drill into the preforms. This can be achieved either by ultrasonic drilling process, in which a bit is vibrated at high frequency against the material surface to induce fractures and subsequently penetration, or by classical drilling with a rotating bit.
As of now, there is no available literature about ultrasonic drilling being used to perforate chalcogenide preforms; standard mechanical drilling, on the other side, has been reported to be an efficient method for doing so. This has been demonstrated for both suspended core fibers [20, 24] and index-guiding PCFs with up to four hexagonal rings of holes [24]. An optical quality close to the one of materials has been obtained in As_2Se_3 fibers produced using this technique, with losses as low as 0.35 dB/m at the standard telecommunications wavelength of 1.55 μm [24]. Moreover, broad supercontinuum generation from 1.5 to 12 μm has been recently demonstrated in a Ge-Sb-Se fiber fabricated by mechanical drilling technique [20].

3.2.3 Extrusion

A well known way to shape a material into a predetermined geometry is to soften it by heat and extrude it through a die with an appropriate cross-section. This method has been successfully applied to the production of holey preforms to be drawn into index-guiding PCFs using silicates [25], fluorides [26], tellurites [27, 28] and chalcogenides [29–31]. Although extremely versatile from the point of view of the obtainable geometries, this technique is deemed to be particularly well suited for the fabrication of suspended core fibers with a large air filling ratio [32].
The successful application of extrusion in fabricating chalcogenide preforms is quite novel, and has been demonstrated in the production of mixed Ge-As-Te-Se (core) and Ge-Sb-Se (cladding) suspended core fibers [29] and of As_2S_3 ones [30, 31], with applications to supercontinuum generation and to sensing. Despite the high promise shown by this method, the losses reported in literature remain notably higher than the intrinsic ones of chalcogenide glasses, namely more than 1dB/m in the best reported case [31].

3.2.4 Molding

The last fabrication method for chalcogenide index-guiding PCFs to be exposed in this chapter, which is also the one chosen for the production of such fibers during this thesis, is molding. This

process was first developed in 2006 for the production of PCFs based on polymers [33] and SF6 glass by Schott [34]. For these two materials, the method consisted in melting them into a metal mold with a structure complementary to the one of the desired preform. The mold was then removed by cooling or heating, exploiting the difference in thermal expansion coefficient between the cast material and the metal, leading to the obtaining of a holey preform.
As it was, this technique was however ill-suited for being used with chalcogenide glasses, from which a metallic mold could not be easily removed. This problem was solved by substituting the metal with silica glass [35], leading to the development of the procedure currently used for chalcogenide glasses. In order to mold this class of materials, they are melted and poured into a mold consisting of silica capillaries thread in an hexagonal holey guide (see Figure 3.8.a,b). This step is carried out in a silica tube, and once the glass has completely filled the mold, the whole system is quenched in order to preserve the glassy state of the material and annealed to achieve the reduction of internal stress. After these steps, hydrofluoric acid is used to dissolve the silica capillaries stuck inside the preform. This is possible because chalcogenide glasses, unlike silica, are resistant to reaction with HF. Once the silica capillaries have been completely removed by the acid, a holey preform is obtained (see Figure 3.8.c).
By using this fabrication process excellent results have been obtained in terms of optical losses in chalcogenide index-guiding PCFs, reaching attenuation levels similar to the intrinsic ones of the constituting glass. Notably, losses of less than 0.05 dB/m have been reported in [36] at a wavelength of 3.7 μm. This result was obtained in an $As_{38}Se_{62}$ suspended core fiber obtained by combining the molding process with the double distillation method for the purification of chalcogenide glasses. Moreover, the one here described is a versatile technique allowing for the production of different fiber geometries such as classic hexagonal rings hole arrangement, polarization maintaining and suspended core.

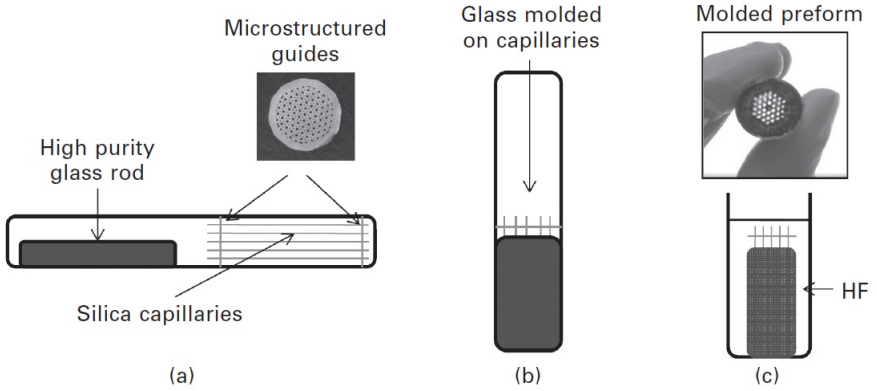

Figure 3.8: *Molding method: (a) mold fabrication, (b) heating and flowing and (c) silica capillary removal [37].*

The remainder of this chapter will be devoted to showing the different chalcogenide index-guiding PCFs produced during the period of this PhD and the results obtained in terms of their characterization and application for mid infrared supercontinuum generation. The fabrication of these fibers was realized in close collaboration with the SelenOptics company, partner organization of the SUPUVIR project.

3.2.4.1 Preparation of endlessly single mode fibers

As briefly explained in Section 1.3.3, normally the number of modes propagating in an optical fiber depends, once fixed the geometry, on the light wavelength. The shorter the wavelength is, the higher the number of observable modes. In the case of index-guiding PCFs this effect can be compensated by the fact that confinement losses are dependent on the fiber geometry, and more specifically, for the case of a fiber with holes regularly arranged in a triangular lattice (Figure 3.9.a), from the $\frac{d}{\lambda}$ ratio. By exploiting this property, a regime can be found in which the modes of

higher order with respect to the fundamental one experience confinement losses high enough to be immediately extinguished. According to theoretical calculations, this phenomenon always happens for $\frac{d}{\lambda} < 0.4$, independently on refractive index, core size and number of hole rings [38].
The possibility to have similar propagation behavior even for very different wavelengths is highly interesting in the domain of chalcogenide fibers, which have a very broad transmission window. An example of endlessly single mode chalcogenide fibers produced by molding technique is the Te-As-Se index-guiding PCF described in [39]. Near field imaging of this fiber shows a similar gaussian profile of the output beam for wavelengths as different as 3.39 μm and 9.3 μm, as shown in Figures 3.9.b and 3.9.c.

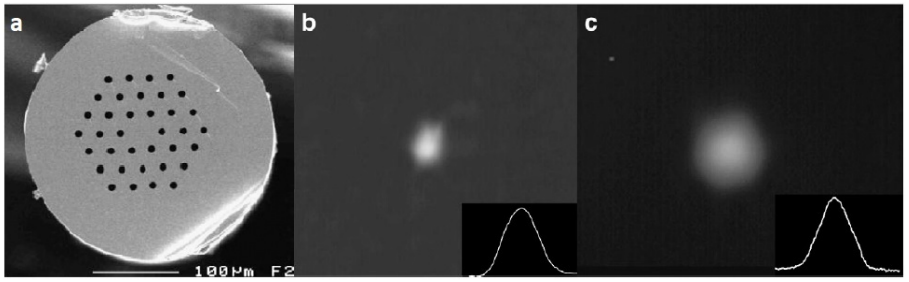

Figure 3.9: *Cross-section (a) and near field imaging (b and c, at 3.39 μm and 9.3 μm respectively) of a Te-As-Se endlessly single mode index-guiding PCF [39].*

The different glass compositions in the Ge-As-Se system prepared in this work, whose synthesis, purification and characterization is described in Chapter 2, have been used for attempting to produce high quality endlessly single mode chalcogenide fibers suitable for supercontinuum generation. The compositions used as a base to start this study are $As_{38}Se_{62}$ and $Ge_{10}As_{22}Se_{68}$, chosen because both of them were already established in literature as good solutions for the production of this kind of fibers [40] and used by SelenOptics at the starting moment of the research for this thesis. By perfecting the purification technique for the precursor glasses (see Chapter 2) a $Ge_{10}As_{22}Se_{68}$ endlessly single mode fiber with remarkably low attenuation over a broad spectral range was developed. The optical losses of this fiber are below 1 dB/m between 2.5 and 9 μm, with the only exception of a sharp peak related to Se-H vibration at 4.5 μm, and have a minimum of less than 0.2 dB/m at 5.5 μm (see Figure 3.10). The absorption induced by this impurity maintains anyway a level below 2 dB/m. This is the best transmission reported up to now in literature for a selenide index-guiding PCF.

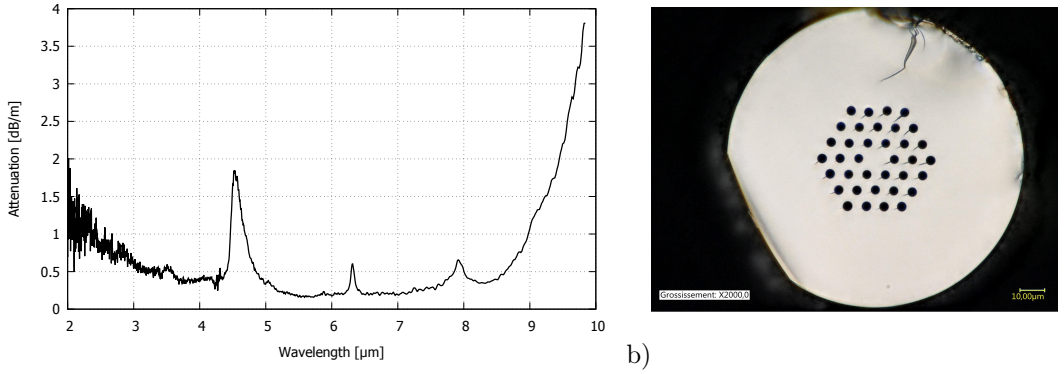

a) b)

Figure 3.10: *Attenuation spectrum (a) and cross section (b) of the Ge-As-Se index-guiding PCF with lowest losses obtained during the development of this thesis [41].*

Increasing the amount of germanium in the composition can have a positive impact in terms of thermal stability of the glass and of power damage threshold of the fibers obtained from it.

The first attempt to pursue these goals was performed with the synthesis of $Ge_{22}As_{20}Se_{58}$, a composition already commercially available under the name of GASIR®1 [42] and sold by Umicore. This glass, however, was found to be incompatible with the molding technique used for obtaining holey preforms, due to the too large concentration of germanium, known to increase network connectivity. Indeed, a rigid glass network increases the sensitivity of the system to the internal stress induced by the presence of silica capillaries in the preform, leading to the formation of cracks despite the presence of an annealing step in the production procedure. To try to address this issue, $Ge_{16}As_{20}Se_{64}$ was produced as an intermediate composition between $Ge_{10}As_{22}Se_{68}$ and $Ge_{22}As_{20}Se_{58}$. With this glass the fabrication of index-guiding PCFs by molding has been proven to be possible, but, once again because of excessive network rigidity, with a success rate too low to lead to the possibility of industrial production.
While the presence of germanium in the composition improves the glass in terms of thermal and mechanical properties, it has shown to increase the optical losses of fibers in the telecommunications window, making them less suitable for applications that require compatibility with standard fibers and sources. This is believed to be due to the high chemical reactivity of germanium with silica, which can cause silica particles to be introduced in the glass during the synthesis and molding steps of preform production. Such particles can act as scattering centers, decreasing the optical quality of the glass. Indeed, most $Ge_{10}As_{22}Se_{68}$ single index fibers produced during this work to test the purity of glass have losses of about 1 dB/m at 1.55 μm, while values of 0.6-0.7 dB/m have been observed at the same wavelength for $As_{38}Se_{62}$.
As a possible solution to this problem, intermediate compositions between the just mentioned two have been studied, with the goal of combining the lower losses at 1.55 μm of $As_{38}Se_{62}$ while keeping the thermal stability of the $Ge_{10}As_{22}Se_{68}$. The first composition tested, $Ge_5As_{25}Se_{70}$, exhibited a glass transition temperature (139°C) too low for the molding process to be applied, and was therefore immediately discarded. In order to increase the value of T_g while keeping the concentration of germanium fixed, more arsenic was included in the glass. The resulting composition, $Ge_5As_{30}Se_{65}$, has given good preliminary results: the glass transition temperature has the same value of $As_{38}Se_{62}$, and the optical losses at telecommunications wavelengths have shown values around 0.7 dB/m in single index fibers over many different syntheses.

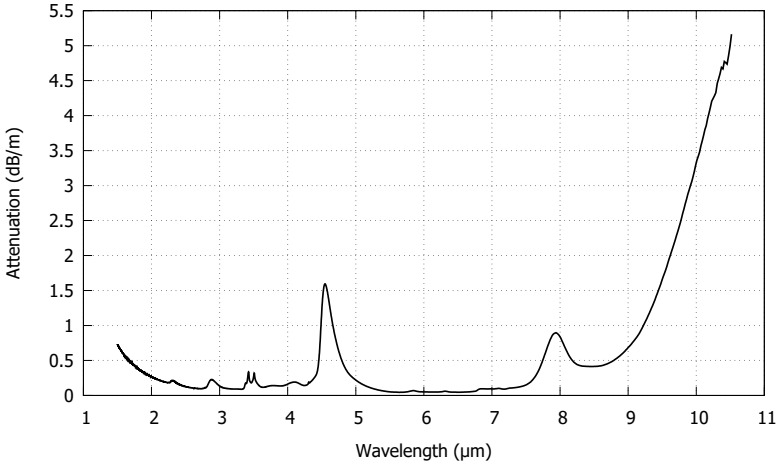

Figure 3.11: *Attenuation spectrum of the* $Ge_5As_{30}Se_{65}$ *single index fiber with lowest losses obtained during the development of this thesis.*

The best sample produced exhibited losses of 0.65 dB/m at 1.55 μm and a minimum attenuation of less than 0.05 dB/m in the mid infrared (see Figure 3.11). The molding process is as of now being adapted to this composition, in the hope to obtain similar values for losses in an index-guiding PCF.

3.2.4.2 Preparation of polarization maintaining fibers

All fibers, independently on the design, exhibit some degree of birefringence, which can be due to stress in the glass network, fiber bending or other effects. Because of this, the polarization of light propagating in the fiber changes in an uncontrolled, wavelength-dependent way along the propagation length. This phenomenon makes standard optical fiber designs not suitable for many applications, such as integrated optics, interferometry and high bit-rate transmission, in which there is need for minimization of polarization mode dispersion and elimination of polarization-dependent effects [12].
This problem was not addressed by attempting a suppression of the intrinsic birefringence of fibers, but instead by exacerbating it. So called "polarization maintaining" fibers exhibit a birefringence way higher than other fibers, and aligned along two well-defined orthogonal axes. If light with polarization aligned to one of these axes is injected in the fiber, this causes the presence of different effective propagation constants for modes with different polarization. If this difference in β_{eff} is pronounced enough, no perturbations occurring in the fiber can couple those modes, leading to the preservation of the initial polarization along propagation.
High birefringence in optical fibers can be obtained in several ways. For step-index fibers, the usual methods are to induce mechanical stress [43, 44] or to use an elliptical core [45]. In index-guiding PCFs an analogous effect can be obtained by altering the shape [46] or size [47, 48] of holes near the core in a way that breaks the structure symmetry along an axis. In index-guiding PCFs, values of birefringence as much as an order of magnitude larger than in step-index fibers can be obtained [12], making them an attractive solution for the production of high performance polarization maintaining fibers. In recent times, the molding technique has been successfully applied to the development of polarization maintaining fibers based on chalcogenide glasses [12].
During the period of development of this thesis, a polarization maintaining fiber has been produced by molding technique, using high purity $As_{38}Se_{62}$ as a starting material. The method used for breaking the symmetry of the fiber was the introduction of two larger holes, whose diameter will be referred to as d_h, in the smaller ring of holes, with diametrically opposed positions with respect to the core (see Figure 3.12). The final geometrical parameters of the obtained fiber, which had an external diameter of 125 μm, were the following: d = 3.35 μm, d_h = 5.8 μm, Λ = 7.025 μm. For this geometry, the core size is considered to be equal to $2\Lambda - d_h$, and it is therefore expected to be equal to 8.25 μm, value in good accordance with the one measured from scanning electron microscopy images (8.11 μm). The $\frac{d}{\Lambda}$ ratio of 0.477 is small enough for the fiber to be single mode over the whole mid infrared range [49], and the large $\frac{d_h}{\Lambda}$ value (0.826) should correspond to a large birefringence [12]. Measurements of attenuation (see Figure 3.13) show optical losses of less than 2 dB/m over the whole range comprised between 2 and 9 μm, with a minimum of 0.25 dB/m at 6.6 μm. Two absorption bands at 4.5 μm and 6.3 μm, related to Se-H bonds and H_2O respectively, are present, but their intensities are low.

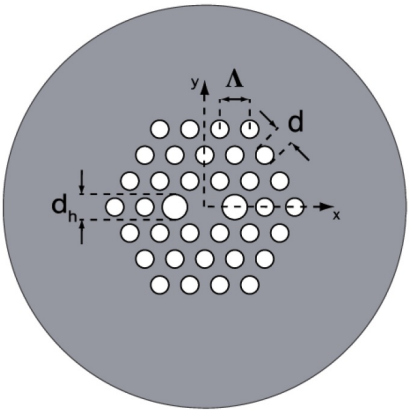

Figure 3.12: *Schematic cross-section of the polarization maintaining index-guiding PCF produced to be tested for supercontinuum generation [12].*

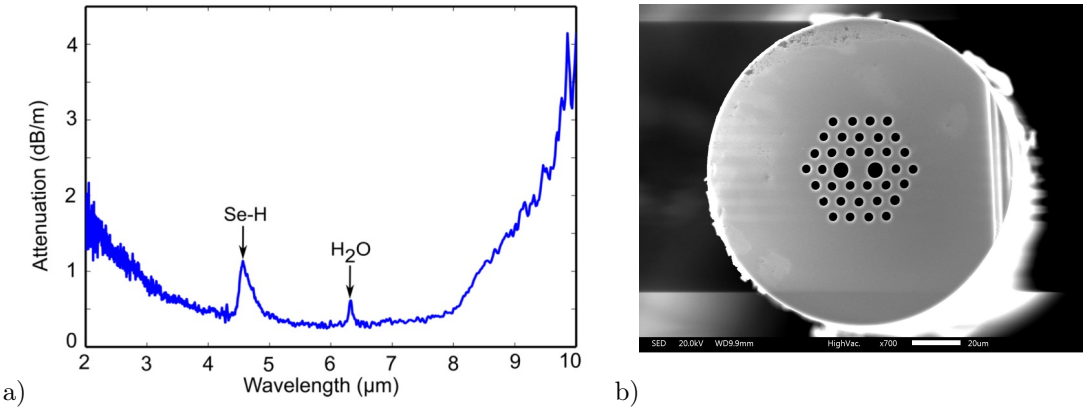

Figure 3.13: *Attenuation spectrum (a) and cross-sectional SEM image (b) of the chalcogenide polarization maintaining index-guiding PCF produced to be tested for supercontinuum generation[50].*

The polarization maintaining fiber described above was chosen for attempting to generate a mid infrared supercontinuum, as detailed in Section 3.4.1.

3.2.4.3 Tapering

As already explained in the previous parts of this chapter, a small size of the core can be used in index-guiding PCFs both for increasing the magnitude of nonlinear effects and for shifting the zero dispersion wavelength of the fiber towards shorter wavelengths. The latter is of particularly high interest for chalcogenide fibers. The direct fabrication of small-core index-guiding PCFs by molding technique, however, is far from being trivial. In addition to this, injecting mid infrared light into such fibers can be tricky, due to the scarcity of proper injection setups working in that range of wavelengths. Both of these problems can be addressed by obtaining small-core fibers through the process of tapering larger core ones.
The tapering process consists in heating a part of fiber in order to soften it, and applying tensile strength to further elongate it, leading to a decrease in diameter. Using the proper temperature and tension, this can be achieved isometrically, thus maintaining the geometrical features of the fiber, just scaled to a smaller size. At the end of the process, the resulting taper, as schematized in Figure 3.14, will have the same diameter of the initial fiber at the ends, a central part of constant smaller diameter (called "waist") and two parts, connecting the waist to the ends, having the diameter smoothly varying along their length (called transitions). The fact that the ends can have a large core size allows for easier light injection.

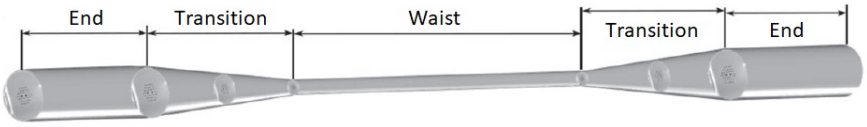

Figure 3.14: *Schematics of the structure of a taper (adapted from [50]).*

The tapers obtained in this work from different fibers were produced on the same drawing tower used for the production of index-guiding PCFs. To do so, one end of the starting fiber is fixed to the preform motion system, heated with an annular furnace under helium atmosphere and pulled by connecting the other end to the rotating drum (see Chapter 2 for the schematics of the drawing tower). As it is in fiber drawing, the final diameter of the waist is determined by the difference in speed between the preform motion system and the drum. It is important to notice that tapers realized in this way are asymmetrical, meaning that the slope of the diameter vs position curve

is different between the two transitions. As this slope has an influence on the confinement losses when light moves from the large core area to the waist, the propagation properties in these tapers are different depending on which end is chosen as the input one.
Another important matter to be considered is the fact that not all glass compositions are suitable for tapering. As an example, $As_{38}Se_{62}$ has been proven in [40] to have a too low thermal stability to tolerate a second heating without quenching after the fiber drawing process. Heating $As_{38}Se_{62}$ fibers results indeed in an irreversible loss of transmittance, probably due to partial crystallization. In the same paper, $Ge_{10}As_{22}Se_{68}$ has been shown to not exhibit this behavior, and all the germanium-containing compositions tested in the present work showed the possibility of obtaining tapers without noticeable increase in optical losses. The composition with less germanium content, $Ge_5As_{30}Se_{65}$, has yet to be tested in this regard.
The capabilities of the compositions produced during the development of this thesis, both in terms of being suitable for molding and of being thermally stable enough for tapering, are summarized in Table 3.2, along with some important properties already described in Chapter 2.

Table 3.2: *Summary of the characteristics of the different attempted compositions. (*: it's been proven to be possible, but often the process fails).*

Composition	$As_{38}Se_{62}$	$Ge_5As_{25}Se_{70}$	$Ge_5As_{30}Se_{65}$	$Ge_{10}As_{22}Se_{68}$	$Ge_{16}As_{20}Se_{64}$	$Ge_{22}As_{20}Se_{58}$
T_g(°C, ±2°C)	165	139	165	175	235	292
Average coordination number	2.38	2.35	2.40	2.42	2.52	2.64
Refractive index @1.55 μm	2.808	-	2.704	2.618	2.579	2.542
Possibility to obtain MOFs by molding	Yes	-	Yes	Yes	Scarce*	No
Possibility to obtain tapers from MOFs	No	-	-	Yes	Yes	-

3.3 Power damage threshold measurements in chalcogenide index-guiding PCFs

As already mentioned in this chapter, one of the main drawbacks in using chalcogenide index-guiding photonic crystal fibers for nonlinear applications is their low power damage threshold. This was one of the reasons for which an attempt was done to increase the germanium content in the glass compositions developed during this thesis. In order to verify the influence of glass composition on the power handling capabilities of chalcogenide fibers, a set of measurements was performed in collaboration with the FEMTO-ST institute in Besançon, one of the academic members of the SUPUVIR consortium. Those measurements, consisting in looking at the evolution of the output power from a length of fiber when increasing the input power, or over time with fixed input power, will be described, and their results discussed, in this section.

3.3.1 Fibers used for testing

For these measurements, index-guiding PCFs with three hexagonal rings of holes arranged in a triangular lattice were used.
Regarding the glass composition, $Ge_{10}As_{22}Se_{68}$ and $Ge_{16}As_{20}Se_{64}$ were chosen between the ones developed during this work, being the two with the highest germanium content for which molding was possible, together with $Ge_{14}As_{20}Se_{66}$, a composition used from Selenoptics. $As_{38}Se_{62}$ was tested as well, to have a comparison between glasses with and without germanium in the composition. The geometrical features of the fibers drawn for these experiments, one for each composition, can be found in Table 3.3.

Table 3.3: *Characteristics of different index-guiding PCFs used for testing power handling capabilities.*

Composition	Core diameter (μm)	$\frac{d}{\Lambda}$	Attenuation at 1750 nm	Attenuation at 2100 nm
$As_{38}Se_{62}$	11.2	0.49	$\sim$ 2.5 dB/m	$\sim$ 2 dB/m
$Ge_{10}As_{22}Se_{68}$	11.0	0.47	$\sim$ 2 dB/m	$\sim$ 1.2 dB/m
$Ge_{14}As_{20}Se_{66}$	11.1	0.50	$\sim$ 6.5 dB/m	$\sim$ 5 dB/m
$Ge_{16}As_{20}Se_{64}$	11.1	0.49	$\sim$ 6.5 dB/m	$\sim$ 5 dB/m

It has to be noticed here that the $\frac{d}{\Lambda}$ ratio is >0.4 for all the fibers, meaning that they are not endlessly single mode. Indeed, as visible in Figure 3.15, at least the LP_{01} and LP_{11} are present at 1.75 μm. This makes it important, in order to have a proper comparison between the measurements, to be sure to always excite the same mode. The fundamental mode was chosen as the one to be used for the testing of power handling, being the only one present in the mid-IR, the spectral region for applications in which these fiber are usually utilized.

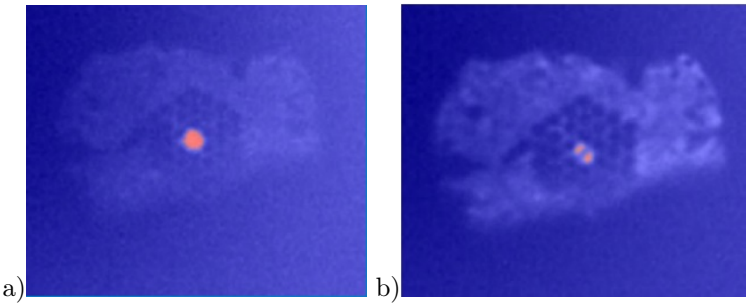

Figure 3.15: LP_{01} *(a) and* LP_{11} *(b) modes excited at 1750 nm in one of the tested fibers.*

As visible in Figure 3.16, the measured fibers have quite different attenuation spectra. This, however, is probably due to scattering rather than to absorption, and as such it shouldn't affect the thermal load put on the fibers by injecting light into them. Indeed, the power handling properties are related to absorption, which we expect to be similar between the fibers. The estimated optical losses of the fibers at the wavelengths used for measuring are reported in Table 3.3 as well. The degree of approximation on this values is quite high, due to the low sensitivity of the detector used for collecting the spectra at wavelengths <2.5 μm.

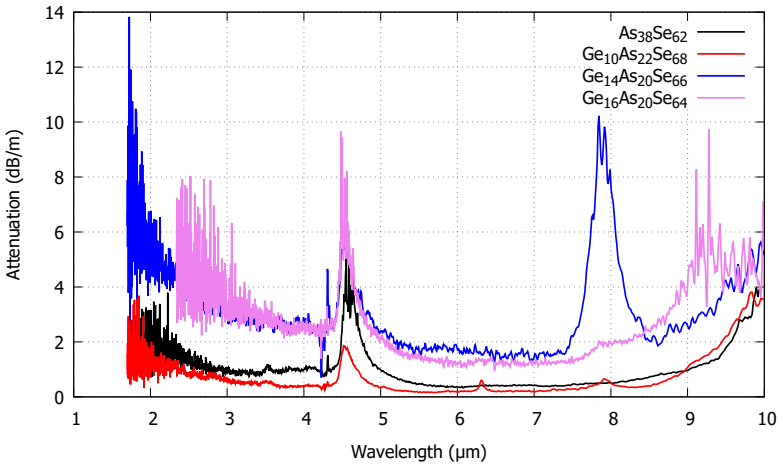

Figure 3.16: *Attenuation spectra of the different fibers whose power handling capability was tested.*

3.3.2 Experimental setup

The experimental setup for measuring the power damage threshold and handling capacity of chalcogenide index-guiding PCFs is shown in Figure 3.17. As a pump laser, a 200-fs optical parametric oscillator (Chameleon Compact OPO-Vis), pumped by a Ti-Sapphire mode-locked laser (Chameleon Ultra II) at an 80 MHz repetition rate, was used. The signal of the OPO is tunable in the range 1–1.6 μm, with mean output powers between 230 mW and 1 W, and the idler can produce wavelengths from 1.7 μm to 4 μm with powers from 90 to 250 mW. In order to match the transmission range of the fibers to be tested, the idler was used for the measurements described in this section. However, the idler maximum power is wavelength-dependent, and for wavelengths longer than 2100 nm it was not sufficient to study the power handling properties of the fibers. 1750 nm and 2100 nm where thus chosen as wavelengths for performing the experiment. It is important to notice here that in this range chalcogenide glasses have high linear and nonlinear absorption coefficients. The performance of the tested fibers in terms of power handling is expected to be significantly better in the mid infrared.
The light was injected into the PCFs through an infrared focusing objective, and its intensity was controlled via a variable attenuator. The input power was measured with a Thorlabs thermal power meter (operating range: 1-10 μm) placed after the attenuator, while the output power was measured with a Thorlabs S132c Ge photodiode with an operating spectral range from 700 to 1800 nm or with a Thorlabs thermal power meter S401C (operating range 0.2 μm-10.6 μm), depending on the wavelength. The coupling efficiency was calculated, knowing in advance the intrinsic attenuation of each fiber, from the ratio between output power and input power.
Before every set of measurements, the detector at the output was substituted with an imaging system composed by an IR camera, wavelength filters and a focusing objective, in order to verify that light was well coupled in the core and that the fundamental mode was excited.

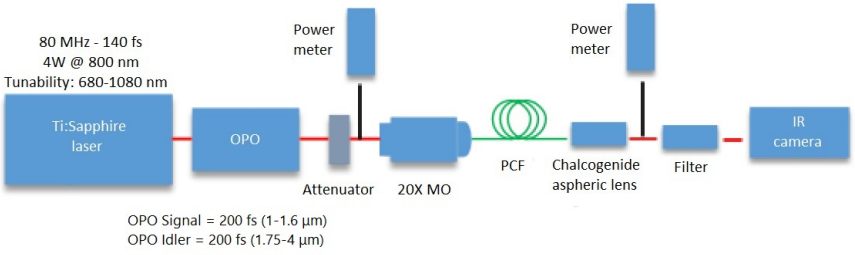

Figure 3.17: *Schematics of the experimental setup used for measuring the power damage threshold and handling capacity of chalcogenide index-guiding PCFs.*

3.3.3 Power handling behavior of the different compositions

Despite the pulse energy delivered by the used lasing setup being relatively low due to the high repetition rate (a few nJ only), the maximum pulse peak power could reach up to 15 kW, leading to a high optical intensity up to several tens of GW/cm^2 in the fiber core with μm-scale radius. This high optical intensity, combined with a high repetition rate, can lead to laser-induced damage of chalcogenide index-guiding PCFs, due to a number of thermal effects (thermally induced stress, fatigue effects, cumulative pulse effects, melting, to cite a few) caused by the local increase in temperature created by linear, nonlinear and free carrier absorption.
The first series of measurements, whose results are shown in Figure 3.19, consisted in observing the response in terms of output power of the fibers to an increasing input power. It was noticed during the experiments that the idler wasn't stable in power, and that spikes could be observed from time to time. For this reason, the error on the obtained data should be regarded as quite large. Nonetheless, the accuracy has been deemed sufficient, with the number of points collected, for deriving at least trends in the fibers' behavior.
Due to the beam quality of the idler output, which is dependent on the wavelength, and to the not reproducible cleaving, for the same laser power the amount P_c of power coupled in the core of the fiber was different for every sample. However, given that the attenuation coefficient in dB/m

α and the length l of the fibers are known, it is possible to estimate a coupling efficiency using the measured input and output powers P_{in} and P_{out}. The percentage coupling efficiency is defined as

$$C_{\%} = \frac{100 \cdot P_{out}}{(1 - R_F)P_{in}} 10^{\frac{\alpha l}{10}}$$

and was calculated for each measured fiber using the lowest input power, in order to avoid power damage effects to affect the value. The factor $(1 - R_F)$ takes into account the Fresnel reflection at the output of the fiber ($R_F = \frac{(n-1)^2}{(n+1)^2}$) (see Figure 3.18).

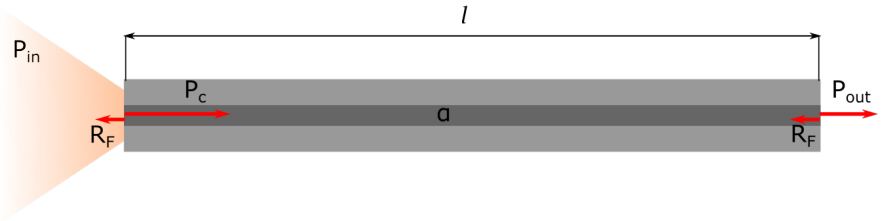

Figure 3.18: *Schematization of the coupling model used to estimate* $C_{\%}$.

Once the coupling efficiency was calculated, the input end of the fiber was kept fixed. The lengths of the fibers used for the measurements performed, together with their estimated coupling efficiency, are reported in Table 3.4. The values of $C_{\%}$ were then used as a conversion factor to obtain the coupled input power from the measured values of P_{in}.

Table 3.4: *Coupling efficiency for the different sets of measurements here reported.*

Composition	Wavelength (nm)	Length (m)	Estimated $C_{\%}$
$As_{38}Se_{62}$	1750	0.47	37%
	2100	0.44	20%
$Ge_{10}As_{22}Se_{68}$	1750	0.25	22%
	2100	0.24	17%
$Ge_{14}As_{20}Se_{66}$	1750	0.65	50%
	2100	0.59	26%
$Ge_{16}As_{20}Se_{64}$	1750	0.45	40%
	2100	0.43	22%

In order to minimize the effects due to accumulation of damage in the fiber, a beam stopper was put in place while the power of the idler was regulated, and light was injected in the fiber for just enough time to have a reading of P_{out}. Due to generally worse coupling and lower power of the idler, it was not possible to reach values of coupled input power at 2100 nm as high as the ones reached at 1750 nm. From the collected data, a common trend seems to appear for all fibers: up to a certain value of coupled input power, for both the studied wavelengths the output grows linearly. After this value, which can be defined as the power damage threshold for 1750 nm, the slope of the data series collected at 2100 nm wavelength is preserved, while the one of the shorter wavelength series is visibly reduced. This change in slope seems to happen at 15-20 mW of coupled power input for $As_{38}Se_{62}$, at about 20 mW for $Ge_{10}As_{22}Se_{68}$, at 25-30 mW for $Ge_{14}As_{20}Se_{66}$ and at $\sim$ 40 mW for $Ge_{16}As_{20}Se_{64}$, suggesting that the increase of germanium content in the composition might improve the power handling capabilities at short wavelengths in these fibers. For all samples, the damage seems to happen in the part of the fiber near to the input end, as the original slope is found again by removing a few centimeters of fiber on that side.

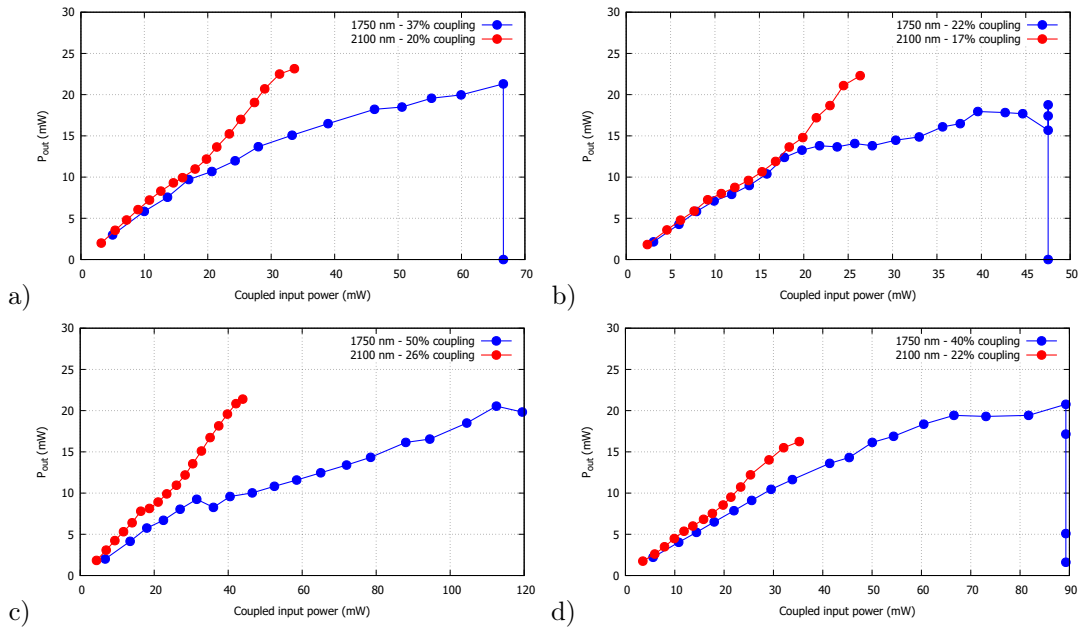

Figure 3.19: *Output power plotted against the estimated input power coupled into the core for* $As_{38}Se_{62}$ *(a),* $Ge_{10}As_{22}Se_{68}$ *(b),* $Ge_{14}As_{20}Se_{66}$ *(c),* $Ge_{16}As_{20}Se_{64}$ *(d).*

The power of the source wasn't sufficient to observe any permanent slope change at 2100 nm, but it is clear that such a change, if present, would be at higher input powers that the one at 1750 nm. This is consistent with the attenuation data, that suggest significantly higher bandgap-related absorption, and thus more thermal load, at 1750 nm with respect to 2100 nm. Two photons absorption, which might be enabled by the relatively high peak power of the pulses used, is also more significant at wavelengths closer to the bandgap.
For all fibers, apart from the one obtained from $Ge_{14}As_{20}Se_{66}$, a sharp fall of output power over a few seconds can be observed when an high enough value of P_c is reached. Checking the input fiber ends with a fiberscope after this phenomenon has happened, the cleave looked completely melted and the holes closed. This suggests that the whole power reaching the surface is involved, not only the part of it coupled into the core. Indeed, while there is apparently no trend relating the coupled input power to the amount of germanium in the composition, when comparing the values of P_{in} for which the fiber burns a clear distinction can be observed between $As_{38}Se_{62}$ (< 180 mW) and germanium containing compositions (>210 mW). Due to the sources of error mentioned before, a comparison between the compositions containing germanium would not be reliable. The results concerning the estimation of the power damage threshold and the power at which the fiber face is burnt are summarized in table 3.5.

Table 3.5: *Estimation of the power at which the slope of the* P_{out} *vs* P_c *curve changes slope (damage threshold) and power at which the fiber face is burnt (burning power) for the different fibers injected with 1750 nm light.*

Composition	**Damage threshold (mW)**	**Burning power (mW)**	
		Coupled	**Total**
$As_{38}Se_{62}$	15-20	67	180
$Ge_{10}As_{22}Se_{68}$	~ 20	47	216
$Ge_{14}As_{20}Se_{66}$	25-30	>120	>230
$Ge_{16}As_{20}Se_{64}$	~ 40	90	223

In order to better understand the phenomena occurring, a study of the accumulation in time of the damage under prolonged exposure to the laser was performed for all the compositions.
At 1750 nm of wavelength, no variation in output power over time was registered for coupled input

powers lower than the damage threshold defined above. For higher powers, however, a considerable decrease can be observed over the span of few minutes, as visible in Figure 3.20. This suggests that the change in slope could be due at least partially to the cumulative effect of the power absorbed while collecting the points, despite the precautions taken to avoid it. Stopping the beam after these measurements to give the fibers time to cool down and then injecting light again, without modifying the input power, reveals that the loss in transmittance is partially reversible. However, even after waiting more than two hours, only a percentage of the initial output is retrieved, meaning that some permanent damage was induced in the fiber.
At 2100 nm of wavelength, no change over time in the value of P_{out} was registered independently on the amount of coupled input power, result in good accordance with the lack of permanent change in slope of the P_{out} vs P_c plot.

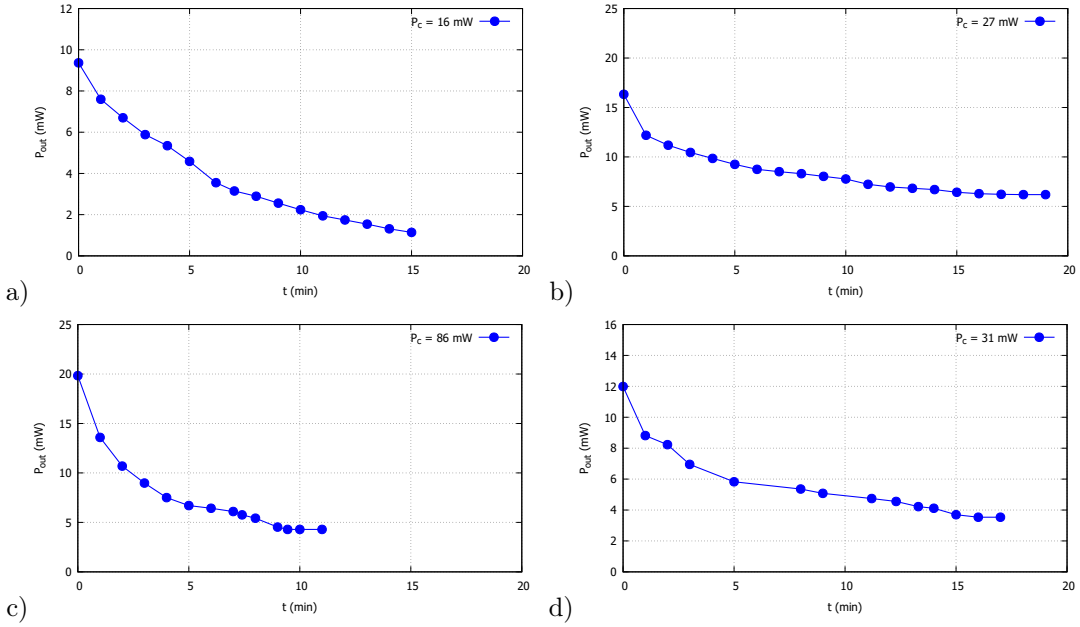

Figure 3.20: *Output power plotted against time, at wavelength of 1750 nm and fixed input power, for* $As_{38}Se_{62}$ *(a),* $Ge_{10}As_{22}Se_{68}$ *(b),* $Ge_{14}As_{20}Se_{66}$ *(c),* $Ge_{16}As_{20}Se_{64}$ *(d).*

The $Ge_{10}As_{22}Se_{68}$ fiber, which for unknown reasons showed a worse coupling efficiency with respect to the other ones and unclear results, will need to be tested again in the future in order to correctly estimate its damage threshold. In addition to this, further measurements will be needed to have a clear understanding of the physical origin of the difference in power handling behavior between the different compositions. On this regard, the better properties exhibited by the fibers with higher scattering losses seem to confirm that the presence of particles inside the glass doesn't significantly affect the amount power-related damage experienced by fibers.

3.4 Experimental results of supercontinuum generation

In this section, some examples of supercontinua in the mid-infrared that were generated in chalcogenide index-guiding PCFs produced during the development of this thesis are presented.

3.4.1 Supercontinuum generation in a chalcogenide polarization maintaining index-guiding PCF

Chalcogenide fibers are an highly suitable platform for supercontinuum generation in the mid infrared spectral range, which is of interest for many applications, thanks to a number of properties that were already thoroughly described in this work. At the same time, supercontinuum generation

in fibers with polarization-preserving properties can enable polarization-dependent applications in interferometric techniques, gas and pressure sensing, integrated-optic devices and polarization-sensitive OCT [51–56]. In addition to this, polarization-maintaining fibers help in minimizing detrimental effects such as polarization noise and instability [57]. All of these reasons make the generation of mid-infrared supercontinuum in chalcogenide polarization-maintaining index-guiding PCFs a very desirable result, which might be applied to a number of fields.
An attempt to achieve it was performed as a collaboration between the University of Rennes 1, the FEMTO-ST institute and the Technical University of Denmark. All of these institutions are academic members of the SUPUVIR consortium. The results reported in this section were published in 2019 in [50].

3.4.1.1 Experimental setup

Figure 3.21 outlines the experimental setup for mid-IR pumping of the chalcogenide-based PM-PCF and measuring the output SC infrared light. The experiment was performed at the Technical University of Denmark.

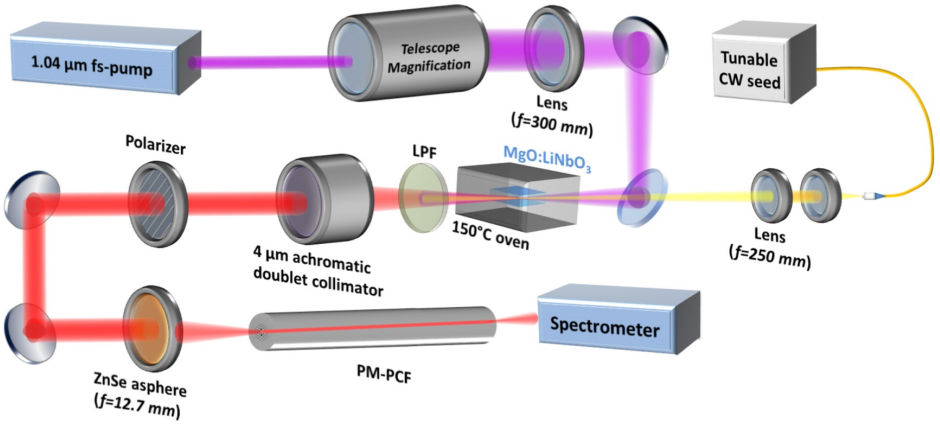

Figure 3.21: *Schematics of the experimental setup used for supercontinuum generation in a chalcogenide polarization maintaining index-guiding PCF [8].*

A 10 mm periodically-poled fan-out MgO:$LiNbO_3$ crystal (MgO:PPLN) was used to generate the mid-IR pump through a single-pass parametric generation process. The nonlinear crystal was pumped by a continuous-wave (CW) seed laser (tunable from 1350 to 1450 nm) along with a 1.04 μm mode-locked Yb:KYW solid-state laser (having a full width at half maximum pulse duration of 250 fs at 21 MHz repetition rate) to stimulate quasi phase-matched parametric anti-Stokes generation. The phase-matching relation was achieved by selecting the appropriate poling period of the fan-out structure using a linear translation stage, and the crystal was kept in an oven at a constant temperature of 150°C to avoid photorefraction. The combination of tunable seed and tunable poling period of the crystal provided a tunable MIR output between 3.7 μm and 4.53 μm whose spectrum corresponds to a 252 fs transform limited pulse train at 4 μm. A reflective long pass filter (LPF) was used after the crystal system in order to eliminate any residual pump and other radiation below 3.5 μm. The mid-IR output beam was then collimated by an achromatic air-space lens doublet, which is optimized for a central wavelength of 4 μm and anti-reflection (AR) coated for the 3–5 μm range. This was injected into the polarization maintaining index-guiding PCF (PM-PCF) through an AR coated ZnSe aspheric lens with a focal length of 12 mm and the coupling power was controlled by rotating a wire grid polarizer relative to the linear polarization of the pump. The generated SC bandwidth was measured using a FTIR from 3 to 10 μm and a monochromator-based spectrometer from 1 to 5 μm. The output power was measured with a thermal power meter. The fiber used was the one described in Section 3.2.4.2, where all its relevant features regarding geometrical parameters and attenuation can be found.

3.4.1.2 Obtained results

The dispersion and birefringence properties of the fiber were simulated in the spectral range between 1.5 and 6.5 μm (see Figure 3.22), using the finite elements method. The fiber cross-section used to perform these simulations was directly taken from a scanning electron microscopy image of the fiber, in order to ensure maximum fidelity. Being the fiber single mode in the mid infrared, all simulations were performed for the LP_{01} mode only. Two dispersion curves were calculated for the fiber, corresponding to the cases of the light polarization being aligned with the slow axis (x-polarization) or with the fast axis (y-polarization). The terms slow axis and fast axis refer to the orthogonal axes of the fiber showing respectively the maximum and minimum values of n_{eff} when the light polarization is aligned with them. The values of ZDW extracted from these simulations are of 4.56 μm for a y-polarized mode and of 4.68 μm for a x-polarized one. The birefringence $B(\lambda)$, defined as the difference in n_{eff} between the two considered polarizations, has, according to the simulations, a large value of $6.5 \cdot 10^{-4}$, and thus strong polarization maintaining properties are expected.

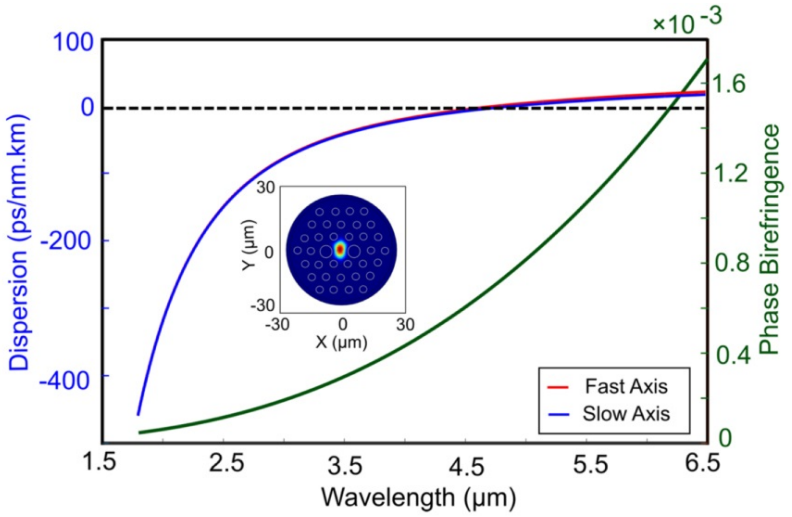

Figure 3.22: *Dispersion and birefringence characteristics of the* $As_{38}Se_{62}$ *PM-PCF simulated for the fundamental mode from SEM image. Blue and red curves: group velocity dispersion of the PM-PCF sample for different polarization axes. Inset: optical power density of the fundamental mode for the fast axis at a wavelength of 2* μm *inside the core of the fiber. Green curve: phase birefringence of the PM-PCF [50].*

Two different pump wavelengths were used for supercontinuum generation in 25 cm of PM-PCF: 4 μm and 4.53 μm. While the one closest in wavelength to the ZDW is theoretically the best one for obtaining a broad output spectrum, the system was able to deliver significantly most power at the shorter wavelength. Because of this, the broadest supercontinuum, spanning from 3.1 to 6.02 μm (at the -30 dB level) and with an output average power of 11 mW, was obtained by pumping the fiber at 4 μm with an average power of 135 mW.
Due to the birefringence of the fiber used, the bandwidth of the generated supercontinuum should, according to theory, be dependent on the polarization of the pump. In order to verify this effect, measurements were performed while rotating the input fiber, which amounts to turning the input pump polarization with respect to the principal axes of the PM fiber. The fiber angle was changed from 0° to 182° with 10° steps, while maintaining a constant input power of 62 mW at 4.53 μm and a constant output power of 3.8 mW. The results of this measurement are presented in Figure 3.23.a .
The polarization dependence of nonlinear pulse propagation and supercontinuum generation in the highly-birefringent PM-PCF was also modeled using a two-polarizations code based on two coupled generalized nonlinear Schrödinger equations (CGNLSE). The calculated results show a polarization dependence of the supercontinuum bandwidth with an angular periodicity of around 90°, and less

SC broadening when pumping off axis, with a minimum at 45°. As shown in Figure 3.23.b, these results are in good agreement with the experimental ones.

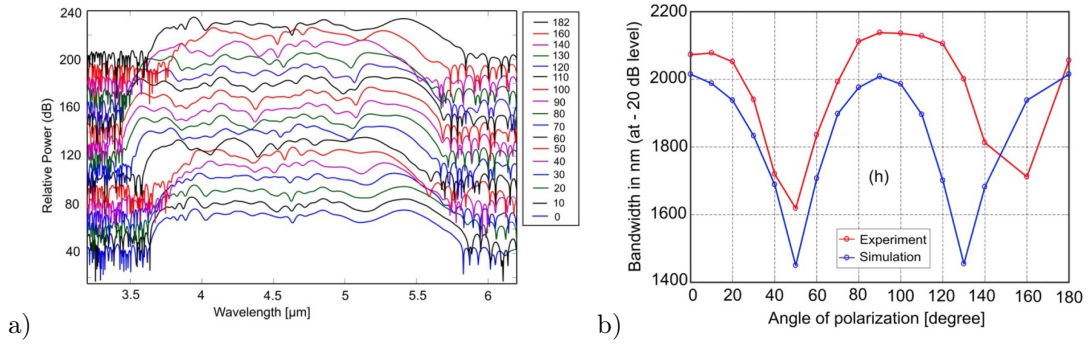

Figure 3.23: *(a) Dependency of SC spectra on the incident angle of polarization from 0° to 182° for pumping at 4.53 μm; (b)Comparison of bandwidth (at -20 dB level) between experimental (red) and simulated (blue) SC spectra at different polarization angle for 4.53 μm pumping [50].*

3.4.2 Generation of supercontinuum by cascaded pumping

Cascaded pumping schemes for generating supercontinua in chalcogenide fibers have been already demonstrated to be effective in the recent past [18]. Starting from this concept, two companies in the SUPUVIR consortium (Leukos and Selenoptics) recently partnered with Le Verre Fluoré, one of the leading companies in the production of fluoride fibers, to develop a compact mid infrared supercontinuum source. The preliminary results of this effort, as well as a possible application, will be presented below.

3.4.2.1 Setup for the supercontinuum generation

The setup for the generation of supercontinuum by cascaded pumping is schematized in Figure 3.24. As a seeding source, a laser operating at 1.55 μm has been chosen. This laser provides 750 mW of average power in the form of 500 ps pulses, with a pulse energy of 8.5 nJ and a peak power of 18 kW. The repetition rate, tunable between 90 and 140 kHz, has been fixed at 100 kHz for the experiment here reported. The output of the laser is fed to the first step of spectral broadening through a 20 cm length of commercially available SMF 28 silica fiber.

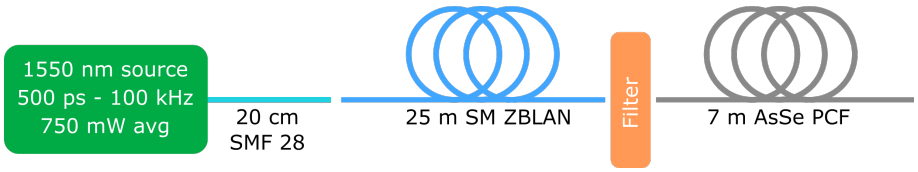

Figure 3.24: *Schematics of the cascaded pumping setup for mid infrared supercontinuum generation.*

The first nonlinear phenomena in the cascading scheme take place in a ZBLAN fluoride step-index fiber, with an external diameter of 125 μm and a core diameter of 8.5 μm. The reported optical losses are of less than 0.06 dB/m over the transparency window. A fiber length of 25 m has been selected for this stage. The fiber's ZDW, namely 1525 nm, is well matched with the wavelength of the seed source, and at its output a supercontinuum extending from about 0.75 to more than 4 μm can be observed (see Figure 3.25). Not all of this bandwidth, however, is suitable to be used for pumping the successive stage of the system. The transparency window of the chalcogenide fiber used for further broadening of the spectrum is strongly shifted towards the mid infrared with respect to the one of the ZBLAN fiber. Therefore, light in the visible and near infrared would not only be lost because of the high optical losses, but would also damage the fiber due to

absorption-related thermal load (see Section 3.3). To avoid this problem, the shortest wavelengths in the output spectrum of the ZBLAN fiber are filtered out before injection in the last step of the cascading.

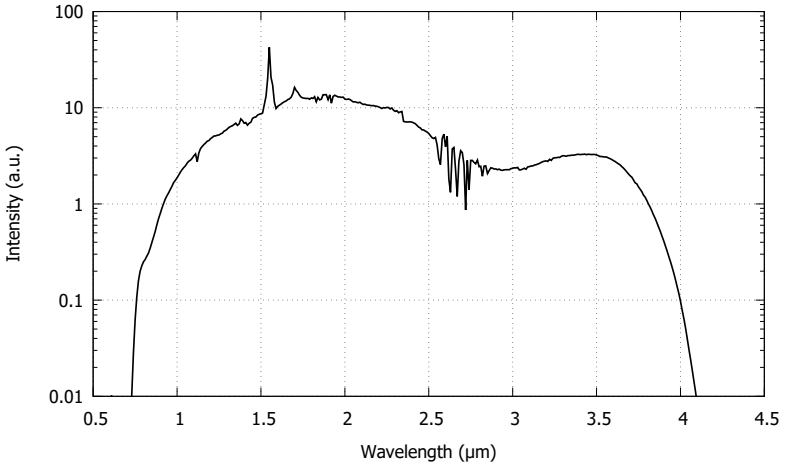

Figure 3.25: *Spectrum at the output of the ZBLAN single mode fiber.*

To extend the spectral range of the supercontinuum further in the mid-IR, a 7 m length of highly nonlinear $As_{38}Se_{62}$ index-guiding PCF has been utilized. This fiber, produced using the molding technique, has a core diameter of 11.2 μm and an external diameter of 125 μm. A $\frac{d}{\Lambda}$ value of 0.454 guarantees the fiber to be single mode over the whole mid infrared range. The optical losses of the fiber are of less than 1 dB/m over the 2-9.3 μm range, with a low intensity absorption peak related to impurities at 4.5 μm, as visible in Figure 3.26.

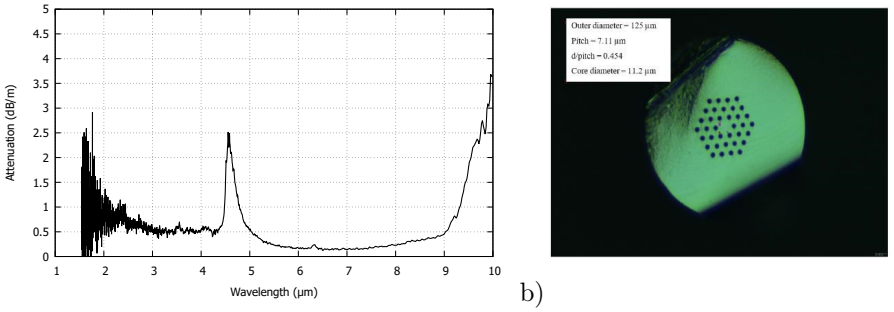

a) b)

Figure 3.26: *Attenuation spectrum (a) and cross-sectional microscope image (b) of the* $As_{38}Se_{62}$ *fiber used for the last stage of cascaded supercontinuum generation.*

The dispersion curve of this index-guiding PCF has been simulated, obtaining a calculated value of about 4.8 μm for its ZDW. Comparing this value with the output spectrum of the ZBLAN fiber, the pumping from the previous step results to happen completely in normal dispersion regime. At the output of the chalcogenide fiber, a broad supercontinuum spanning from 2 to 10 μm has been registered, as visible in Figure 3.27, with an average output power of 15 mW.
As of now, no supercontinuum sources reaching so far in the mid infrared can be found on the market. Indeed, black body radiation sources and synchrotrons are the only available solutions for broadband light in this spectral range. Thanks to their high compactness, brightness and spatial coherence, as well as to the versatility of use typical of fibers, sources as the one here presented can enable progress in many fields, such as spectroscopy, remote sensing, microscopy and tomography, to name a few.

An experimental demonstration of a possible application for the detection of organic molecules with spectroscopic fingerprints in the mid infrared is reported in the next section.

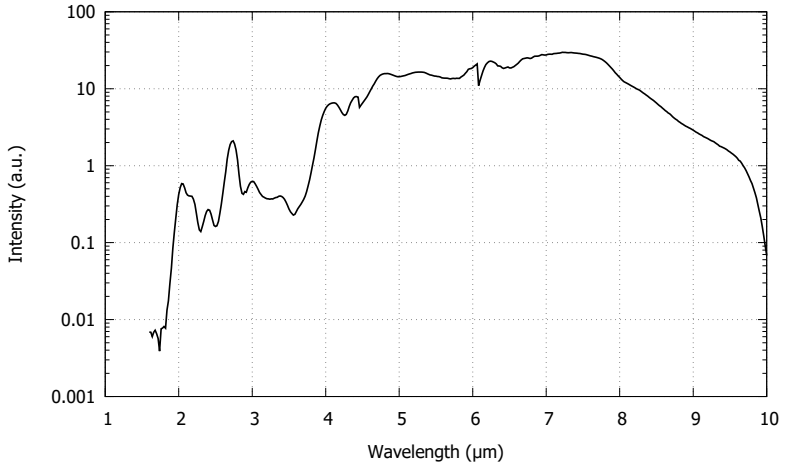

Figure 3.27: *Spectrum at the output of the chalcogenide index-guiding PCF.*

3.4.2.2 Application to mid-infrared spectroscopy

To verify the suitability of the presented prototype for spectroscopic measurements, a setup was realized as schematized in Figure 3.28.

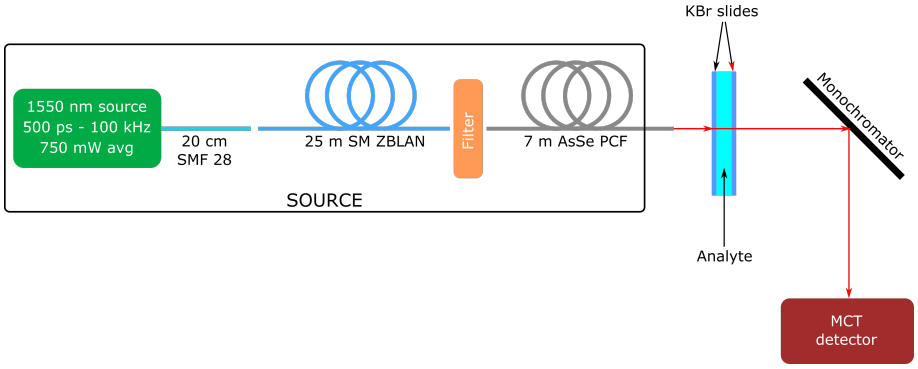

Figure 3.28: *Schematics of the spectrometer built using the cascaded ZBLAN-*$As_{38}Se_{62}$ *supercontinuum source.*

The cascaded supercontinuum source described in Section 3.4.2.1 was used to provide broad spectrum, high brilliance mid infrared light. After passing through a thin layer of liquid analyte placed between two slides of KBr glass, the light was diffracted by a motorized rotating diffraction grating used as monochromator. A MCT detector was used to collect the resulting signal while the monochromator scanned, with a step of 0.02 μm, through the whole supercontinuum spectrum.
In order to test this setup, methyl salicylate was selected as an analyte. This choice is justified by the mid infrared spectrum of this substance, which is rich in features between 5 and 10 μm, the wavelengths in which this source differentiates itself from the other commercially available ones. At first, a reference spectrum was recorded without any liquid between the KBr slides. Then, a second spectrum was collected with the presence of the analyte. The optical density spectra presented in Figure 3.29 were finally obtained by taking the base 10 logarithm of the ratio between the reference spectrum and the second one.
The reliability the obtained results was verified by comparing the position the peaks in the measured optical density with the tabulated transmission data found in [58]. Looking at Figure 3.29.a,b,

a resemblance in shape between the measured and registered spectra can be seen. However, the positions of the peaks appear to be slightly shifted. Supposing that the reason could a problem with the alignment of the monochromator, an attempt was done to apply a correction, shifting or multiplying by a constant the values on the x axis. Indeed, multiplying the wavenumber in the measured data by 0.988 results in a match between the spectra. The presence of a multiplicative constant suggests the problem to be an error, in the order of magnitude of 1%, in the step size of the monochromator.

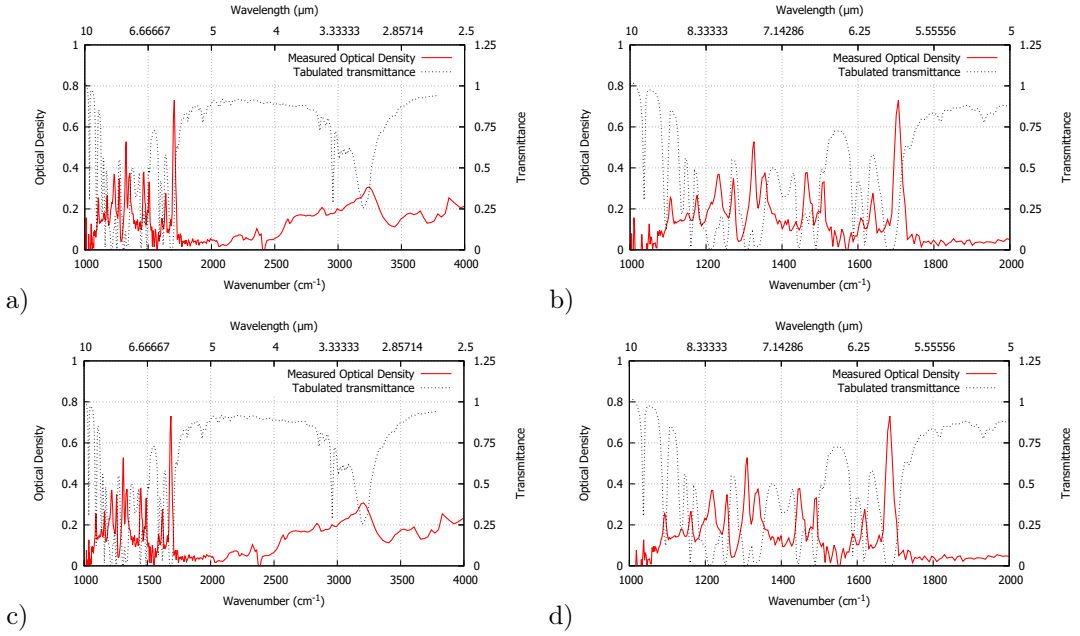

Figure 3.29: *Optical density of methyl salicylate measured using the cascaded ZBLAN-$As_{38}Se_{62}$ SC source, compared with the transmittance tabulated data from [58] (a) and a zoom on the interested area (b). In (c) and (d) the same comparison after applying a correction to the measured data to compensate a small error in the monochromator's step size.*

3.5 Conclusions

In this chapter, the main characteristics of chalcogenide index-guiding PCFs have been described, showing that they are an highly interesting conversion medium to be used for mid infrared supercontinuum generation. The different possible techniques which can be used for their fabrication have also been detailed, with a particular focus on molding, which is the one used for producing fibers during the development of this thesis. Some direct applications of the produced fibers have been shown, between which are notably present the prototype of the first commercial compact supercontinuum source reaching a wavelength of 10 μm and the demonstration of its suitability for spectroscopic applications in the mid-IR.

Bibliography

[1] Johann Troles, Laurent Brilland, Celine Caillaud, and Jean-Luc Adam. "Original designs of chalcogenide microstuctured optical fibers". In: *Advanced Device Materials* 3.1 (2017), pp. 7–13.

[2] James A Savage. "Optical properties of chalcogenide glasses". In: *Journal of Non-Crystalline Solids* 47.1 (1982), pp. 101–115.

[3] GE Snopatin, VS Shiryaev, VG Plotnichenko, EM Dianov, and MF Churbanov. "High-purity chalcogenide glasses for fiber optics". In: *Inorganic materials* 45.13 (2009), p. 1439.

[4] MF Churbanov. "High-purity chalcogenide glasses as materials for fiber optics". In: *Journal of non-crystalline solids* 184 (1995), pp. 25–29.

[5] Tim A Birks, Jonathan C Knight, and P St J Russell. "Endlessly single-mode photonic crystal fiber". In: *Optics letters* 22.13 (1997), pp. 961–963.

[6] Gilles Renversez, Frédéric Bordas, and Boris T Kuhlmey. "Second mode transition in microstructured optical fibers: determination of the critical geometrical parameter and study of the matrix refractive index and effects of cladding size". In: *Optics letters* 30.11 (2005), pp. 1264–1266.

[7] John Ballato, Heike Ebendorff-Heidepriem, Jiangbo Zhao, Laeticia Petit, and Johann Troles. "Glass and Process Development for the Next Generation of Optical Fibers: A Review". In: *Fibers* 5.1 (2017), p. 11.

[8] Christian Rosenberg Petersen, Rasmus D Engelsholm, Christos Markos, Laurent Brilland, Céline Caillaud, Johann Trolès, and Ole Bang. "Increased mid-infrared supercontinuum bandwidth and average power by tapering large-mode-area chalcogenide photonic crystal fibers". In: *Optics express* 25.13 (2017), pp. 15336–15348.

[9] Johann Troles, Laurent Brilland, Frédéric Smektala, P Houizot, Frédéric Désévédavy, Quentin Coulombier, N Traynor, Thierry Chartier, Thanh Nam Nguyen, Jean-Luc Adam, et al. "Chalcogenide microstructured fibers for infrared systems, elaboration modelization, and characterization". In: *Fiber and Integrated Optics* 28.1 (2009), pp. 11–26.

[10] Frederic Zolla, Gilles Renversez, and Andre Nicolet. *Foundations of photonic crystal fibres, 2nd edition*. Imperial College Press, 2012.

[11] Mohammed El-Amraoui, Julien Fatome, Jean-Charles Jules, Bertrand Kibler, Grégory Gadret, Coraline Fortier, Frédéric Smektala, Igor Skripatchev, CF Polacchini, Younes Messaddeq, et al. "Strong infrared spectral broadening in low-loss As-S chalcogenide suspended core microstructured optical fibers". In: *Optics express* 18.5 (2010), pp. 4547–4556.

[12] Celine Caillaud, Clement Gilles, Laurent Provino, Laurent Brilland, Thierry Jouan, Simon Ferre, Mathieu Carras, Mickael Brun, David Mechin, Jean-Luc Adam, et al. "Highly birefringent chalcogenide optical fiber for polarization-maintaining in the 3-8.5 μm mid-IR window". In: *Optics express* 24.8 (2016), pp. 7977–7986.

[13] Darren D Hudson, Sergei Antipov, Lizhu Li, Imtiaz Alamgir, Tomonori Hu, Mohammed El Amraoui, Younes Messaddeq, Martin Rochette, Stuart D Jackson, and Alexander Fuerbach. "Toward all-fiber supercontinuum spanning the mid-infrared". In: *Optica* 4.10 (2017), pp. 1163–1166.

[14] Dinghuan Deng, Lai Liu, Tong Hoang Tuan, Yasuhiro Kanou, Morio Matsumoto, Hiroshige Tezuka, Takenobu Suzuki, and Yasutake Ohishi. "Mid-infrared supercontinuum covering 3–10 μm using a As2Se3 core and As2S5 cladding step-index chalcogenide fiber". In: *Journal of the Ceramic Society of Japan* 124.1 (2016), pp. 103–105.

[15] O Mouawad, J Picot-Clémente, F Amrani, C Strutynski, J Fatome, B Kibler, F Désévédavy, G Gadret, J-C Jules, D Deng, et al. "Multioctave midinfrared supercontinuum generation in suspended-core chalcogenide fibers". In: *Optics letters* 39.9 (2014), pp. 2684–2687.

[16] Weiqing Gao, Mohammed El Amraoui, Meisong Liao, Hiroyasu Kawashima, Zhongchao Duan, Dinghuan Deng, Tonglei Cheng, Takenobu Suzuki, Younès Messaddeq, and Yasutake Ohishi. "Mid-infrared supercontinuum generation in a suspended-core As 2 S 3 chalcogenide microstructured optical fiber". In: *Optics express* 21.8 (2013), pp. 9573–9583.

[17] Jas S Sanghera, Leslie B Shaw, Paul Pureza, Vinh Q Nguyen, Dan Gibson, Lynda Busse, Ishwar D Aggarwal, Catalin M Florea, and Frederic H Kung. "Nonlinear properties of chalcogenide glass fibers". In: *International Journal of Applied Glass Science* 1.3 (2010), pp. 296–308.

[18] Christian Rosenberg Petersen, Peter M Moselund, Christian Petersen, Uffe Møller, and Ole Bang. "Spectral-temporal composition matters when cascading supercontinua into the mid-infrared". In: *Optics Express* 24.2 (2016), pp. 749–758.

[19] Arnaud Lemière, Frédéric Désévédavy, Bertrand Kibler, Pierre Mathey, Grégory Gadret, Jean-Charles Jules, Christophe Aquilina, Pierre Béjot, Franck Billard, Olivier Faucher, et al. "Mid-infrared two-octave spanning supercontinuum generation in a Ge–Se–Te glass suspended core fiber". In: *Laser Physics Letters* 16.7 (2019), p. 075402.

[20] Yuan Yuan, Kelun Xia, Yingying Wang, Zijun Liu, Nan Zhang, Jingxiang Su, Li Jiang, Peiqing Zhang, and Shixun Dai. "Precision fabrication of a four-hole Ge 15 Sb 15 Se 70 chalcogenide suspended-core fiber for generation of a 1.5–12 μm ultrabroad mid-infrared supercontinuum". In: *Optical Materials Express* 9.5 (2019), pp. 2196–2205.

[21] Tanya M Monro, Yvonne D West, Daniel W Hewak, NGR Broderick, and DJ Richardson. "Chalcogenide holey fibres". In: *Electronics Letters* 36.24 (2000), pp. 1998–2000.

[22] Laurent Brilland, Fréderic Smektala, Gilles Renversez, Thierry Chartier, Johan Troles, Thanh Nam Nguyen, Nicholas Traynor, and Achille Monteville. "Fabrication of complex structures of holey fibers in chalcogenide glass". In: *Optics Express* 14.3 (2006), pp. 1280–1285.

[23] Laurent Brilland, Johan Troles, Patrick Houizot, Frederic Desevedavy, Quentin Coulombier, Gills Renversez, Thierry Chartier, Thanh Nam Nguyen, Jean-Luc Adam, and Nicolas Traynor. "Interfaces impact on the transmission of chalcogenides photonic crystal fibres". In: *Journal of the Ceramic Society of Japan* 116.1358 (2008), pp. 1024–1027.

[24] M El-Amraoui, G Gadret, JC Jules, Julien Fatome, C Fortier, F Désévédavy, I Skripatchev, Younes Messaddeq, Johann Troles, L Brilland, et al. "Microstructured chalcogenide optical fibers from As 2 S 3 glass: Towards new IR broadband sources". In: *Optics express* 18.25 (2010), pp. 26655–26665.

[25] VV Ravi Kanth Kumar, AK George, WH Reeves, JC Knight, P St J Russell, FG Omenetto, and AJ Taylor. "Extruded soft glass photonic crystal fiber for ultrabroad supercontinuum generation". In: *Optics Express* 10.25 (2002), pp. 1520–1525.

[26] Heike Ebendorff-Heidepriem, Tze-Cheung Foo, Roger C Moore, Wenqi Zhang, Yahua Li, Tanya M Monro, Alexander Hemming, and David G Lancaster. "Fluoride glass microstructured optical fiber with large mode area and mid-infrared transmission". In: *Optics letters* 33.23 (2008), pp. 2861–2863.

[27] VV Ravi Kanth Kumar, AK George, JC Knight, and P St J Russell. "Tellurite photonic crystal fiber". In: *Optics Express* 11.20 (2003), pp. 2641–2645.

[28] Xian Feng, TM Monro, V Finazzi, RC Moore, K Frampton, P Petropoulos, and DJ Richardson. "Extruded singlemode, high-nonlinearity, tellurite glass holey fibre". In: *Electronics Letters* 41.15 (2005), pp. 835–837.

[29] Bo Wu, Zheming Zhao, Xunsi Wang, Youmei Tian, Nan Mi, Peng Chen, Zugang Xue, Zijun Liu, Peiqing Zhang, Xiang Shen, et al. "Mid-infrared supercontinuum generation in a suspended-core tellurium-based chalcogenide fiber". In: *Optical Materials Express* 8.5 (2018), pp. 1341–1348.

[30] Nian Si, Lihong Sun, Zheming Zhao, Xunsi Wang, Qingde Zhu, Peiqing Zhang, Shuo Liu, Zhanghao Pan, Zijun Liu, Shixun Dai, et al. "Supercontinuum generation and analysis in extruded suspended-core As 2 S 3 chalcogenide fibers". In: *Applied Physics A* 124.2 (2018), p. 171.

[31] Peiqing Zhang, Leilei Wang, Liang Zhu, Wenqiang Ma, Dandan Yang, Xunsi Wang, and Shixun Dai. "Mid-infrared gas detection using a chalcogenide suspended-core fiber". In: *Journal of Lightwave Technology* (2019).

[32] Xian Feng, Arshad K Mairaj, Daniel W Hewak, and Tanya M Monro. "Nonsilica glasses for holey fibers". In: *Journal of lightwave technology* 23.6 (2005), p. 2046.

[33] Yani Zhang, Kang Li, Lili Wang, Liyong Ren, Wei Zhao, Runcai Miao, Maryanne CJ Large, and Martijn A Van Eijkelenborg. "Casting preforms for microstructured polymer optical fibre fabrication". In: *Optics express* 14.12 (2006), pp. 5541–5547.

[34] Zhou Guiyao, Hou Zhiyun, Li Shuguang, and Hou Lantian. "Fabrication of glass photonic crystal fibers with a die-cast process". In: *Applied optics* 45.18 (2006), pp. 4433–4436.

[35] Quentin Coulombier, Laurent Brilland, Patrick Houizot, Thierry Chartier, Thanh Nam N'guyen, Frédéric Smektala, Gilles Renversez, Achille Monteville, David Méchin, Thierry Pain, et al. "Casting method for producing low-loss chalcogenide microstructured optical fibers". In: *Optics Express* 18.9 (2010), pp. 9107–9112.

[36] Johann Troles, Quentin Coulombier, G Canat, M Duhant, W Renard, Perrine Toupin, Laurent Calvez, Gilles Renversez, Frédéric Smektala, Mohamed El Amraoui, et al. "Low loss microstructured chalcogenide fibers for large non linear effects at 1995 nm". In: *Optics Express* 18.25 (2010), pp. 26647–26654.

[37] Jean-Luc Adam and Xianghua Zhang. *Chalcogenide glasses: preparation, properties and applications*. Woodhead publishing, 2014.

[38] Luc Thévenaz. *Advanced fiber optics*. EPFL press, 2011.

[39] Clément Conseil, Quentin Coulombier, Catherine Boussard-Plédel, Johann Troles, L Brilland, G Renversez, D Mechin, Bruno Bureau, Jean-Luc Adam, and Jacques Lucas. "Chalcogenide step index and microstructured single mode fibers". In: *Journal of Non-Crystalline Solids* 357.11-13 (2011), pp. 2480–2483.

[40] Perrine Toupin, Laurent Brilland, Johann Trolès, and Jean-Luc Adam. "Small core Ge-As-Se microstructured optical fiber with single-mode propagation and low optical losses". In: *Optical Materials Express* 2.10 (2012), pp. 1359–1366.

[41] Marcello Meneghetti, Celine Caillaud, Radwan Chahal, Elodie Galdo, Laurent Brilland, Jean-Luc Adam, and Johann Troles. "Purification of Ge-As-Se ternary glasses for the development of high quality microstructured optical fibers". In: *Journal of Non-Crystalline Solids* 503 (2019), pp. 84–88.

[42] Mathieu Rozé, Laurent Calvez, Joël Rollin, Patrick Gallais, Jacques Lonnoy, Sophie Ollivier, Marilyne Guilloux-Viry, and Xiang-Hua Zhang. "Optical properties of free arsenic and broadband infrared chalcogenide glass". In: *Applied Physics A* 98.1 (2010), p. 97.

[43] T Hosaka, K Okamoto, T Miya, Y Sasaki, and T Edahiro. "Low-loss single polarisation fibres with asymmetrical strain birefringence". In: *Electronics Letters* 17.15 (1981), pp. 530–531.

[44] RD Birch, David N Payne, and MP Varnham. "Fabrication of polarisation-maintaining fibres using gas-phase etching". In: *Electronics Letters* 18.24 (1982), pp. 1036–1038.

[45] Ro B Dyott, JR Cozens, and DG Morris. "Preservation of polarisation in optical-fibre waveguides with elliptical cores". In: *Electronics Letters* 15.13 (1979), pp. 380–382.

[46] Yang Yue, Guiyun Kai, Zhi Wang, Tingting Sun, Long Jin, Yunfei Lu, Chunshu Zhang, Jianguo Liu, Yan Li, Yange Liu, et al. "Highly birefringent elliptical-hole photonic crystal fiber with squeezed hexagonal lattice". In: *Optics letters* 32.5 (2007), pp. 469–471.

[47] A Ortigosa-Blanch, JC Knight, WJ Wadsworth, J Arriaga, BJ Mangan, TA Birks, and P St J Russell. "Highly birefringent photonic crystal fibers". In: *Optics letters* 25.18 (2000), pp. 1325–1327.

[48] Theis P Hansen, Jes Broeng, Stig EB Libori, Erik Knudsen, Anders Bjarklev, Jacob Riis Jensen, and Harald Simonsen. "Highly birefringent index-guiding photonic crystal fibers". In: *IEEE Photonics Technology Letters* 13.6 (2001), pp. 588–590.

[49] Masanori Koshiba and Kunimasa Saitoh. "Applicability of classical optical fiber theories to holey fibers". In: *Optics letters* 29.15 (2004), pp. 1739–1741.

[50] Amar Nath Ghosh, Marcello Meneghetti, Christian R Petersen, Ole Bang, Laurent Brilland, Sebastien Venck, Johann Troles, John M Dudley, and T Sylvestre. "Chalcogenide-glass polarization-maintaining photonic crystal fiber for mid-infrared supercontinuum generation". In: *Journal of Physics: Photonics* (2019).

[51] J Noda, K Okamoto, and I Yokohama. "Fiber devices using polarization-maintaining fibers". In: *Fiber & Integrated Optics* 6.4 (1987), pp. 309–329.

[52] Luc Thévenaz, Vincent de Coulon, and Jean-Pierre Von der Weid. "Polarization-mode interferometry in birefringent single-mode fibers". In: *Optics letters* 12.8 (1987), pp. 619–621.

[53] HY Fu, HY Tam, Li-Yang Shao, Xinyong Dong, PKA Wai, Chao Lu, and Sunil K Khijwania. "Pressure sensor realized with polarization-maintaining photonic crystal fiber-based Sagnac interferometer". In: *Applied optics* 47.15 (2008), pp. 2835–2839.

[54] Erich Götzinger, Bernhard Baumann, Michael Pircher, and Christoph K Hitzenberger. "Polarization maintaining fiber based ultra-high resolution spectral domain polarization sensitive optical coherence tomography". In: *Optics express* 17.25 (2009), pp. 22704–22717.

[55] Hui Wang, Muhammad K Al-Qaisi, and Taner Akkin. "Polarization-maintaining fiber based polarization-sensitive optical coherence tomography in spectral domain". In: *Optics letters* 35.2 (2010), pp. 154–156.

[56] Niels M Israelsen, Christian R Petersen, Ajanta Barh, Deepak Jain, Mikkel Jensen, Günther Hannesschläger, Peter Tidemand-Lichtenberg, Christian Pedersen, Adrian Podoleanu, and Ole Bang. "Real-time high-resolution mid-infrared optical coherence tomography". In: *Light: Science & Applications* 8.1 (2019), p. 11.

[57] Iván Bravo Gonzalo, Rasmus Dybbro Engelsholm, Mads Peter Sørensen, and Ole Bang. "Polarization noise places severe constraints on coherence of all-normal dispersion femtosecond supercontinuum generation". In: *Scientific reports* 8.1 (2018), p. 6579.

[58] National Institute of Standards and Technology. *Methyl salicylate*. URL: https://webbook.nist.gov/cgi/cbook.cgi?ID=C119368&Units=SI&Type=IR-SPEC&Index=1#IR-SPEC.

Chapter 4

Development of chalcogenide graded index fibers by stack and draw technique

The management of dispersion profile in fibers is of fundamental importance for supercontinuum generation. This general fact is especially true for chalcogenide fibers, due to the scarcity of available pumping systems at the long wavelengths where the ZDWs of these materials are. One quite common approach to address this problem is to use index-guiding PCFs as the ones described in the previous chapter of this work, which allow a higher degree of dispersion shaping with respect to step index fibers.
Another well known possibility for the engineering of the dispersion profile, as well as of mode area, modal loss and intermodal dispersion, is using graded index fibers [1]. The modified chemical vapor deposition technique used for producing the commercially available silica graded index (Grin) fibers, however, is not compatible with chalcogenide glasses. On the other side, other common techniques, such as ion exchange or controlled crystallization, do not have the same flexibility in the design of the refractive index profile as MCVD.
Recently, a versatile technique for producing optical elements with arbitrarily shaped refractive index profiles has been introduced [2], based on the stack-and-draw process. It consists in the creation of a 2D binary pattern of two materials with different refractive index, with each element of it being subwavelength, in order to obtain an effective medium whose refractive index at every point is the local spatial average of the two of the used materials. The resulting profile of refractive index is therefore dependent on the pattern arrangement, which can be chosen freely. This fabrication method has been already demonstrated to be suitable for the production of borosilicate graded index optical fibers [3].
In 2017, chalcogenide Grin fibers produced by stack and draw technique have been simulated [4], showing in theory the possibility of an high degree of control on the dispersion curve and the possibility of obtaining flat, all normal dispersion profiles over the mid infrared range. The latter property is of high interest for increasing resolution or precision in some applications of supercontinuum generation [5], such as as optical coherence tomography [6], ultrashort pulse generation [7], and communications[8]. Using all-normal dispersion (ANDi) fibers allows for a spectral broadening mainly based on SPM, without the influence of the noise-sensitive soliton dynamics (which is possible only in anomalous dispersion regime), thus increasing the coherence of the supercontinuum [9]. Indeed, broad supercontinuum generation with excellent properties in terms of coherence has been recently experimentally demonstrated in all normal dispersion chalcogenide step index fibers and tapers [5, 10].
In this chapter, the development of the first chalcogenide graded index fiber is presented, as a collaboration between two academic participants of the SUPUVIR project: University of Rennes 1 (UR1) and Instytut Technologii Materiałów Elektronicznych (ITME). For its fabrication, the technique based on stack and draw mentioned above was employed, using chalcogenide glasses in the Ge-As-Se system as starting materials.

4.1 Fabrication of chalcogenide Grin fibers

For the production of preforms, and subsequently fibers, with a graded refractive index profile of the core, the following route was devised: chalcogenide rods with a diameter of 450 μm, obtained from two compositions with different refractive indices, were produced at UR1. The rods were produced in a way similar to the one described in Section 2.2, but using a capstan to pull the glass instead of a rotating drum. Subsequently, a proper configuration for the core of the fiber was calculated at ITME, where the rods were sent and stacked in hexagonal preforms. In order to have a stack with size suitable for processing using the furnaces at UR1 (less than 15 mm), the hexagonal structures were simulated with 33 rods on the diagonal, corresponding to 817 rods in total. These preforms were then drawn into graded index compact canes at UR1, to be used as cores for a classical rod-in-tube fiber drawing. The cladding tubes were also produced in UR1 by rotational casting, using the same glass composition used for the rods with lower refractive index. How this route was implemented will be explained in detail in this section.

4.1.1 First attempt

In order to verify the suitability of this fabrication method for the development of graded index chalcogenide fibers, a first attempt was performed as a proof of concept, with the idea of further optimizing the process if the first results were promising.

4.1.1.1 Precursor glasses

Between the different compositions produced in this thesis, $As_{38}Se_{62}$ and $Ge_{10}As_{22}Se_{68}$ were chosen, being the most similar ones to the compositions used for the simulations in [4]. These compositions exhibit a significant refractive index difference ($\Delta n \simeq 0.2$ @1.55 μm), allowing for an high contrast refractive index profile of the fiber's core. At the same time, these two glass have similar enough values of T_g (175°C for the composition containing germanium and 165°C for the arsenic selenide) and viscosity behaviors to allow for simultaneous drawing. The refractive indices of these glasses, estimated as explained in Section 2.1, are reported in Figure 4.1.

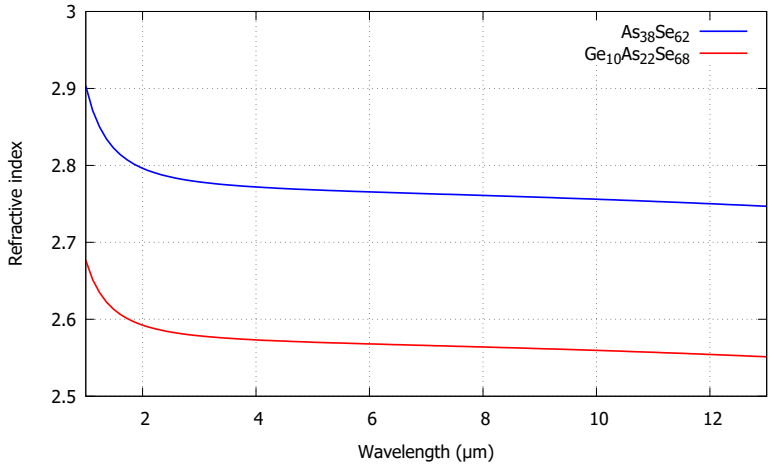

Figure 4.1: *Calculated refractive indices of* $As_{38}Se_{62}$ *and* $Ge_{10}As_{22}Se_{68}$ *over the spectral region of interest.*

Being this only the first step in the development of the project, with no assurance we would find a way to actually preserving the pattern of the core during drawing, it was decided to use non-purified glasses as a basis. However, while this led to no particular problems during the preparation of the $As_{38}Se_{62}$ rods, the presence of a large amount of impurities resulted in the impossibility to produce $Ge_{10}As_{22}Se_{68}$ with a constant enough diameter. For this reason, for the composition containing germanium a double distillation process (see Section 2.3) was performed before drawing the rods.

The attenuation spectrum of one the purified $Ge_{10}As_{22}Se_{68}$ batches used, together with a typical one of non-purified $As_{38}Se_{62}$, are shown as an example Figure 4.2.

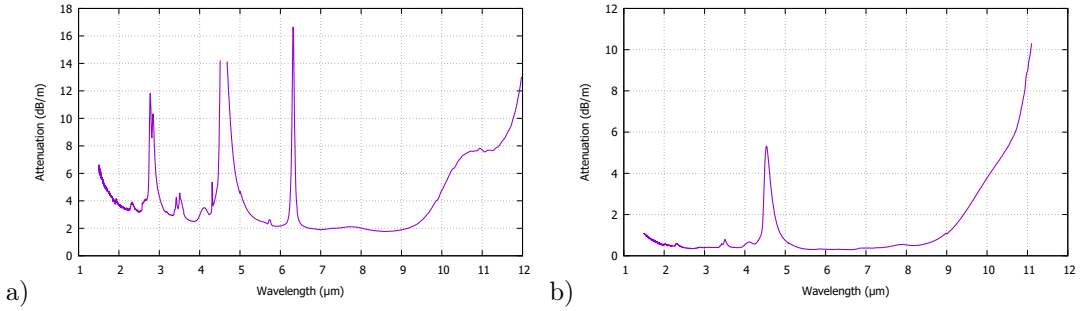

a) b)

Figure 4.2: *a) Typical attenuation of a single index fiber from non purified* $As_{38}Se_{62}$*. b) Attenuation of a single index fiber obtained from the one of the preforms used for drawing the rods.*

4.1.1.2 Rods preparation

The rods to be used as elements to compose the core were produced on the same drawing tower used for the fibers described in the rest of this thesis, using the same kid of annular furnace for heating. Before starting to heat the preform, a 30 min purge of the furnace with argon was performed. After this, the gas was switched from Ar to He, with a flow of 1.5 L/min ,and the furnace was heated up to drawing temperature. A capstan was installed below the furnace to pull the preform into rods after the drop formation, because using a drum would impress a permanent curvature to chalcogenide fibers of such large thickness.
An error of 20 μm on the final diameter of the rods was deemed as acceptable for this preliminary attempt. Only in the drawing of arsenic selenide such large diameter fluctuations were observed, while the rods produced starting from $Ge_{10}As_{22}Se_{68}$ showed an almost perfectly constant diameter. This further confirmed that the purification of the glass is of fundamental importance in this process, not only in terms of improved attenuation but also for a better homogeneity of the final product.
The rods were then cut into pieces of different lengths: 9 cm for the lower refractive index composition, 10 cm for the higher refractive index ones. This is fundamental to recognize the two type of rods during the stacking process, as the two glasses are indistinguishable in color to the naked eye.

4.1.1.3 Structure simulation and preform stacking

A parabolic profile of the refractive index has been chosen for this fiber's core. The number of elements to be used in the design of the pattern has been decided as a compromise between different factors: the accuracy in reproducing the desired profile, which increases by increasing the number of elements, the fact that small rods are more difficult to manually stack and can become flexible if the diameter is not large enough, and the fact that in the furnaces used for the drawing of canes there is a limit to the size of preforms that can be heated uniformly. All of these considerations brought to a final choice of using 33 rods on the diagonal of the preform (meaning a total number of 817 elements in the structure), with a diameter of 450 μm each, for a preform size of about 1.5 cm at its largest point.
Once fixed these parameters, the distribution of the rods was determined by simulated annealing [2], a Monte Carlo method similar to direct binary search. At the beginning of the simulation, a completely random distribution of the two compositions in the pattern is generated. The calculation then proceeds in a step by step fashion. At every step, the composition of one random element is changed, and the standard deviation of the averaged index distribution to the desired index pattern is calculated. If its value is smaller with respect to the previous step, the change is always accepted. If it is larger, the change is accepted with a probability $p = k \cdot e^{-\frac{\Delta}{T(I)}}$, where k is a constant, Δ is the (positive) difference in standard deviation, and T(I) is a parameter that is decreased exponentially

with the number I of iteration steps. At the end of this process, the structure visible in Figure 4.3.c was obtained.
Once the structure had been determined, the rods of the two different compositions were stacked following it with the help of an hexagonal guide. Finally, hexagonal metallic rings were put near the ends of the stack to keep the rods in place and the whole structure was removed from the guides, obtaining an about 10 cm long preform (Figures 4.3.a,b).

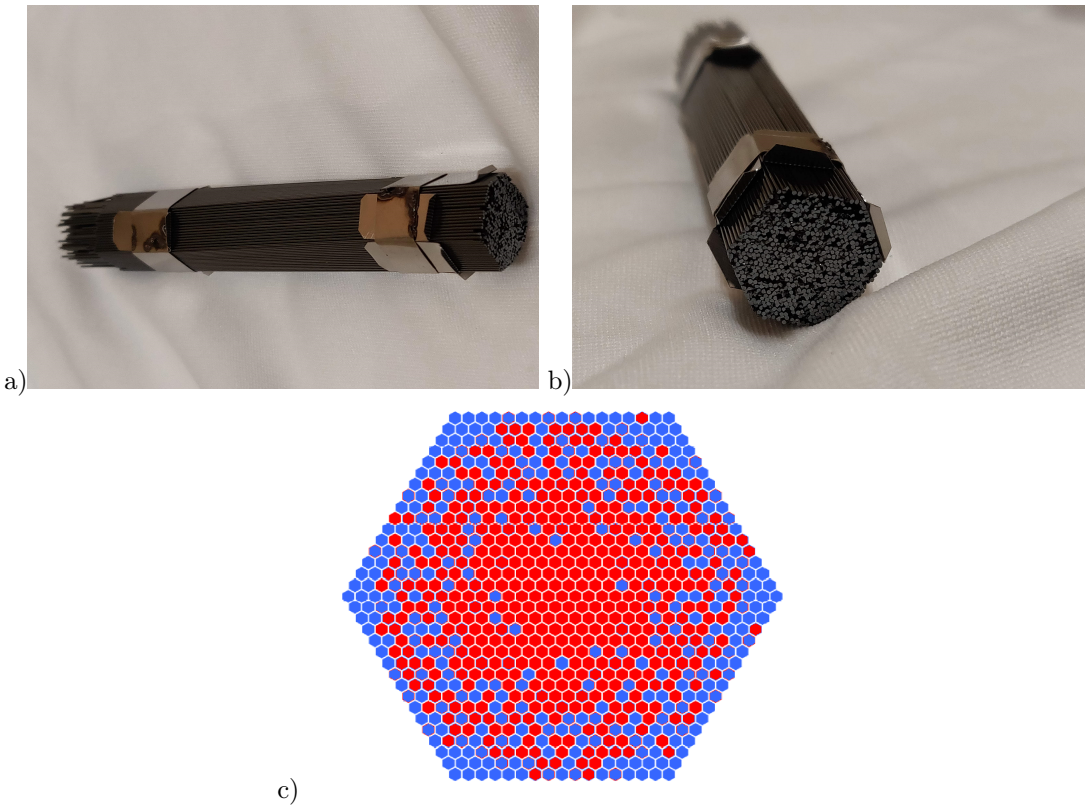

Figure 4.3: *Stack for the graded index core rod (a,b) and corresponding simulated configuration (c), with the low n rods in blue and the high n ones in red. The stack is 1.5 cm wide on the diagonal.*

4.1.1.4 Fabrication of the core cane

In order to collapse the aforementioned stack into a compact cane, two drawing steps are needed: one to achieve partial collapsing and one to actually obtain the cane.
The goal of partial collapsing is to use temperature to stick together the external layers of the stack. This is fundamental, because for the successive step the lateral surface of the preform needs to be airtight. To obtain this effect, the following procedure was adopted: at first, the stack was covered with an airtight cladding of teflon tape (see Figure 4.4.a), and while the interior part was cleaned with helium and put under low vacuum (-50 mbar), the furnace was fluxed with argon for 30 min. After this, the furnace atmosphere was switched from Ar to He and the temperature was slowly increased. The vacuum was maintained through the whole heating and collapsing in order to favor, together with the force applied by the elasticity of the teflon, the adhesion of the rods. Finding the appropriate strength of the vacuum is important in this phase, as a good sticking of the rods in the external layers is needed while avoiding a too large partial collapse of the internal ones, which might be detrimental to the uniformity of the finished cane. Once a reduction in size of the stack was visible by eye in the hot zone, meaning the softening temperature had been reached, the preform motion was started at an high speed of 5 mm/min, in order to heat the whole length of the preform without any part of it staying for a too long time in the hot zone. Indeed, a too long duration of the heating could lead to excessive collapsing and increase the risk of crystallization.

The resulting partially collapsed preform, after the removal of the teflon coating, can be seen in Figure 4.4.b.
The partially collapsed preform was afterwards drawn, once again using the capstan, into a cane to be used as core for the graded index fiber. As in the previous step, vacuum was applied inside the preform to help the process of closing the interstitial holes between the rods. During the drawing, the speed of the capstan was varied in order to obtain three different diameters along the cane: 1, 2 and 3 mm. The goal was to use the 1 mm rod, in order to obtain a 125 μm $\varnothing$ fiber with a core of around 10 μm $\varnothing$, corresponding to a diameter of around 300 nm for each element of the core structure. The other two sizes were drawn in case of impossibility in using the 1 mm one, a problem that might arise in the case of a too large mismatch between the cane diameter and the hole size of the tube to be used as cladding. As visible in Figure 4.4.c, the structure of the stack appears to have been properly translated to the cane's cross-section. Not all of the empty spaces between rods were completely collapsed, leading to the presence of the small holes visible in the cane. This problem, however, can be addressed during the fiber drawing, assuming the holes are through along the whole system, and therefore able to be eliminated by applying vacuum, or if closed filled with vacuum, which would lead to their spontaneous collapse during the drawing.

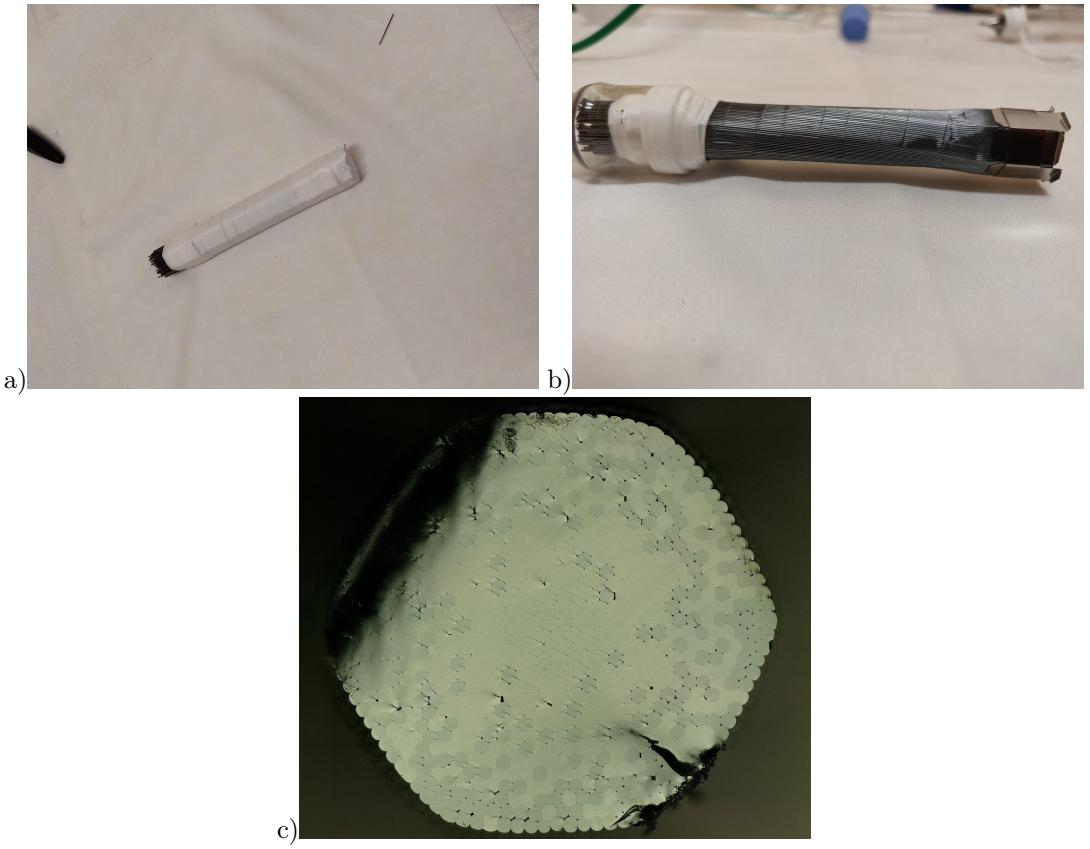

Figure 4.4: *a) Starting stack before the partial collapsing step, already cladded in teflon tape; b) partially collapsed stack after the removal of teflon; c) cross-sectional microscope image of the core cane.*

4.1.1.5 Fiber drawing

The tubes to be used as cladding for the Grin fiber were prepared by rotational casting technique. This technique consists in cooling down molten glass in a cylindrical tube which is rotating at high speed around its axis. The centrifugal force from the rotation shapes the melt into a tube, shape that is preserved when the glass is cold. The diameter of the hole obtained this way is determined entirely by the dimensions of the cylinder and by the amount of glass inserted into it.

It is important to notice that there is an intrinsic lower limit to the size of holes obtainable by rotational casting, which is related to the thermal expansion coefficient of the glass: the volume of the melt cannot exceed at any point the internal volume of the cylinder. This fabrication method is particularly well suited for chalcogenide glasses, which are sensitive to contamination from the lubricants used for standard drilling.
The tubes used for the experiment here described were prepared starting from shards of high purity $Ge_{10}As_{22}Se_{68}$, that were placed in 10 cm-long silica tubes to be sealed under high vacuum. The internal diameter of the silica tubes was of 12 mm. The glass was afterwards melted at 550°C and, as soon as it was taken out of the furnace, spun at 3000 rpm until it cooled down to a temperature slightly higher than T_g (for the system in exam, this happened in around $6'30''$). The resulting tubes were annealed at 170°C for $30'$.
Once the tubes and core canes were prepared, a standard rod-in-tube technique was used to draw the final fibers. To begin, the core rod was placed in the tube and fixed in place with the use of teflon tape, carefully avoiding to completely close the tube's hole. This whole system was then placed on the drawing tower, to be drawn with the standard procedure already described in this work, using a rotating drum to pull it. Upon formation of the drop, vacuum was applied to the internal part of the tube, helping it to collapse around the rod.

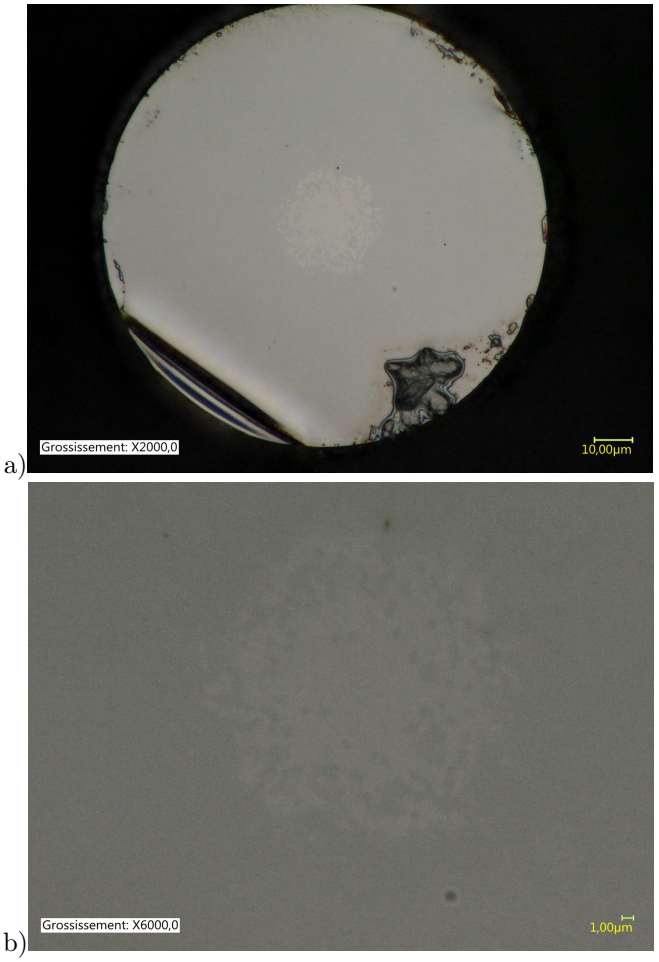

Figure 4.5: *Cross-section of the 30 µm core fiber obtained (a). In (b), a zoom on the core's nanostructure.*

A first drawing attempt was performed with a core cane of 1 mm diameter inserted in a tube with a hole diameter of 5.5 mm. With these parameters, it resulted impossible to obtain a fiber with a good cross section: lowering the drawing temperature allowed for a good core shape, but rendered it impossible to collapse the hole around it, whereas increasing it caused complete collapse

of the hole but at the price of a strong deformation of the core. Hoping to solve this problem, a second drawing was performed with both reduced hole diameter of the tube (3.9 mm) and an increased diameter of the cane (3 mm). With these last parameters, it was indeed possible to produce a fiber with both a good core shape and completely collapsed hole (see Figure 4.5). This fiber had an external diameter of 125 μm, corresponding to a core diameter of about 30 μm. No light propagation was however achieved in this fiber, mainly due to the tendency of $As_{38}Se_{62}$ to crystallize when multiple drawing steps are performed [11], as better explained in Section 4.2.1.

4.1.2 Second attempt

The first attempt of production of a graded index chalcogenide fiber demonstrated the suitability of the fabrication method for this class of glasses, at least in terms of preservation of the structure through the process. However, due to the high number of steps in which the glass was heated without quenching, a crystallization of $As_{38}Se_{62}$ was observed. In order to overcome this problem, for the successive attempt two compositions of glass containing germanium were chosen: $Ge_5As_{30}Se_{65}$ and $Ge_{10}As_{22}Se_{68}$. As for the first attempt, these glasses exhibit a difference in T_g of only 10°C, small enough for simultaneous drawing, and similar viscosity behavior. In this case the refractive index difference is $\Delta n \simeq 0.1$ @1.55 μm (see Figure 4.6), which while being smaller then the previous attempt is still large enough for an high contrast refractive index profile of the core.

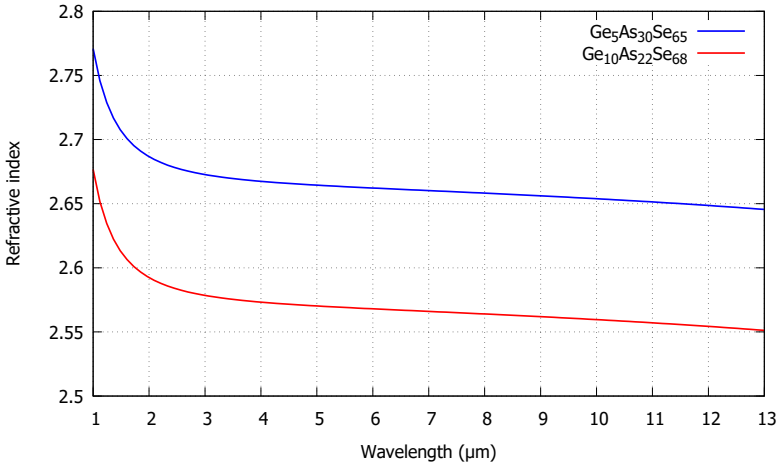

Figure 4.6: *Calculated refractive indices of* $Ge_5As_{30}Se_{65}$ *and* $Ge_{10}As_{22}Se_{68}$ *over the spectral region of interest.*

Due to the high levels of scattering-related attenuation shown by the glasses prepared for this attempt even after the double distillation process, a second step of purification was implemented, as described in Section 2.4.1. The attenuation curves of the different batches of glass prepared for rod production are presented in Figure 4.7.
It can be noticed that one of the batches of $Ge_{10}As_{22}Se_{68}$ glass, namely the one coded as "Ge10-4", has an higher attenuation baseline with respect to the other ones even after the multi-step distillation. Because of this, precautions have been taken to use as few rods as possible prepared with it, and to place them on the edges of the stack. This should have minimized any effects of their higher attenuation on the overall losses of the finished fibers.
The preparation of the rods from these glasses followed the same procedure already described for the first attempt. Notably, this second time the diameter fluctuations were way smaller, thanks to the higher purity of the glasses. The error on the diameter value can be considered to be below 1% for these rods. More rods than in the previous attempt were also produced, in order to prepare two stacks and have room for corrections in the fabrication process if needed.
Two different simulations were ran for the structural designs of the two preforms to be prepared. Due to the stochastic nature of the method used to perform them, they resulted in two different

arrangements of the core pattern, which will be referred to as "preform A" and "preform B" (see Figure 4.8). The procedure followed for drawing the two stacks produced following these designs into core canes, as well as the one followed to produce the cladding tubes with $Ge_{10}As_{22}Se_{68}$ glass and the final fibers, are once again the same ones used for the previous attempt in producing a chalcogenide Grin fiber. The only significant exception is the application of a stronger vacuum in the preforms while producing the canes, with the goal to reduce the number of residual interstitial holes. As visible in Figure 4.8, the quality of the obtained canes is higher in this respect when compared to the ones produced in the first attempt.

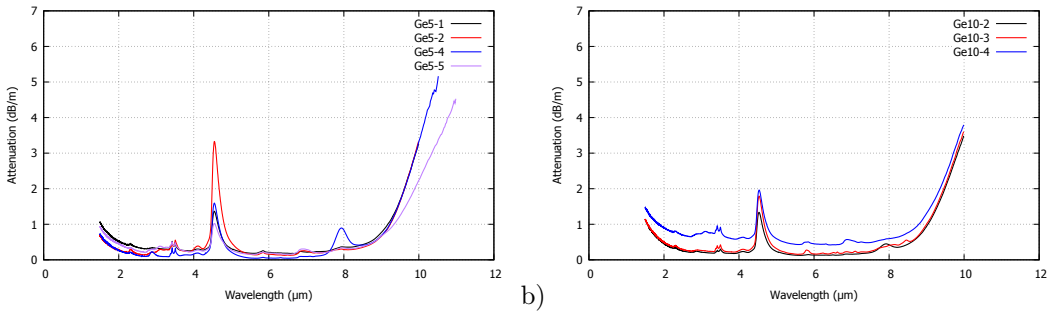

a) b)

Figure 4.7: *Attenuation spectra of the batches of* $Ge_5As_{30}Se_{65}$ *(a) and* $Ge_{10}As_{22}Se_{68}$ *(b) used to produce rods for the second attempt of chalcogenide Grin fiber production.*

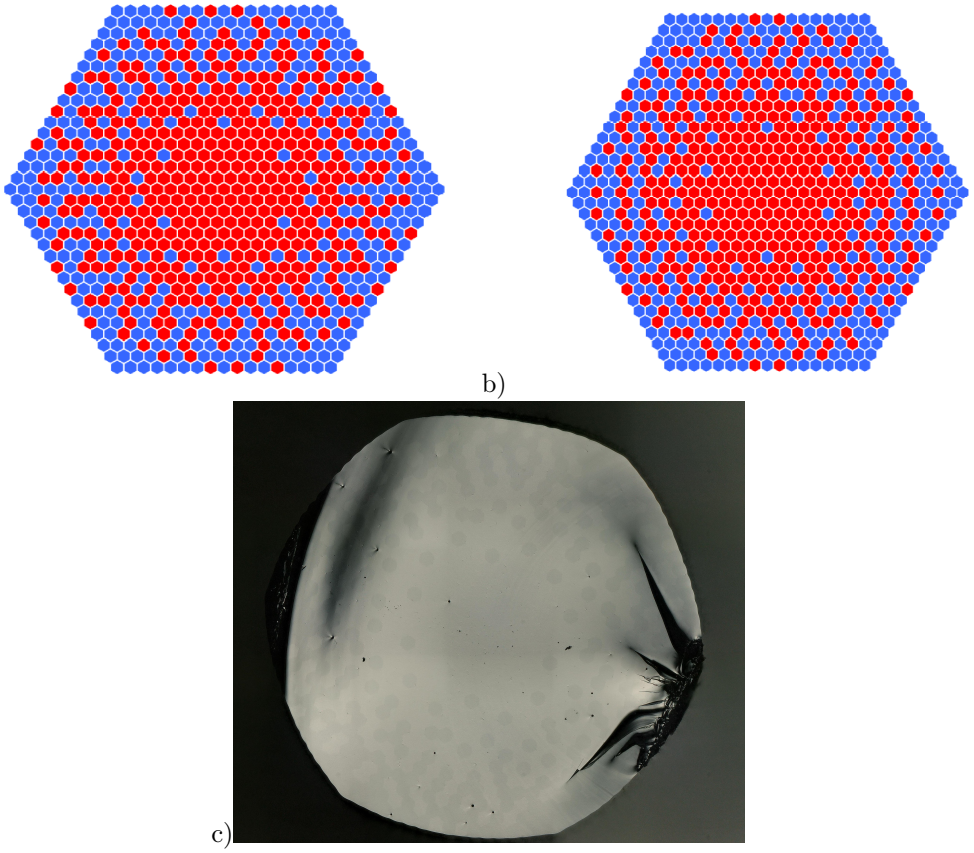

a) b) c)

Figure 4.8: *Stack configuration simulated for preform A (a) and preform B (b), with the low n rods in blue and the high n ones in red. In c), cross-section of a cane obtained from preform B.*

At first, due to the higher probability of failing to produce a well collapsed fiber using 1 mm diameter canes, drawings were performed using 2 mm diameter ones. As a result, two fibers with different diameter were drawn for each core pattern, one with 250 μm external diameter and 40 μm core diameter and one with 125 μm external diameter and 20 μm core diameter. Having these drawings succeeded for both preform A and preform B, an attempt was made to use 1 mm canes to obtain fibers with a core diameter of 10 μm, as per the initial goal. Once again, it was possible to obtain fibers with good quality from both preforms.
For the fiber with 10 μm core diameter obtained for preform B, an attempt was done to increase the diffusion of germanium between the core elements, thus reducing scattering- and diffraction-related losses, by strongly increasing the temperature during the drawing. This, however, led to a strong deformation of the core, causing it to become heavily elliptical.
As it will be further detailed in Section 4.2.2, all fibers produced in this second attempt have shown light transmission in the mid infrared, even if the optical losses remain high with respect to the ones of the precursor glasses. In particular, the ones obtained from preform B appear to perform better in this regard. For this reason, the 10 μm core diameter fiber obtained preform B was chosen to be used as starting fiber for the preparation of tapers with core diameters spanning between 4.4 and 7 μm, to be used for a better study of the core size influence on the light propagation properties in this kind of Grin fibers. The procedure used for tapering is the same that was described in Section 3.2.4.3. All of the produced tapers exhibited light transmission. In order to avoid the measured properties to be an average between the ones of the waist and the ones of the ends, after ascertaining the possibility of light propagation all tapers were cut to remove the ends and transitions, leaving only the waists.

4.2 Characterization of the obtained fibers

4.2.1 $As_{38}Se_{62}$ – $Ge_{10}As_{22}Se_{38}$ Grin fiber

4.2.1.1 Morphology

In order to understand the reasons for the complete lack of transmission in this fiber, a number of different cleaves were checked using both an optical and an electron microscopes. In the core of the large majority of them the presence of crystals of various size, as well as small holes, was observed.
While the matter of holes is one that can be solved by correcting the parameters used in the various steps of drawing, crystallization is related to the thermal properties of the materials. To confirm the hypothesis of arsenic selenide being the compound causing the crystallization, some cleaves (see Figure 4.9) were chosen and used for checking the composition of the crystals by energy dispersive spectroscopy.
Six crystals of different sizes and shapes, shown in Figure 4.9, were individuated for this analysis, and for all of them EDS spectra were collected. All crystals presented clear characteristic peaks related to the K and L edges of arsenic and selenium, while no peaks indicating the presence of germanium were identified in any of the collected spectra. As visible from the results of the quantitative EDS analysis, reported in Table 4.1, within some variation in stoichiometry all of the impurities seem to arise from the crystallization of As_2Se_3. These results, while not being an absolute confirmation of it, are well compatible with the hypotesis of the $As_{38}Se_{62}$ elements in the fiber's core being the source of the crystals' growth.

Table 4.1: *Results of the quantitative EDS analysis performed on 6 different crystals in the fiber's core.*

Crystal	% of As (±0.1)	% of Se (±0.1)
1	39.9	60.1
2	35.7	64.3
3	40.9	59.1
4	39.9	60.1
5	36.7	63.3
6	40.1	59.9

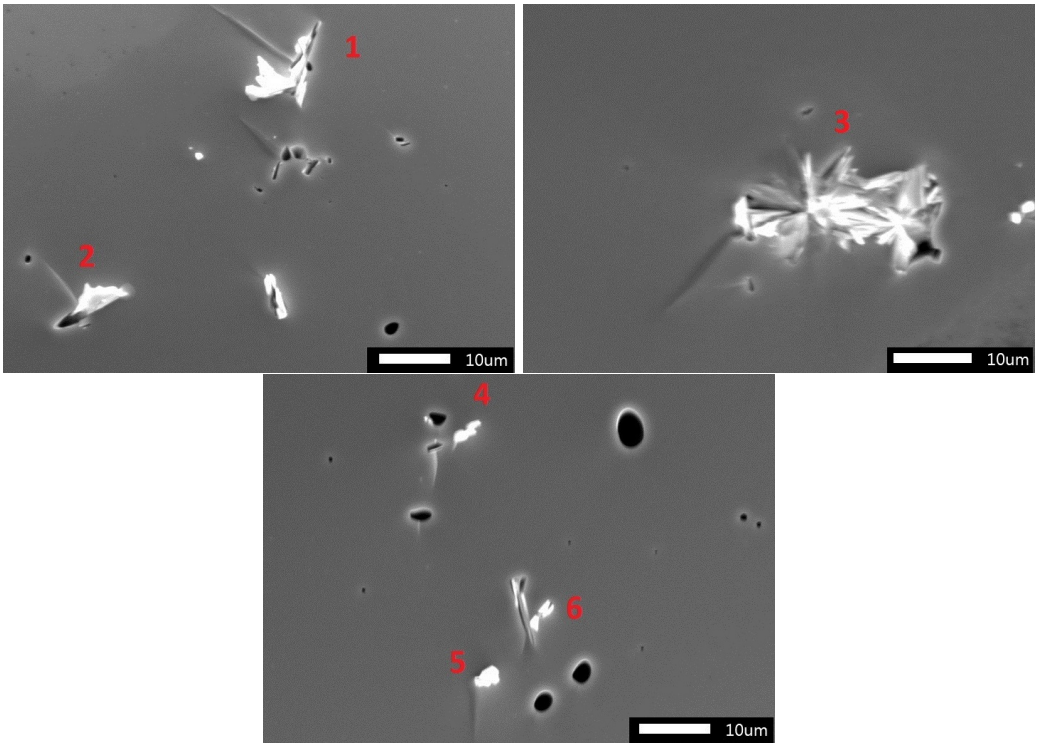

Figure 4.9: *SEM images of the cross section of three cleavings of the nGrin fiber. The crystals chosen for EDS measurements are numbered in red.*

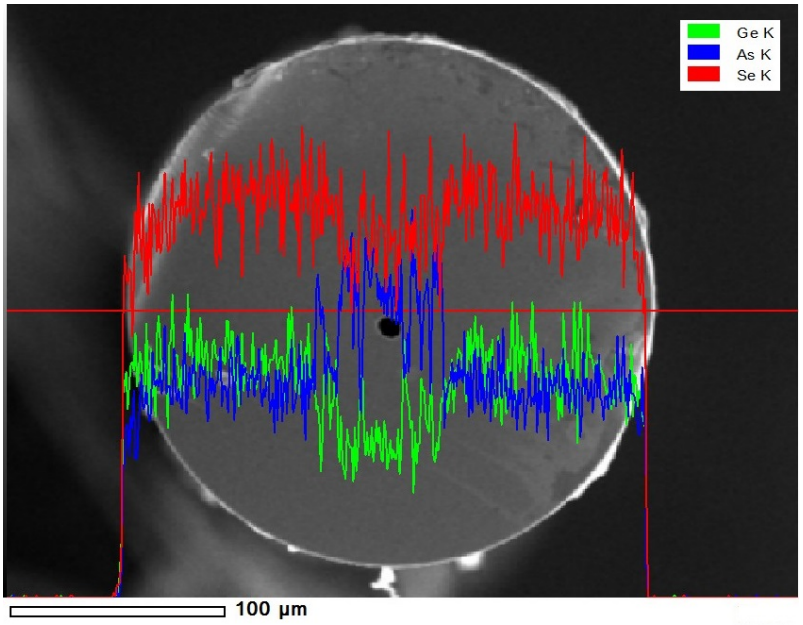

Figure 4.10: *Measurement of the intensity of the peaks related to Ge, As and Se across the fiber diameter.*

In order to verify the distribution of compositions (and therefore refractive index) in the core of the fiber, an EDS measurement along the fiber diameter was performed too, comparing the relative intensities of peaks related to germanium, arsenic and selenium in function of the position. For this measurement, a cleave was chosen for which a diameter not crossing any crystal or hole could be

found. As visible in Figure 4.10, a gradual loss in selenium and germanium, and a corresponding increase of arsenic content, happen in the core when moving towards the center. This trend is well compatible with the expected parabolic graded index profile.

4.2.1.2 Optical characterization of the core cane

Due to the impossibility of transmitting light through the fiber, no optical characterization of it could be performed. Some relevant information, however, could be extrapolated from the propagation properties of light in the cane used as core for the drawing. In order to do so, light with a wavelength of 10.6 μm from a CO_2 laser was injected into a 6 cm long piece of 1 mm diameter cane. For the injection, a 125 μm single index fiber of $Ge_{10}As_{22}Se_{68}$ was used. Despite this fiber being multimode and therefore transmitting irregularly distributed light, as visible in Figure 4.11.a and .b, and despite the fiber not being centered with respect to the rod, a seemingly regular near field image at the output of the cane can be ovserved (Figure 4.11.c,d). Indeed, a centered, quasi-parabolic profile of the field can be seen here, indicating some sort of lensing effect along the propagation length. This would be in good accordance with the expected graded refractive index distribution across the cane's cross-section.
Infrared imaging of the cane's side while light was injected in it reveals a large leak of light, presumably due to scattering, along its length (Figure 4.12.a). This phenomenon could be an indicator of the presence of a partial crystallization of arsenic selenide already at this stage of the fiber's fabrication process. In order to estimate the scattering losses of the cane, the base 10 logarithm of the radiance measured from the IR camera was plotted against the distance from the injection point (Figure 4.12.b). A linear fit of such plot resulted in a value of losses of $\sim$ 20dB/m. This is, however, a largely approximated result, and should be taken as a vague indication only. It is also important to consider that, after the production of the cane, another heating step was performed to obtain the fiber, probably inducing further crystallization of arsenic selenide. The number of scattering centers can be therefore expected to be consistently higher after drawing.

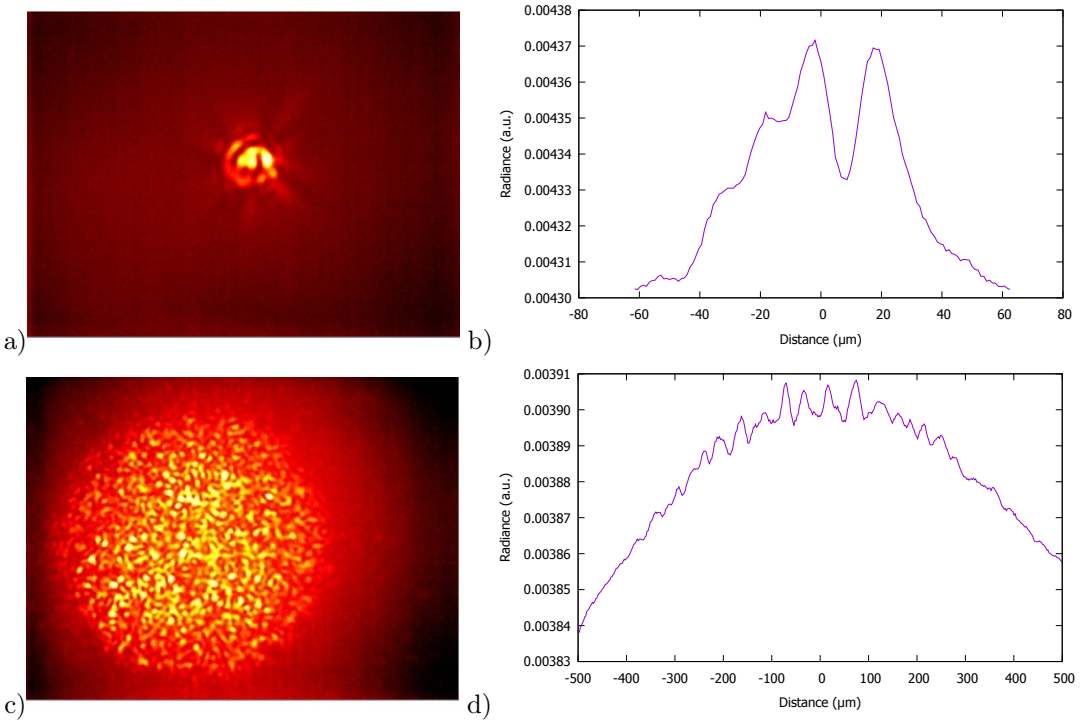

Figure 4.11: *Comparison between the near field images, and corresponding field profiles, of the multimode fiber used for injection (a,b) and of a short piece of graded index core cane (c,d) when injected with light at* $\lambda = 10.6$ μm.

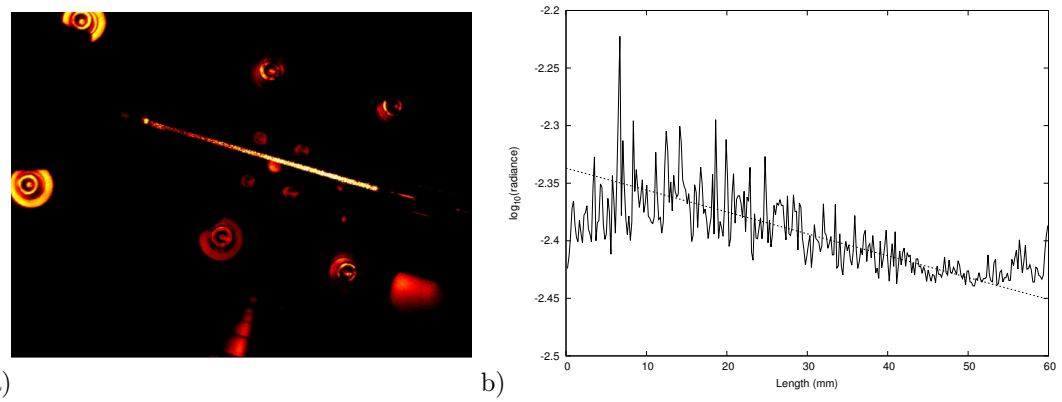

Figure 4.12: *In a), infrared imaging of a part of core rod when injected with light at $\lambda = 10.6$ μm; in b), the logarithm of radiance along the longitudinal profile, plotted against the distance from the light injection point, with the linear fit used to estimate scattering losses.*

4.2.2 $Ge_5As_{30}Se_{65} - Ge_{10}As_{22}Se_{38}$ Grin fibers

4.2.2.1 Morphology

All the fibers drawn in the second attempt of production of a chalcogenide graded index fibers were sampled in a large number of different points and imaged using a Keyence VHX 5000 digital optical microscope, in order to check for the presence of defects. No crystals were found in any of the samples, confirming the fact that the source of the crystallization noticed in the first attempt was the presence of $As_{38}Se_{62}$ elements.
Along most of the fibers, no holes in the core nanostructure were found, and even if faintly the core was visible, as shown in Figure 4.13.a. This allowed for an estimation of the different core diameters, which seems to be corresponding to the expected ones, with errors $\leq 1\%$. The only exceptions were the fibers with a target core diameter of 10 μm, which resulted to have a core larger than intended of more than 5%. This, however, should cause a rather small difference in terms of propagation properties.

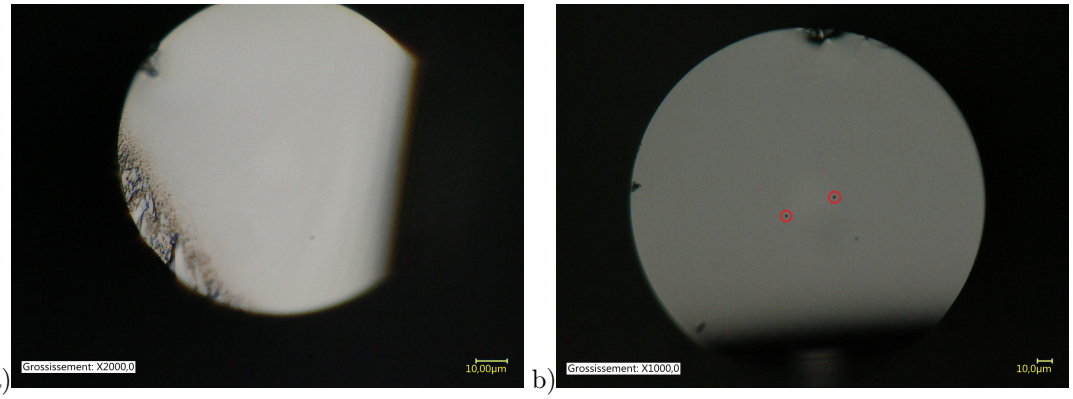

Figure 4.13: *Optical microscope image of the 10 μm core fiber obtained from Preform A (a). In b), small holes (circled in red) in the core of a 40 μm core fiber obtained from Preform B.*

In some parts of the fiber, as visible in Figure 4.13.b, small round holes have been found to be present inside the core. A likely explanation for the phenomenon is the presence of a few air-filled bubbles in the precursor canes due to incomplete collapsing of the original stack. From the fact that these holes usually persist across a length of fiber measuring no more than 0.5-1 meter, we can suppose such bubbles to have been rather small in size.

As for the previous attempt, measurements performed by EDS along the diameter of the fibers show a compositional variation compatible with the desired refractive index profile for the fibers derived from both preform A and preform B (Figure 4.14). Even with the scanning electron microscope used for these measurements, for most samples it was not possible to recognize any defect at the interfaces between the elements composing the core.

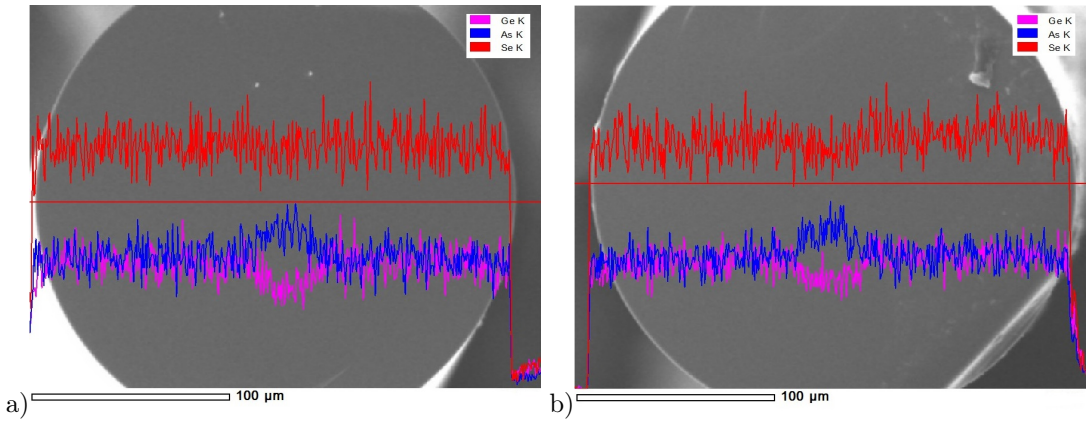

Figure 4.14: *Measurement of the intensity of the peaks related to Ge, As and Se across the the diameter of 40 µm core fibers obtained from preform A (a) and preform B (b).*

4.2.2.2 Light transmission properties

As a first mean to verify light transmission in the six fibers initially obtained (10, 20 and 40 μm cores from both preform A and preform B), they were injected with light from a 1.55 μm CW laser, and their output field was imaged using a microscope objective coupled with a CCD camera. This wavelength can be a good indicator of performance for chalcogenide fibers, being one in which they tend to be lossy. Graphite dissolved in alcohol was applied on the outer surface of the fibers near the injection point, in order to remove eventual light injected in the cladding. Confinement losses could be observed for all the fibers measured, in the form of a non-negligible amount of light transferred from the core to the cladding during propagation. In the case of the fibers with 40 and 20 μm core diameters with preform A geometry, notably, losses were so strong that the core was not visible with this setup. This phenomenon, however, appeared to decrease in strength for smaller core diameters. Moreover, it seemed to be less intense for the fibers obtained from preform B, based on the intensity of the output. The low amount of transmitted light, however, suggested the presence of other strong sources of losses. Concerning the field distribution at the output, all fibers showed a strongly multimode behavior at this wavelength.
Using a CO_2 tunable laser, a proper lensing system and a FLIR A-600 series infrared camera, images of the output field of the fibers were collected at wavelengths between 9.3 and 10.6 μm. Once again, graphite was applied on the external fiber surface. At these wavelengths, it was possible to observe light propagation in the core for all the fibers. While the ones with 20 and 40 μm core diameters showed to be multimode even in this spectral range, for a core size of 10 μm core fibers, for both preforms, a single mode behavior with nearly gaussian mode profile was found. As an example, the output field images collected at a wavelength of 10.5 μm, along with the corresponding mode profiles, are shown in Figure 4.15. The rings of light that can be clearly observed around the core in this figures are due to pinhole-like diffraction, as the wavelength of the light is very close to the core diameter.
With the goal of having a first comparison between the different fibers produced, transmission spectra in the $1-12.5$ μm range were collected on a Bruker T37 FTIR apparatus, using an external MCT detector to collect the signal. In order to obtain comparable spectra, the same length of 20.5 ± 0.3 cm was used for all the fibers to be measured. After being cleaved and placed in the setup with the use of fast connectors, the exposed part of each fiber was completely covered with graphite, to avoid a difference in the amount of graphite placed between different samples.

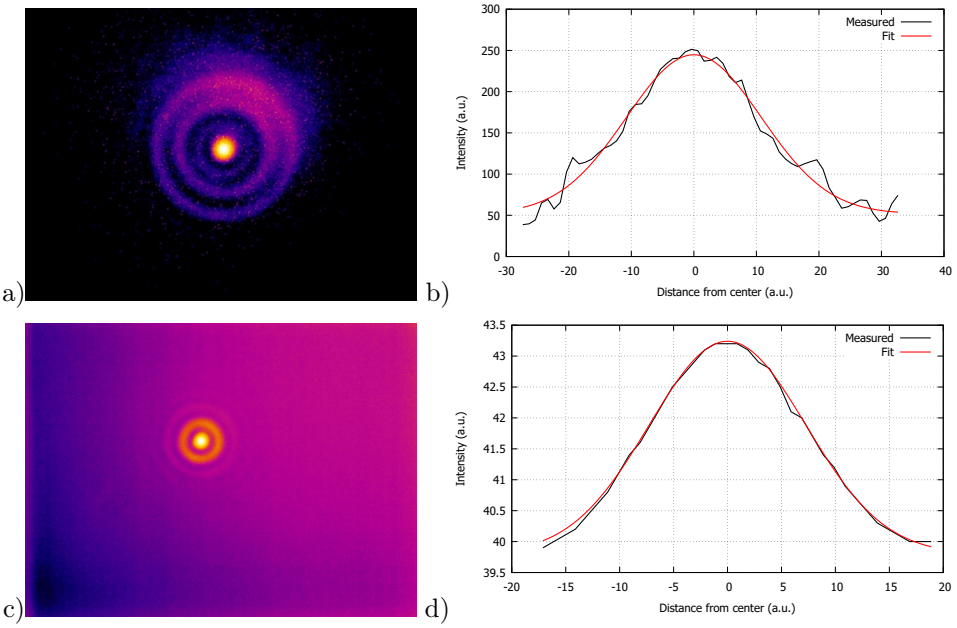

Figure 4.15: *Mode images and corresponding profiles of the 10 µm core diameter fibers obtained from Preform A (a,b) and preform B (c,d) when injected with a 10.5 µm laser. The profiles were fitted with a gaussian function as a guide for the eye.*

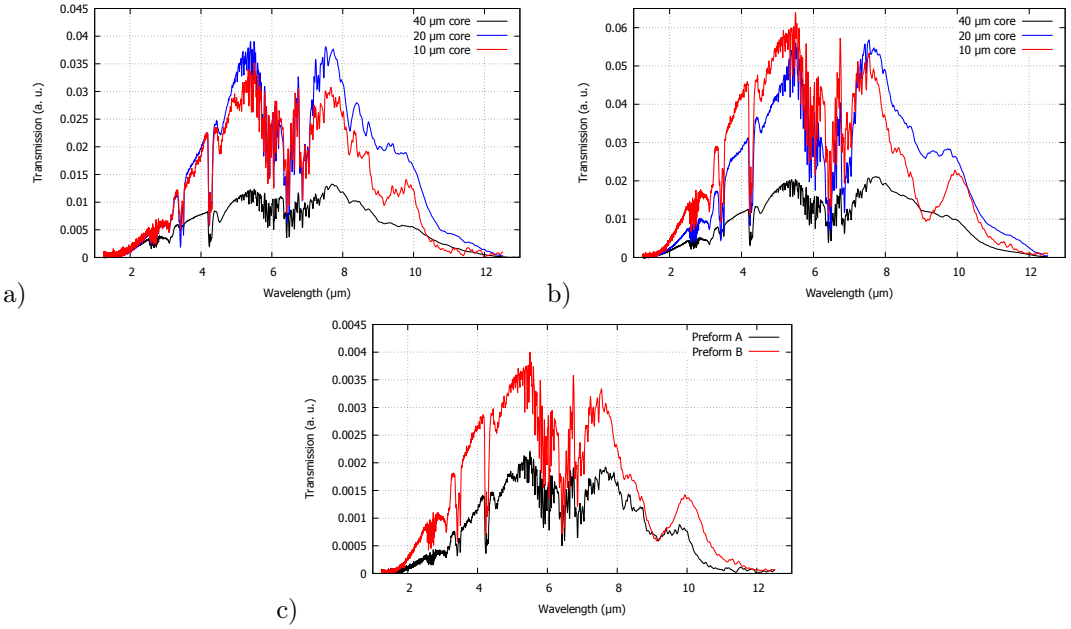

Figure 4.16: *Transmission spectra, normalized by core area, of the fibers obtained from Preform A (a) and preform B (b). In c), a comparison between the transmission spectra of the fibers with a core diameter of 10 µm obtained from the two preforms.*

Assuming the light was efficiently removed from the clad, to compare the spectra of fiber with different core sizes the transmittance was normalized by dividing the recorded intensity by the core area. The results are visible in Figure 4.16.a,b. Since the fibers with the smaller core diameter seem to be the most interesting for both modal properties in the mid-IR and losses at the telecommunications wavelengths, a further comparison was done between the fibers with a core size of 10

μm obtained from both preforms. As visible in Figure 4.16.c, the one with such core diameter and the structure type of preform B seems to be the overall best performing fiber for the largest number of possible applications. For this reason, all of the measurements reported in the remainder of this chapter, for what concerns fibers, will be referring to the preform B 10 μm core fiber or to tapers obtained from it.
The attenuation in the mid infrared of the 10 μm core fiber obtained from preform B was measured with the same setup used for obtaining the transmission spectra, using a standard cutback technique. Due to the very low transmittance observed, only a single cutback with a length of about 10 cm was performed. The optical losses of the fiber, according to this measurement (Figure 4.17 - black line), are of two orders of magnitude larger than the ones of the starting materials.
In order to get more reliable information on the attenuation at short wavelengths, a second measurement was performed. For this, light from a supercontinuum source produced by LEUKOS, with a spectral range spanning from 200 to 2400 nm was injected in the fiber, and a Yokogawa AQ6375B optical spectrum analyzer operating in the wavelength range between 1200 and 2400 nm, was used to detect the signal. The light with wavelengths shorter than 1.2 μm was filtered out from the output of the supercontinuum source in order to avoid absorption-related damage to the fiber. Two attenuation curves were collected, from two cutbacks of $\sim$ 5 cm each, and their average was taken. The resulting attenuation spectrum (Figure 4.17 - blue line) seems well compatible with the one obtained using the FTIR. The mismatch where the two curves join is attributed to the lower sensitivity of the FTIR at wavelengths below 2.5 μm, combined with the small amount of light coupled into the fiber and the high level of attenuation causing a low output signal.

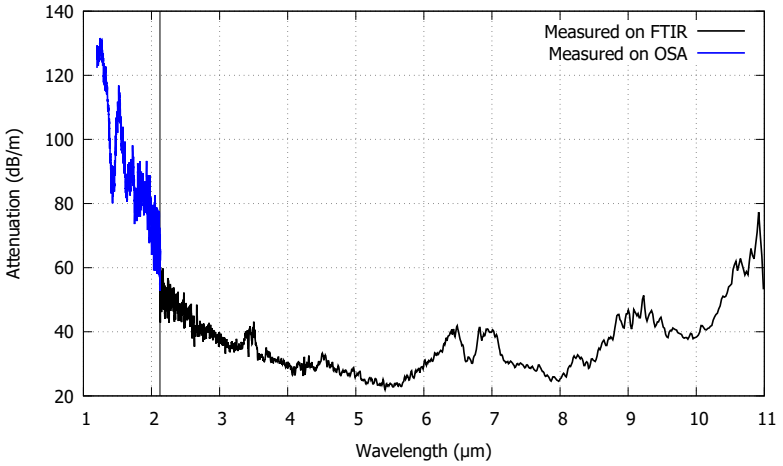

Figure 4.17: *Attenuation spectrum of the 10 μm core fiber with preform B geometry, obtained combining the measurements performed with the FTIR and with the optical spectrum analyzer.*

The absence of crystals or visible defects at the interfaces between the rods suggests that this excess of losses could be related to the interaction between the light and the core's structure itself, leading to scattering or diffraction caused by the elements of different refractive index. This, if true, would cause the attenuation to be strongly dependent on the size of the elements.
In order to verify this hypothesis, tapers were drawn starting from the measured fiber in order to check their optical losses. Three different core diameters were produced: 4.4 μm, 5.6 μm and 7 μm. Due to the difficulty of injecting light in such small cores using the optical setup of the FTIR, the attenuation of these tapers was measured only using the supercontinuum source and optical spectrum analyzer described above.
As visible in Figure 4.18, all tapers performed better than the original fiber in terms of optical losses in the measured range, with a difference of more than 20 dB/m. Furthermore, comparing the tapers a trend is visible, with reduced attenuation for the smaller core diameters. Because of the high level of noise in the collected spectra, however, the magnitude of the difference in losses between the three tapers couldn't be estimated. More measurements of attenuation, with a

spectral range extending to longer wavelengths in the mid infrared, have been planned in order to further investigate this matter. Nevertheless, these preliminary results seem to confirm a correlation between the size of the individual elements composing the core and the level of losses, suggesting that for future prototypes a larger number of rods should be used, either by increasing the size of the stack or decreasing the size of the rods. This, for an equivalent size of the core, should increase both the optical quality and the fidelity of the refractive index profile to the intended one.

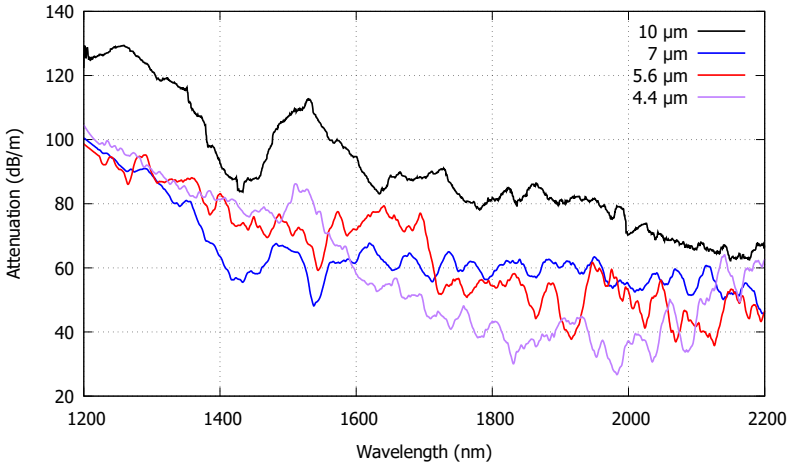

Figure 4.18: *Comparison between the attenuation, measured using the optical spectrum analyzer, of the tapers obtained from the 10 µm diameter core fiber with perform B geometry and of the fiber itself.*

4.2.2.3 Dispersion profile

The dispersion profile for the fundamental mode in the produced graded index fiber was simulated, starting from the core pattern configuration of preform B, using a finite difference method (FDE). The calculations were performed for different core diameters, namely 40, 20, 10 and 6 μm, in order to evaluate the dependence of dispersion on the size of the core. The resulting curves are presented in Figure 4.19

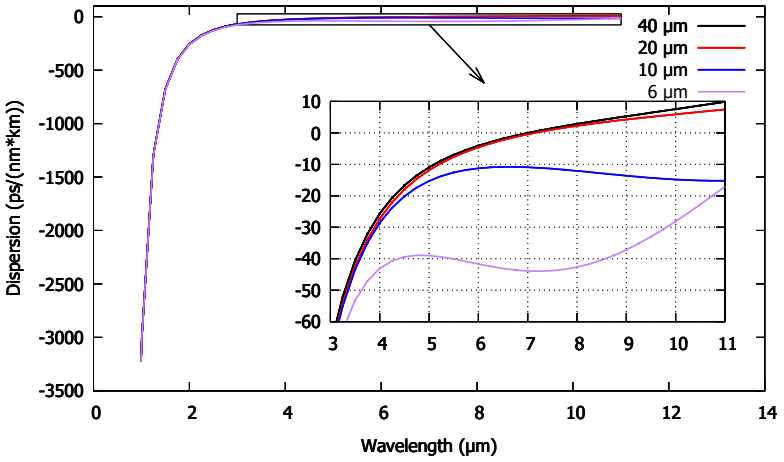

Figure 4.19: *Simulated dispersion profiles for different core diameters of the grin fiber obtained from preform B. In the inset, a zoom on the mid infrared region of the spectrum.*

It can be noticed that the two fibers with larger core size have, according to simulations, their zero dispersion wavelength at around 7 μm. This value is compatible with the one of the starting glasses,

as reported in [12]. Reducing the core size results in a strong deviation from the material's behavior, with both simulated fibers having an all-normal dispersion profile over the whole transparency window. More specifically, the 10 μm core fiber has an extremely flat dispersion profile over a large range of wavelengths, while the 6 μm core one exhibits a saddle-like shape.
For applications in high coherence supercontinuum generation, where a flat dispersion is of great importance, a value of around 10 μm for the core diameter seems to be ideal. Nonetheless, the definite change of behavior visible at 6 μm is an indicator of a great versatility of the presented fabrication technique in tailoring the dispersion profile by choosing appropriately both the design of the core pattern and the size of the core.
Experimental measurements of the dispersion were performed on the 10 μm core fiber and on the tapers produced to measure the attenuation. In order to do so, a Mach-Zehnder interferometer was set up, in a configuration similar to the one described in [13] (see Figure 4.20). The light source and detector used in this setup were the same supercontinuum source and optical spectrum analyzer used for the attenuation measurements. Light in the signal arm was coupled into a short piece of fiber, causing an optical path difference (OPD) with respect to the reference arm. After balancing the reference arm in order to be able to detect the largest possible number of interference fringes, the group refractive index (defined as $N(\lambda) = n(\lambda) - \lambda\frac{dn(\lambda)}{d\lambda}$) was measured as a function of the equalization wavelength in the range between 1200 and 2400 nm.

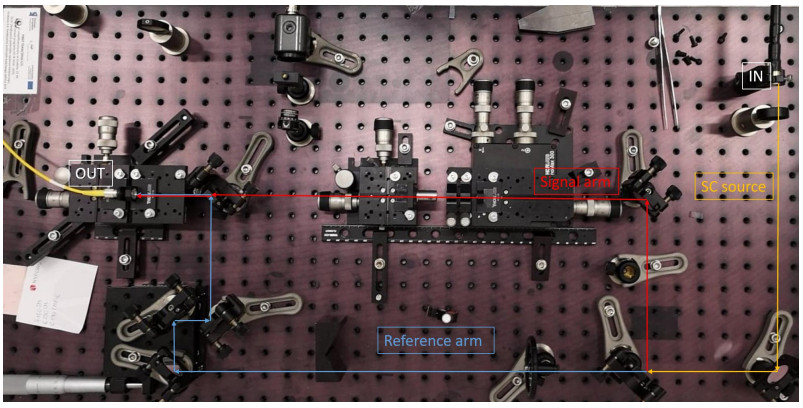

Figure 4.20: *Setup of the Mach-Zender interferometer used for measuring the dispersion of the fiber and tapers discussed in this section.*

For the calculation of $N(\lambda)$, the small OPD induced by the optical elements in the setup was also taken into consideration. This was done by applying a correction to the raw data, derived from the dispersion characteristics and thicknesses of the lenses and filters used. The group refractive index was then fitted to a 5 parameters functions:

$$N(\lambda) = \frac{A_1}{\lambda^4} + \frac{A_2}{\lambda^2} + A_3 + A_4\lambda^2 + A_5\lambda^4$$

The dispersion of the fiber is defined as $D(\lambda) = \frac{1}{c}\frac{dN(\lambda)}{d\lambda}$. Approximating the speed of light as $c = 3 \cdot 10^8 \ \frac{m}{s}$ and applying the proper unit conversions, the following expression was derived:

$$D(\lambda) = \frac{10^4}{3}\left(\frac{-4A_1}{\lambda^5} + \frac{-2A_2}{\lambda^3} + 2A_4\lambda + 4A_5\lambda^3\right)$$

and, by inserting into it the fitting parameters for $N(\lambda)$ into it, the dispersion curves presented in Figure 4.21 were obtained.
According to the simulations the dispersion in the near infrared seems to be independent on the core diameter, at least for cores as small as 6 μm. Despite this fact, a difference between the samples is visible in the measured data. It has to be considered, however, that a non-negligible source of error was present when obtaining the experimental curves: the highly multimode nature of these

fibers at the wavelengths used for the measurement rendered the excitation of the fundamental mode alone impossible. The dispersion curves of different interfering modes were being measured at the same time, and the difference between the samples could be due to the dependence of the number of modes on the diameter of the core.
This error, together with the lower sensitivity of the measurement setup for wavelengths above 2200 nm and the low output power of the source above 2000 nm, should be kept in mind also when comparing the results with the simulation. Nevertheless, a good accordance between the two can be observed over most of the measured spectral range for the 10 μm core fiber. Dispersion measurements in the mid infrared have been planned for the near future, in order to check the validity of the simulated curves in the region showing the most outstanding features.

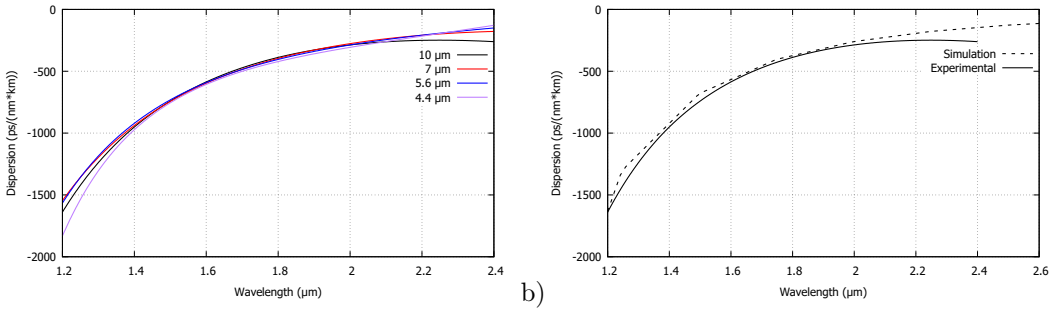

Figure 4.21: *a): Measured dispersion curves in the near infrared range for the the fiber and tapers discussed in this section. In b), the simulated and experimental curves for the 10 μm diameter fiber were plotted for comparison.*

4.2.2.4 Numerical aperture

A measurement of the numerical aperture was performed on the same set of fibers used to estimate attenuation and dispersion. The simple experimental setup used consists in a continuous wave 1550 nm laser as a light source and a near infrared sensitive camera as a detector. By measuring the spreading of the intensity profile for different distances between the output of the fibers and the camera's sensor, the divergence angle of the beam was estimated. The sine of this angle corresponds to the numerical aperture of the fiber. In order to better study the variation of NA with different core diameters, the fiber with 20 μm core obtained from preform B was measured too. The results are presented in Table 4.2.

Table 4.2: *Measured numerical aperture of different fibers obtained from preform B.*

Core size (μm)	20	10	7	5.6	4.4
Numerical aperture ($\pm$0.01)	0.57	0.54	0.54	0.55	0.5

As expected, all of the measured fibers exhibit a value of NA inferior to the one of an hypothetical step index fiber having core and clad refractive indices equal to the maximum and minimum values, respectively, of the refractive index profile of the Grin fiber [14]. Indeed, the numerical aperture of such a fiber, calculated as $\mathrm{NA} = \sqrt{n_{core}^2 - n_{clad}^2}$, would be of 0.68.
The significantly different values reported show the presence of a trend, with NA decreasing in fibers with smaller cores. Such a trend is well compatible with the findings of Matsumura [14]: the acceptance angle of graded index fibers is not uniform, strongly decreasing for light injected near the edge of the core. As the spot size of light at the injection end of the fiber could be considered to be nearly the same in all measurements, and to be always aligned near the center of the fiber, when decreasing the core's size a larger percentage of light was reaching it near its edges, causing the average numerical aperture measured to be lower. With the sensitivity of the setup used, no difference is visible between the numerical apertures of the fibers with core diameters of 10, 7 and 5.6 μm.

4.3 Chalcogenide graded index microlenses

Thanks to the growth in the microelectronics and optical fiber industries, micro-optics recently flourished as a research field. Sub-millimetric optical components are indeed needed for the coupling of light at the input and output ends of fibers, to improve the efficiency of devices such as LCD panels and CCDs, and to shape the light emitted by LEDs. Moreover, there is an increasing range of applications for micro-optics in biomedicine, driven by the demand for low-cost and minimally invasive devices for in vivo imaging and lab-on-a-chip devices [15]. These reasons, combined with the growing interest in applications requiring broad mid infrared transparency, make chalcogenide-based micro-optical elements a highly desirable solution.
Microlenses, in particular, are fundamental elements for all the applications mentioned above. As a further advantage other than the sheer size compatibility with fibers and microelectronics components, linear aberrations in small lenses decrease with their size [15]. Typically, microlenses are shaped as plano-convex lenses, and are fabricated by a variety of methods [16] such as moulding, hot embossing and UV imprint lithography, to name a few. In chalcogenide glasses, another currently used fabrication method is to obtain the desired profile using the phenomenon of giant photoexpansion [17–19].
Another approach to the development of microlenses is to exploit the light-bending properties of radial graded index profiles to smoothly and continually redirect light rays towards an image point [20] (see Figure 4.22). Thanks to this particular functioning principle, graded index microlenses can have flat, parallel faces, bringing a series of advantages: such a geometry removes the need for tightly controlled surface curvatures, can accommodate anti-reflection coatings and is easy to couple to flat surfaces such as optical fibres [21].
Because of these many interesting properties, as well as of the strong versatility of the fabrication method for Grin structures described in the previous part of this chapter, it was decided to try to use the same core canes from which the already discussed fibers were fabricated for the production of graded index microlenses.

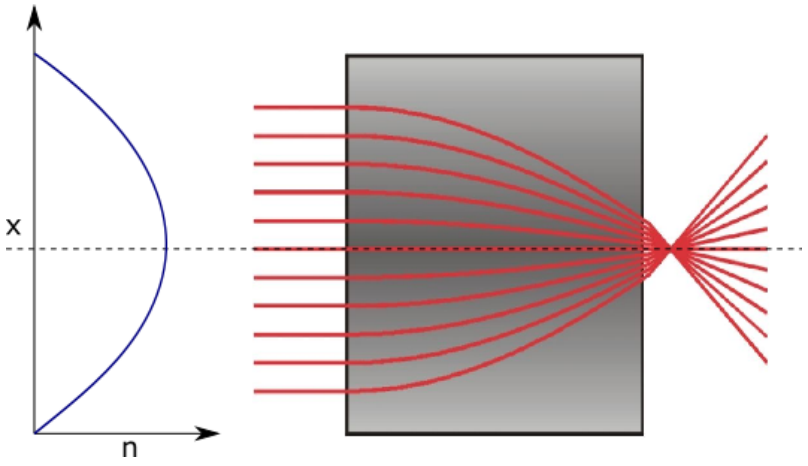

Figure 4.22: *Schematics of the functioning principle of a graded index microlens.*

4.3.1 Fabrication

As a base for the production of microlenses, canes with a graded index core were drawn with the same method used for the fabrication of graded index fibers. Three core diameters were chosen for this study: 80, 120 and 160 μm. Due to the large external diameters of the canes (500, 750 and 1000 μm respectively), the capstan was used for the drawing. The preform B geometry was once again chosen for the core pattern.
Once fixed the geometry and diameter of the grin structure, the other defining parameter of microlenses is their thickness, which is usually expressed as a fraction of their pitch. When talking about Grin lenses, the pitch is defined as the length of a full period of the sinusoidal path that

a ray of light entering the lens perpendicularly to its surface follows while propagating in it. Its value can be calculated as

$$\Lambda = \frac{2\pi}{\sqrt{g}} \quad ,$$

where g is the gradient constant describing the shape of the refractive index variation on the lens surface [22]. As the pattern of the lenses in exam has been designed to correspond to a parabolic profile centered on the optical axis, this constant can be expressed as

$$g = \frac{2(n_{max} - n_{min})}{n_{max} \cdot r^2} \quad .$$

A collimated beam impinging on the lens would be theoretically focused to a point after a quarter of the pitch (Q-pitch).
For the first attempt of fabrication, it was decided to use thicknesses smaller than the Q-pitch length, in order to have the focal point outside of the lens. The distance between the lens surface and the focal point is the so-called working distance

$$WD = f \cdot \cos(\sqrt{g} \cdot l) \quad ,$$

where l is the lens thickness and f is the focal length calculated as

$$f = \frac{1}{n_{max} \cdot \sqrt{g} \cdot \sin(\sqrt{g} \cdot l)} \quad .$$

In order for the lenses to be usable in any applications, they should have values of WD higher than 20 μm. Furthermore their characterization, because of the setup that will be used, becomes easier and more precise for far longer working distances (ideally more than 500 μm). WD, however, increases when decreasing the lens thickness, and with the procedure used for the fabrication of these lenses it's impossible to produce samples with $l < 50$ μm. The precise values of thickness to be used will need to be the best compromise between the desired optical properties of the lenses and the maximization of WD. The working distances for two industrial standards for l (0.1Λ and 0.22Λ) are presented in Table 4.3, together with other significant geometrical parameters. As it can be seen, the typically used thickness of 0.22Λ is not feasible for the lenses in exam.
All of the values in Table 4.3 were calculated for a wavelength of 1.55 μm. They can, however, be considered to be valid for the whole mid-IR range. Indeed, in this spectral region the variation of refractive index with the wavelength can be considered negligible with respect to the error in thickness typical of the fabrication method (± 10 μm).
To produce the lenses, the canes were cut into 3 cm long rods, which were glued to silica plates using epoxy resin. Grooves were preemptively carved in the plates using a diamond saw with micrometric precision to ensure a perfect alignment of the rods. An heat treatment at 140°C was performed in order to further harden the resin, significantly increasing the gluing force.
The plates were then cut at equal spacing of 1.5 mm, with an automatized high pressure water cutting machine. The resulting micro-lens preforms, still embedded in resin, will be glued with hot wax onto holders and reduced to the target thickness by polishing them on both sides. While normally the lenses would be mechanically removed from the epoxy resin after detaching them from the holders, for these samples it was decided to not do so, in order to avoid damage to the soft chalcogenide glass. This will not be detrimental to the measurements, and allows to obtain easier to handle microlenses embedded in an epoxy jacket.

Table 4.3: *Geometrical parameters of the Grin microlenses in exam, calculated for a wavelength of 1.55 μm.*

Core diameter (μm)	**g (μm^{-2})**	**Q-Pitch (μm)**	**WD for $l = 0.22\Lambda$ (μm)**	**WD for $l = 0.1\Lambda$ (μm)**
80	$3.9 \cdot 10^{-5}$	249	11	81
120	$1.8 \cdot 10^{-5}$	374	17	121
160	$0.99 \cdot 10^{-5}$	438	22	161

A characterization of these chalcogenide Grin microlenses, including measurements of output field profile, focal length and size of the focused beam waist, has been planned for the near future.

4.4 Conclusions

In this chapter the first example of chalcogenide graded index fiber was demonstrated, with a nanostructured core composed by elements of different refractive indices. Despite the high losses, light transmission was achieved in the fiber both in the near and mid infrared. A correlation appears to be present between the level of losses and the size of the elements composing the core pattern, showing a possibility to achieve better attenuation in the future. According to the simulations performed, this method to produce fibers enables an high versatility in the management of dispersion, notably with the possibility to have an ultra-flat ANDi profile over the whole mid-IR spectral region. Starting from the same preform used for the fibers, graded index microlenses are currently being produced, with the goal to pave the road to new coupling schemes for mid infrared light up to 17-19 μm.

Bibliography

[1] Alexis Méndez and Ted F Morse. *Specialty optical fibers handbook*. Elsevier, 2011.

[2] F Hudelist, R Buczynski, AJ Waddie, and MR Taghizadeh. "Design and fabrication of nanostructured gradient index microlenses". In: *Optics express* 17.5 (2009), pp. 3255–3263.

[3] Ryszard Buczyński, Mariusz Klimczak, Tomasz Stefaniuk, Rafał Kasztelanic, Bartłomiej Siwicki, Grzegorz Stępniewski, Jarosław Cimek, Dariusz Pysz, and Ryszard Stępień. "Optical fibers with gradient index nanostructured core". In: *Optics express* 23.20 (2015), pp. 25588–25596.

[4] Bartłomiej Siwicki, Adam Filipkowski, Rafał Kasztelanic, Mariusz Klimczak, and Ryszard Buczyński. "Nanostructured graded-index core chalcogenide fiber with all-normal dispersion–design and nonlinear simulations". In: *Optics express* 25.11 (2017), pp. 12984–12998.

[5] Nan Zhang, Xuefeng Peng, Yingying Wang, Shixun Dai, Yuan Yuan, Jingxiang Su, Guangtao Li, Peiqing Zhang, Peilong Yang, and Xunsi Wang. "Ultrabroadband and coherent mid-infrared supercontinuum generation in Te-based chalcogenide tapered fiber with all-normal dispersion". In: *Optics express* 27.7 (2019), pp. 10311–10319.

[6] Boris Povazay, K Bizheva, Angelika Unterhuber, Boris Hermann, H Sattmann, AF Fercher, W Drexler, A Apolonski, WJ Wadsworth, JC Knight, et al. "Submicrometer axial resolution optical coherence tomography". In: *Optics letters* 27.20 (2002), pp. 1800–1802.

[7] John M Dudley and Stéphane Coen. "Fundamental limits to few-cycle pulse generation from compression of supercontinuum spectra generated in photonic crystal fiber". In: *Optics Express* 12.11 (2004), pp. 2423–2428.

[8] H Takara, T Ohara, K Mori, K Sato, E Yamada, Y Inoue, T Shibata, M Abe, T Morioka, and K-I Sato. "More than 1000 channel optical frequency chain generation from single supercontinuum source with 12.5 GHz channel spacing". In: *Electronics Letters* 36.25 (2000), pp. 2089–2090.

[9] Alexander M Heidt. "Pulse preserving flat-top supercontinuum generation in all-normal dispersion photonic crystal fibers". In: *JOSA B* 27.3 (2010), pp. 550–559.

[10] Kai Jiao, Jinmei Yao, Zheming Zhao, Xiange Wang, Nian Si, Xunsi Wang, Peng Chen, Zugang Xue, Youmei Tian, Bin Zhang, et al. "Mid-infrared flattened supercontinuum generation in all-normal dispersion tellurium chalcogenide fiber". In: *Optics express* 27.3 (2019), pp. 2036–2043.

[11] Perrine Toupin, Laurent Brilland, Johann Trolès, and Jean-Luc Adam. "Small core Ge-As-Se microstructured optical fiber with single-mode propagation and low optical losses". In: *Optical Materials Express* 2.10 (2012), pp. 1359–1366.

[12] Harshana G Dantanarayana, Nabil Abdel-Moneim, Zhuoqi Tang, Lukasz Sojka, Slawomir Sujecki, David Furniss, Angela B Seddon, Irnis Kubat, Ole Bang, and Trevor M Benson. "Refractive index dispersion of chalcogenide glasses for ultra-high numerical-aperture fiber for mid-infrared supercontinuum generation". In: *Optical Materials Express* 4.7 (2014), pp. 1444–1455.

[13] Petr Hlubina, Miroslava Kadulová, and Dalibor Ciprian. "Spectral interferometry-based chromatic dispersion measurement of fibre including the zero-dispersion wavelength". In: *Journal of the European Optical Society-Rapid publications* 7 (2012).

[14] H Matsumura. "The light acceptance angle of a graded index fibre". In: *Optical and Quantum Electronics* 7.2 (1975), pp. 81–86.

[15] R Stevens and T Miyashita. "Review of standards for microlenses and microlens arrays". In: *The Imaging Science Journal* 58.4 (2010), pp. 202–212.

[16] H Ottevaere, R Cox, Hans-Peter Herzig, T Miyashita, K Naessens, M Taghizadeh, R Völkel, HJ Woo, and H Thienpont. "Comparing glass and plastic refractive microlenses fabricated with different technologies". In: *Journal of Optics A: Pure and Applied Optics* 8.7 (2006), S407.

[17] H Hisakuni and Ke Tanaka. "Giant photoexpansion in As2S3 glass". In: *Applied Physics Letters* 65.23 (1994), pp. 2925–2927.

[18] H Hisakuni and Ke Tanaka. "Optical fabrication of microlenses in chalcogenide glasses". In: *Optics letters* 20.9 (1995), pp. 958–960.

[19] Akira Saitoh, Tamihiro Gotoh, and Keiji Tanaka. "Chalcogenide-glass microlenses for optical fibers". In: *Journal of non-crystalline solids* 299 (2002), pp. 983–987.

[20] SH Wang, CJ Tay, C Quan, and HM Shang. "Collimating of diverging laser diode beam using graded-index optical fiber". In: *Optics and lasers in engineering* 34.2 (2000), pp. 121–127.

[21] C Quan, SH Wang, CJ Tay, I Reading, and ZP Fang. "Integrated optical inspection on surface geometry and refractive index distribution of a microlens array". In: *Optics communications* 225.4-6 (2003), pp. 223–231.

[22] R Buczynski, A Filipkowski, B Piechal, HT Nguyen, D Pysz, R Stepien, A Waddie, MR Taghizadeh, M Klimczak, and R Kasztelanic. "Achromatic nanostructured gradient index microlenses". In: *Optics express* 27.7 (2019), pp. 9588–9600.

General conclusions and perspectives

The main objective of the SUPUVIR European project is to advance the current state of supercontinuum sources in the visible, ultraviolet, near infrared and mid infrared spectral regions, both by advancing current supercontinuum generation (SCG) techniques, which requires highly nonlinear PCFs or waveguides specifically tailored or developed for the purpose, and by improving current applications and developing novel ones, enabled by the advances in SC sources in the project.
In this framework, the goal of this thesis was the development of microstructured optical fibers for mid-IR SCG, starting from the individuation of proper chalcogenide glasses and the improvement of the techniques for their synthesis. Regarding this, different compositions of glasses in the Ge-As-Se system have been characterized in terms of optical and thermodynamical properties to verify their suitability for SCG applications, and the purification process to obtain high quality fibers with the lowest possible attenuation has been thoroughly studied. The influence of the chemical compounds used on the results of the purificaton has been demonstrated, and, when the standard purification has proven to not be sufficient to properly reduce scattering-related losses, solutions have been devised to overcome this problem.
The glasses produced have been tested to verify the possibility to use them to produce index-guiding PCFs and tapers with the molding technique. Notably, the fiber of this kind with the lowest attenuation reported in literature with this glass system has been produced during the thesis. Using the compositions that allowed for the drawing of good quality fibers, a comparative study of the power handling properties has been performed, showing the positive influence of the addition of germanium to the composition when high power densities are required to propagate in the fibers. Some of the produced fibers have been used for supercontinuum generation in collaboration with different partners: polarization-dependent supercontinuum generation in an arsenic selenide polarization maintaining fiber has been demonstrated, and a prototype for an all fiber mid-IR supercontinuum source based on a cascaded pumping scheme has been produced. This prototype has a spectrally broad output extending up to 10 μm, and its viability for the spectroscopic identification of organic molecules has been shown.
In a collaboration with the Instytut Technologii Materiałów Elektronicznych (ITME) of Warsaw, the glasses produced during the thesis have been used to develop the first example of chalcogenide graded index fibers, using the stack and draw method to obtain a patterned core composed by hundreds of elements. The parabolic index profile was obtained by properly designing the arrangement of the elements in this nanostucture, made of two glasses with large refractive index difference. Mid infrared light transmission was observed in the produced fibers; the optical losses, however, are currently two orders of magnitude larger than the ones of the starting materials. Possible ways to avoid this excess of attenuation are being studied. Simulations performed for fibers with different sizes of the core show a large versatility in the management of dispersion, notably with the possibility to have an ultra-flat ANDi profile over the whole mid-IR spectral region. With the same method used for the production of these fibers, graded index microlenses with transmission spanning the whole infrared region up to 17-19 μm are being developed.
Overall, the presented research shows open possibilities in the future for the development of all-fiber supercontinuum sources in the mid-IR, reaching wavelengths that as of now can be obtained only with black body radiation sources and synchrotrons. Thanks to their high compactness, brightness and spatial coherence, as well as to the versatility of use that is typical of fiber-based instruments, sources like the cascaded pumping prototype presented can enable progress in many fields, such as spectroscopy, remote sensing, microscopy and tomography. In addition, the process developed for producing chalcogenide graded index fibers could, when perfected, open the way to a wide variety

of new devices and applications. Indeed, this fabrication method is highly versatile: it can be used not only to produce Grin fibers with arbitrarily engineered index profiles, but also for other designs such as multicore fibers and polarization maintaining fibers. Finally, the development of graded index microlenses with broadband infrared transmission could enable new coupling and imaging systems with wide applicability in fields going from fiber optics to medical devices.

Acknowledgment

This project has received funding from the European Union's Horizon 2020 research and innovation program under Grant Agreement No. 722380.

Publications and communications authored during the development of the thesis

Publications in peer reviewed journals

Amar Nath Gosh, Marcello Meneghetti, Christian Rosenberg Petersen, Ole Bang, Laurent Brilland, Sebastien Venck, Johann Troles, John Michael Dudley, Thibaut Sylvestre: *Chalcogenide Glass Polarization-Maintaining Photonic Crystal Fiber for Mid-Infrared Supercontinuum Generation.* Journal of Physics: Photonics 1.4 (2019): 044003. DOI:10.1088/2515-7647/ab3b1e

Yiming Wu, Marcello Meneghetti, Johann Troles, Jean-Luc Adam: *Chalcogenide Microstructured Optical Fibers for Mid-Infrared Supercontinuum Generation: Interest, Fabrication, and Applications.* Applied Sciences 09/2018; 8(9):1637. DOI:10.3390/app8091637

Marcello Meneghetti, Celine Caillaud, Radwan Chahal, Elodie Galdo, Laurent Brilland, Jean-Luc Adam, Johann Troles: *Purification of Ge-As-Se ternary glasses for the development of high quality microstructured optical fibers.* Journal of Non-Crystalline Solids 09/2018. DOI:10.1016/j.jnoncrysol.2018.09.028

Conference proceedings

Amar Nath Gosh, Marcello Meneghetti, Christian Rosenberg Petersen, Ole Bang, Laurent Brilland, Sebastien Venck, Johann Troles, John Michael Dudley, Thibaut Sylvestre, *Chalcogenide Glass Polarization-Maintaining Photonic Crystal Fiber for Mid-Infrared Supercontinuum Generation*, Conference on Lasers & Electro-Optics / Europe 2019

Marcello Meneghetti, Celine Caillaud, Radwan Chahal, Laurent Brilland, Johann Troles: *Fabrication of high optical quality Ge-As-Se glasses for the development of low-loss microstructured optical fibers.* Optical Components and Materials XVI (Vol. 10914, p. 109140X). International Society for Optics and Photonics; 2019, DOI:10.1117/12.2506267

Oral communications

Johann Troles, Marcello Meneghetti et. al: *Mid-infrared detection of organic compounds with a 2-10 μm supercontinuum source generated from concatenated fluoride and chalcogenide fibers*, SPIE Photonics West 2020 – BIOS, 1-7 February 2020, San Francisco, USA

Thibaut Sylvestre, Marcello Meneghetti et. al: *2-10 μm Mid-Infrared Supercontinuum Generation in Cascaded Optical Fibers: Experiment and modelling*, SPIE Photonics West 2020 – BIOS, 1-7 February 2020, San Francisco, USA

Johann Troles, Laurent Brilland, Marcello Meneghetti, Radwan Chahal, Catherine Boussard, Bruno Bureau, Sebastien Venck, Jean-Luc Adam, *Chalcogenide microstructured optical fibers for optical sensing*, Invited talk at 25th International Congress on Glass (ICG 2019), 9-14 June 2019, Boston, USA

Johann Troles , Marcello Meneghetti, Celine Caillaud, Laurent Brilland, Sébastien Venck, Jean-Luc Adam, Maxime Duris, Damien Deubel, Loïc Bodiou, Joel Charrier, Mathieu Carras, Mickael Brun, *Fabrication of low loss chalcogenide microstructured optical fibers for Mid-IR QCL pigtailing*, Invited talk at 25th International Congress on Glass (ICG 2019), 9-14 June 2019, Boston, USA

Amar Nath Gosh, Marcello Meneghetti, Christian Rosenberg Petersen, Ole Bang, Laurent Brilland, Sebastien Venck, Johann Troles, John Michael Dudley, Thibaut Sylvestre, *Chalcogenide Glass Polarization-Maintaining Photonic Crystal Fiber for Mid-Infrared Supercontinuum Generation*, Conference on Lasers & Electro-Optics / Europe, 23-27 June 2019, Munich, Germany

Marcello Meneghetti, Céline Caillaud, Radwan Chahal, Laurent Brilland, Johann Troles: *Fabrication of high optical quality Ge-As-Se glasses for the development of low-loss microstructured optical fibers*, SPIE Photonics West 2019 – OPTO, 2-7 February 2019, San Francisco, USA

Johann Troles, Marcello Meneghetti, Laurent Brilland, Celine Caillaud, Sebastien Venck, Yiming Wu, Jean-Luc Adam: *Fabrication of chalcogenide microstructured optical fibers for the 2-10* μm *Mid-IR window*, Invited talk at Advanced architectures in photonics 2018, 2-5 September 2018, Cambridge, UK

Johann Troles , Celine Caillaud, Marcello Meneghetti, Yiming Wu, Christian Rosenberg Petersen , Ole Bang , Jean-Luc Adam, Laurent Brilland: *Fabrication of tapered chalcogenide microstructured optical fibers for enhancing the non linear properties*, ACERS GOMD 2018, May 20-24 2018, San Antonio, USA

Johann Troles, Celine Caillaud, Marcello Meneghetti, Christian Rosenberg Petersen, Ole Bang, Jean-Luc Adam, Laurent Brilland: *Elaboration of chalcogenide microstructured optical fibers for generation of mid-IR supercontinuum*, Invited talk at 5th Workshop on Speciality Optical Fibers and Their Applications, 11-13 October 2017, Limassol, Cyprus

UNIVERSITE MATIERE BRETAGNE MOLECULES LOIRE ET MATERIAUX

UNIVERSITÉ DE RENNES 1

Title: Microstructured optical fibers based on chalcogenide glasses for mid-IR supercontinuum generation

Keywords: chalcogenide glasses, chemical purification, optical fibers, supercontinuum

Abstract:
In the framework of the SUPUVIR project, whose objective is to improve supercontinuum sources from the ultraviolet to the mid infrared, this work is focused on the development and fabrication of mid-IR optical fibers. More specifically the objective set was to realize high quality infrared (in the 2-12 μm wavelength range) fibers based on chalcogenide glasses, with a dispersion profile tailored by combining glass sciences and innovative fiber shaping techniques, to be used for mid-IR supercontinuum generation. In order to be suitable for this application, the fiber design needs to be a best compromise between nonlinear parameters (mainly controlled by the core size and chalcogenide composition), position of the zero dispersion wavelength (depending on desired pump wavelength), power handling properties and breadth of the transmission window. In this thesis, the production and characterization of microstructured fibers is detailed, starting from the choice and purification of the most proper chalcogenide glasses up to the production of a working prototype of commercial mid infrared supercontinuum fiber source, spanning from 2 to 10 μm, and to its application to spectroscopy. In addition, the development of the first chalcogenide graded index (Grin) fiber reported in literature is described, together with its characterization and the application of its production technique to the fabrication of Grin microlenses.

Titre: Fibres microstructurés en verres de chalcogénures pour la génération de supercontinuum dans le moyen infrarouge

Mots clés: verres de chalcogénures, purifications, fibres optiques infrarouges, supercontinuum

Résumé:
Ce travail de thèse s'est déroulé dans le cadre d'un projet européen, nommé SUPUVIR, dont l'objectif est d'améliorer les sources de supercontinuum de l'ultraviolet ou moyen infrarouge (MIR). Dans ce contexte, le travail de thèse s'est concentré sur le développement et la réalisation de fibres optiques en verres de chalcogénures transparentes dans le moyen infrarouge. Plus précisément, l'objectif était de réaliser des fibres infrarouges transparentes dans la plage de longueurs d'onde allant de 2 à 12 μm avec un profil de dispersion sur mesure en associant la science du verre et des techniques innovantes de mise en forme des fibres afin de les utiliser pour la réalisation de nouvelles sources dans le moyen infrarouge. Afin de convenir à cette application, la fibre optique doit présenter le meilleur compromis entre les paramètres non linéaires (principalement contrôlés par la taille du cœur et la composition du verre), la position de la longueur d'onde de dispersion nulle (en fonction de longueur d'onde souhaitée de la pompe) et la fenêtre de transmission infrarouge. Au cours de ces travaux, des fibres microstructurées avec des verres de haute pureté ont pu être fabriquées. L'utilisation de ces fibres a permis l'obtention de supercontinua étendus de 2 à 10 μm. L'utilisation de cette source a ensuite permis la détection de signatures infrarouges d'un composé chimique et aussi montré le fonctionnement d'un spectromètre original utilisant un supercontinuum. Enfin, au cours de ces travaux de thèse, la première fibre optique à gradient d'indice en verres de chalcogénures a été fabriquée et ses propriétés de transmission et de dispersion ont été mesurées et étudiées.